UAB
Universitat Autònoma de Barcelona

# New Analytical Strategies for Heavy Metals Monitoring in Water Samples using Carbon Dots

**Alex Pascual Esco**

**ADVERTIMENT.** L’accés als continguts d’aquesta tesi queda condicionat a l’acceptació de les condicions d’ús establertes per la següent llicència Creative Commons: cc BY SA https://creativecommons.org/licenses/?lang=ca

**ADVERTENCIA.** El acceso a los contenidos de esta tesis queda condicionado a la aceptación de las condiciones de uso establecidas por la siguiente licencia Creative Commons: cc BY SA https://creativecommons.org/licenses/?lang=es

**WARNING.** The access to the contents of this doctoral thesis it is limited to the acceptance of the use conditions set by the following Creative Commons license: cc BY SA https://creativecommons.org/licenses/?lang=en

Universitat Autònoma de Barcelona

# New Analytical Strategies for Heavy Metals Monitoring in Water Samples using Carbon Dots

**Alex Pascual Esco**

TESI DOCTORAL

Programa de Doctorat en Química

Directora: Maria del Mar Puyol Bosch

Departament de Química

Facultat de Ciències

2023

Memòria presentada per aspirar al Grau de Doctor per

**Alex Pascual Esco**

Vist i plau

**Maria del Mar Puyol Bosch**

Professora Titular

Departament de Química

Bellaterra, 21 de Setembre de 2023

This thesis was carried out with the following financial support:

- **Grant PRE2018-084834** funded by MCIN/AEI/10.13039/501100011033 and by "ESF Investing in your future".

- **CTQ2017-85011-R**: "Lab on a Chip multiparamétricos para aplicaciones aeroespaciales, medioambientales, agroalimentarias y biomédicas". Ministerio de Economía y Competitividad, co-funded by FEDER.

- **PID2020-117216RB-I00:** "Estrategias innovadoras de sensado basadas en la tecnología de microsistemas para las demandas analíticas actuales en medio ambiente, agroalimentario y biomedicina". Ministerio de Ciencia e Innovación, co-funded by FEDER.

- **2017SGR-220**: Grup de Sensors i Biosensors. Departament d'Universitats, Recerca i Societat de la Informació. Generalitat de Catalunya.

- **2021SGR00124**: Grup de Sensors i Biosensors. Departament d'Universitats, Recerca i Societat de la Informació. Generalitat de Catalunya.

# Acknowledgements

Quiero aprovechar estas líneas para dar la gracias a todas las personas que me han acompañado en un momento u otro de este largo trayecto que ha supuesto el Doctorado.

En primer lugar, quería dar las gracias a Mar, mi directora de tesis, por la confianza que depositó en mí y por toda su ayuda y dedicación durante la realización de la tesis. También le quería agradecer las correcciones y comentarios de la tesis que han permitido elevar el nivel de este trabajo. Valoro mucho todos estos años que hemos pasado juntos en los que he aprendido mucho. De la misma manera quería agradecer a Julián que también apostase por mí para la realización de esta tesis y por todos los conocimientos que me ha transmitido durante esta etapa.

También quiero agradecer al resto de miembros del grupo de microsistemas analíticos con los que he compartido esta etapa, tanto los que ya se fueron como los que siguen en el grupo, en especial quiero destacar a Bea con la que he compartido gran parte del Doctorado (es de agradecer tener a alguien con quien compartir los problemas que surgen durante este tortuoso trayecto), y a Toni y a Eva que siempre han estado ahí con cualquier problema o duda que haya podido tener (lo cual valoro mucho), de los que he aprendido mucho y con los que he compartido muchos momentos. No me quiero olvidar tampoco de Pedro y Natàlia con los que también he compartido algún tiempo y me han aportado conocimientos que aparecen reflejados en este trabajo.

También quiero destacar a Miki que fue el que me introdujo en el tema del que trata esta tesis y me enseñó infinidad de cosas y trucos que me han sido muy útiles para el desarrollo de la tesis y a Mariona con la que compartí los primeros años de investigación en el laboratorio de ópticos y con la que viví muchos buenos momentos y también algunos malos. Te deseo que te vaya muy bien en todo lo que hagas. No me quiero olvidar tampoco de los TFGs que han ido pasando por el laboratorio de ópticos y que me han ayudado a sacar adelante este trabajo, Wenqian, Roger, Pau y, por último, Pere.

Quiero mencionar al personal de Secretaría del Departamento de Química de la UAB, en especial a Elena, que tantas dudas me ha resuelto durante todo el Doctorado, y a otras personas que han hecho posible la realización de esta tesis: al personal del SAQ de la UAB (en especial a Ignasi Villarroya), a Martí de Cabo del Servei de Microscòpia de la UAB, y a Javier Saiz y a Bernat Mundet del ICN2.

Una etapa muy importante del Doctorado fue mi estancia en el grupo de Analytical Development del LAQV Requimte de la Universidade do Porto. Durante mi tiempo allí aprendí mucho sobre electroquímica, un ámbito bastante desconocido para mí hasta ese momento. Quiero agradecer al Profesor Alberto Araújo que fue el responsable de mi estancia, pero no sólo eso, durante mi tiempo allí se convirtió en una persona muy importante que me ayudó en todo lo que necesité, y con el que compartí muchos buenos momentos, incluso fuimos a ver un partido del Oporto. No olvidaré todo lo que hizo por mi durante esos meses. Asimismo, quiero agradecer también al resto de personas con las que conviví en esa etapa: Carina, Diana y Renato, mis compañeros de laboratorio que me ayudaron con todo desde el primer momento, y a los

Profesores/as Célia Amorim, João Prior, Marcela Segundo y Maria da Conceição con los que también compartí el día a día durante mi estancia en Oporto. Muito obrigado!

Por último, pero no por eso menos importante, quiero agradecer a mi familia el apoyo, en especial a mis padres, mis dos pilares principales a los que les debo todo lo que soy y lo que he conseguido y que siempre han estado ahí en los momentos difíciles. También quiero dar las gracias a mis amigos, tanto de la UAB como de mi infancia, en especial a Alejandro, mi mejor amigo, con el que he compartido tantas risas y tantos viajes.

En fin, seguro que me dejo a alguien y espero que me perdone si es así, pero quería destacar a todas estas personas que son las que me han acompañado en este trayecto.

# Abstract

The increasing demand for new automated analytical instrumentation and procedures for the continuous monitoring of different pollutants affecting water quality acquires special importance due to the consequences for human health and for the environment that the use or consumption of contaminated water causes. In this sense, micro-Total Analysis Systems or Lab-On-a-Chip devices have experienced a notable development in recent years owing to the enhanced mass and energy transport, miniaturization, integration, and automation that these systems are capable to achieve over macroscopic systems. All these features open the door to performing on-site measurements.

Furthermore, the use of nanoparticles has demonstrated to improve sensitivity and limits of detection (LODs) in analytical measurements. Taking this context into account, this work is focused on the use of Carbon Dots (CDs) as optical and electrochemical probes for the rapid determination of heavy metals in water. CDs have recently drawn great attention from the scientific community due to their excellent luminescent properties, high biocompatibility, ease of preparation, low cost, and high electrical conductivity, compared to other nanomaterials. These properties make CDs suitable for a wide range of applications, such as (bio)sensing, bioimaging, nanomedicine, and catalysis.

In this thesis, two different approaches for heavy metals determination employing CDs have been developed. In the first one, CDs are employed as optical probes and the determination of heavy metal ions is based on its quenching effect on the fluorescence of the CDs. In the second one, CDs have been used to modify Screen-Printed Carbon Electrodes (SPCEs) to determine $Cd^{2+}$ ions by stripping voltammetry.

Chronologically, an automated equipment based on a reverse Flow Injection Analysis protocol, that included a Cyclic Olefin Copolymer (COC) microfluidic platform, and a customized miniaturized optical detection system was developed to monitor heavy metals with CDs as optical probes. Different types of CDs were synthesized in batch using several hydrothermal and microwave-assisted methods and five heavy metal ions ($Co^{2+}$, $Cu^{2+}$, $Hg^{2+}$, $Ni^{2+}$, and $Pb^{2+}$) could be selectively determined using the developed experimental setup.

In order to improve reproducibility and reliability, microreactor technology was applied for the efficient synthesis of homogeneous and reproducible CDs. Therefore, Low Temperature Co-Fired Ceramics (LTCC) microreactors were fabricated and used for the synthesis of the CDs previously synthesized in batch. The syntheses were performed automatically with better control of the synthetic parameters. Some of the synthetic methods were adapted and optimized to be performed in the microreactors and four of the five heavy metal ions previously determined ($Co^{2+}$, $Cu^{2+}$, $Hg^{2+}$, and $Pb^{2+}$) could be also selectively determined. The obtained nanomaterials were used as optical probes in the previously developed automatic equipment. The LODs obtained for three of the four heavy metal ions were below the limits set for drinking water, while in the case of $Hg^{2+}$, it was slightly higher.

Finally, to demonstrate the applicability of the analytical equipment for on-site monitoring of heavy metals in water, an integrated system including the direct synthesis of the optical probes by means of a microreactor was designed, fabricated, and evaluated. To validate the proposal, one type of CDs was synthesized and directly used for the selective determination of $Co^{2+}$ in the customized miniaturized optical detection system.

Synthetic and real water samples were analyzed obtaining good results in terms of accuracy and precision demonstrating the potential of the developed system for on-site monitoring of heavy metals in water.

In the scope of a research stay in the group Analytical Development LAQV Requimte from the Universidade do Porto, the effect of modifying SPCEs with CDs and carbon nanotubes to determine $Cd^{2+}$ ions by stripping voltammetry was tested. The methodology established allowed the selective determination of $Cd^{2+}$ ions with a LOD below the limit set for drinking water.

The obtained results through all the research work demonstrate the great potential of miniaturized analytical systems based on the use of CDs for the monitoring of heavy metals in water using different techniques.

# Resumen

La creciente demanda de nueva instrumentación y procedimientos analíticos automatizados para la monitorización continua de diferentes contaminantes que afectan a la calidad del agua adquiere especial importancia debido a las consecuencias para la salud humana y para el medio ambiente que provoca el uso o consumo de agua contaminada. En este sentido, los Microsistemas de Análisis Total o dispositivos *Lab-On-a-Chip* han experimentado un notable crecimiento en los últimos años debido a la mejora en el transporte de masa y energía, la miniaturización, la integración y la automatización que estos sistemas son capaces de lograr frente a los dispositivos macroscópicos. Todas estas características abren la puerta a la realización de mediciones *in situ*.

Además, se ha demostrado que el uso de nanopartículas mejora la sensibilidad y los límites de detección en las medidas analíticas. Teniendo en cuenta este contexto, este trabajo se centra en el uso de Puntos de Carbono (CDs, por sus siglas en inglés) como sensores ópticos y electroquímicos para la determinación de metales pesados en agua. Recientemente, los CDs han llamado mucho la atención de la comunidad científica debido a sus excelentes propiedades luminiscentes, alta biocompatibilidad, facilidad de preparación, bajo coste y buena conductividad eléctrica en comparación con otros nanomateriales. Estas propiedades hacen que los CDs sean adecuados para una amplia gama de aplicaciones, como la (bio)detección, la bioimagen, la nanomedicina, o la catálisis.

En esta tesis, se han desarrollado dos métodos diferentes para la determinación de metales pesados usando CDs. En el primero de ellos, los CDs se utilizan como sensores ópticos y la determinación de iones de metales pesados se basa en su efecto de atenuación sobre la fluorescencia de los CDs. En el segundo, los CDs se usan para modificar Electrodos de Carbono Serigrafiados (SPCEs, por sus siglas en inglés) para determinar iones $Cd^{2+}$ mediante voltamperometría de redisolución.

Cronológicamente, se desarrolló un equipo automatizado basado en un protocolo de análisis de inyección en flujo reverso, que contiene una plataforma microfluídica de Copolímero de Olefina Cíclica (COC, por sus siglas en inglés) que se inserta en un sistema personalizado y miniaturizado de detección óptica para monitorizar metales pesados usando CDs como sensores ópticos. Se sintetizaron en discontinuo (*batch*) diferentes tipos de CDs utilizando varios métodos hidrotermales y asistidos por microondas y se pudieron determinar selectivamente cinco iones de metales pesados ($Co^{2+}$, $Cu^{2+}$, $Hg^{2+}$, $Ni^{2+}$ y $Pb^{2+}$) utilizando la configuración experimental desarrollada.

Para tratar de mejorar la fiabilidad, se aplicó la tecnología de microreactores para aumentar la eficiencia, la reproducibilidad y la homogeneidad en la síntesis de CDs. Por este motivo, se fabricaron y utilizaron microreactores de Cerámica de Cocción a Baja Temperatura (LTCC, por sus siglas en inglés) para la síntesis de los CDs previamente sintetizados en *batch*. Las síntesis que se desarrollan en los microreactores LTCC se realizan de forma automática y permiten un mejor control de los parámetros de síntesis. Algunos de los métodos sintéticos fueron adaptados y optimizados para ser realizados en los microreactores y cuatro de los cinco iones de metales pesados previamente determinados ($Co^{2+}$, $Cu^{2+}$, $Hg^{2+}$ y $Pb^{2+}$) también

pudieron determinarse selectivamente con estos CDs. Los nanomateriales obtenidos, se utilizaron como sensores ópticos en el equipo automatizado previamente desarrollado. Los límites de detección obtenidos para tres de los cuatro iones de metales pesados estuvieron por debajo de los límites establecidos para el agua potable, mientras que en el caso del $Hg^{2+}$, el límite de detección obtenido fue ligeramente superior.

Finalmente, se diseñó, fabricó y evaluó un sistema integrado que incluye la síntesis directa de CDs usando un microreactor para demostrar la aplicabilidad del equipo para la monitorización *in situ* de metales pesados en agua. Para validar la propuesta, se sintetizó un tipo de CDs y se utilizó directamente para la determinación selectiva de $Co^{2+}$ en el sistema de detección óptica.

Se analizaron muestras de agua sintéticas y reales obteniéndose buenos resultados en términos de exactitud y de precisión demostrando el potencial del sistema desarrollado para el control *in situ* de metales pesados en agua.

Dentro del marco de la estancia en el grupo de *Analytical Development* del LAQV Requimte de la Universidade do Porto, se estudió el efecto de la modificación de SPCEs con CDs y nanotubos de carbono para la determinación de iones $Cd^{2+}$ mediante voltamperometría de redisolución. Se consiguió determinar selectivamente iones $Cd^{2+}$ con un límite de detección por debajo del límite establecido para agua potable.

Los resultados obtenidos durante la realización de este trabajo demuestran el gran potencial de los sistemas analíticos miniaturizados basados en el uso de CDs para la monitorización de metales pesados en agua mediante diferentes técnicas.

# Resum

La creixent demanda de nova instrumentació i procediments analítics automatitzats per a la monitorització contínua de diferents contaminants que afecten la qualitat de l'aigua pren una gran importància a causa de les conseqüències per a la salut humana i per al medi ambient que provoca l'ús o el consum d'aigua contaminada. En aquest sentit, els Microsistemes d'Anàlisi Total o dispositius *Lab-On-a-Chip* han experimentat un notable creixement en els darrers anys a causa de la millora en el transport de massa i energia, la miniaturització, la integració i l’automatització que aquests sistemes són capaços d’aconseguir en comparació als dispositius macroscòpics. Totes aquestes característiques obren la porta a la realització de mesures *in situ*.

A més, s'ha demostrat que l'ús de nanopartícules millora la sensibilitat i els límits de detecció de les mesures analítiques. Tenint en compte aquest context, aquest treball es basa en l'ús de Punts de Carboni (CDs, per les sigles en anglès) com a sensors òptics i electroquímics per a la determinació de metalls pesants en aigua. Recentment, els CDs han cridat molt l'atenció de la comunitat científica a causa de les seves excel·lents propietats luminescents, l’alta biocompatibilitat, la facilitat de preparació, el baix cost i la bona conductivitat elèctrica en comparació amb altres nanomaterials. Aquestes propietats fan que els CDs siguin adequats per a una àmplia gamma d'aplicacions, com la (bio)detecció, la bioimatge, la nanomedicina o la catàlisi.

En aquesta tesi, s’han desenvolupat dos mètodes diferents per la determinació de metalls pesants utilitzant CDs. En el primer, els CDs s’utilitzen com a sensors òptics i la determinació d’ions de metalls pesants es basa en el seu efecte d’atenuació sobre la fluorescència dels CDs. En el segon, els CDs s’utilitzen per modificar Elèctrodes de Carboni Serigrafiats (SPCEs, per les sigles en anglès) per determinar ions $Cd^{2+}$ mitjançant voltamperometria per redissolució.

Cronològicament, es va desenvolupar un equip automatitzat basat en un protocol d'anàlisi per injecció en flux revers, que conté una plataforma microfluídica de Copolímer d'Olefina Cíclica (COC, per les sigles en anglès) que s'insereix en un sistema personalitzat i miniaturitzat de detecció òptica per monitoritzar metalls pesants utilitzant els CDs com a sensors òptics. Es van sintetitzar en discontinu (*batch*) diferents tipus de CDs utilitzant diversos mètodes hidrotermals i assistits per microones i es van poder determinar selectivament cinc ions de metalls pesants ($Co^{2+}$, $Cu^{2+}$, $Hg^{2+}$, $Ni^{2+}$ i $Pb^{2+}$) utilitzant la configuració experimental desenvolupada.

Per tal de millorar la fiabilitat, es va aplicar la tecnologia de microreactors per augmentar l’eficiència, la reproductibilitat i la homogeneïtat en la síntesi dels CDs. Per aquest motiu, es van fabricar i utilitzar microreactors de Ceràmica de Cocció a Baixa Temperatura (LTCC, per les sigles en anglès) per a la síntesi dels CDs prèviament sintetitzats en *batch*. Les síntesis en els microreactors LTCC es realitzen de forma automàtica i permeten un millor control dels paràmetres de síntesi. Alguns dels mètodes sintètics van ser adaptats i optimitzats per ser realitzats als microreactors i quatre dels cinc ions de metalls pesants prèviament determinats ($Co^{2+}$, $Cu^{2+}$, $Hg^{2+}$ i $Pb^{2+}$) també es van poder determinar selectivament amb aquests CDs. Els nanomaterials obtinguts es van utilitzar com a sensors òptics en l’equip automatitzat prèviament desenvolupat. Els límits de detecció obtinguts per a tres dels quatre ions

de metalls pesants estaven per sota dels límits establerts per a l'aigua potable, mentre que en el cas del $Hg^{2+}$, el límit de detecció obtingut va ser lleugerament superior.

Finalment, es va dissenyar, construir, i avaluar un sistema integrat que inclou la síntesi directa de CDs utilitzant un microreactor per demostrar l'aplicabilitat del sistema per a la monitorització *in situ* de metalls pesants en aigua. Per validar la proposta, es van sintetitzar un tipus de CDs i es van utilitzar directament per a la determinació selectiva de $Co^{2+}$ al sistema de detecció òptica.

Es van analitzar mostres d'aigua sintètiques i reals obtenint bons resultats en termes d’exactitud i de precisió demostrant el potencial del sistema desenvolupat per al control *in situ* de metalls pesants en aigua.

En el marc de l’estada en el grup de *Analytical Development* del LAQV Requimte de la Universidade do Porto, es va estudiar l’efecte de la modificació de SPCEs amb CDs i nanotubs de carboni per la determinació d’ions $Cd^{2+}$ mitjançant voltamperometria per redissolució. Es va aconseguir determinar selectivament ions $Cd^{2+}$ amb un límit de detecció per sota del límit establert per a l’aigua potable.

Els resultats obtinguts durant la realització d’aquest treball demostren el gran potencial dels sistemes analítics miniaturitzats basats en l’ús de CDs per a la monitorització de metalls pesants en aigua mitjançant diferents tècniques.

# Table of Contents

# Acronyms

| | |
|---|---|
| **µTAS** | micro-Total Analysis System |
| **AAS** | Atomic Absorption Spectroscopy |
| **ACR CDs** | CDs synthesized from acrylic acid and ethylenediamine |
| **ATR** | Attenuated Total Reflectance |
| **BPR** | Back-Pressure Regulator |
| **CAD** | Computer-Aided Design |
| **CDs** | Carbon Dots |
| **CL** | Chemiluminescence |
| **CNC** | Computer Numerical Control |
| **CNDs** | Carbon Nanodots |
| **CNTs** | Carbon Nanotubes |
| **COC** | Cyclic Olefin Copolymer |
| **CQDs** | Carbon Quantum Dots |
| **CV** | Cyclic Voltammetry |
| **D** | Dialyzed |
| **DAQ** | Data Acquisition Card |
| **DLS** | Dynamic Light Scattering |
| **DPV** | Differential Pulse Voltammetry |
| **EA CDs** | CDs synthesized from glycerol and ethylenediamine |
| **ECL** | Electrochemiluminescence |
| **ED** | Ethylenediamine |
| **ED CDs** | CDs synthesized from citric acid and ethylenediamine |
| **EU** | European Union |
| **FIA** | Flow Injection Analysis |
| **FRET** | Förster Resonance Energy Transfer |
| **FTIR** | Fourier Transformed Infrared Spectroscopy |
| **GO** | Graphene Oxide |
| **GQDs** | Graphene Quantum Dots |

| | |
|---|---|
| **GSB** | Group of Sensors and Biosensors |
| **HOMO** | Highest Occupied Molecular Orbital |
| **HRTEM** | High Resolution Transmission Electron Microscopy |
| **ICP-MS** | Inductively Coupled Plasma Mass Spectrometry |
| **ICP-OES** | Inductively Coupled Plasma Optical Emission Spectroscopy |
| **IFE** | Inner Filter Effect |
| **IPCA** | 5-oxo-1,2,3,5-tetrahydroimidazo[1,2-]pyridine-7-carboxylic acid |
| **ISC** | Intersystem Crossing |
| **$K_{SV}$** | Stern-Volmer quenching constant |
| **LED** | Light Emitting Diode |
| **LOC** | Lab-on-a-Chip |
| **LOD** | Limit of Detection |
| **LTCC** | Low Temperature Co-Fired Ceramics |
| **LUMO** | Lowest Unoccupied Molecular Orbital |
| **MET CDs** | CDs synthesized from acrylic acid and methionine |
| **MWCNTs** | Multi-Walled Carbon Nanotubes |
| **ND** | Non-Dialyzed |
| **nFIA** | normal Flow Injection Analysis |
| **PA CDs** | CDs synthesized from sodium citrate and polyacrylamide |
| **PCB** | Printed Circuit Board |
| **PEI CDs** | CDs synthesized from citric acid and polyethyleneimine |
| **PET** | Photoinduced Electron Transfer |
| **PL** | Photoluminescence |
| **QDs** | Quantum Dots |
| **QYs** | Quantum Yields |
| **rFIA** | reverse Flow Injection Analysis |
| **RSD** | Relative Standard Deviation |
| **RTP** | Room Temperature Phosphorescence |
| **SD** | Standard Deviation |
| **SPCE** | Screen-Printed Carbon Electrode |
| **SPR** | Surface Plasmon Resonance |

| | |
|---|---|
| **STEM** | Scanning Transmission Electron Microscopy |
| **SWCNTs** | Single-Walled Carbon Nanotubes |
| **SWSV** | Square Wave Stripping Voltammetry |
| **SWV** | Square Wave Voltammetry |
| **TEM** | Transmission Electron Microscopy |
| $T_g$ | Glass Transition Temperature |
| **UREA CDs** | CDs synthesized from citric acid and urea and modified with imidazole |
| **US EPA** | United States Environmental Protection Agency |
| **UV** | Ultraviolet |
| **Vis** | Visible |
| **WHO** | World Health Organization |

# List of Figures

# List of Tables

# 1 Introduction

## 1.1 Contamination of water bodies

Water is one of the most essential resources of nature because it is necessary for all living beings. However, the presence of water on Earth is limited, even more, if it is freshwater. The fast growth of the population in the last decades and the development of society by means of industrialization have increased the demand for freshwater globally and, considering that it is crucial for human beings to have access to safe and good-quality water, its contamination has emerged as a public concern [1].

Surface freshwater can be contaminated by geogenic contaminants but considering that the contact time of water with its geographical space is short due to the flow, its impact is lower than that coming from anthropogenic sources like mining, farming, and domestic and industrial use [2]. The intake of polluted water can cause a lot of different diseases, including diarrhea, dysentery, typhoid fever, or salmonellosis, as the most common ones, but the presence of contaminants in water also increases the risk of having cancer, cardiovascular diseases, and mental disorders [3].

The contaminants present in drinking water can be generally divided into physical contaminants (that affect the physical properties or appearance of water, for example, suspended sediments), biological contaminants (parasites, bacteria, viruses, etc.), radiological contaminants (like plutonium and uranium), and chemical contaminants that include a large variety of substances (some of the most common ones are pesticides, metals, or drugs) [4].

### 1.1.1 Heavy metals pollution

Among all the chemicals that can contaminate water, heavy metals pose a serious threat to human health. Heavy metals can be defined as those metals with a specific density larger than 5 g/cm$^3$ [5,6]. They are naturally present in the environment at low concentrations but some anthropogenic activities, including mining, the use of pesticides, and the disposal of industrial and agricultural wastes, contribute to their accumulation [7]. Its danger comes from their solubility in water and the capability of being absorbed by living beings considering that are not biodegradable and have the tendency to accumulate in different tissues, becoming toxic. While some of them are highly toxic even at very low concentrations (arsenic, cadmium, lead, mercury, etc.), others are nutritionally essential at low concentrations (chromium, cobalt, copper, iron, nickel, zinc, etc.), but become toxic at higher concentrations [8-10]. The presence of heavy metals in the body above threshold levels causes a wide variety of negative effects:

- Arsenic: many health problems are associated with arsenic including skin lesions, disturbances in cognitive development, diabetes, cardiovascular diseases, and different types of cancer [11].

● Cadmium: $Cd^{2+}$ ions tend to replace $Ca^{2+}$ ions, thus producing some affectations in the bones like osteoporosis. Cadmium is stored in the kidneys and liver which causes problems in both organs. It also increases the risk of having different types of cancer [12].

● Chromium: the problems involved with chromium normally include hair loss, abnormalities of teeth like discoloration and erosion, diarrhea, and renal and cardiac disorders. It also has a carcinogenic impact, mainly on the respiratory system [13].

● Cobalt: an excessive amount of cobalt in the body can cause asthma, rhinitis, gastritis, and, in severe cases, cardiomyopathy [14,15].

● Copper: the accumulation of this element in humans is associated with brain damage, liver diseases such as cirrhosis, anemia, and gastrointestinal problems [16].

● Iron: is one of the most important nutrients for humans but an excess, causes different undesired effects, for example, gastrointestinal problems and different blood-related diseases [5,17].

● Lead: is a non-essential heavy metal and when enters the body it normally attacks the brain and the central nervous system. Some of the most common effects produced by lead are loss of short-term memory, impaired development, problems in coordination, hypertension, and an enhanced risk for cardiovascular diseases. Its carcinogenic effect is also very important [1,18].

● Mercury: is one of the most dangerous heavy metals due to its capability of accumulating in the bodies of animals and human beings. It causes renal damage and affects the nervous system and the brain producing effects like depression, loss of memory, trembling, insomnia, or vision problems. Mercury is also cataloged as carcinogenic [18].

● Nickel: the presence of high concentrations of nickel in the human body can cause chronic asthma, cardiovascular and kidney diseases, and dermatitis. It also has been reported to induce cancer [19].

● Zinc: toxicity of zinc is associated with depression, fatigue, giddiness, and different neurological problems [1].

Taking these effects into account, it is essential to set heavy metal concentration limits in drinking water. Different organizations such as the European Union (EU), the United States Environmental Protection Agency (US EPA), and the World Health Organization (WHO) have established heavy metals maximum levels in drinking water, and some of them are listed in Table 1.1.

Table 1.1: EU, US EPA, and WHO standards for some heavy metals in drinking water

| Heavy metal | EU standard (mg/L) | US EPA standard (mg/L) | WHO standard (mg/L) |
|---|---|---|---|
| Arsenic | 0.01 | 0.01 | 0.01 |
| Cadmium | 0.005 | 0.005 | 0.003 |
| Chromium | 0.05 | 0.1 | 0.05 |
| Cobalt | - | 0.1 | - |
| Copper | 2.0 | 1.3 | 2.0 |
| Iron | 0.2 | 0.3 | - |
| Lead | 0.01 | 0.015 | 0.01 |
| Mercury | 0.001 | 0.002 | 0.006 |
| Nickel | 0.02 | - | 0.07 |
| Zinc | - | 5.0 | - |

### 1.1.2 Environmental control of heavy metals in water

Multiple techniques for heavy metal detection in water are available, but up to now the control of heavy metals in water is still based on manual sampling and then transportation of the sample to perform laboratory analysis. The most common techniques used for the detection of heavy metals in water samples are inductively coupled plasma mass spectrometry (ICP-MS), inductively coupled plasma optical emission spectroscopy (ICP-OES), atomic absorption spectroscopy (AAS), and X-ray fluorescence (XRF) [20]. The mentioned techniques are well established due to their adequate analytical performance (low limits of detection (LODs), sensitivity, precision, and accuracy), but they present some important drawbacks such as the need for bulky and expensive equipment and trained personnel for making the analysis [7]. Other types of methods have appeared to overcome these limitations, and some of them are even used in control stations to monitor the concentration of heavy metals continuously by using them in combination with flow injection analysis (FIA) techniques.

The first type of methods are the electrochemical ones that do not require specialized personnel, are more economic, and are less time-consuming than spectroscopic techniques. This group of techniques are based on the change of different electrical parameters such as current, voltage, or impedance that produce the presence of heavy metal ions in water. Based on the parameter affected, they can be classified into voltammetry (these, in turn, are classified into Cyclic Voltammetry (CV), Differential Pulse Voltammetry (DPV), and Square Wave Voltammetry (SWV)), potentiometry, amperometry, coulometry, impedance, and electrochemiluminescence (ECL). These techniques normally show lower sensitivity and higher LODs compared to other techniques, but this performance can be improved by the modification of the sensing electrodes. These modifications can also enhance the selectivity towards specific heavy metal ions [21].

Another type of methods employed are the ones that take profit from the optical properties of different materials in contact with heavy metal ions and include absorption, reflection, and photoluminescent spectroscopy. A wide variety of compounds/materials are used for the optical detection of heavy metals like indicator dyes, chromoionophores, photoluminescent probes, etc. These techniques normally use selective optical probes for the determination of a heavy metal ion [22].

Most of the techniques described in this section can be used for the multiparametric determination of different heavy metals and several examples can be found in the literature. Some examples can be found for ICP-MS [23,24], ICP-OES [25,26], AAS [27], CV [28], DPV [29-31], SWV [32-34], colorimetric methods [35,36], and fluorescent methods [37,38].

### 1.1.3 Flow injection analysis

FIA is based on the injection of a sample into a continuously flowing stream (carrier), which is automatically directed towards a detector [39,40]. FIA was first introduced in 1975 by Ruzicka and Hansen [41] and arose in the last decades because of the growing trend towards automation of analytical processes. Unlike other techniques, the analytical signal is transitory and can be optimized to achieve larger sampling rates, and improved LODs and selectivity [42].

Automation avoids human errors in measurements and, in addition to that, presents the following advantages: reduction of reagent and sample consumption, reduction of waste generation, increased repeatability, and reduction of analysis time [40,43]. Along with automation, FIA presents other advantages like simplicity, flexibility, and adaptability [42].

Although the above description of FIA is understood as normal flow injection analysis (nFIA), other configurations can be used. Among them, one of the most important is reverse flow injection analysis (rFIA), in which reagents are injected into a sample carrier [44,45]. This technique is suited when the amount of reagent is limited [46]. Some of the advantages of rFIA compared to nFIA are:

- The reduction of reagent consumption. This is particularly important for expensive or environmentally dangerous reagents. Consequently, it also offers less maintenance for reagents withdrawal [35].

- Sample dispersion is reduced, leading to an improvement in sensitivity [44].

- Higher baseline stability [47].

One of the most important limitations of the technique is the need for large sample volumes. For this reason, a lot of rFIA-based systems have been developed for water analysis applications, where sample volume is not an issue [43].

## 1.2 Miniaturization of analytical systems

The increasing demand for rapid, efficient, and exact analytical methods for environmental control has boosted the research and development of miniaturized systems. Miniaturization in analytical systems can generally be defined as the trend to downscale chemical systems, which present some advantages compared to conventional ones. These are discussed in Section 1.2.3, but briefly, such systems are capable of performing on-site analysis of samples in real time, at low cost, with a high sample throughput, with less amount of reagents, and consuming less energy.

In this context, the concept of micro-Total Analysis System (µTAS), also known as Lab-on-a-chip (LOC) (Figure 1.1), appeared in 1990 [48] and gave a push on the development of miniaturized analytical systems. These devices work at the microscale, taking advantage of the properties of microfluidics, where the increased surface-to-volume ratio stands out, enabling quick and efficient heat and mass transfer [49].

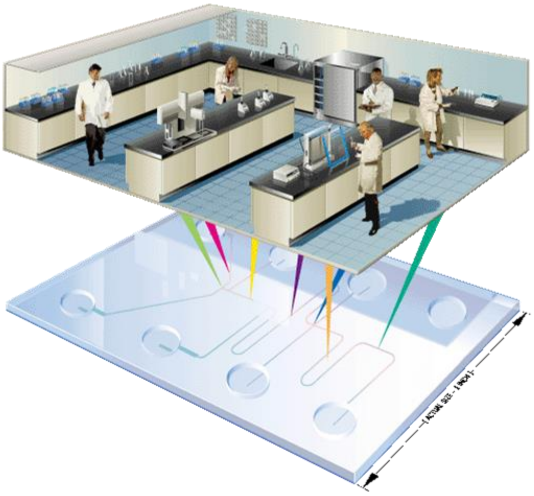

Figure 1.1: Concept of LOC devices [50]

Taking all these aspects into account, there is no doubt that miniaturized chemical analysis systems have enormous potential. For instance, it is expected that these types of devices can find the market of environmental monitoring [51], food analysis [52], industry [53], study of complex cellular processes [54-56], and medicine [57,58].

### 1.2.1 Theoretical aspects

The first aspect to consider is that many of the advantages that microfluidics present are originated from the differential behavior of fluids on the microscale compared to the macroscale [59]. As commented before, the high surface-to-volume ratio plays an important role on the microscale, empowering surface phenomena like viscosity and surface tension, as the phenomena that control the properties of fluids at this scale, instead of volume phenomena, such as gravity or inertia, that control properties of fluids at the macroscale [60]. As viscous forces dominate over inertial forces at the microscale, laminar flow is observed, as opposed to the turbulent flow observed at the macroscale (Figure 1.2).

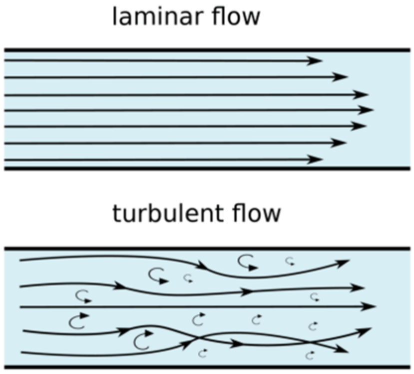

Figure 1.2: Schematic representation of laminar and turbulent flow regimes [61]

Reynolds number is a dimensionless parameter that is used to characterize the type of flow, and can be calculated by the following equation:

$$R_e = \frac{\rho\, D_h\, \vartheta}{\mu} \qquad \text{Equation 1}$$

where ρ is the fluid density, $D_h$ is the hydraulic diameter of the channel, $\vartheta$ is the fluid velocity and μ is the dynamic viscosity. The lower the value of $R_e$, the closer the behavior of the flow to a laminar flow. Generally, systems are considered to be in the laminar flow regime for $R_e$ values below 2000. This value is well below for microfluidic systems [62,63].

Given the fact that fluids are in the laminar flow regime, diffusion is an important parameter, since it is the only phenomenon by which mixing occurs. Diffusion is defined as the process of spreading molecules from a region of higher concentration to one of lower concentration by Brownian motion, which results in a gradual mixing. Diffusion is described mathematically using Fick's law:

$$j = -D\frac{d\varphi}{dx} \qquad \text{Equation 2}$$

where φ is the species concentration, x is the position of the species, and D is the diffusion coefficient. Although mixing in microfluidic systems is limited only to diffusion, the reduced dimensions of the channels (l) imply very low diffusion times ($t_D$):

$$t_D = \frac{l^2}{D} \qquad \text{Equation 3}$$

For instance, diffusion time is only 100 ms for devices of a typical length of 10 mm [63].

Another important parameter regarding microfluidics is the thermal Péclet number ($P_e$), which is a dimensionless parameter that measures the relative importance of advection and diffusion in heat transfer [49,62], and it can be calculated by the following equation:

$$P_e = \frac{\rho\, C_p\, d\, \vartheta}{k} \qquad \text{Equation 4}$$

where ρ is the fluid density, $C_p$ is the specific heat capacity, d is the channel diameter, $\vartheta$ is the fluid velocity and k is the thermal conductivity. This parameter indicates that when heat is applied to a microfluidic channel, it can be transported in the direction in which the fluid is moving (advective transport) or from the wall of the microfluidic channel to the center of the fluid (diffusive transport). In microfluidics, values of $P_e$ are lower than 1, enabling the prevalent diffusive transport. This, at the same time, leads to a more homogeneous temperature distribution [64,65].

### 1.2.2 Microfluidic platforms

Microfluidic platforms are essential elements in the development of miniaturized analytical systems. They are devices that provide connectivity between the different operations of the chemical analysis [66]. However, microfluidic platforms usually require some external instrumentation to be completely functional, for instance, to perform fluid management. Taking this into account, microfluidic platforms can be divided into different groups according to the propulsion principle that is being used. Mainly, passive fluid control techniques (capillarity [67]) or external actuators based on different principles (pressure-driven [68,69], centrifugal [70], electrokinetic [71,72], and acoustic systems [73]) can be used. Throughout this thesis, only pressure-driven flow has been used.

Pressure-driven flow hydraulic behavior through a circular channel can be explained by Poiseuille's theory. The Poiseuille flow is characterized by a parabolic velocity profile; with the maximum velocity in the center of the channel, decreasing toward the walls of the microchannel (Figure 1.3) [69]. Pressure-driven flow is widely used due to its versatility and simple operation.

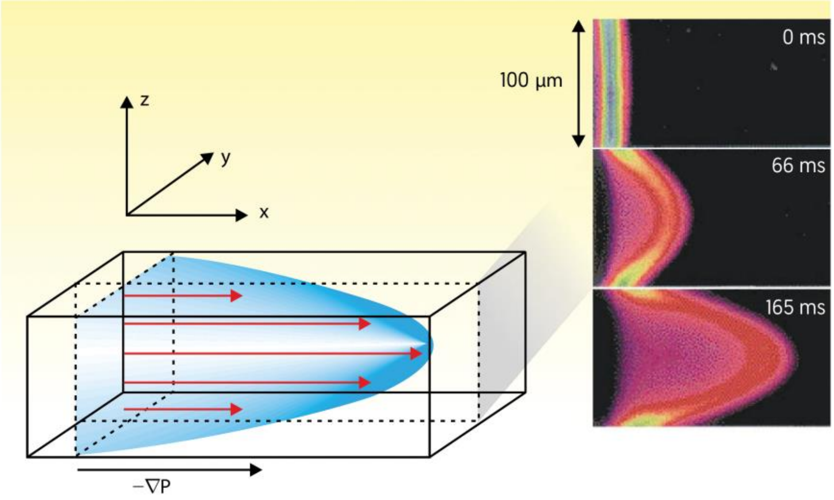

Figure 1.3: Schematic representation of pressure-driven flow profile [74]

Another important aspect regarding microfluidic platforms is mixing, because as mentioned before in microfluidics a laminar flow regime is established, where the mass transport is mainly controlled by diffusion. The incorporation of mixers into microfluidic platforms plays a major role since they enhance the mixture of reagents by generating turbulent flows or increasing the surface-to-volume ratio. Based on the strategy used to obtain homogeneous mixtures, they can be divided into active or passive mixers [63].

In active mixers, external energy is used to induce a disturbance in the flow. Different types of active mixers can be distinguished depending on the external disturbance applied, for instance, ultrasound, acoustically induced vibrations, integrated micropumps and microvalves, electrokinetic instabilities, magneto-hydrodynamic action, etc [75]. Despite being very efficient, they are difficult to implement as they need complex setups and external power sources.

On the other hand, passive mixers only depend on diffusion as the transport mechanism and no external power sources are needed. To improve mixing using this approach, changes in the geometry of the microfluidic channels are introduced [63,76]. Some of the typical microstructure designs employed for passive mixing are T- and Y-flow configurations (Figure 1.4A and B), zigzag or meander-like channels (Figure 1.4C and D), hydrodynamic focusing structures (Figure 1.4E), or flow obstacles within microchannels (Figure 1.4F) [75]. These types of mixers are easy to integrate on complex platforms. For this reason, they were used in the development of the microfluidic platform used in this thesis.

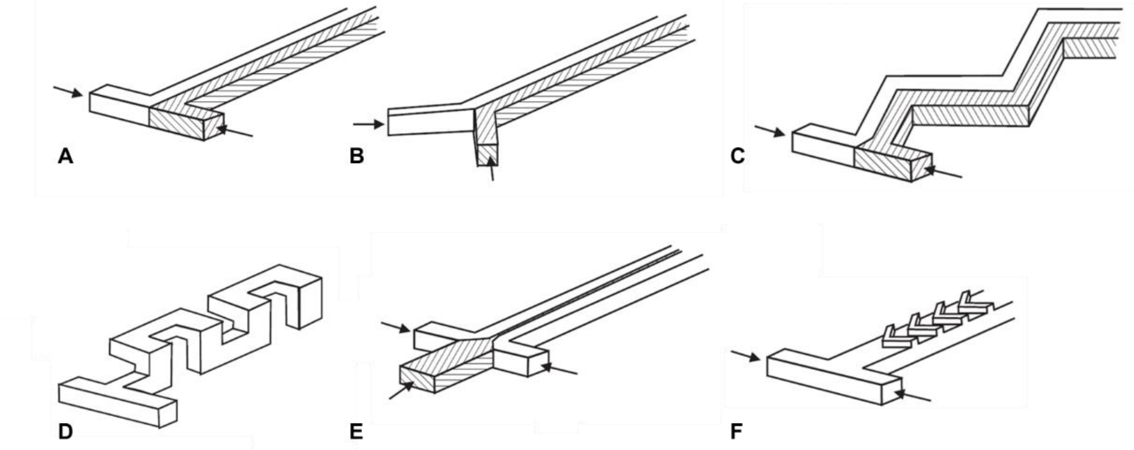

Figure 1.4: Schematic representation of typical microstructure designs employed for passive mixing: A) T- and B) Y-flow configurations, C) zigzag or D) meander-like channels, E) hydrodynamic focusing structure, and F) flow obstacles within microchannels [76]

### 1.2.3 Advantages

The different behavior of fluids at the microscale confers µTAS some interesting properties and some advantages compared to macroscopic systems. Some of them are the following:

- Automation: µTAS devices can integrate different laboratory operations without the need for any intervention, reducing the errors associated with manual operations [56].
- Portability: is obvious that the use of these devices leads to a reduction in the size of the systems, making them portable. This is of great importance for diagnostics and environmental monitoring [60].
- High throughput: the reduction of the size enables parallelization for multiple sample processing [77].

- Enhanced mass and heat transfer: these processes are more efficient in µTAS devices due to the smaller dimensions [78]. This is important in synthetic applications.
- Short analysis times: the enhanced mass transfer reduces the time needed for a sample to be analyzed [56].
- Reduction of costs: processes, where expensive reagents are needed, are affected since the volume required is greatly reduced [60].
- Safety: processes in which toxic reagents or dangerous reactions are involved are carried out in confined systems, thus reducing the hazard [79].
- Environmental friendliness: the consumption of energy is reduced. Moreover, µTAS generates less waste [60].

However, it should not be forgotten that this is a technology still in development, and not all the advantages described above can be assigned to a single µTAS device.

### 1.2.4 Limitations

Despite all the advantages that microfluidics presents, it also has some important limitations like the need of bulky equipment for performing some operations such as the pumping, the actuation control, or the detection, reducing the portability of the LOC devices [80]. Another drawback is the surface adsorption that can occur in the microchannels due to the high surface-to-volume ratio that can be overcome by passivating the surface of the channels [81], that add complexity to the fabrication process. Finally, the lack of standardized components, as the development of LOC devices is focused on individual components for specific applications, represents a challenge in the scale-up industrial fabrication.

## 1.3 Microfabrication technology

Microfabrication technology has undergone a great evolution in recent years and new materials have appeared as substrates for µTAS devices. Historically, silicon has been the most used substrate for microfabrication, but other materials have emerged as potential substrates for LOC devices fabrication [82]. In fact, substrate selection is key in order to integrate all the necessary operations and is strictly related to the final application. Several are the characteristics to consider, some of them being the intrinsic properties of the material (chemical stability, flexibility, transparency, etc.), the compatibility with other materials (for instance, for the integration of electronic components), the prototyping simplicity, or the cost.

The microfabrication technique used in this thesis for the construction of the LOC devices is the multilayer approach (Figure 1.5) that is based on the union of several layers to form the final device. Previously, each layer is individually cut with a pattern and then all the layers are aligned and laminated together [83-85]. This technique enables the creation of complex 3D structures, despite the lower resolution achieved compared to the photolithographic techniques.

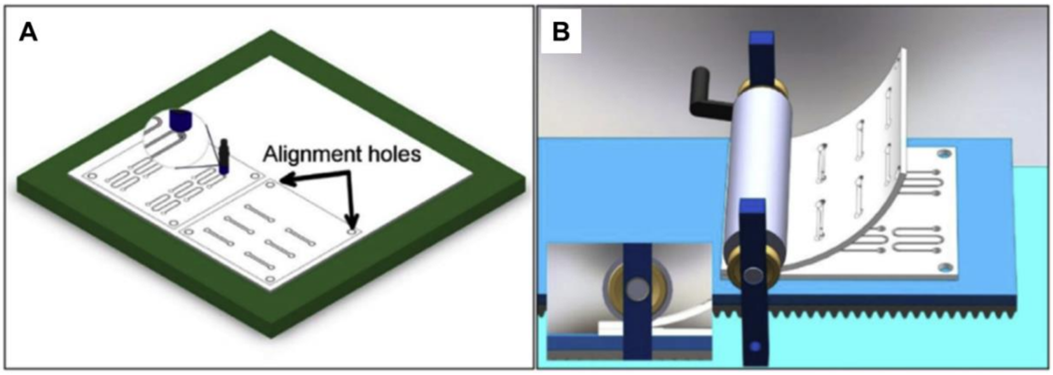

Figure 1.5: Illustration of the multilayer approach: A) Patterning of the different layers and B) Alignment and lamination of the layers [86]

For the development of the microfluidic structures, two different materials have been used as substrates in this work: Cyclic Olefin Copolymer (COC) and Low Temperature Co-Fired Ceramics (LTCC) and they will be described in more detail in the following sections.

### 1.3.1 Cyclic Olefin Copolymer (COC)

COC is a thermoplastic polymer formed by norbornene and ethene monomers (Figure 1.6) [87]. The structure of COC is amorphous and the presence of norbornene stiffens and reinforces the polymer, increasing its glass transition temperature ($T_g$). The higher the norbornene/ethylene ratio, the higher the $T_g$ [88]. Commercially available COC $T_g$ ranges from 70 ºC to 170 ºC [89].

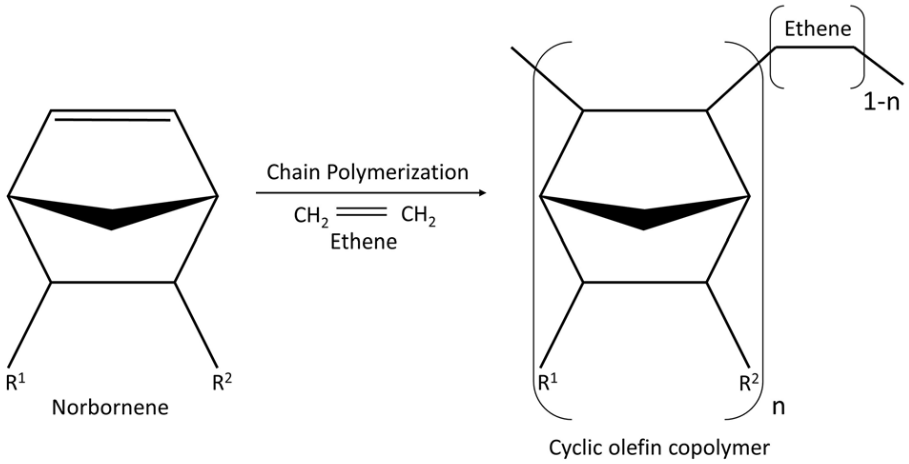

Figure 1.6: Chain copolymerization of norbornene with ethene [90]

Different fabrication methods can be used to create microfluidic networks in COC, such as laser ablation, micromilling, or replication methods (hot-embossing, injection molding, etc.) [91,92]. Among all these techniques, micromilling was the one used in this work to fabricate COC microfluidic platforms due to its easy and fast conversion from a Computer-Aided Design (CAD) to a prototype by using a Computer Numerical Control (CNC) micromilling machine. This machine uses rotating cutting tools to remove bulk material [89].

Bonding of the different substrate layers to enclose the channels remains as one of the most challenging steps in the fabrication process. The existence of COC substrates with different $T_g$ enables a simple bonding method by thermal diffusion. In this thesis, layers of COC substrate with higher $T_g$ are used as structural layers where the microfluidic structures are micromachined, while COC substrates with lower $T_g$ are used as sealing layers. Bonding is performed when the two substrates are put together and heated above the $T_g$ of the sealing layer. Once cold, high-strength bonds are established [84,91,93].

Some characteristics that make COC highlight for the fabrication of μTAS devices are its high transparency in near-ultraviolet and visible regions [94,95], low water absorptivity (< 0.01%) [96], high chemical resistance (for instance, to acids, bases and polar solvents) [92], good biocompatibility [90] or good electrical insulation [89].

### 1.3.2 Low Temperature Co-Fired Ceramics (LTCC)

LTCC technology is based on the use of tapes or layers, which are composed of organic material, glass, and ceramic powder (normally alumina), of different thicknesses. Before firing, these layers are malleable and can be easily microstructured. Glass is added to these ceramics to lower the sintering temperature below 950 ºC (compared to classic ceramic materials), in order to be able to sinter the LTCC tapes together with other materials, usually metals with high electric conductivity like silver, copper, or gold and their alloys (used to create electrodes) that have melting temperatures around 1000 ºC [97,98]. The organic components present in the LTCC tapes give them very important properties, such as flexibility, or an appropriate viscosity and drying rate [99].

The fabrication of an LTCC microfluidic device (Figure 1.7) is based on a multilayer approach, developed in our research group, the Group of Sensors and Biosensors (GSB), that enables the easy fabrication of 3D structures [100,101]. The process starts with the design of the different layers. Then, the layers are machined. There are four main groups of LTCC machining methods: punching, laser cutting, milling, and hot embossing, the first two being the most widely used [102]. After that, electrical conduction lines and electrodes are formed by the screen-printing of conductive pastes. Finally, the different layers are aligned and laminated. The laminated device is then sintered [98,102-104].

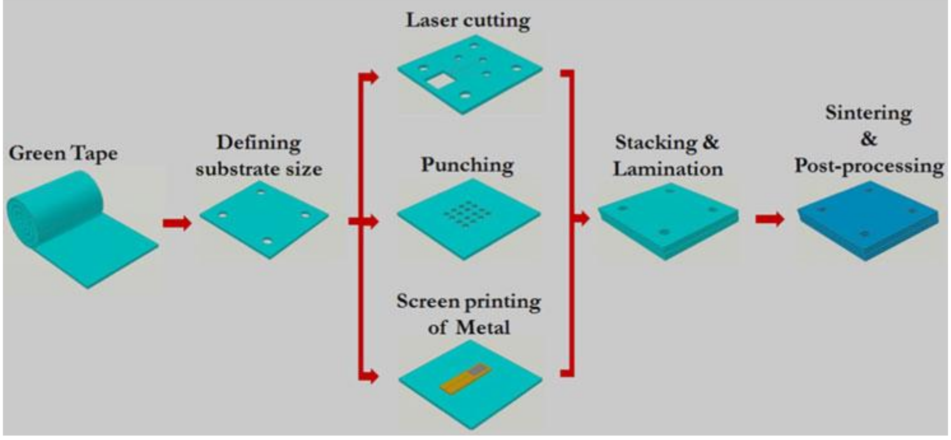

Figure 1.7: Schematic representation of the fabrication process of a typical LTCC microfluidic device [105]

Sintering is one of the most critical steps in the fabrication of LTCC devices. In this process, the glass is in the liquid state and the alumina grains that are in the solid state, diffuse into the glass. When the temperature decreases the glass-ceramic vitrification is produced, thus obtaining a hard material [99].

The interesting mechanical properties of LTCC make it suitable for analytical and synthetic applications [106-108]. Moreover, the simple prototyping, the integration of electronics and fluidics, the high chemical resistance, and the capability to withstand extreme conditions make LTCC stand out as a substrate for µTAS devices fabrication [109-111].

## 1.4 Nanotechnology in analytical chemistry

Nanotechnology can be defined as the understanding, control, and manipulation of matter at a scale of 1 to 100 nm. Nanotechnology includes the nanomanufacturing of nanomaterials, and their application into physical, chemical, and biological systems at scales ranging from individual atoms or molecules to submicron dimensions, as well as the integration of the resulting nanostructures into larger systems. The importance of this field arises from the fact that properties of matter at the nanometric scale are different from those at the macroscale, and these unique physical and chemical properties of nanomaterials can be employed in a huge variety of disciplines including analytical chemistry [112,113].

Two significant differences between materials at the nanoscale and those belonging to the micro or macro scale (Figure 1.8) are the higher surface-to-volume ratios and the greater chemical reactivities. The quantum confinement effects allow them to have different optical, electrical, magnetic, and other properties compared to their macroscale analogous [114,115]. Taking all this information into account, a good definition of nanomaterials could be that they are materials with at least one dimension in the range of 1-100 nm and with at least one property different from the macroscale counterpart [116].

Nanoparticles can be composed of a huge variety of materials, such as metals, carbon, polymers, organic molecules, biomolecules, metal oxides, etc., and can have a lot of different shapes and sizes [113]. Nanoparticles are present in a lot of different ambits like medicine, electronics, chemical synthesis, textiles, and construction materials, to enumerate just a few [117].

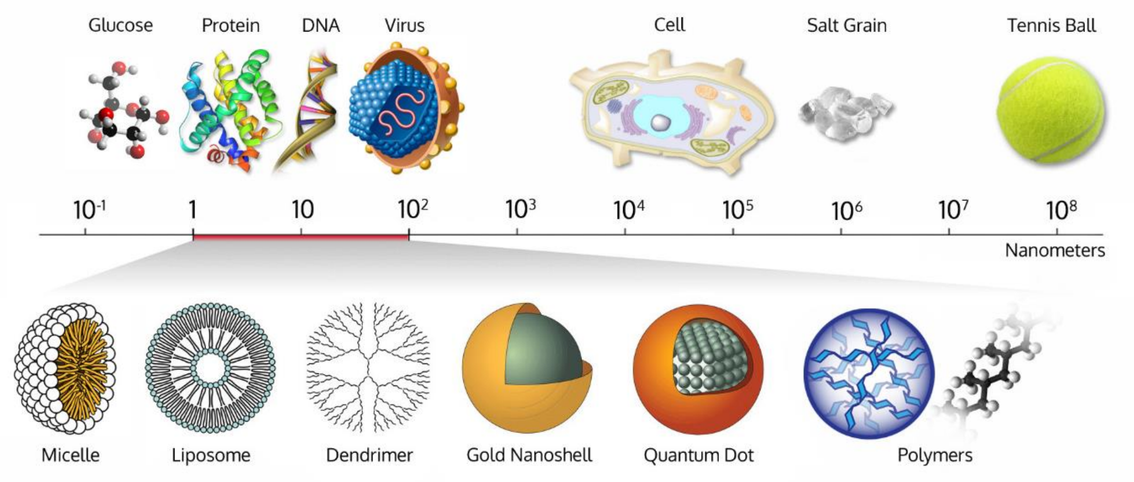

Figure 1.8: Size comparison: from nano to macro [118]

Thanks to the outstanding properties of materials at the nanoscale, they have been used to enhance the sensitivity of a great variety of analytical methods [119]. In the same way, different techniques have been used to characterize some parameters affecting the properties of nanomaterials like the size, the elemental composition, the shape, etc. to be able to use them in analytical methods [120].

### 1.4.1 Enhanced chemical sensors

A chemical sensor (Figure 1.9) is a device able to transform chemical information of an analyte into a useful analytical signal [121]. Sensors require two key features, a recognition element, that selectively interacts with the analyte generating a primary signal, and a transducer element, which plays an essential role in the performance of sensor devices; it transforms the primary signal into a secondary signal, normally electrical, that can be processed to obtain the analytical information of the sample [122,123]. Chemical sensors are developed to simplify analytical processes by incorporating a selective recognition element that allows the analysis of samples without the need for pretreatment steps and their small size increases their portability, and thus enables the capability of obtaining real-time and on-site information [124].

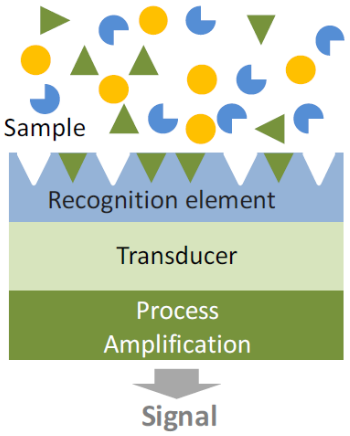

Figure 1.9: General scheme of a chemical sensor [125]

The use of nanoparticles in chemical sensing have demonstrated to enhance sensitivity, selectivity, and reproducibility. The most common nanoparticle-based sensors can be divided into electrochemical sensors and optical sensors.

Nanoparticle-based electrochemical sensors are based in the modification of the working electrode. The chemical modification of a conventional electrode surface allows to combine the high sensitivity of electrochemical techniques with the improved selectivity provided by the modifier [122]. The most common techniques to modify the electrodes is by directly attaching the nanoparticles by deposition or by using another material as an interface like a polymer material or a conductive material (carbon nanotubes (CNTs), graphene oxide (GO), etc.) [126]. The main advantages of using nanoparticles as electrode modifiers are the enhanced electron transfer between the analyte and the electrode, the increased mass transport, the better control over local microenvironment, and the catalytic activity of the nanoparticles due to the high surface-to-volume ratio [127-129].

Some types of nanoparticles used to modify electrodes are gold nanoparticles [130], silver nanoparticles [131,132], magnetic nanoparticles [133,134], and carbon nanoparticles [135]. Depending on the measurable electrical properties, electrochemical sensors can be broadly classified into potentiometric, amperometric, impedimetric, and voltametric sensors [136].

On the other hand, with nanoparticle-based optical sensors better results concerning LODs and reproducibility are obtained. They will be described in more detail in the following section.

### 1.4.2 Nanoparticles as optical probes

Optical methods based on the use of nanoparticles can be divided into two groups:

- Colorimetric methods: they are based on the detection of the color change as a signal. The most widely used nanoparticles for colorimetric assays are gold [137-139] and silver nanoparticles [138,140] because of the following unique optical properties: they show a Surface Plasmon Resonance (SPR) band which depends on the size, shape, and aggregation state of the particles in solution. When these parameters change (due to the interaction of the metal nanoparticles with the analyte), changes in the SPR are observed (intensity or wavelength shifts), leading to a color change [141,142]. For instance, dispersed gold nanoparticles exhibit red color, while their aggregation cause surface plasmon couplings, leading to a shift in the absorption band, with a color change to blue [143,144].

- Photoluminescence-based methods: in this group two types of methods can be found: the fluorescence-based methods and the phosphorescence-based methods. The photoluminescence (PL) that some nanoparticles possess could come from the quantum confinement effect [145,146] or from their attachment with small fluorescent molecules [147]. Fluorescence is based on the measurement of light emitted by molecules, that have been excited to higher energy levels by the absorption of electromagnetic radiation. Fluorescence-based sensing can be performed by using different approaches, but all of them are based on the change in emission intensity of the nanomaterial (fluorescence quenching, fluorescence enhancement, and Förster Resonance Energy Transfer (FRET)) [136]. Possible mechanisms for fluorescence quenching and enhancement are depicted in Figure 1.10.

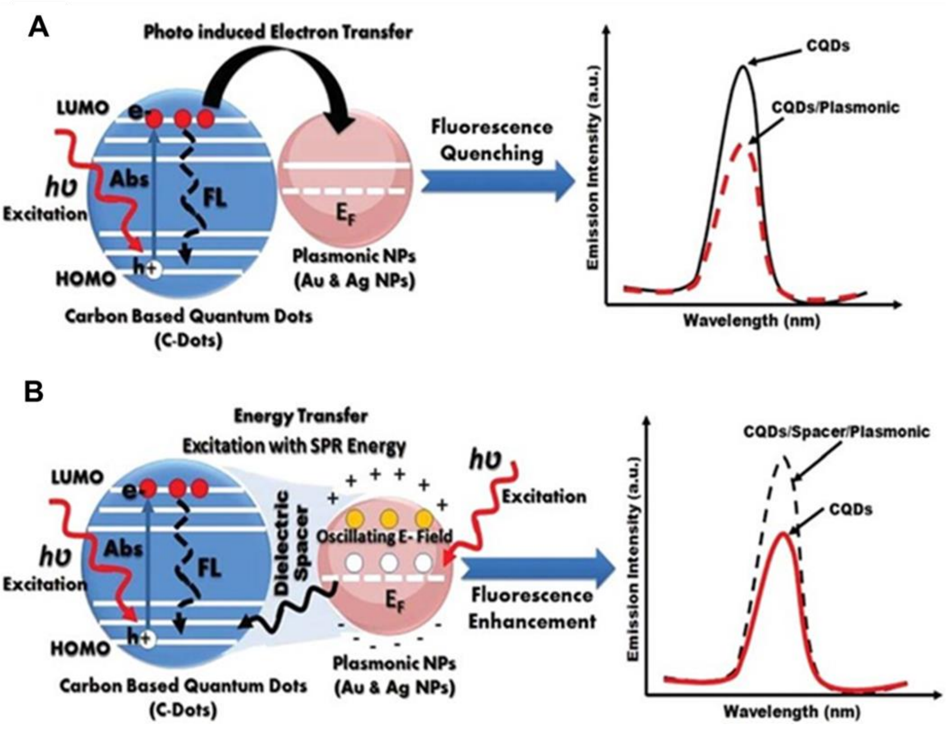

Figure 1.10: Schematic illustration for possible mechanisms for fluorescence A) quenching, and B) enhancement [148]

FRET is a process in which an energy transfer is established from an excited donor to an acceptor that can result in the quenching of the donor, which causes a decrease in its photoluminescent emission intensity, while the acceptor can show an emission enhancement or can release the energy by non-radiative relaxation. FRET occurs when the emission spectrum of the donor overlaps with the excitation spectrum of the acceptor [149,150].

Phosphorescence is based on the same principle as fluorescence but, in this case, the electromagnetic radiation absorbed is not immediately emitted. Light is emitted after the radiation source is removed. Phosphorescence-based sensing, as fluorescence-based sensing, is based on the change of phosphorescent emission intensity produced by the target analyte [151]. In this work, a fluorescence-based method is used and for this reason, this type of methods will be described more in depth.

The most common nanoparticles used as fluorescent probes or labels are gold nanoparticles [144] and nanoclusters [152], which suffer from the drawback of having low Quantum Yields (QYs), and Quantum Dots (QDs), that are nanosized crystals made of semiconductor materials with a diameter ranging from 2-10 nm with high QYs [153]. The most reported QDs are made of CdS [154], CdSe [155], or CdTe [156]. Another important type of QDs are the core-shell QDs that present an enhanced PL compared with single QDs [157,158]. As can be seen, they are composed of heavy metals, making them toxic. Moreover, the QDs are not soluble in water.

Another type of nanoparticles more lately employed are Carbon Dots (CDs). Even though they show lower QYs than QDs, they present low toxicity, and are photochemically stable and biocompatible thanks to its carbonaceous nature [159]. They are described in the following section.

## 1.5 Carbon Dots

CDs are carbon nanoparticles with different levels of surface coating and with sizes less than 10 nm [160]. Their shape is quasi-spherical, and they are composed of a carbon core either amorphous or crystalline mainly formed by $sp^2$ graphitic carbon and $sp^3$ hybridized carbon. On the surface, they contain some common functional groups like carbonyl, carboxyl, and hydroxyl groups [161-163]. Due to the presence of these functional groups on the surface, which are ionizable, they show excellent water solubility and are susceptible to being functionalized with organic, inorganic, or biological molecules [164].

To be precise, the functionalization of CDs is of major importance since it provides unique properties. More specifically, heteroatom doping of CDs is a powerful technique to adjust their structure and electron distribution. Therefore, the fluorescence performance of CDs is enhanced with the presence of different types of heteroatom dopants. Non-metallic dopants (N, P, S, etc.) can be used to improve the QYs of the CDs [165,166]. Especially, the introduction of nitrogen produces new surface states that capture electrons and suppresses non-radiative recombination, thus increasing the QY [167-169]. Moreover, N-doping on CDs decreases cytotoxicity [165].

CDs can be classified based on their different chemical structures into Graphene Quantum Dots (GQDs), Carbon Quantum Dots (CQDs), and Carbon Nanodots (CNDs) (Figure 1.11). The main differences between them rely on the crystalline structure, dimensionality, and quantum confinement. The carbon nanoparticles that present quantum confinement and crystalline structure can be divided into CQDs which are quasi-spherical QDs composed of multiple layers of graphitic sheets and GQDs that contain one or a few layers of graphene sheets. On the other hand, the CNDs are amorphous quasi-spherical carbon nanoparticles without quantum confinement [170,171].

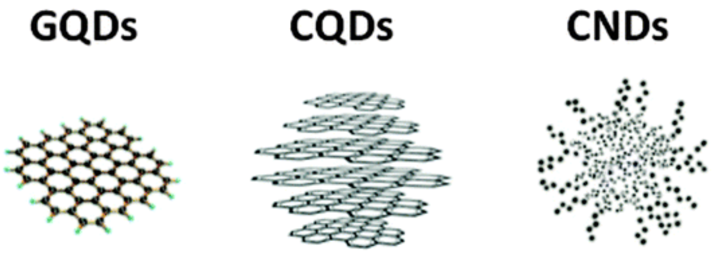

Figure 1.11: Classification of fluorescent CDs. Illustration of GQDs, CQDs, and CNDs structures [170]

CDs were accidentally discovered in 2004 when some researchers were using an electrophoretic method for the purification of single-walled carbon nanotubes (SWCNTs) obtained from arc-discharge soot, and they obtained fluorescent nanoparticles [172]. But the first reported synthesis of CDs was published in 2006 when quantum-sized carbon nanoparticles were prepared by laser ablation of graphite [173]. Since then, the publications related to CDs greatly increased, and they have attracted a lot of attention in the scientific community, due to their outstanding optical and chemical properties which will be addressed in Sections 1.5.3 and 1.5.4.

### 1.5.1 Methods of synthesis

Existing methods to synthesize CDs can be divided into two groups: top-down and bottom-up approaches (Figure 1.12). The top-down techniques are based on the exfoliation and cutting of bulk carbon materials such as graphite, carbon soot, CNTs, etc. into nanoparticles of less than 10 nm. From this approach, GQDs are generally obtained. On the other hand, bottom-up techniques are based on the production of CDs from small organic molecules or polymers by applying external energy such as microwave and heating. With this approach, CQDs and CNDs are produced [174].

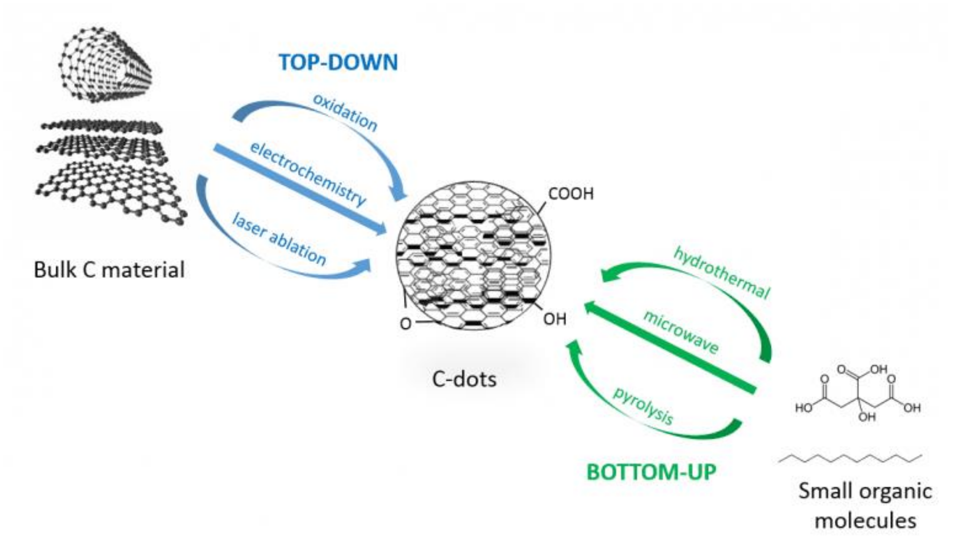

Figure 1.12: “Top-down” and “bottom-up” approaches for the synthesis of CDs [175]

#### 1.5.1.1 Top-down methods

The main top-down methods used for the synthesis of CDs are the following:

- Arc discharge: this method uses high energy from electric arc to destroy bulk carbon sources like graphite or CNTs. The obtained CDs have small sizes and good fluorescence; however, they exhibit low yields and low homogeneity [165,172,176].

- Laser ablation: this technique is based on the irradiation of a carbon material target with a laser beam, causing the detachment of carbon nanoparticles from the solid substrate. The main advantage of this method is its simplicity, but, on the other hand, it needs a great amount of carbon material, complex and expensive equipment, and the CDs QYs are low [173,177,178].

- Chemical oxidation: this method consists of the oxidation of a carbon source (starch, carbon soot, graphene, etc.) with a strong oxidant ($HNO_3$ and $H_2SO_4$ as the most common ones) to prepare nanosized CDs. Despite this method does not require special equipment, the need for strong oxidants presents some drawbacks like the high cost and the environmental risks that are associated with their use [165,179].

- Electrochemical oxidation: consists of applying a voltage to a carbon electrode, that causes corrosion and exfoliation of the carbon material to obtain CDs. The carbon materials used include CNTs, carbon fibers, and graphite rods, among others. This method is simple to operate and environmentally friendly but presents the drawback of being time-consuming [180,181].

#### 1.5.1.2 Bottom-up methods

The most important bottom-up methods for the synthesis of CDs are the following:

- Hydrothermal synthesis: in this method the precursors, usually small organic molecules, are dissolved in water, sealed in a hydrothermal reactor (Teflon-lined stainless-steel autoclave is the most common) and left to react at high temperature (between 100 and 300 ºC) and high pressure. This method presents the advantages of being simple, economic, and environmentally friendly, since in case of using toxic precursors, their reaction in an enclosed container prevents their volatilization. Moreover, the CDs obtained exhibit high QYs. However, the main drawbacks are that the size of the CDs is not homogeneous and the need for further purification steps [167,182,183].

- Solvothermal synthesis: this method is very similar to the hydrothermal one but in this case, the precursors are dissolved in one or several solvents different from water. Several solvents like ethanol, formamide, dimethylformamide (DMF), etc. can be used. The polarity of the solvent used has a great influence on the properties of the synthesized CDs. This method presents the drawbacks of being more toxic than the hydrothermal method due to the solvents used, the need for separation and purification processes, and, in some cases, the need of additional steps to make them water-soluble [180,184].

- Microwave-assisted synthesis: this method is based on the formation of CDs from small precursors under the uniform heating effects of microwave radiation. The molecules of the precursors are heated through the absorption of microwave radiation instead of conductively or convectively [185,186]. This method is simple and fast since CDs are synthesized within a few minutes. However, it suffers from the same problems as the hydrothermal method: poor nanoparticle size control, and the need for separation and purification processes [178].

- Pyrolysis: it consists of the carbonization of carbon precursors at high temperatures. This method does not require the use of a solvent, it is fast and simple, and a lot of natural products can be used as precursors. The main drawbacks are that it requires high-concentrated alkali or acid to obtain CDs from a carbon powder, and the low homogeneity of particle sizes [187,188].

As can be seen, the main problems of the CDs syntheses methods are the low homogeneity of particle sizes obtained and the poor reproducibility between batches. These issues originate from the difficulty of having proper control of reagent mixing and conditions of the process (temperature and pressure, for instance). In this sense, microfluidic reactor technology appeared as a solution for the synthesis of CDs in particular and nanoparticles in general.

### 1.5.2 Microreactors for CDs synthesis

Microreactors improve the synthetic processes by offering a more efficient heat and mass transfer and lower diffusion times [189]. Moreover, reagents and energy consumption are reduced as well as the reaction time [107]. Another interesting feature is the possibility to automate the entire procedure by using computer-controlled elements (pumps and valves) which leads to more autonomous and reproducible syntheses and reduces the risk associated with the use of toxic or hazardous reagents, as they are confined inside the microreactor [190].

Up to now, different types of microreactors for the synthesis of CDs have been reported in the literature. Some of them will be summarized in this section. The most used strategy for the synthesis of CDs in a microreactor consists of using microfluidic tubing that is submerged in an oil bath that is heated at the desired temperature [191,192]. More recently, pressure-control has been added to this method by means of using a back pressure valve [193]. A similar approach was recently reported, also consisting of a microreactor pipe, but in this case, it was submerged in a water bath, so the reaction was performed at lower temperatures [194]. Another approach consisting of a foamy copper microreactor with different porosities was also published [195-197].

In this thesis, LTCC is proposed as the substrate for the fabrication of a microreactor for the synthesis of CDs. As stated in Section 1.3.2, LTCC has some advantages like the capability to withstand harsh temperature and pressure conditions, the chemical inertness, and the possibility to incorporate screen-printed elements, which enables the inclusion of electrical elements, such as heaters to control temperature [189,198]. Moreover, the substrate properties and the multilayer approach that was used for the fabrication, makes feasible the design and fabrication of 3D microfluidic structures, which are desired to enhance and control mixing [107].

Our research group, the GSB, has extensive experience in the fabrication of LTCC microfluidic reactors for the synthesis of nanoparticles like QDs [199,200], gold nanoparticles [107], and CDs [201,202].

### 1.5.3 Optical properties

#### 1.5.3.1 Absorption in the UV-Vis

One of the main properties of CDs is the ultraviolet-visible (UV-Vis) radiation absorption. The absorption bands that appear when a dispersion of CDs is analyzed correspond to the SPR bands that appear because of the coupling between the wavelength of the radiation source and the external electrons at the surface of the CDs. CDs synthesized from different precursors and through different methods present different absorption behavior, but generally they show strong absorption in the UV spectral region with a weak absorption in the visible region [203]. The SPR bands can be modulated through surface functionalization techniques [167]. Normally, the strong SPR band located below 300 nm could be assigned to a π-π* transition involving aromatic sp$^2$ carbons (C=C bonds), and the SPR band located between 300 and 400 nm could be assigned to n-π* transitions of the C=O, C-N, C=N or C-S bonds [187,196,204,205].

#### 1.5.3.2 Photoluminescence

PL is one of the most important properties of CDs. Compared to other fluorescent materials like organic dyes, CDs have some advantages like better fluorescence stability, larger Stokes shifts and resistance to photobleaching [205,206]. CDs usually have a wide emission peak, and the PL emission wavelength depends on the wavelength of the excitation radiation, which is a unique property of CDs. However, the PL emission of CDs can also be fixed to a single wavelength, making it independent of the excitation wavelength [207].

The brightness of PL can be quantitatively determined by the QY value, which is the number of emitted photons relative to the number of absorbed photons [163]. As stated in Section 1.5, surface functionalization can greatly increase the QY of CDs.

The PL mechanism is of great importance to improve CDs' synthetic methods, but up to now, there is not a unified conclusion about the fluorescence origin [208]. Some theories have been proposed to explain this feature:

- Surface state: the surface state controlled by the degree of surface oxidation (namely, the number of oxygen-related groups) and the surface functional groups is closely related with the fluorescence of the CDs [209]. The higher the degree of surface oxidation, the greater the amount of surface defects, leading to various emission sites, enhancing the CDs fluorescence [210,211]. The presence of surface functional groups like C=O and C-N/C=N can tune the fluorescence of CDs, as they introduce two energy levels (HOMO-n$_O$ and HOMO-n$_N$) that are non-bonding orbitals where the electrons of the N and O atoms are located, and further produce new electron transitions (Figure 1.13) [212,213].

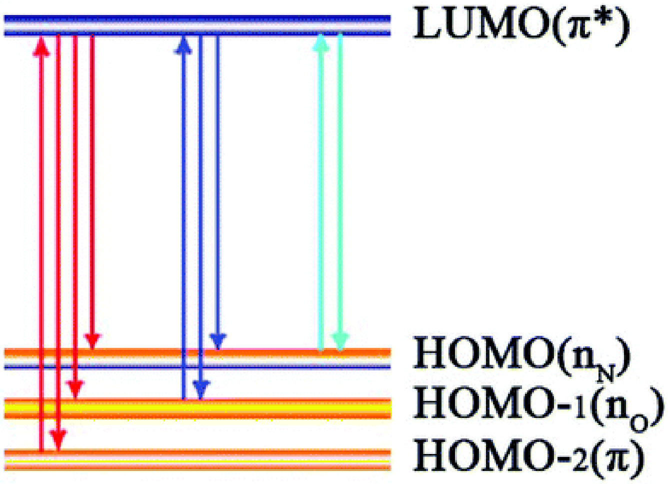

Figure 1.13: Schematic illustration of the proposed energy level and electron transition diagrams of the N-CDs [213]

- Quantum confinement effect: the PL of CDs can be adjusted by changing the size of the crystalline carbon core due to the quantum confinement effect, as the size is directly related with the bandgap in the CDs. The higher the core size, the greater extent of π-electron system, causing a reduction in the energy gap between the lowest unoccupied molecular orbital (LUMO) and the highest occupied molecular orbital (HOMO) [203,214,215].

- Molecular fluorescence: the formation of fluorescent impurities during the synthesis of CDs could contribute to their PL emission as well [159]. Recently, it has been demonstrated that the high QY of CDs synthesized from citric acid and ethylenediamine (ED) can be assigned to a fluorescent molecule (5-oxo-1,2,3,5-tetrahydroimidazo[1,2-]pyridine-7-carboxylic acid, IPCA). This molecular fluorophore that is attached to the CDs, contributes to the strong blue fluorescence [216]. This molecular fluorescence, that comes from organic molecules, suffers from photobleaching as the organic dyes, making the CDs not as stable as the QDs.

Another interesting feature regarding CDs is that they possess up-conversion fluorescence. This is an anti-Stokes emission, where the emission wavelength is shorter than the excitation wavelength [187,217]. The CDs' up-conversion properties can be attributed to a multi-photon activation process, in which the simultaneous absorption of two or more photons is observed (Figure 1.14) [169,183].

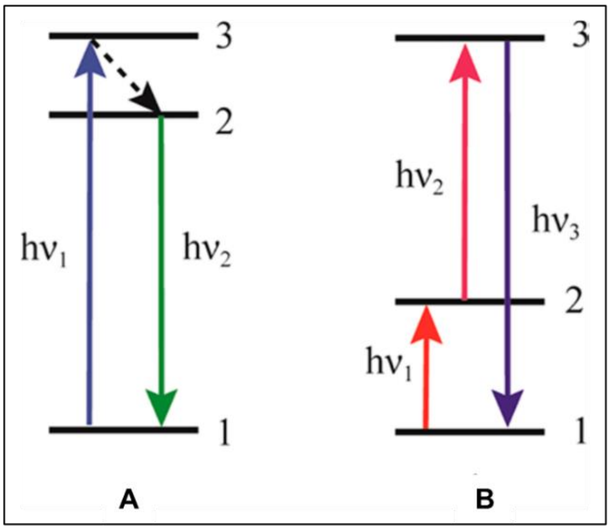

Figure 1.14: Schematic representation of (A) conventional luminescence and (B) up-conversion luminescence processes [217]

Taking the excellent PL properties of the CDs into account, they have been applied for the detection of numerous analytes and mainly based on fluorescence quenching due to their interaction with the analyte (quencher) [218]. The decrease in the CDs fluorescent emission intensity can be correlated with the concentration of the analyte by using the Stern-Volmer equation:

$$\frac{F_0}{F} = 1 + K_{SV}[Q] \qquad \text{Equation 5}$$

where $F_0$ and F are the fluorescence intensities in the absence and presence of the quencher, $K_{SV}$ is the Stern-Volmer quenching constant, and [Q] is the concentration of the quencher [219,220].

There are several mechanisms responsible for the fluorescence quenching of CDs (Figure 1.15):

- Static quenching: occurs when a nonfluorescent ground-state complex is formed through the interaction between the CDs and the quencher [186].

- Dynamic quenching: occurs when the excited state of the fluorophore (CDs) returns to the ground state due to a collision between the quencher and the CDs [218].

- FRET: this mechanism is based on the energy transfer between CDs in the excited state (donor) and quencher in the ground state (acceptor). The emission spectrum of the CDs overlaps with the absorption spectrum of the quencher. The distance between the two molecules must be lower than 10 nm [221].

- Photoinduced Electron Transfer (PET): this mechanism is based on the internal redox reaction between the excited state of the CDs and the quencher that can donate or accept an electron. The complex formed between the two species can return to the ground state without the emission of a photon [222]. PET can be oxidative or reductive. In reductive PET the CDs receive an electron from the quencher, and it is driven by the energy gap between the LUMO of the quencher and the HOMO of the CDs, while in oxidative PET the CDs donate an electron to the quencher, and it is driven by the energy gap between the LUMO of the CDs and the LUMO of the quencher [223].

- Inner Filter Effect (IFE): occurs when the absorption spectrum of the quencher overlaps with the emission or excitation spectra of the CDs. This mechanism is not exactly a quenching process but causes an attenuation of the excitation beam or an absorption of the emitted radiation by an excess of CDs concentration or by the quencher. This mechanism also occurs when the distance between the molecules is higher than 10 nm [186,221].

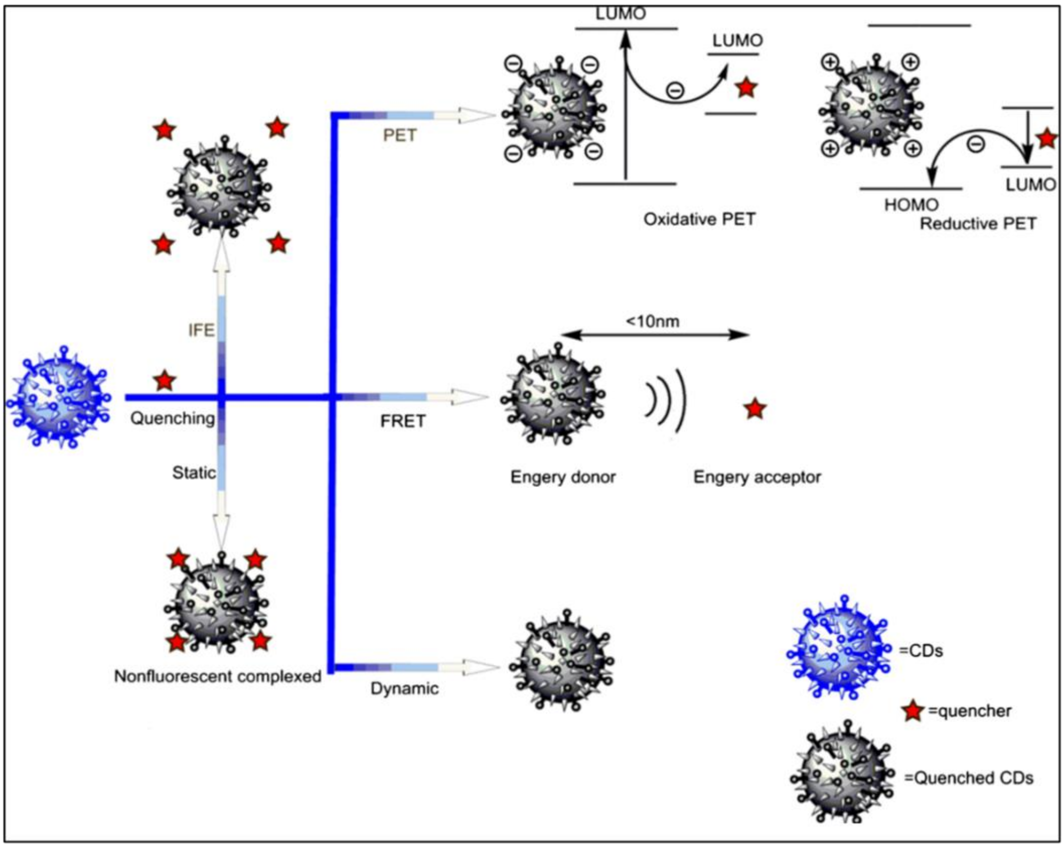

Figure 1.15: Schematic representation of the quenching mechanisms of fluorescent CDs [223]

### 1.5.3.3 Phosphorescence

CDs also exhibit Room Temperature Phosphorescence (RTP) that is produced by intersystem crossing (ISC) from the lowest excited singlet state ($S_1$) to a triplet state and then radiative transition from the lowest excited triplet state ($T_1$) to the ground state ($S_0$) [224]. Knowing this, an effective ISC process is needed, but in most cases the $T_1$ state can be quenched by oxygen causing a nonradiative decay [215]. For this reason, CDs are often doped with heteroatoms like N, P, and halogens, that favor the ISC processes [205]. Up to now, CDs with lifetime phosphorescence up to 1 s have been synthesized [225,226].

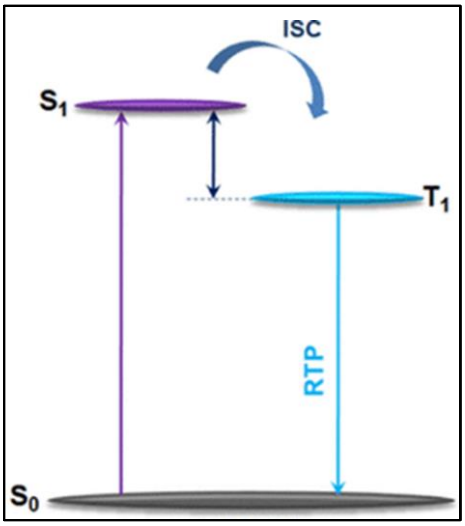

Figure 1.16: Schematic representation of the RTP mechanism of the CDs [227]

### 1.5.3.4 Chemiluminescence

Chemiluminescence (CL) can be defined as the generation of electromagnetic radiation as light by energy transfer from chemical reactions [228]. CL is caused by redox reactions where an electronically excited intermediate either directly emits light or transfers its energy to another fluorescent material, which returns to the ground state by radiating light [229].

The use of CDs in CL systems presents some advantages like their tunable luminescence or their adjustable energy levels that can enhance the chemical energy transfer [230]. CDs can generate CL when they react with strong oxidants like $KMnO_4$ and cerium(IV) [231]. In another publication, CDs produced strong CL in the presence of $NaNO_2$ and $H_2O_2$. The mechanism of the CL can be seen in Figure 1.17 and can be explained by radiative electron-hole annihilation between hole-injected and electron-injected CDs. On one hand, the formed ONOOH (oxidant) and OH· act as hole injectors and transform the CDs into positive radicals. On the other hand, the $O_2\cdot^-$ formed, donate electrons to the CDs charging them negatively. The electron-hole annihilation between the positively and negatively charged CDs results in an energy release [232].

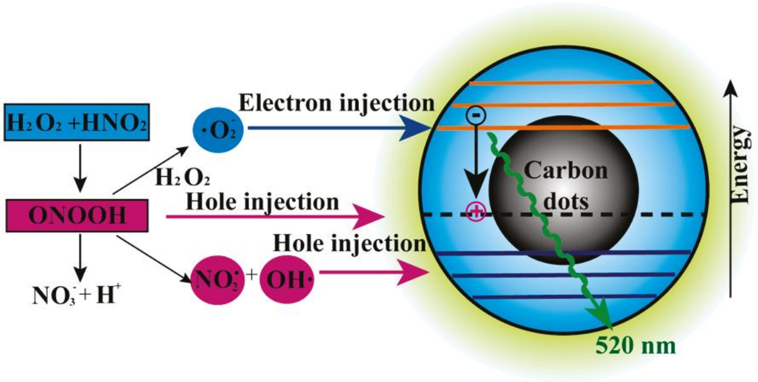

Figure 1.17: Schematic illustration of the CL mechanism of CDs-$NaNO_2$-$H_2O_2$ system [232]

#### 1.5.3.5 Electrochemiluminescence

ECL is very similar to CL, but in this case, the species between which the redox reaction takes place, are electrochemically generated in an electrode. These species undergo electron transfer reactions to produce excited states that emit light when they return to the ground state [174,233]. ECL presents some advantages like enhanced selectivity because the generation of the excited states can be controlled varying the electrode potential, or the wide response range [234].

CDs normally follow the cathodic ECL mechanism using $K_2S_2O_8$ as co-reactant [233]. In this mechanism (Figure 1.18), $CDs^{\bullet-}$ radicals are generated and strongly oxidizing $SO_4^{\bullet-}$ radicals are also generated by the reduction of the $K_2S_2O_8$. The two radicals react to form the excited states ($CDs^{*+}$) that produce the ECL emission [235]. Other co-reactants like sulfite [236] or hydrogen peroxide [237] were also used. Besides the cathodic ECL mechanism, tripropylamine can also be used as a co-reactant to produce the anodic ECL of CDs [238].

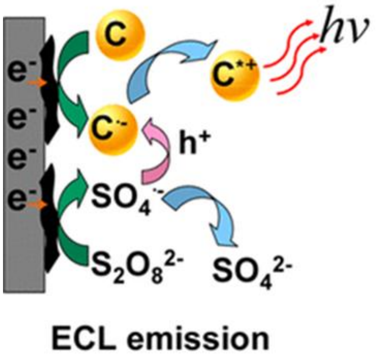

Figure 1.18: ECL cathodic mechanism of CDs using $K_2S_2O_8$ as co-reactant [235]

### 1.5.4 Other properties

- Catalytic properties: due to the high surface-to-volume ratio and high adsorption capacity of CDs, they have been used in different catalytical processes. To improve their function, they can be combined with a wide variety of materials to obtain CD-based composites, that can be used in photocatalysis or electrocatalysis, for instance [239]. Additionally, their excellent fluorescence behavior and photoelectron transfer properties enable their use as high-performance photocatalysts [240].

- Electrochemical properties: GQDs are very attractive for electrochemical applications since they have a high electrical conductivity due to the π-conjugated structure [241]. Modification of electrodes with CDs provide fast electron transfer kinetics due to the high electrical conductivity and an increased surface area due to the high surface-to-volume ratio. Moreover, the hydroxyl, carboxyl, carbonyl, and other functional groups present in the surface of the CDs enhance the electrocatalytic activity of traditional semiconductor electrocatalysts due to the acceleration of the intermolecular electroconductivity [242]. However, the surface chemical groups present on CDs also reduce their conductivity compared to GQDs, so it is necessary to combine them with other conductive materials like GO [243,244], CNTs [245], or conductive polymers [246] to be able to use them for electrochemical applications.

Doping CDs with heteroatoms like nitrogen, sulfur, phosphorous, etc., improve their electronic attributes significantly due to the intramolecular charge transferability. The heteroatom-doped CDs show an enhanced electrochemical performance due to the improvement of intrinsic activity of surface functional sites, and the changes on their electronic configuration [247,248].

### 1.5.5 Applications

As stated before, the excellent and, in some cases, unique properties of CDs make them suitable for a wide variety of applications and some of the most important ones are summarized in this section. The fields within the CDs have important applications are the following:

- Chemical sensing: this is one of the fields in which the CDs have more applications due to the water solubility, great chemical stability and photostability. They have been used as sensors to detect several metal ions, anions, and molecules [249]. Some of the metal ions detected include $Al^{3+}$ [250], $Ag^{+}$ [251,252], $Cd^{2+}$ [182,253], $Co^{2+}$ [15,254], $Cr^{6+}$ [255], $Cu^{2+}$ [256,257], $Fe^{3+}$ [258,259], $Hg^{2+}$ [260,261], $Ni^{2+}$ [262], $Pb^{2+}$ [263,264], and $Zn^{2+}$ [265,266]. In this case, most of the procedures are based on the quenching effect that the metal ion produces on the CDs. In addition to metal ions, CDs have also been used for the detection of some anions like $ClO^{-}$ [267], $CN^{-}$ [268], $I^{-}$ [269], $F^{-}$ [270,271], $PO_4^{3-}$ [272], $S^{2-}$ [273,274]; and some small organic molecules such as ascorbic acid [275], dopamine [276], hydrogen peroxide [277], or glucose [278]. Another sensing application of CDs is to measure pH [279,280], which sensitivity can be attributed to the protonation or deprotonation of the surface functional groups.

- Biosensing: CDs can also be used in biosensing due to their good biocompatibility, ease of surface functionalization, and good cell permeability [165]. They have played an important role in the detection of nucleic acids [281,282] and in immunoassays as fluorescent labels [283,284].

- Bioimaging: it could be described as a group of non-invasive techniques that allow the visualization of intracellular compartments, cells, and tissues, providing a better understanding of biological processes [185]. Due to the low cytotoxicity and the photochemical stability of CDs, they are suitable for fluorescence imaging of living organisms. Moreover, they can be easily excreted from the body [285]. With all these merits, CDs have drawn great attention for both *in vivo* [286,287] and *in vitro* imaging [288-290].

- Nanomedicine: CDs have a lot of applications in this field. Due to the high surface-to-volume ratio and the possibility of functionalization, CDs have shown a lot of potential as drug and gene delivery systems for the treatment of cardiovascular diseases, genetic disorders, and cancer [291-295]. Besides this, CDs have also an important role in phototherapy, a noninvasive cancer treatment based on the conversion of the radiating light into reactive oxygen species and heat, with the collaboration of photosensitizers, previously accumulated in the tumor tissue, that cause the apoptosis of cancerous cells. CDs have demonstrated to be powerful tools in both photodynamic [296-298] and photothermal therapy [299-301].

- Catalysis: CDs' unique fluorescence behavior and photoelectron transfer properties make them a promising candidate as greener high-performance photocatalysts. They have demonstrated to be highly efficient catalysts in different organic reactions [240]. One of the main interests in the photocatalysis field is the exploitation of sunlight as a renewable energy source. The combination of CDs with traditional semiconductor photocatalysts enhances the electron transfer and broadens the light absorption range, thus increasing the solar energy conversion efficiency [302-304]. Redox reactions used in electrochemical energy conversion and storage devices like oxygen evolution reaction, oxygen reduction reaction and carbon dioxide reduction reaction are normally catalyzed by platinum, but CDs and CD-composite materials have arisen as alternatives [305-309].

- Optoelectronic devices: among the various optoelectronic devices, Light Emitting Diodes (LEDs) received increasing interest in the last years. CDs have a lot of potential as alternatives to replace expensive rare-earth-based phosphors and toxic metal-based semiconductor QDs in LEDs [310,311].

## 1.6 Characterization of nanoparticles

The development of new types of nanoparticles demand techniques to determine their chemical, physical and structural information to be able to know their properties and consequently unravel their potential applications. In the case of CDs, since their potential relies on their optical features, spectroscopical techniques will be crucial to understand their optical characteristics. In this section the methods to characterize nanoparticles, more concretely CDs, will be summarized. The ones used in this work will be described in more detail.

### 1.6.1 Physical characterization

In this section methods to know some physical features of the nanoparticles like the size, shape, and crystallinity are described:

- Transmission Electron Microscopy (TEM): This technique is based on the transmission of an electron beam (energy between 100 and 400 keV) through a sample in vacuum (approximately $10^{-4}$ Pa) to create an image. This image is formed from the elastically or inelastically scattered electrons of the sample, magnified with different magnetic lenses and focused onto an imaging device, for instance, a fluorescent screen [312]. A scheme of the structure of a TEM instrument can be seen in Figure 1.19. TEM gives details about the particle size, morphology, composition, and crystallography of nanoparticles. Nowadays, high resolution TEM (HRTEM) is mostly used for studying the structure of CDs, since it is sensitive to crystal lattice defects. Some of the drawbacks that this technique present is that the acquisition of images depends on the contrast between the sample and the background, and that the preparation of the sample can be a complex process [313]. In the case of CDs, samples are prepared by the deposition of a drop of a dispersion onto support grids.

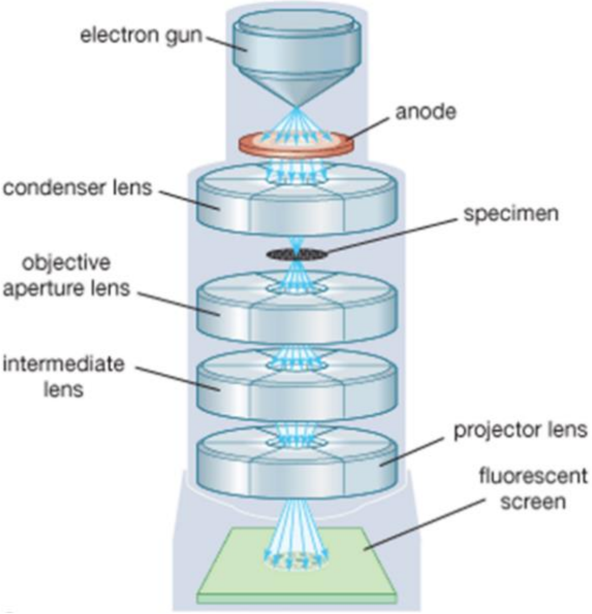

Figure 1.19: Components of a TEM instrument [314]

- Dynamic Light Scattering (DLS): This technique is used to determine the size distribution of small particles in solution, providing their hydrodynamic diameters. Also known as Photon Correlation Spectroscopy (PCS), this technique is based on the scattering of light by moving particles when they are irradiated with monochromatic and polarized light. The photons that collide with the nanoparticles in solution are scattered at different angles depending on their size [315-317]. A schematic representation of a DLS equipment can be observed in Figure 1.20.

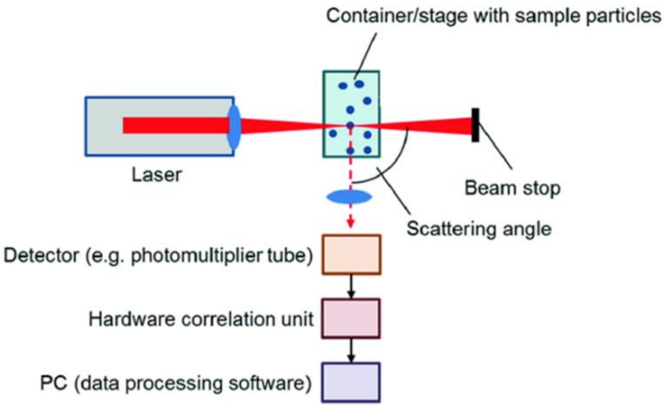

Figure 1.20: A Schematic representation of a DLS instrument [318]

- Other methods: X-ray diffraction (XRD), that is used to evaluate the crystalline structure of nanoparticles and the particle size, Atomic Force Microscopy (AFM), a high-resolution scanning probe microscopic method that is used to obtain a topographical image of the surface of the nanoparticles, Zeta-potential (ζ), that can be used to determine the surface charge and the particle size, giving information of the functionalization on the surface of nanoparticles, and Selected Area Electron Diffraction (SAED), that is used to determine the crystalline structure of nanoparticles and their defects.

### 1.6.2 Chemical structure characterization

- Fourier Transformed Infrared Spectroscopy (FTIR): This technique is used to study the functional groups that are present in the surface of the nanoparticles. Infrared absorption bands can be associated with fundamental vibrations of functional groups and the Fourier transform mathematical process is used to convert the raw data into a spectrum [319,320].

- X-ray Photoelectron Spectroscopy: This method is used to determine the elements that are present in the surface of the nanoparticles and its chemical state. X-rays impact on the material and the kinetic energy of the emitted electrons is measured [321,322].

- Energy-Dispersive X-ray Spectroscopy: This technique is used to analyze the elemental composition of nanoparticles. It is based on focusing high energy X-ray beams onto the sample, their interaction, and the measurement of the emission of X-rays radiated from the sample using an electron microscope [323].

- ICP-MS: It is used to determine the chemical structures of nanoparticles. It is based on the use of inductively coupled plasma to ionize the sample, forming atomic and small polyatomic ions, which are then detected by mass spectrometry [248].

- ICP-OES: This technique is used to quantify an element in a sample and is suitable for multielement analysis providing the ratio of the elements in the sample. It is based on the ionization of the sample and then the registration of an emission spectrum. The electromagnetic radiation emitted is displayed as atomic spectral lines at wavelengths that are characteristic of each particular element [324].

- Other methods: Raman spectroscopy, is used to determine the vibrational modes of molecules by measuring the inelastic scattering of photons, and Nuclear Magnetic Resonance spectrometry (NMR), that is used to provide information about the chemical bonds and elemental composition of nanoparticles by measuring the magnetic fields around the atoms.

### 1.6.3 Optical properties characterization

- UV-Vis spectroscopy: This technique is based on focusing a beam of UV-Vis radiation through the sample. When radiation crosses the sample, some photons are absorbed by the nanoparticles, which are promoted to a higher energy level, and relaxed by nonradiative processes. The equipment measures transmitted light and calculates the absorbance as the negative logarithm of the transmittance ($P/P_0$), where $P_0$ is the incident light intensity and P is the transmitted light intensity. The concentration of the analyte can be related with the measured absorbance through the Lambert-Beer law (Equation 6):

  $$A = \log\left(\frac{P_0}{P}\right) = b \times C \times \varepsilon \qquad \text{Equation 6}$$

  where A is the absorbance, b is the path length, C is the concentration of the analyte, and ε the molar absorptivity at a specific wavelength [325].

  The absorption bands that appear when a dispersion of nanoparticles is analyzed correspond to the SPR bands that appear because of the coupling between the wavelength of the radiation source and the external electrons at the surface of the nanoparticles. The intensity and the position of the bands provide valuable information about the surface of the nanoparticles, their interaction with the environment around them, the size and shape, and the stability of the nanoparticles. The SPR band width is closely related to the size particle dispersion.

- Fluorescence spectroscopy: This technique is based on the measurement of light emitted by molecules, that have been excited to higher energy levels by the absorption of electromagnetic radiation. The equipment measures the intensity of light emitted by the sample and in this case, the detector is located at an angle of 90º with respect to the source to only measure the radiation emitted from the sample [219,325]. With this technique the intensity and position of the emission and excitation bands can be elucidated. This information is related to the size and shape of the nanoparticles. Moreover, with this technique some important parameters can also be calculated, like the Stokes shift and the QY that is an indicative of the fluorescence efficiency of the luminescent nanoparticles.

# 2 Objectives

The main objective of this thesis is the study and development of new analytical strategies for the on-site monitoring of environmental pollutants in water, specifically heavy metals, taking advantage of nanotechnology and the miniaturization and automation of analytical techniques.

In terms of the use of nanotechnology, the aim is to reproducibly obtain nanoparticles that are selective to different heavy metals and that can be used as sensors in flow systems, exploiting their optical and/or electrical properties.

In terms of miniaturization and automation, the aim is to develop a portable device that operates as autonomously as possible and consumes few reagents so that it requires little maintenance. Therefore, the design and manufacturing of a microfluidic platform on which to carry out a Flow Injection Analysis (FIA) will be addressed.

In order to achieve them, the specific objectives of this thesis are specified below:

- Study and optimization of the synthesis of several types of doped Carbon Dots (CDs) from different precursors to make them selective to specific heavy metal ions.

- Construction of a Low Temperature Co-Fired Ceramics (LTCC) microreactor for the reproducible synthesis of the studied CDs.

- Construction of a Cyclic Olefin Copolymer (COC) microfluidic platform to carry out heavy metal analysis due to the quenching effect of heavy metals on the fluorescence of the synthesized CDs.

- Development of an automated miniaturized analytical system for the multiparametric analysis of heavy metals, integrating the live synthesis of the selective CDs.

- Modification of Screen-Printed Carbon Electrodes (SPCEs) with CDs for the selective electrochemical determination of heavy metal ions.

# 3 Experimental

## 3.1 Development of a miniaturized analytical system for the analysis of heavy metals using CDs as optical probes

### 3.1.1 Materials and Reagents

Every reagent used for the synthesis and characterization of CDs devoted to optical detection, and for the analysis of heavy metals by fluorescence quenching is listed in Table 3.1.

Table 3.1: Reagents used for the synthesis and characterization of CDs as optical probes, and determination of heavy metals by fluorescence quenching

| Reagent | Provider | Purity |
|---|---|---|
| Citric acid ($C_6H_8O_7$) | Sigma-Aldrich | 99% |
| Acrylic acid ($C_3H_4O_2$) | Sigma-Aldrich | 99% |
| Glycerol ($C_3H_8O_3$) | Sigma-Aldrich | ≥99.5% |
| Ethylenediamine ($C_2H_8N_2$) | Sigma-Aldrich | ≥99% |
| Imidazole ($C_3H_4N_2$) | Sigma-Aldrich | ≥99% |
| Urea ($CH_4N_2O$) | Sigma-Aldrich | ≥99% |
| Polyethyleneimine, MW 10.000 ($(C_2H_5N)_n$) | Alfa Aesar | 99% |
| Polyacrylamide ($(C_3H_5NO)_n$) | Sigma-Aldrich | - |
| Methionine ($C_5H_{11}NO_2S$) | Sigma-Aldrich | ≥99% |
| Sodium citrate tribasic dihydrate ($(C_6H_5Na_3O_7) \cdot 2H_2O$) | Sigma-Aldrich | ≥99% |
| Quinine hemisulfate salt monohydrate ($C_{20}H_{24}N_2O_2 \cdot 0.5H_2SO_4 \cdot H_2O$) | Sigma-Aldrich | ≥90% |
| Sulfuric acid ($H_2SO_4$) | Sigma-Aldrich | 95-98% |
| Mercury(II) nitrate monohydrate ($Hg(NO_3)_2 \cdot H_2O$) | Sigma-Aldrich | ≥98.5% |
| Cobalt(II) nitrate hexahydrate ($Co(NO_3)_2 \cdot 6H_2O$) | Sigma-Aldrich | ≥98% |
| Lead(II) nitrate ($Pb(NO_3)_2$) | Sigma-Aldrich | ≥99% |
| Iron(III) nitrate nonahydrate ($Fe(NO_3)_3 \cdot 9H_2O$) | Sigma-Aldrich | ≥98% |
| Copper(II) nitrate trihydrate ($Cu(NO_3)_2 \cdot 3H_2O$) | Sigma-Aldrich | ≥99% |
| Nickel(II) nitrate hexahydrate ($Ni(NO_3)_2 \cdot 6H_2O$) | Sigma-Aldrich | ≥98.5% |
| Cadmium nitrate tetrahydrate ($Cd(NO_3)_2 \cdot 4H_2O$) | Sigma-Aldrich | 98% |
| Zinc nitrate hexahydrate ($Zn(NO_3)_2 \cdot 6H_2O$) | Sigma-Aldrich | 98% |
| Chromium(III) nitrate nonahydrate ($Cr(NO_3)_3 \cdot 9H_2O$) | Sigma-Aldrich | 99% |
| Sodium nitrate ($NaNO_3$) | Sigma-Aldrich | ≥99% |
| Calcium chloride dihydrate ($CaCl_2 \cdot 2H_2O$) | Sigma-Aldrich | ≥99% |
| Calcium nitrate tetrahydrate ($Ca(NO_3)_2 \cdot 4H_2O$) | Sigma-Aldrich | 99% |
| Magnesium chloride hexahydrate ($MgCl_2 \cdot 6H_2O$) | Sigma-Aldrich | ≥99% |
| Magnesium nitrate hexahydrate ($Mg(NO_3)_2 \cdot 6H_2O$) | Sigma-Aldrich | 99% |
| Potassium chloride (KCl) | Sigma-Aldrich | ≥99% |

| | | |
|---|---|---|
| Potassium carbonate ($K_2CO_3$) | Sigma-Aldrich | ≥99% |
| Uranyl acetate ($C_4H_6O_6U$) | Polysciences, Inc. | 98% |

Materials used for the fabrication of the LTCC microreactor and the COC microfluidic platform are listed in Table 3.2.

Table 3.2: Materials used for the fabrication of the LTCC microreactor and the COC microfluidic platform

| **Material** | **Provider** |
|---|---|
| LTCC 951PX green tapes (254 µm thick prior to firing) | DuPont Corporation, USA |
| LTCC 951PT green tapes (114 µm thick prior to firing) | DuPont Corporation, USA |
| DuPont 5742 gold co-fireable paste | DuPont Corporation, USA |
| DuPont 6141 silver co-fireable paste | DuPont Corporation, USA |
| PT100 temperature sensor | Innovative Sensor Technology, Switzerland |
| 400 µm Topas 5013 COC layers | TOPAS Advanced Polymers GmbH, USA |
| 25 µm Topas 8007 COC layers | TOPAS Advanced Polymers GmbH, USA |
| EPO-TEK H20E epoxy paste | Epoxy Technology Inc., USA |

### 3.1.2 Microfabrication techniques

#### 3.1.2.1 LTCC microreactor

The LTCC microreactor fabrication process is based on a multilayer approach, as mentioned in Section 1.3.2. A scheme of all the steps is depicted in Figure 3.1. Briefly, the different layers that compose the final device were first individually designed, microstructured by laser ablation, and the ones requiring conducting elements were screen-printed. After the proper alignment, the different layers were thermolaminated and finally, the device was sintered following a specific temperature profile. This microreactor was previously designed and tested in our research group [326].

Design of the different layers was performed with CAD software considering that the final 3D structure must be broken down in different layers. In this case, a structure based on a 3D hydrodynamic flow focusing strategy (Figure 3.2A) was applied to have better control over reagents diffusion and mixing [327], and thus, to obtain nanoparticles in a more homogeneous and reproducible way. Moreover, this approach can also avoid channel occlusion. To achieve this purpose, the middle inlet has a smaller height than the other two inlets and the microfluidic channel (Figure 3.2B).

The different layers designed on the CAD software were transferred to the Circuit Master program, which was the software used to cut patterns with the laser machining equipment.

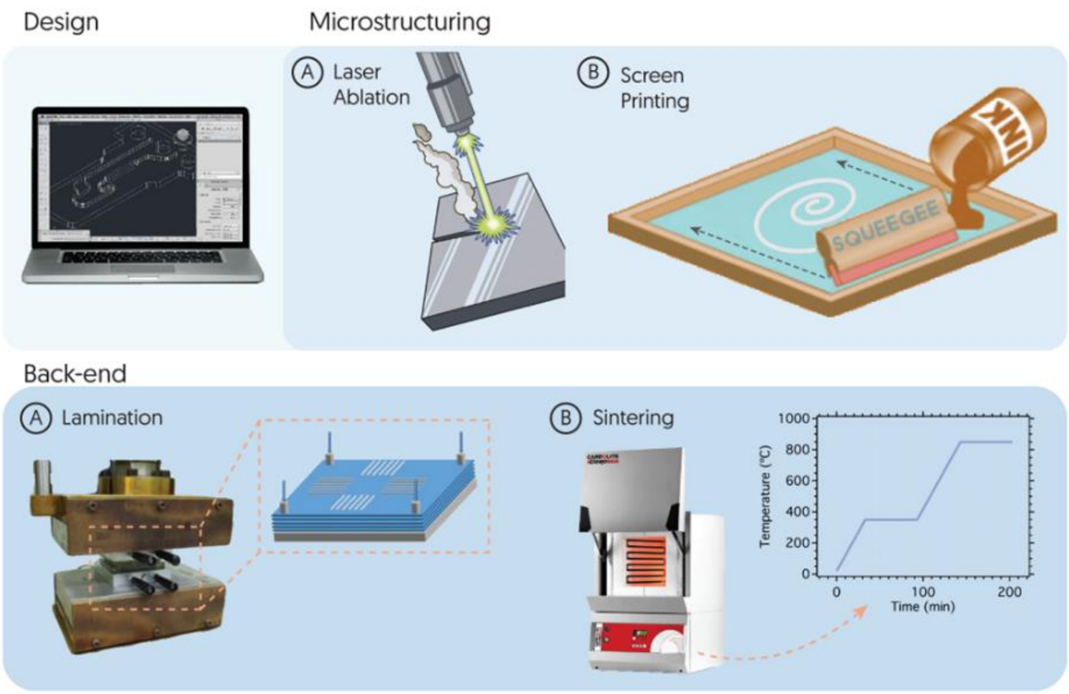

Figure 3.1: Scheme of the general fabrication procedure of the LTCC microreactor [326]

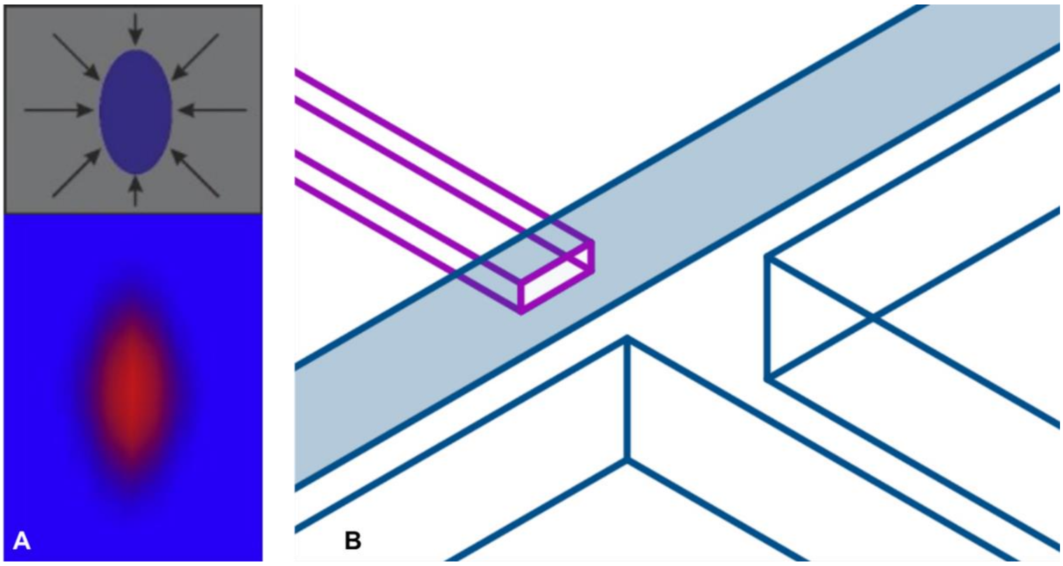

Figure 3.2: A) Schematic representation of 3D hydrodynamic flow focusing [328] and B) view of the inlet area that allows the 3D hydrodynamic flow focusing [326]

The fluidic elements of the device were micromachined onto LTCC 951 green tapes layers using a ProtoLaser 200 (LPKF Laser & Electronics AG, Garbsen, Germany), that consisted of a Nd:YAG (neodymium-doped yttrium aluminum garnet) laser type, that works in the infrared region at 1064 nm, and with a laser beam diameter of 25 µm. The Circuit Master software enabled the modification of some parameters like the beam intensity, the location in the z-axis of the substrate, and the mark speed. For instance, 254 and 114 µm green tapes were cut through with mark speeds of 25 and 50 mm/s, respectively.

Once the different layers containing the fluidic elements had been micromachined, they were laminated. This is an essential step in the construction process, and it is important to choose the right temperature, pressure, and lamination time to avoid liquid leakage or obstructions of the microfluidic structure. The alignment of the layers that will be laminated is crucial and for this reason, four holes at the four corners of each LTCC layer were drilled. Then, the different layers were placed between two metallic plates that have four pivots, in which the four holes drilled perfectly fitted. The whole block was placed in a hydraulic press with two hot plates of 25 x 15 cm (Talleres Francisco Camps SA, Granollers, Spain). The temperature and pressure, which can be perfectly controlled, are normally specified in the datasheet of the LTCC material, and for the Dupont LTCC 951 green tapes these conditions were 70ºC and 25 bar. To prevent the adhesion of the LTCC layers to the metallic plates the use of a plastic film (Mylar), which was provided with the ceramic tapes, was necessary.

Once the LTCC fluidic block was laminated, it was placed in the working table of a DEK 248 screen printer (Asflex Internacional, Algete, Spain). A DuPont 5742 gold co-fireable paste was applied to create the resistor pattern on the reverse side of the fluidic block. The screen with the corresponding pattern is composed of a metal frame and a mesh where a stencil with open areas is defined. The conductive paste was transferred to the fluidic block when extended and squeezed with a squeegee. The paste was dried for 15 minutes at 80 ºC, and the final gold resistor can be observed in Figure 3.3.

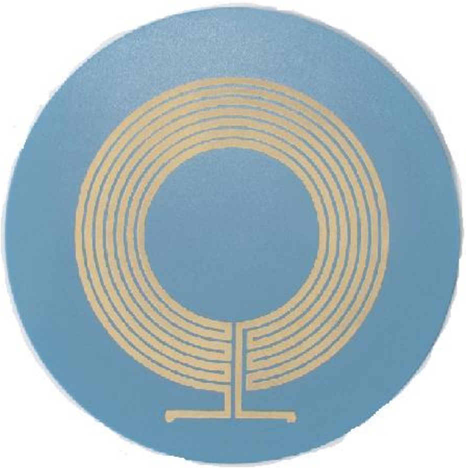

Figure 3.3: Gold resistor screen-printed on the fluidic block

On top of the gold resistor, a block of three LTCC layers was laminated to encapsulate it. Two holes were machined on this block to create the vias, and another serigraphy with the DuPont 6141 silver co-fireable paste was performed to fill the vias and create pads for the electrical connections. This can be seen in Figure 3.5B. The paste was dried for 30 minutes at 80 ºC in this case.

Finally, the LTCC microreactor was sintered in a CBCWF11/23P16 programmable box furnace (Carbolite Gero, Afora, Spain). The temperature profile applied, recommended by the provider, consisted of: a ramp of temperature until 350 ºC at a rate of 10 ºC/min, and stay for 1 hour to produce volatilization of organic components; another ramp of temperature until 850 ºC at a rate of 10 ºC/min, and stay for 1 hour to produce the interpenetration of alumina particles between the layers; and finally, a cooling process until 25 ºC at approximately 5 ºC/min, where the vitrification of the LTCC took place, thus obtaining a hard device. An important aspect regarding the sintering of the device is that it suffers shrinkage due to the loss of organic material. In the case of LTCC 951 tapes, the shrinkage data is provided by the manufacturer as 12.7 ± 0.3% on the x and y-axis, and 15.0 ± 0.5% on the z-axis.

The last step for the fabrication of the microreactor was the attachment of a PT100 temperature sensor using EPO-TEK H20E epoxy paste, which was cured at 80 ºC overnight.

In Figure 3.4, a scheme including the microfluidic structure and the heating resistor can be observed. The fluidic structure consists of three inlets: the carbon source precursor is introduced through the central inlet and the nitrogen source precursor is introduced through the other two inlets, thus creating a 3D hydrodynamic flow focusing, as mentioned before; a spiral-shaped channel where the reaction takes place; and an outlet. The heating resistor was designed to occupy the same area as the microfluidic channel to obtain a good temperature distribution. The top layer of the device only consisted of an LTCC 951PT layer to be able to monitor the formation of the photoluminescent CDs inside the microreactor channel with a UV lamp if necessary. For this reason, the microfluidic inlet and outlet channels were microstructured below the microreactor channel (Figure 3.4).

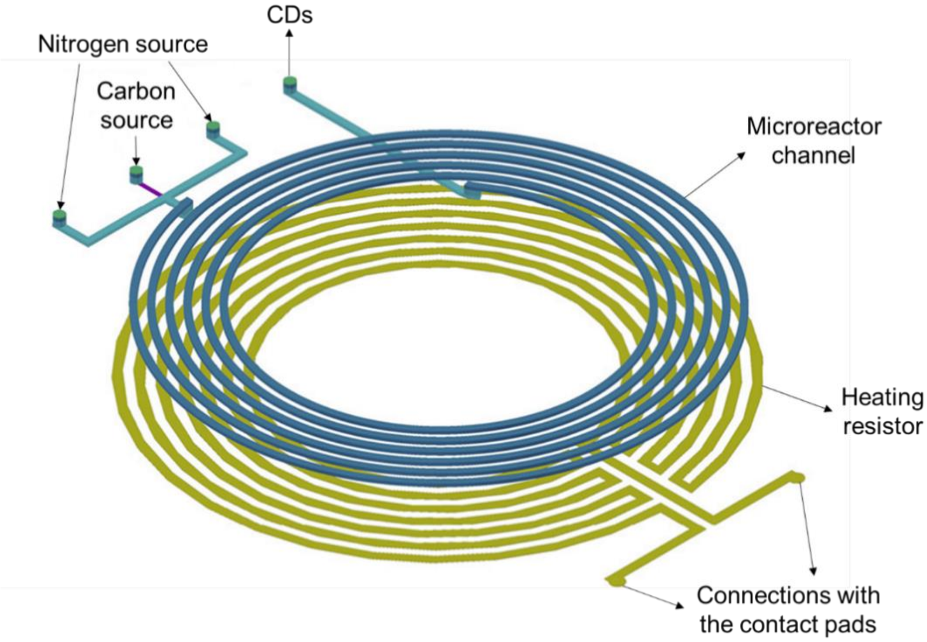

Figure 3.4: 3D representation of the microfluidic structures inside the microreactor and the heating resistor

The microreactor fabricated had a circular shape with a diameter of 6 cm and a total thickness of approximately 3 mm. The total volume of the microreactor channel is about 100 µL, with a total length of 630 mm and cross-section dimensions of 525 µm wide per 290 µm high. In Figures 3.5A and B, the top and bottom views of the final device can be seen.

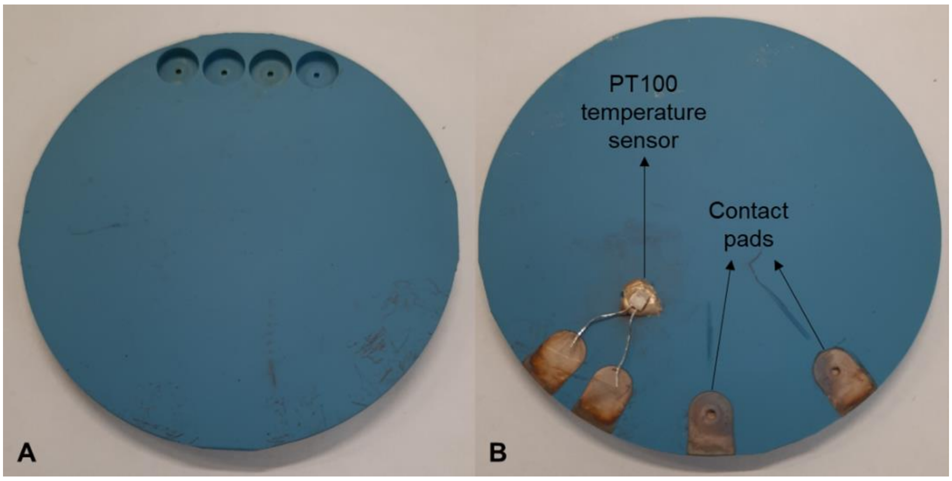

Figure 3.5: A) Top view of the microreactor, with the inlets and outlet. B) Bottom view of the microreactor, with the PT100 temperature sensor and the contact pads for the heating resistor

The temperature was controlled by means of a Printed Circuit Board (PCB) containing all the control electronics (Figure 3.6). The temperature sensor attached to the LTCC device sends the temperature input signal to a PIC18F4431 microcontroller (Microchip Technology Inc., Chandler, AZ, USA). This signal is compared to the target temperature, and a Proportional-Integral-Derivative (PID) system compensates for it. This system was previously developed by our research group [326].

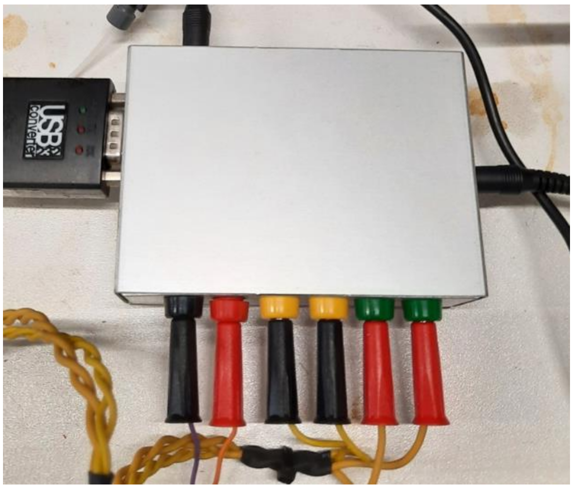

Figure 3.6: Aluminum box that contains the PCB with all the electronics for the temperature control

### 3.1.2.2 COC microfluidic platform

The COC microfluidic platform was fabricated with a multilayer approach, like the LTCC microreactor, and all the steps can be seen in Figure 3.7. In this case, the fabrication process is simpler. First, the different layers that compose the COC device were designed, then they were microstructured with a CNC micromilling machine, and finally the different layers were laminated to obtain the device.

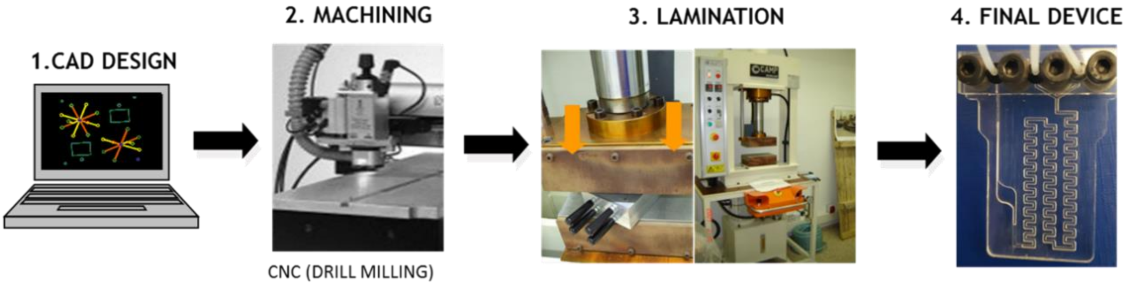

Figure 3.7: Scheme of the general fabrication procedure of the COC microfluidic platform

The fabrication process of the microfluidic platform starts with the design of the different layers with CAD software. The CAD files were then transferred to the Circuit Master software that will be used to micromachine the patterns designed.

Every COC layer substrate was micromachined using a Protomat S63 CNC micromilling machine (LPKF Laser & Electronics AG, Garbsen, Germany). This equipment allows the use of a broad set of tools including drills and different types of mills with a wide variety of diameters. The microfluidic platform is formed by a structural layer and two more layers acting as top and bottom covers. The structural layer is composed of three 400 μm Topas 5013 COC layers and two 25 μm Topas 8007 COC layers that have been previously laminated. The microfluidic structure includes a two-dimensional meander micromixer that was milled at a depth of 1 mm creating a low relief instead of cutting through the material.

Once all the layers were micromachined the lamination was performed by thermocompression bonding. The same metallic plates with the four alignment pivots and the same hydraulic press used for LTCC tapes lamination were used for the lamination of COC layers. Instead of using Mylar films to prevent adhesion, plastic blocks were used in the case of COC substrate. Moreover, these plastic blocks provide a uniform pressure to the layers that will be laminated. In this case, the COC layers were laminated at a pressure of approximately 6 bar, and the temperature was fixed at a value of 100 ºC. But the metallic plates must be introduced between the hot plates of the hydraulic press when they are at room temperature, and then a ramp until 100 ºC is established. When the temperature reached 100 ºC or a little bit higher value, the block was left for 5-10 minutes and finally it was left for cooling to room temperature again. As mentioned in Section 1.3.1, the availability of COC layers with different $T_g$ allowed the application of specific thermocompression conditions. In this case, two types of COC substrates were used, the 400 μm Topas 5013 COC layers with a $T_g$ of 134 ºC and the 25 μm Topas 8007 COC layers with a $T_g$ of 78 ºC [329]. So, with the temperature profile applied, layers with lower $T_g$ melted, and when the laminated block cooled down, they acted as sealing layers.

The COC microfluidic platform (30 mm wide, 50 mm high, and 2 mm deep) has two inlets, a two-dimensional meander micromixer (0.8 mm wide and 1 mm deep), an optical flow cell (4.5 mm diameter and 1 mm deep), and an outlet. It can be seen in Figure 3.8.

Figure 3.8: COC microfluidic platform with the tubing connected

### 3.1.3 Experimental setups

The experimental setup for the optical detection system is based on a rFIA approach (Figure 3.9), where CDs are sequentially injected into samples containing heavy metal ions, since in an environmental application for water analysis, the amount of the reagent (i.e., CDs) is the limiting one. The main features of rFIA technique and its advantages have already been explained in Section 1.1.3. This setup includes a pre-buffering step of the samples that is automatically performed by using an in-line T connector mixer, through which the sample and the buffer are introduced in a 1:1 ratio. The flow management is performed with a Minipuls 2 peristaltic pump (Gilson Inc., Middleton, WI, USA), 0.8 mm internal diameter Teflon tubing (Tecnyfluor, Barcelona, Spain), and 1.14 mm internal diameter Tygon tubing (Ismatec, Wertheim, Germany). An MVP six-port injection valve (Hamilton Company, Bonaduz, Switzerland) is used to inject the CDs, and the connections with the microfluidic platform are secured with FPM75 O-rings (Epidor, Barcelona, Spain).

Fluorescence emission is measured using a customized miniaturized optical detection system, that was developed in collaboration with the Photonics Technology Group at the University of Zaragoza [200]. It consists of an XSL-365-5E LED (Roithner Lasertechnik, Vienna, Austria) that has its emission peak at 365 nm, tilted 45º with respect to the microfluidic platform to reduce interferences on the detection, a MF460/60 25 mm emission band-pass filter (Thorlabs, Munich, Germany), used to avoid that the light coming from the LED reaches the detector, and a PIN S1337-66BR photodetector with 33 $mm^2$ of active area (Hamamatsu Photonics, Shizuoka, Japan). All these elements are integrated in a PCB.

The LED is controlled with a NI USB-6211 Data Acquisition Card (DAQ) (National Instruments, Austin, TX, USA). This device is also used to transfer the detected signal to a computer, that is also used to power both the DAQ and the PCB with all the elements mentioned before.

The PCB is accommodated in a custom-made poly(methyl methacrylate) (PMMA) structure. The insertion of the microfluidic platform in this structure is based on a “Lock-and-Key” concept also developed by our research group [330]. For the application of this approach, it is necessary to fabricate a cartridge with a complementary shape to the microfluidic platform, that allows a reproducible positioning of the platform with respect to the LED and the photodetector. A schematic representation can be seen in Figure 3.10. Also, photographs of the microfluidic platform in its personalized cartridge (Figure 3.11A) and the microfluidic platform inserted in the customized miniaturized optical detection system (Figure 3.11B) are presented.

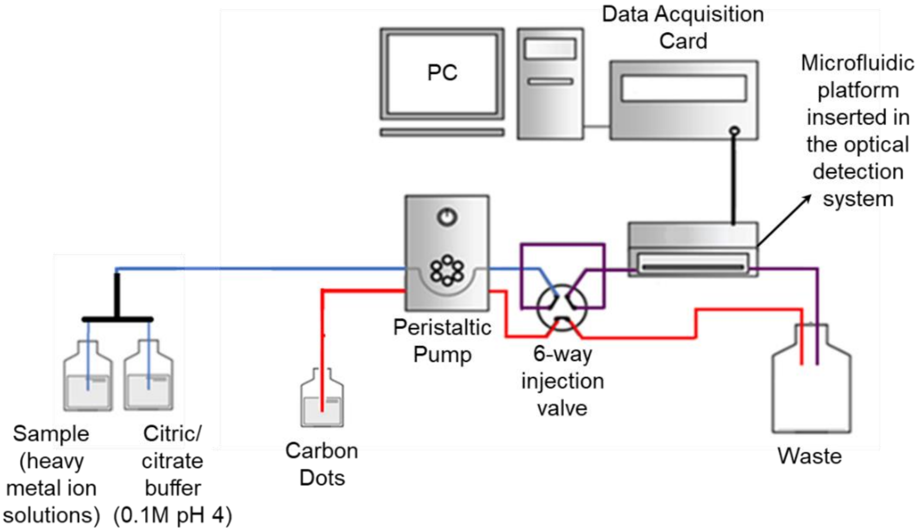

Figure 3.9: Schematic representation of the detection experimental setup

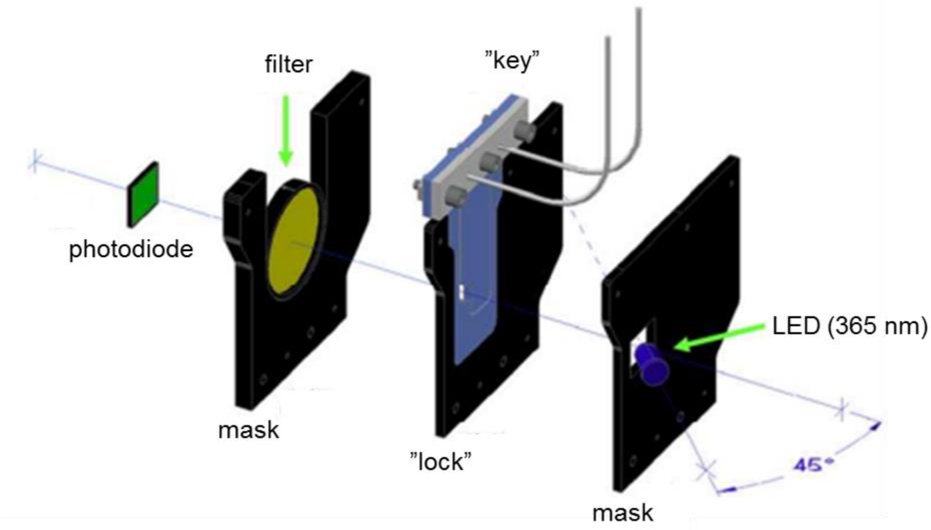

Figure 3.10: Schematic depiction of the “lock-and-key” approach. Adapted from [330]

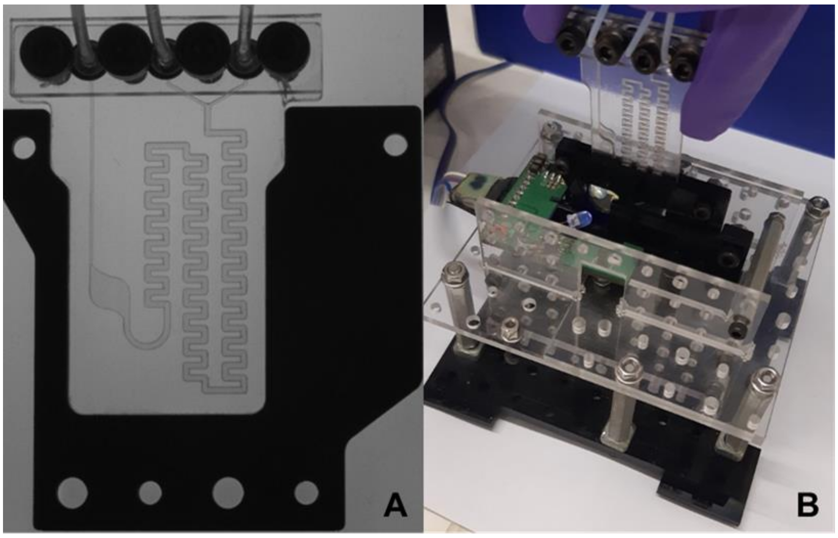

Figure 3.11: A) Photograph of the microfluidic platform in its personalized cartridge and B) photograph of the microfluidic platform inserted in the customized miniaturized optical detection system [331]

The setup for the synthesis of CDs using the LTCC microreactor (Figure 3.12) is composed of three Gastight 1000 TLL glass syringes (Hamilton, Bonaduz, Switzerland) filled with the precursors mounted on three NE-500 OEM syringe pumps (New Era Pump Systems Inc., Farmingdale, NY, USA). These syringes are connected to the fabricated LTCC microreactor using 0.8 mm internal diameter Teflon tubing and the connections are secured with FPM75 O-rings and a custom-built aluminum connector, that can be observed in Figure 3.13. As mentioned in Section 3.1.2.1, to improve the mixing of the carbon source precursor, it is introduced through the middle inlet, while the nitrogen source precursor is introduced through the other two inlets.

Synthesis of CDs requires high temperatures and pressures. Temperature is controlled with the PCB described in Section 3.1.2.1, and pressure is regulated by a P-788 250 psi Back-Pressure Regulator (BPR) (IDEX Health & Science, Oak Harbor, WA, USA) connected to the outlet. CDs are collected using Eppendorf tubes.

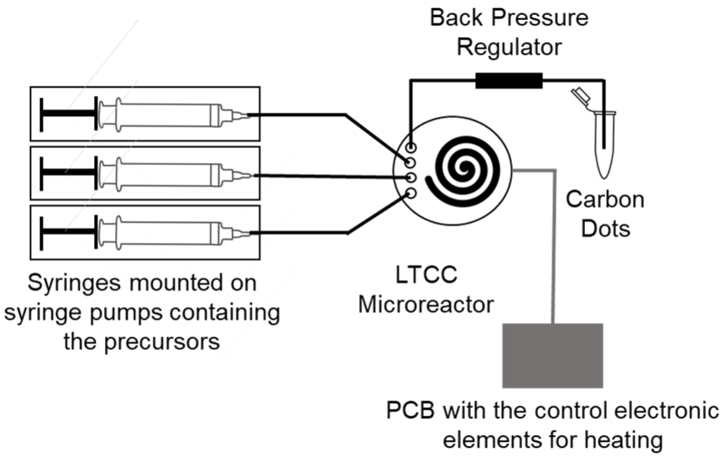

Figure 3.12: Schematic representation of the CDs synthesis experimental setup

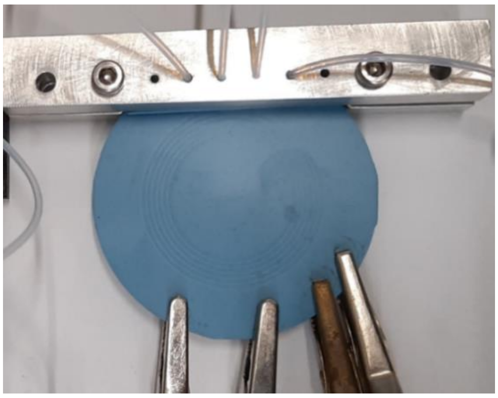

Figure 3.13: LTCC microreactor with connection tubing and custom-built aluminum connector and clamps for the electrical connections

Finally, and since one of the main objectives of the work is to develop an automated system, which integrates the direct synthesis of CDs without the need for any intervention before the determination of heavy metals, the connection of the two described experimental setups is performed by using a 161T031 three-way solenoid valve (NResearch, West Caldwell, NJ, USA). This valve, that is computer-controlled, allows the automatic dilution and buffering of the CDs obtained from the synthesis. 0.8 mm internal diameter Teflon tubing is used for fluidic connections and a FlowTest automated controller (BioTray, Villeurbanne, France) controls the operation of the solenoid valve. It is programmed with the CosDesigner software. In Figure 3.14, the integrated setup can be observed, with the coupling part highlighted in green.

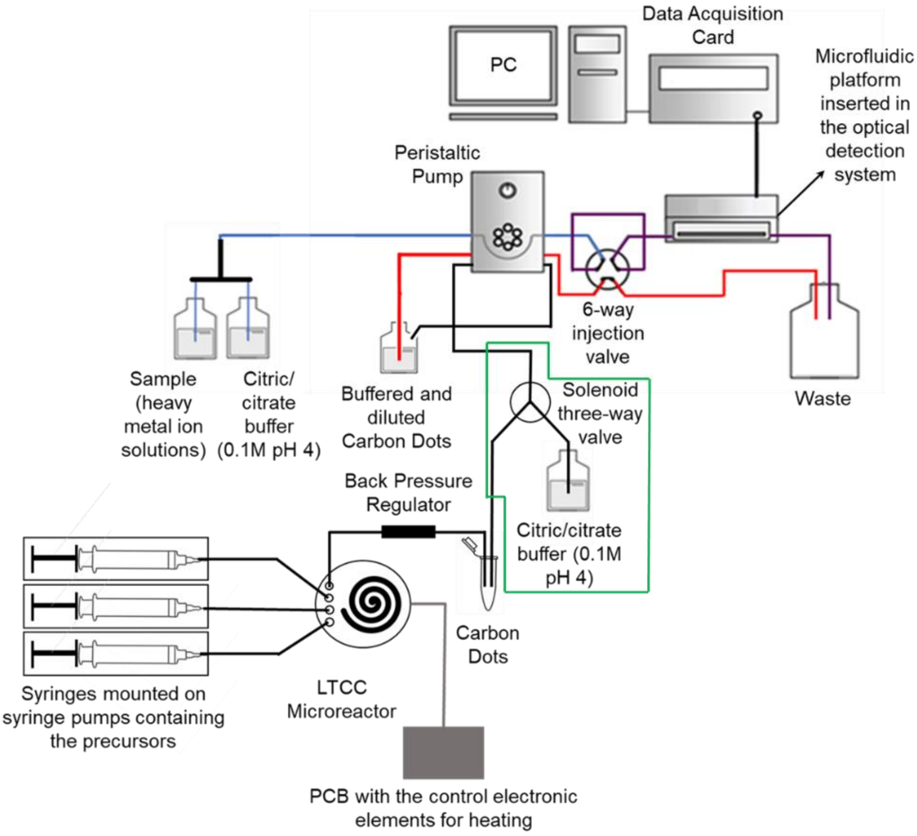

Figure 3.14: Setup for the CDs synthesis and direct use for the detection of heavy metal ions

### 3.1.4 Synthesis of CDs

#### 3.1.4.1 Synthesis of CDs in batch

A wide variety of CDs to selectively determine different heavy metal ions were synthesized by different hydrothermal and microwave-assisted methods. The syntheses methods were extracted from the literature and some of them were modified. The reason to perform synthesis procedures already published, with known properties and selectivity, was to develop, optimize and evaluate the microanalyzer for heavy metals determination. In this section all the performed syntheses are described:

- CDs synthesized from citric acid and ethylenediamine (ED microwave CDs): they were synthesized using a microwave-assisted method. 1.0 g of citric acid and 385 µL of ethylenediamine were mixed with 10 mL of MilliQ water. This mixture was put into a Bifinett KH 1106 domestic microwave oven (Lidl Stiftung & Co. KG, Neckarsulm, Germany). The power was adjusted at 800 W and the mixture was put into the microwave oven for 3 minutes. The brown-black solid was dissolved in MilliQ water to obtain the CDs dispersion [332].

- CDs synthesized from citric acid and ethylenediamine (ED CDs): they were synthesized from the same precursors but following a hydrothermal method. 1.0 g of citric acid and 335 µL of ethylenediamine were mixed and dissolved in 10 mL of MilliQ water. This mixture was put into a Teflon lined stainless-steel autoclave and in an IDL.AI36 oven (Labolan, Esparza de Galar, Spain) at 200 ºC for 5 hours. Then the CDs' resulting solution was left to cool down to room temperature [333]. The reaction involved in the formation of the CDs can be seen in Figure 3.15. As mentioned in Section 1.5.3.2, this reaction results in the formation of IPCA, a molecular fluorophore that is attached to the CDs.

- CDs synthesized from citric acid and polyethyleneimine (PEI CDs): they were synthesized with a microwave-assisted method. 1.0 g of citric acid and 0.5 g of polyethyleneimine were dissolved in 20 mL of hot MilliQ water. The mixture was placed in a Teflon kettle, it was put in a MARS 5 digestion microwave (CEM Corporation, Matthews, NC, USA), and heated at 180 ºC for 5 minutes at a power of 850 W. The resulting dispersion was left to cool down at room temperature [257].

- CDs synthesized from acrylic acid and ethylenediamine (ACR CDs): they were synthesized by a hydrothermal method. 1.2 mL of acrylic acid and 1.0 mL of ethylenediamine were mixed with 20 mL of MilliQ water and the mixture was introduced in a Teflon reaction kettle and in an oven at 200 ºC for 5 hours. The obtained dispersion was allowed to cool down at room temperature [334].

- CDs synthesized from acrylic acid and methionine (MET CDs): they were synthesized with a hydrothermal method. 335 µL of acrylic acid and 0.15 g of methionine were mixed and dissolved in 10 mL of MilliQ water. This mixture was put in a Teflon-lined stainless-steel autoclave and heated at 200 ºC for 12 hours in an oven. Then the dispersion was cooled down to room temperature [335].

- CDs synthesized from sodium citrate and polyacrylamide (PA CDs): these CDs were synthesized with a hydrothermal method. 1.0 g sodium citrate tribasic and 0.5 g of polyacrylamide were dissolved in 20 mL of MilliQ water, and the solution was introduced in a Teflon reaction kettle and heated at 200 ºC for 3 hours in an oven. Then the resulting dispersion was cooled down to room temperature [264].

- CDs synthesized from glycerol and ethylenediamine (EA CDs): they were synthesized with a microwave-assisted method. 5 mL of glycerol and 20 µL of ethylenediamine were mixed with 10 mL of MilliQ water and the mixture was introduced in a domestic microwave oven and heated at a power of 800 W for 10 minutes. The brown solid obtained was dispersed in water. The dispersion was then left to cool down at room temperature [336].

- CDs synthesized from citric acid and urea and modified with imidazole (UREA CDs): they were synthesized by a hydrothermal method. First, 3 g of citric acid and 3 g of urea were dissolved in 10 mL of MilliQ water. The mixture was heated in a domestic microwave oven for 4 minutes at a power of 800 W. 100 mg of the dark brown solid obtained were added to a solution containing 0.5 g of imidazole in 20 mL of MilliQ water and left to react with stirring at 80 ºC for 12 hours under a nitrogen atmosphere [337].

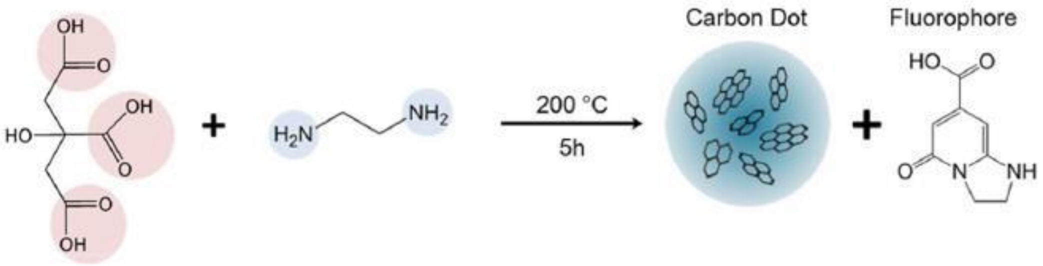

Figure 3.15: Products formed in the ED CDs reaction. The fluorophore IPCA is attached to the surface of the CDs [216]

All dispersions obtained from these synthetic methods were purified in the same way. A Pur-A-Lyzer Mega 1000 dialysis kit purchased from Sigma-Aldrich was used. The dispersion containing the CDs was introduced in a dialysis tube with a membrane with a cut-off of 1000 Da, and it was dialyzed against MilliQ water for 48-72 hours.

Once dialyzed, dispersions containing CDs were stored in a refrigerator at 4 ºC for further characterization and use.

#### 3.1.4.2 Synthesis of CDs in the LTCC microreactor

Once a variety of CDs were synthesized in batch, characterized, and used for the selective determination of different heavy metal ions, some of the synthesis methods described in the previous section were adapted to be performed in the microreactor. As mentioned in Section 3.1.2.1, the carbon precursor was introduced into the microreactor through the middle inlet and the nitrogen precursor was introduced through the other two inlets, thus creating a 3D hydrodynamic flow focusing effect. So, for each synthesis one syringe was filled with the solution containing the carbon precursor and the other two syringes were filled with the solution containing the nitrogen precursor. The precursors were pumped at a total flow rate of 10 µL/min (3.33 µL/min through each inlet) for all the syntheses made in the LTCC microreactor. Considering that the microreactor has an approximate volume of 100 µL, the residence time was about 10 minutes. The pressure was fixed at 17 bar with the BPR, since during a previous optimization of the syntheses, a continuous flow inside the microreactor was assured without the formation of bubbles, even working at temperatures as high as 190 ºC [326].

The first two syntheses were already adapted in a previous work [326] and they were reproduced here with slight modifications. Briefly:

- CDs synthesized from citric acid and ethylenediamine (ED CDs): the solution of citric acid, that was pumped through the central inlet was prepared by dissolving 0.58 g in 15 mL of MilliQ water, and the solution of ethylenediamine, that was pumped through the other two inlets was prepared by mixing 200 µL of ethylenediamine with MilliQ water to a total volume of 15 mL. This synthesis was performed at 190 ºC.

- CDs synthesized from citric acid and polyethyleneimine (PEI CDs): the solution of citric acid was prepared by dissolving 0.58 g in 15 mL of MilliQ water as in the previous synthesis, and the solution of polyethyleneimine was prepared by dissolving 0.25 g in 15 mL of MilliQ water. This synthesis was also performed at 190 ºC.

Another two of the syntheses performed in batch were adapted to be performed in the LTCC microreactor. In these two cases they were performed at 17 bar as the previous ones, but in this case, three different temperatures and three different concentrations of the nitrogen precursors were tested to optimize the synthesis process to obtain the CDs with the highest QYs:

- CDs synthesized from glycerol and ethylenediamine (EA CDs): the solution of glycerol was prepared by mixing 3 mL with MilliQ water to a total volume of 15 mL (2.74 M). Three solutions of ethylenediamine were prepared by mixing 20, 40, and 60 µL of ethylenediamine with MilliQ water to a total volume of 20 mL in the three cases (0.015, 0.030, and 0.045 M, respectively). Syntheses were performed at 150, 170, and 190 ºC.

- CDs synthesized from acrylic acid and ethylenediamine (ACR CDs): the solution of acrylic acid was prepared by mixing 1.6 mL with MilliQ water to a total volume of 10 mL (2.33 M). Three solutions of ethylenediamine were prepared by mixing 0.5, 1.0, and 1.5 mL of ethylenediamine with MilliQ water to a total volume of 20 mL in the three cases (0.37, 0.75, and 1.12 M, respectively). Syntheses were performed at 150, 170, and 190 ºC.

In the case of the CDs synthesized in the LTCC microreactor, the CDs were split into two fractions, one of them, as for the CDs synthesized in batch, was purified by dialysis with the Pur-A-Lyzer Mega 1000 dialysis kit against MilliQ water for 48-72 hours, and the other one that was used as obtained without further treatment. Some analytical quality parameters like sensitivity, LOD, and repeatability, as well as the QY were compared between the two fractions of the CDs to assess if the effect of the purification is significant. Dispersions containing the CDs were stored in a refrigerator at 4 ºC for further characterization and use.

### 3.1.5 CDs characterization

Different methods for characterizing the synthesized CDs were used. As already mentioned, the physical, chemical, structural, and optical characterization is important in order to know their properties and therefore their potential applications. In this thesis the techniques used to characterize the CDs are as follows:

- UV-Vis Spectroscopy: absorption spectra were registered between 300 and 650 nm with a UV-3101PC UV-Vis-NIR double beam spectrophotometer (Shimadzu, Kyoto, Japan). To avoid self-attenuation of CDs in PL measurements and to calculate QY, CDs were diluted with a pH 4 citric/citrate buffer until the absorbance was approximately 0.05 a.u.

- Fluorescence spectroscopy: fluorescence emission and excitation spectra were registered with a Fluorolog FL3-11 spectrofluorometer (Horiba Jobin Yvon, Longjumeau, France). As the electronic transitions involved in fluorescence emission have lower energy than that involved in absorption, the emission peak appears at a higher wavelength. So, to register emission spectra, excitation wavelength was fixed at the same wavelength where the absorption maximum appeared, and emission was registered between approximately 10 nm over the excitation wavelength and until 650 nm. Excitation spectra were registered from 300 nm to a wavelength approximately 10 nm under the emission maximum. All the spectra were registered using a slit width of 1 nm. As mentioned in Section 1.5.3.2, an important value regarding PL is the QY, which is the number of emitted photons relative to the number of absorbed photons. The most common method to calculate it is the optically dilute measurement method [338], in which the QY is calculated using quinine sulfate in 0.1 M sulfuric acid as a reference, as follows:

$$\varphi_x = \varphi_{st} \times \frac{I_x}{I_{st}} \times \frac{A_{st}}{A_x} \times \frac{\eta_x^2}{\eta_{st}^2} \qquad \text{Equation 7}$$

  Where φ is the PL QY, I the integrated area of the corrected emission spectrum, A the absorbance, and η the refractive index of the solvent. The subindexes x and st refer to the sample and the reference standard, respectively. Considering that both are dissolved in water, the last term of the equation can be ignored. Before performing the measurements for the calculation of the QY, the CDs dispersions were bubbled with a nitrogen flow to remove all the oxygen, that could act as a quencher. The emission spectrum registered was a corrected spectrum, since for the calculation of the QY the value needed is the integrated area of the corrected spectrum.

- DLS: measurements were carried out using two different instruments, a Nanotrac Flex (Microtrac, Krefeld, Germany) and a Zetasizer Nano ZS (Malvern Panalytical, London, England) to obtain the particle size distribution of the CDs. In the first instrument, it is enough to introduce the probe with the laser in the CDs dispersion to acquire data, but some characteristics of the nanoparticles (shape and transparency) and of the solvent (refractive index and viscosity) must be introduced in the software before the measurement. In the second instrument, the sample containing the nanoparticles is introduced in a cuvette and the measurement is directly performed. In both cases, the instruments give information about the concentration of the sample, indicating if the concentration is too high or too low. If it is too high the CDs dispersion has to be diluted.

- HRTEM: images were taken with two different instruments, the JEM-2011 Microscope (Jeol Ltd., Tokyo, Japan), and the Tecnai G2 F20 HR(S)TEM (Field Electron and Ion Company, Hillsboro, OR, USA). For the preparation of samples, a drop of the CDs’ dispersion, obtained directly from the purification, was placed in Holey Carbon Films with Cu 400 mesh grids (Quantifoil Micro Tools GmbH, Jena, Germany) and then it was left 24 hours for the solvent evaporation. Then the grid was put in the sample holder and images were taken. In general, images were difficult to obtain due to the low contrast between the carbon nanoparticles and the carbon-based grid support. Once the images were taken, they were processed with ImageJ 1.51n software.

- FTIR: the infrared spectra of the CDs were acquired with a Tensor 27 FTIR spectrometer (Bruker, Billerica, MA, USA). The Attenuated Total Reflectance (ATR) accessory of the instrument allows the direct analysis of a solid sample. 20 µL of the CDs dispersion were introduced in an oven at 50 ºC for two days to evaporate water. Only CDs synthesized using the LTCC microreactor were analyzed because batch synthesized CDs FTIR spectra were previously described in the literature.

### 3.1.6 Optimization of the CDs synthesis and the analysis equipment of heavy metals

As explained in Section 3.1.3, the analysis of heavy metals is based on a rFIA protocol, in which a solution flows to the detector at a certain flow rate and with which the baseline signal is measured. Then, a certain volume of CDs is injected into the buffer solution at the same flow rate with which a maximum emission peak is obtained. This value corresponds to the fluorescence signal without quencher ($F_0$). After that, CDs are also injected into different standards containing increasing concentrations of the analyte. In this case, the signal decreases due to the quenching effect. These values correspond to the fluorescence signals in presence of the quencher (F). Finally, samples were analyzed, into which the same quantity of CDs is injected. $F_0$ is divided by the signal obtained and the value is interpolated in the Stern-Volmer calibration plot to obtain the concentration of the analyte in each sample.

The height of the peaks depends on the flow rate, the injection volume of CDs and their concentration and the pH of the solutions, so these parameters must be optimized. Moreover, to work with the maximum signal and the minimum noise, some operational parameters of the microanalyzer, such as integration time and signal amplification must be optimized as well. All these parameters were optimized using a univariate optimization procedure and taking as compromise the signal-to-noise ratio and the sensitivity (as slope of the calibration plot) of the measurements.

The first parameters optimized were the buffer pH value and concentration. A citric/citrate buffer was chosen, and it was prepared at four different pH values (3, 4, 5, and 6) and three different concentrations (0.01, 0.1 and 1 M). Every composition and pH were tested to obtain the maximum fluorescence signal and considering the solubility of the different heavy metal ions at the specific pH value.

As mentioned before, some hydrodynamic parameters of the rFIA system used for the determination of the heavy metals were also optimized. The first one was the flow rate (0.5, 1.0, 1.5, 2.0 mL/min). The effect of flow rate into the obtained signal was studied by performing an injection of ED CDs into the buffer solution. Then, CDs injection volume (0.1, 0.25, 0.5, 1.0 mL) was optimized. The effect of injection volume into the obtained signal was studied by performing an injection of ED CDs into the buffer solution. Finally, the CDs concentrations were also optimized. As CDs are obtained as a dispersion from the synthesis, dilution factors were used as an approximate measurement. Moreover, in cases when a reference material is not available to perform a calibration plot to calculate the absolute concentration of nanomaterials in a dispersion, it is common to give dilution factors. In this sense, different dilution factors (10, 50, 100, 500, 1000) were tested for the synthesized CDs. For this optimization, the CDs have been injected into citric/citrate buffer, 0.1, 0.5 and 1 ppm solutions of the heavy metal ion for which each type of CD is selective to, and then the results were linearized with the Stern-Volmer equation explained in Section 1.5.3.2 and the sensitivities were compared.

Moreover, some parameters affecting the optical signal of the customized miniaturized optical detection system like signal amplification and integration time were optimized. In this case, ED CDs were injected into the buffer solution and 0.01 ppm $Hg^{2+}$ standard solution to evaluate the signal-to-noise ratio.

Finally, and as explained in Section 3.1.4.2, parameters affecting the QY of the CDs synthesis processes adapted to the LTCC microreactor like the concentration and molar relation of the precursors and the temperature, which affects the degree of carbonization, were optimized to obtain the highest QY and thus the highest signal-to-noise ratio when used as optical probes.

### 3.1.7 Photoluminescence quenching measurements

#### 3.1.7.1 Selectivity tests

Before performing the fluorescence quenching measurements with the miniaturized optical detection system, the selectivity of the different CDs was tested using the spectrofluorometer against different heavy metal ion solutions ($Cd^{2+}$, $Co^{2+}$, $Cu^{2+}$, $Cr^{3+}$, $Fe^{3+}$, $Hg^{2+}$, $Ni^{2+}$, $Pb^{2+}$, $Zn^{2+}$) at a concentration of 10 ppm, and other potentially interfering ions present in water ($Na^{+}$, $Mg^{2+}$, $Ca^{2+}$, $Cl^{-}$, $CO_3^{2-}$) at a concentration of 1000 ppm. An emission spectrum was recorded by mixing in a quartz cuvette an aliquot of 0.5 mL of CDs dispersion at the optimized dilution factor to have an approximate absorption of 0.05 a.u. to avoid possible self-attenuation effects and 2.5 mL of citric/citrate buffer. This was the reference emission value. Then, to observe the effect of the ions tested on the fluorescence of the CDs, aliquots of 0.5 mL of CDs were mixed individually with 2.5 mL of buffered solutions of each mentioned ion, and emission spectra were recorded.

#### 3.1.7.2 Analytical quality parameters

Once the CDs' selectivity was evaluated, calibration plots were obtained by injecting per triplicate each type of CDs synthesized in batch and in the LTCC microreactor in standard solutions containing increasing concentrations of the heavy metal studied in each case (0.01, 0.05, 0.1, 0.5, and 1 ppm). With this technique, a transient signal is established, with a maximum value when CDs are injected into a solution without the heavy metal ion, and quenched values when the solution contains the heavy metal ion for which the CDs are selective to. Fluorescence intensity was obtained as the peak height and can be correlated with the quencher concentration through the Stern-Volmer equation, which has been explained in Section 1.5.3.2. $K_{SV}$ is the Stern-Volmer quenching constant, which indicates the sensitivity of the method. LOD was calculated as three times the standard deviation (SD) of the blank signal (citric/citrate buffer) divided by the slope of the calibration plot ($K_{SV}$). Repeatability of the system was also evaluated by performing ten injections of each type of CDs into a standard solution containing 0.5 ppm of the heavy metal studied and it was calculated as the relative standard deviation (RSD).

#### 3.1.7.3 Analysis of synthetic and real samples with the CDs synthesized in batch

To assess the applicability of the method for the multiparametric determination of different heavy metal ions, spiked tap water samples and extracts of polluted soil samples were analyzed with the CDs synthesized in batch as optical probes. Tap water samples were spiked to obtain concentrations of 0.03, 0.06, 0.1, 0.4, and 0.8 ppm of the heavy metal studied in each case and the recovery rates were calculated. Also, nitric acid extracts of polluted soil samples coming from the neighborhood of a smelter plant (located in Torreón, Mexico) and containing high concentrations of $Cu^{2+}$, $Co^{2+}$, $Ni^{2+}$, and $Pb^{2+}$, as well as other metallic ions were analyzed. Samples were previously analyzed with a reference method (ICP-OES with an Optima 4300DV spectrometer (PerkinElmer Inc., Waltham, MA, USA)) for comparison purposes. Extracts of soil samples were obtained as follows: 0.5 g of each sample was digested with 10 mL of nitric acid in an Ultrawave microwave digestion system (Milestone Inc., Shelton, CT, USA) at 175ºC for 15 min. Samples were filtered with a 0.45 µm filter and diluted to 50 mL with MilliQ water before analysis. As stated in Section 3.1.3, to avoid pH changes, samples were automatically buffered in the developed analytical system before the injection of the CDs.

Calibration plots were performed with standard solutions at different concentration ranges depending on the analyte, which are specified in Section 4.1.1.5.

#### 3.1.7.4 Analysis of synthetic and real samples with the CDs synthesized in the LTCC microreactor

In the same way as for the CDs synthesized in batch, to demonstrate the potential of the system to monitor heavy metals in water, in this case, tap water samples and river water samples (Besòs river, Spain) were analyzed. The two types of samples were spiked with different concentrations of the heavy metal for which every type of CDs was selective to (0.10, 0.25, 0.50, and 0.75 ppm) and recovery rates and RSD of a triplicate were calculated for accuracy and precision evaluation, respectively.

Finally, $Co^{2+}$ spiked tap water and river water samples (0.10, 0.25, 0.50, and 0.75 ppm) were also analyzed with the integrated analytical equipment developed for the monitoring of $Co^{2+}$ as a demonstrator with the direct and freshly synthesis of ACR CDs by means of a coupled microreactor. The concentration of $Co^{2+}$ in tap and river water was determined by ICP-OES prior to the spiking process and found under the LOD. Therefore, the concentration of $Co^{2+}$ in real samples before the spiking process was considered zero and the spiked concentration was considered the true value for the calculation of recoveries.

## 3.2 Electrochemical detection of heavy metals with CDs

### 3.2.1 Reagents

The listed reagents used for the synthesis, characterization, modification of SPCEs, and electrochemical determination of heavy metals is shown in Table 3.3.

Table 3.3: Reagents used for the synthesis, characterization, modification of SPCEs, and electrochemical determination of heavy metals

| Reagent | Provider | Purity |
|---|---|---|
| Citric acid ($C_6H_8O_7$) | Sigma-Aldrich | 99% |
| Urea ($CH_4N_2O$) | Sigma-Aldrich | ≥99% |
| Mercury(II) nitrate monohydrate ($Hg(NO_3)_2 \cdot H_2O$) | Sigma-Aldrich | ≥98.5% |
| Cobalt(II) nitrate hexahydrate ($Co(NO_3)_2 \cdot 6H_2O$) | Sigma-Aldrich | ≥98% |
| Lead(II) nitrate ($Pb(NO_3)_2$) | Sigma-Aldrich | ≥99% |
| Copper(II) nitrate trihydrate ($Cu(NO_3)_2 \cdot 3H_2O$) | Sigma-Aldrich | ≥99% |
| Nickel(II) sulfate hexahydrate ($NiSO_4 \cdot 6H_2O$) | Sigma-Aldrich | ≥98% |
| Cadmium nitrate tetrahydrate ($Cd(NO_3)_2 \cdot 4H_2O$) | Sigma-Aldrich | 98% |
| Zinc sulfate heptahydrate ($ZnSO_4 \cdot 7H_2O$) | Sigma-Aldrich | 99% |
| Iron(III) nitrate nonahydrate ($Fe(NO_3)_3 \cdot 9H_2O$) | Sigma-Aldrich | ≥98% |
| Sodium nitrate ($NaNO_3$) | Sigma-Aldrich | ≥99% |
| Calcium nitrate tetrahydrate ($Ca(NO_3)_2 \cdot 4\ H_2O$) | Sigma-Aldrich | 99% |
| Magnesium nitrate hexahydrate ($Mg(NO_3)_2 \cdot 6\ H_2O$) | Sigma-Aldrich | 99% |
| Acetic acid ($C_2H_4O_2$) | Sigma-Aldrich | ≥99% |
| Sodium acetate trihydrate ($C_2H_3O_2Na \cdot 3H_2O$) | Sigma-Aldrich | ≥99% |
| Quinine hemisulfate salt monohydrate ($C_{20}H_{24}N_2O_2 \cdot 0.5H_2SO_4 \cdot H_2O$) | Sigma-Aldrich | ≥90% |
| Sulfuric acid ($H_2SO_4$) | Sigma-Aldrich | 95-98% |
| Graphene Oxide 4 mg/mL, dispersion in $H_2O$ | Aldrich | - |
| Carbon nanotube, multi-walled, carboxylic acid functionalized | Aldrich | - |
| Carbon nanotube, single-walled, octadecylamine functionalized | Aldrich | - |

### 3.2.2 Synthesis of CDs and characterization

For this part of the work, CDs from citric acid and urea were synthesized with a hydrothermal method adapting a synthesis method published in the literature [339]. 2.0 g of citric acid and 1.8 g of urea were dissolved in 10 mL of MilliQ water, and the mixture was introduced in a Teflon-lined stainless-steel autoclave. It was heated at 160 ºC for 4 hours in an oven. Finally, the solution was left to cool down to room temperature.

The CDs dispersion was dialyzed with a Pur-A-Lyzer Mega 1000 dialysis kit purchased from Sigma-Aldrich. The dispersion containing CDs was introduced in a dialysis tube with a membrane with a cut-off of 1000 Da, and it was dialyzed against MilliQ water for 48-72 hours. Once dialyzed, the dispersion was stored in a refrigerator at 4 ºC. Since the concentration of the CDs is unknown, dilution factors in acetate buffer were used as an approximate measurement. All the dispersions of the CDs and the metal ions were buffered at pH 4 with a 0.2 M acetate buffer.

For characterization purposes, UV-Vis spectra of the synthesized CDs were registered with a V-660 UV-Vis double-beam spectrophotometer (Jasco, Inc., Tokyo, Japan) between 300 and 650 nm. As for the CDs synthesized in Section 3.1, they were diluted until the absorbance was approximately 0.05 a.u to avoid self-attenuation of CDs to perform PL measurements and to calculate the QY.

Fluorescence emission and excitation spectra were recorded with an FP-6500 spectrofluorometer (Jasco, Inc., Tokyo, Japan). To register emission spectra, the excitation wavelength was fixed at the same wavelength where the absorption maximum appeared, and the emission was registered between approximately 10 nm over the excitation wavelength and 600 nm. Excitation spectra were registered from 300 nm to a wavelength approximately 10 nm under the emission maximum. QYs were calculated with the optically dilute measurement method as well, using quinine sulfate in 0.1 M sulfuric acid as the reference, and recording the corrected emission spectra. All the spectra were registered using a slit width of 1 nm.

The CDs were optically characterized since the information obtained like intensity and the position of the bands provides information about the size of the nanoparticles.

FTIR spectra of the CDs were acquired with a Frontier FTIR spectrometer (PerkinElmer Inc., Waltham, MA, USA) with a Universal ATR sampling accessory. For the preparation of the CDs, 20 µL of the CDs dispersion was introduced in an oven at 50 ºC for two days to evaporate water in the sample.

### 3.2.3 Experimental setup

To perform electrochemical measurements, DRP 110 SPCEs (Metrohm DropSens, Oviedo, Spain) were used. SPCEs (Figure 3.16A) are low-cost and disposable electrodes designed to work with low volumes of samples. Working (4 mm of diameter) and counter electrodes are made of carbon, while reference electrode is made of silver. The SPCE is inserted in a DSC4mm boxed connector (Metrohm DropSens, Oviedo, Spain) (Figure 3.16B) that acts as an interface between the SPCEs and the PalmSens4 potentiostat (PalmSens BV, Houten, The Netherlands) (Figure 3.16C) that is used to perform the voltametric measurements.

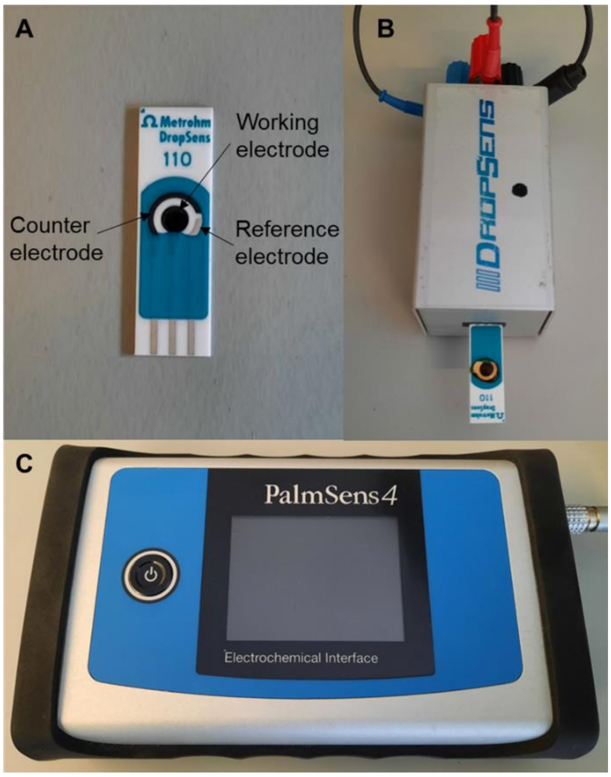

Figure 3.16: A) DRP 110 SPCE with the three electrodes, B) DSC4mm boxed connector with the SPCE inserted, and c) the PalmSens4 potentiostat

In this work, the CDs synthesized from citric acid and urea were used to selectively determine $Cd^{2+}$ ions. Modification of electrodes with CDs provides fast electron transfer kinetics due to the high electrical conductivity and an increased surface area due to the high surface-to-volume ratio. Moreover, the hydroxyl, carboxyl, carbonyl, and other functional groups present in the surface of the CDs provide different selectivity depending on the precursors used for their synthesis. As the potentiostat used allows to perform electrochemical measurements using different techniques the first thing that was made was the selection of the detection technique. CV, DPV, and Square Wave Stripping Voltammetry (SWSV) techniques were evaluated, obtaining the best sensitivity for $Cd^{2+}$ determination with SWSV. Therefore, it was the selected technique for further experiments.

Different approaches were explored to determine $Cd^{2+}$ ions. The first one was to work with bare SPCE and then place a drop of 50 µL of a mixture of CDs and $Cd^{2+}$, to explore the possibility of the continuous monitoring of $Cd^{2+}$ in water. The next possibility explored was to deposit 6 µL of the CDs in the surface of the working electrode, let them dry for 2 hours, and then place a drop of 50 µL of a $Cd^{2+}$ solution. To increase the sensitivity of the measurement, the surface of the working electrode was modified. A solution of 1 mg/mL of Multi-Walled Carbon Nanotubes (MWCNTs) functionalized with carboxylic acid (MWCNT-COOH) in ethanol absolute, a solution of 1 mg/mL of SWCNTs functionalized with octadecylamine (SWCNT-amine) in ethanol absolute, and a solution of 1 mg/mL of GO in MilliQ water were used to modify the surfaces of the working electrodes of the SPCEs. The process started with the deposition of 2 µL of each one of the solutions in different electrodes and let them dry for 1 hour in the case of GO solution and 15 minutes in the case of the MWCNT-COOH and SWCNT-amine solutions. Then, 6 µL of the CDs were deposited in the modified surface of the working electrode, let them dry for 2 hours and, finally, a drop of 50 µL of a $Cd^{2+}$ solution was placed for the measurement.

### 3.2.4 Optimization

Once the process for the SPCE modification was stated, some experimental parameters (deposition time, deposition potential, amplitude, frequency, and dilution factor of the CDs) were optimized systematically to get the maximum peak current for $Cd^{2+}$.

Considering that the CDs were kept in solution, dilution factors were used as an approximate measurement since the concentration of CDs is unknown, and different dilution factors of the CDs (10, 100, 1000) were also tested in order to obtain the higher peak currents of $Cd^{2+}$.

Some parameters affecting the sensitivity of SWSV measurements were optimized after the electrode modification process was established. These parameters were the deposition potential (-0.5, -0.6, and -0.7 V were the values selected), the deposition time (2, 4, 6, and 8 min), the amplitude (2.5, 5.0, 7.5, and 10.0 mV), and finally the frequency (5, 25, and 50 Hz).

To make this optimization, a solution containing 1 ppb of $Cd^{2+}$ was deposited on the modified SPCEs and the response was acquired.

### 3.2.5 Cadmium analysis

Selectivity was also evaluated by adding different heavy metal ions ($Co^{2+}$, $Cu^{2+}$, $Fe^{3+}$, $Hg^{2+}$, $Ni^{2+}$, $Pb^{2+}$ and $Zn^{2+}$) and other metal ions present in water ($Ca^{2+}$, $Mg^{2+}$, and $Na^{+}$) to the standard solutions containing $Cd^{2+}$. 1 ppm of the potential interferent heavy metal ions and 100 ppm of the other metal ions present in water were individually added to the solution containing 1 ppb of $Cd^{2+}$ and, the current signals were compared with the one obtained with the solution only containing 1 ppb of $Cd^{2+}$.

A calibration plot was obtained by recording the stripping voltammograms of different solutions containing increasing concentrations of $Cd^{2+}$ (0.2, 0.4, 0.6, 0.8, 1.0, 2.5, 5.0, 7.5, and 10.0 ppb) with the modified SPCEs. The analytical performance of the proposed method for $Cd^{2+}$ determination was evaluated under optimal conditions (CDs 10-times diluted, -0.6V as deposition potential, 6 min as deposition time, 5 mV as amplitude, and 25 Hz as frequency). With the Current vs. Concentration plot, sensitivity was obtained, as well as the LOD. The LOD was calculated from 3SD/S (SD is the standard deviation of 1 ppb $Cd^{2+}$ measurements (n=10) and S is the slope of the calibration plot). Finally, repeatability was obtained by calculating the RSD from the same 10 measurements.

# 4 Results and Discussion

## 4.1 Optical detection of heavy metal ions

### 4.1.1 Optical detection of heavy metal ions with CDs synthesized in batch

#### 4.1.1.1 Synthesis and characterization

The CDs were synthesized following the methods described in Section 3.1.4.1. The solutions obtained had different colors and viscosities: ED microwave CDs (dark brown suspension), ED CDs (dark brown suspension), PEI CDs (light brown suspension), ACR CDs (dark brown suspension), MET CDs (yellowish suspension), PA CDs (green/brown viscous suspension), EA CDs (dark brown suspension), and UREA CDs (dark brown suspension).

All the CDs obtained exhibited blue PL upon irradiation with a UV lamp. They present similar absorbance spectra (Figure 4.1), with absorption bands located between 325 and 360 nm in all cases. As mentioned before, the CDs were diluted until an approximate absorption of 0.05 a.u. was reached, to avoid possible self-attenuation effects.

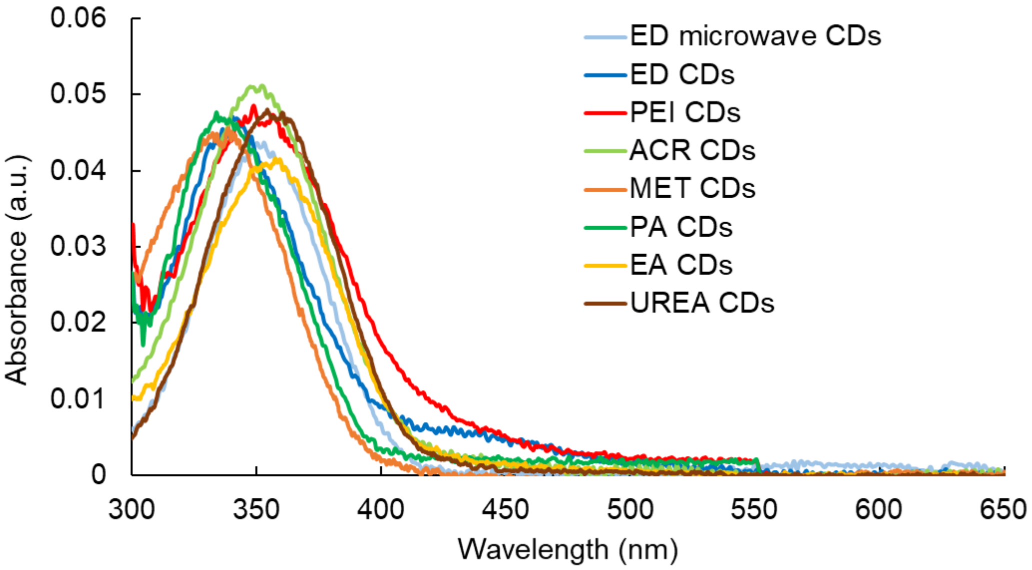

Figure 4.1: UV-Vis spectra of the different CDs synthesized in batch

From the spectra, the wavelengths at which the maximum absorbance of the different synthesized CDs appeared are summarized in Table 4.1:

Table 4.1: Wavelengths for the SPR band of the CDs synthesized in batch

| **Type of CDs** | **Wavelength of the maximum absorbance (nm)** | **Type of CDs** | **Wavelength of the maximum absorbance (nm)** |
|---|---|---|---|
| ED microwave CDs | 353 | MET CDs | 329 |
| ED CDs | 340 | PA CDs | 334 |
| PEI CDs | 349 | EA CDs | 357 |
| ACR CDs | 352 | UREA CDs | 354 |

Regarding PL, all the synthesized CDs showed wide excitation bands with maximums around 350 nm and wide emission bands with maximums around 450 nm. The Stokes shifts, calculated as the difference between the band maxima of the excitation and emission spectra, were approximately 100 nm in all cases, as it can be seen in Figure 4.2. The maximum values and the Stokes shifts are summarized in Table 4.2. These results indicate that the synthesized CDs can be used as optical reagents with the experimental setup described in Section 3.1.3, using the same excitation light source emitting at 365 nm.

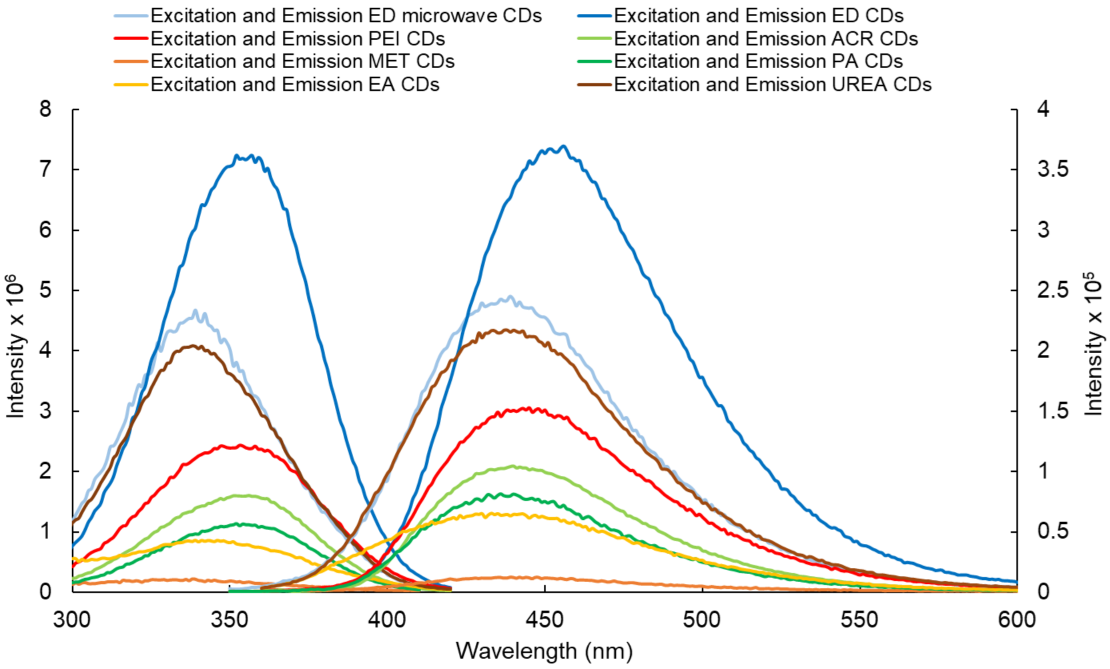

Figure 4.2: Excitation and emission spectra of the CDs synthesized in batch

Table 4.2: Maximum emission and excitation wavelengths and Stokes shifts of the CDs synthesized in batch

| Type of CDs | Maximum emission wavelength (nm) | Maximum excitation wavelength (nm) | Stokes shift (nm) |
|---|---|---|---|
| ED microwave CDs | 439 | 339 | 100 |
| ED CDs | 456 | 357 | 99 |
| PEI CDs | 445 | 353 | 92 |
| ACR CDs | 440 | 352 | 88 |
| MET CDs | 434 | 338 | 96 |
| PA CDs | 436 | 352 | 84 |
| EA CDs | 443 | 343 | 100 |
| UREA CDs | 443 | 342 | 101 |

Another important aspect regarding PL is the QY, which was calculated with the optically dilute measurement method [338], in which the experimental is done using quinine sulfate in 0.1 M sulfuric acid as a reference. The results obtained for the CDs synthesized in batch are presented in Table 4.3.

Table 4.3: QY values of the CDs synthesized in batch

| Type of CDs | QY (%) | Type of CDs | QY (%) |
|---|---|---|---|
| ED microwave CDs | 46 | MET CDs | 7 |
| ED CDs | 78 | PA CDs | 22 |
| PEI CDs | 32 | EA CDs | 16 |
| ACR CDs | 25 | UREA CDs | 44 |

The QY values are comparable with those obtained from literature. However, the composition of the final product and the QYs depend on several experimental parameters like the concentration of the precursors, the reaction time, the temperature, and the pressure, for instance.

The size distribution of the CDs was studied through DLS measurements. Results showed that CDs have average sizes between 2 and 5 nm. Only six measurements were registered because the amount of MET CDs and PA CDs obtained were not enough to perform the measurement. In Figure 4.3, the size distribution of the measured CDs synthesized in batch can be seen, and in Table 4.4, the particle size of the CDs is shown.

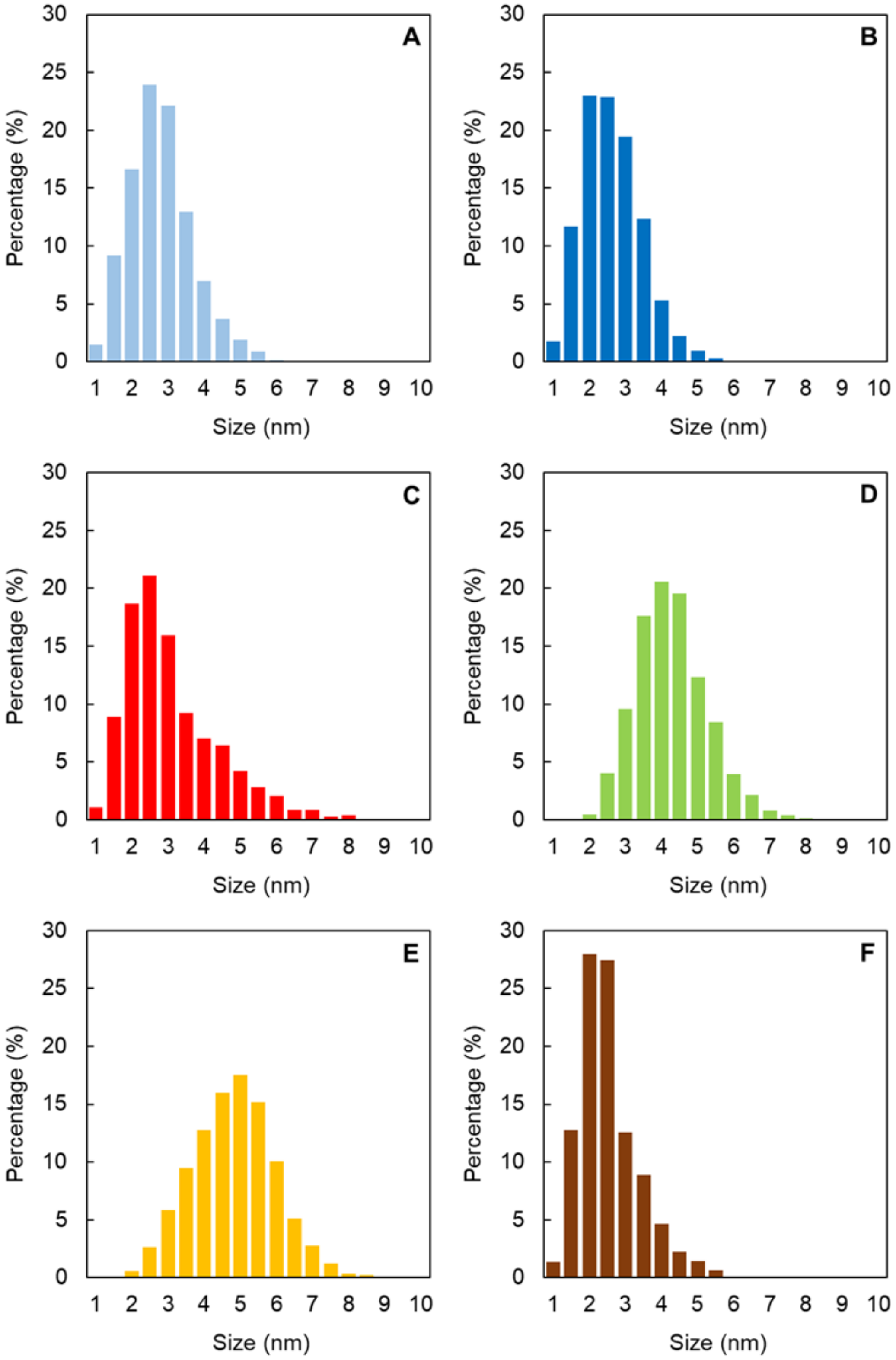

Figure 4.3: Size distribution of the CDs synthesized in batch: ED microwave CDs (A), ED CDs (B), PEI CDs (C), ACR CDs (D), EA CDs (E), and UREA CDs (F)

Table 4.4: Particle size of the CDs synthesized in batch

| Type of CDs | Particle size (nm) | Type of CDs | Particle size (nm) |
|---|---|---|---|
| ED microwave CDs | 2.8 ± 1.1 | ACR CDs | 4.3 ± 1.7 |
| ED CDs | 2.6 ± 1.4 | EA CDs | 4.8 ± 2.5 |
| PEI CDs | 3.1 ± 2.0 | UREA CDs | 2.5 ± 1.0 |

The morphology and size distribution of the CDs was also studied through HRTEM images. However, it was very difficult to obtain high-quality images, due to multiple factors. The first one was the low contrast between the CDs and the carbon-coated copper grids, the second one was the reduced dimensions of the CDs (less than 10 nm), and finally the formation of two fractions of CDs, one with a crystalline structure (carbon core particles), that can be identified thanks to the observation of the diffraction planes, and another one that is amorphous and suggests the formation of polymer dots. These polymer dots have molecular fluorophore moieties embedded, causing the enhancement of the QY but making it more difficult to obtain TEM images [340].

In Figure 4.4, an HRTEM image of the ED CDs can be observed. The different CDs, highlighted in yellow, could be distinguished thanks to the diffraction planes after the treatment with the dedicated ImageJ 1.51n software. The ED CDs had a quasi-spherical shape and an approximate size of 2-4 nm (like the one obtained with the DLS measurement), although the population was not big enough to extract a representative value of this parameter with the images.

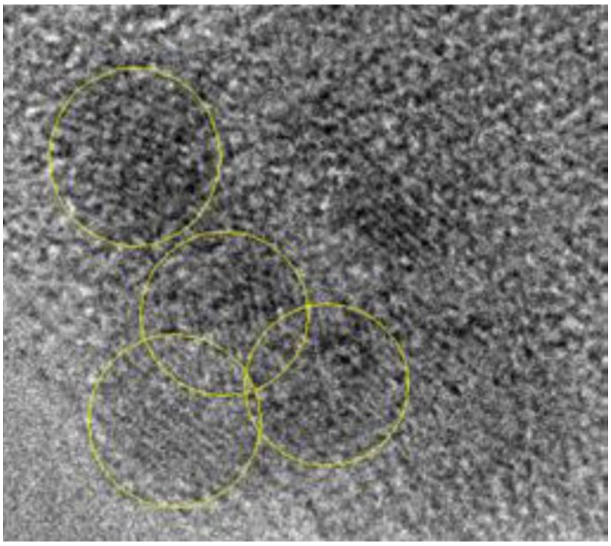

Figure 4.4: HRTEM image of the ED CDs synthesized in batch

Due to the difficulty observing the CDs, a different sample treatment was studied. This process is based on the negative staining of the CDs using uranyl acetate. For the preparation of the sample, a drop of the ED CDs was placed in the carbon-coated copper grids, drying the excess with a filter paper after some minutes. After that, the procedure was repeated with a drop of uranyl acetate. With this technique everything around the nanoparticles was dyed. Therefore, when observing the samples with the TEM, the imprint left by the CDs in a white color over a dark background [341-343] should be observed. An image obtained with the HRTEM using this sample treatment can be observed in Figure 4.5.

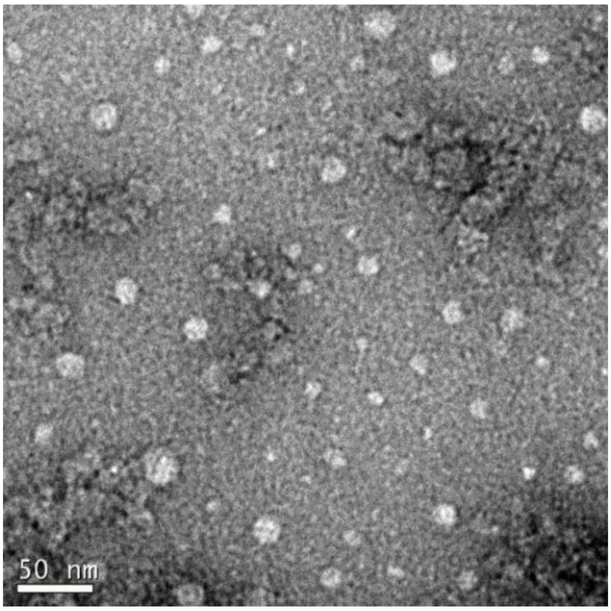

Figure 4.5: HRTEM image of the ED CDs synthesized in batch prepared with a negative staining process

As can be seen, clearer areas appeared that could correspond to ED CDs. However, since the sizes obtained differ greatly from those obtained by DLS, it was suspected that they correspond to the presence of crystals of the staining substance itself.

#### 4.1.1.2 Selectivity tests

Once characterized, another key issue to assess the application of the synthesized CDs as fluorescent probes was their selectivity. The interaction between the CDs and the heavy metal ions could be explained by the chelating effects of the groups present in the surface of the CDs towards the heavy metal ions.

As explained in Section 3.1.7.1, to evaluate selectivity, emission spectra of the CDs in the presence of different heavy metal ion solutions ($Cd^{2+}$, $Co^{2+}$, $Cu^{2+}$, $Cr^{3+}$, $Fe^{3+}$, $Hg^{2+}$, $Ni^{2+}$, $Pb^{2+}$, $Zn^{2+}$) at a concentration of 10 ppm, and other potentially interfering ions present in water ($Na^{+}$, $Mg^{2+}$, $Ca^{2+}$, $Cl^{-}$, $CO_3^{2-}$) at a concentration of 1000 ppm, were registered in the spectrofluorometer. Their quenching effect on the fluorescence of the different CDs was determined by representing the ratio between the fluorescence after the addition of the studied ions to the CDs dispersion and the fluorescence of the CDs dispersion itself ($F/F_0$) as can be seen in the next figures.

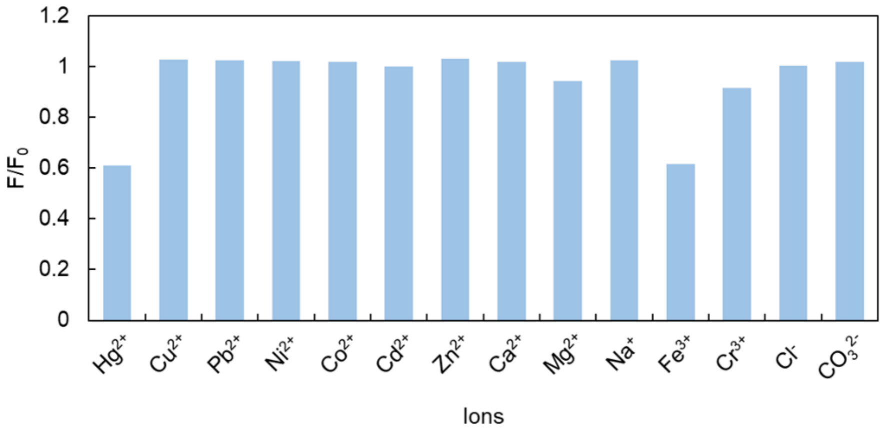

Figure 4.6: Ratio between the fluorescence after the addition of different ions to the ED microwave CDs and the fluorescence of the ED microwave CDs

As can be seen in Figure 4.6, the fluorescence of the ED microwave CDs was quenched by $Hg^{2+}$, as expected from the literature [332], but it was also quenched in the presence of $Fe^{3+}$. For the other ions studied the quenching effect was not significant.

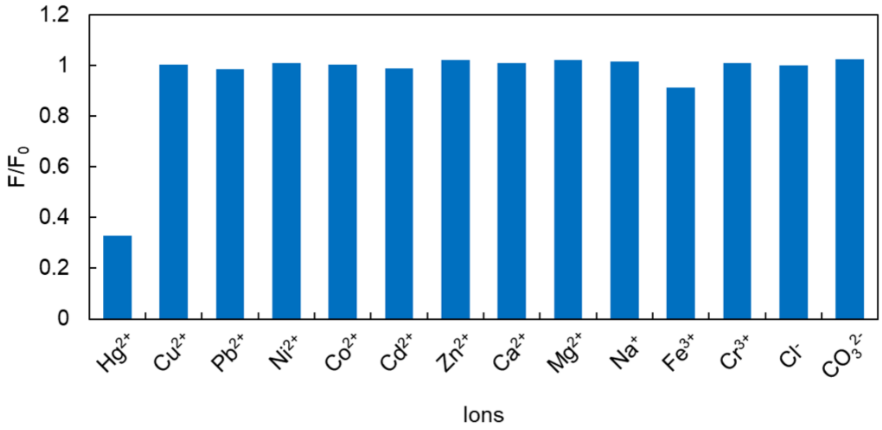

Figure 4.7: Ratio between the fluorescence after the addition of different ions to the ED CDs and the fluorescence of the ED CDs

In Figure 4.7, it can be clearly seen that the fluorescence of the ED CDs was quenched by $Hg^{2+}$, as expected [333], and was slightly quenched by $Fe^{3+}$. The other ions studied did not present quenching effects on the fluorescence of ED CDs. Taking these results into account and also considering the higher QY of the ED CDs, these were used to determine $Hg^{2+}$ in subsequent experiments.

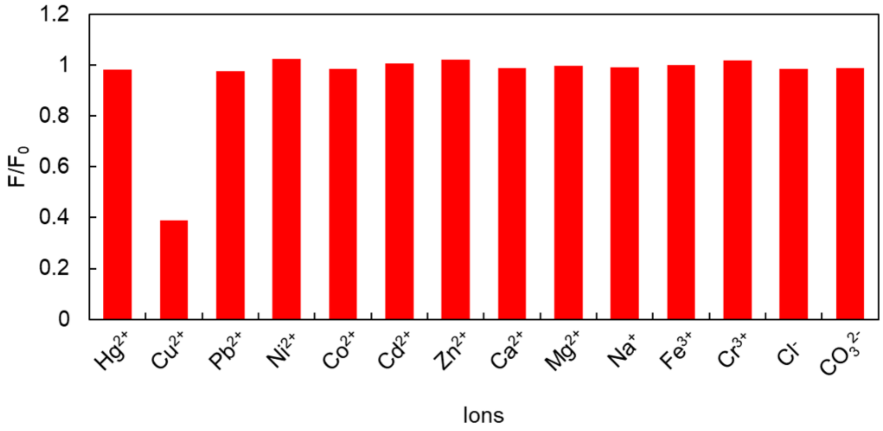

Figure 4.8: Ratio between the fluorescence after the addition of different ions to the PEI CDs and the fluorescence of the PEI CDs

As can be seen in Figure 4.8, the fluorescence of the PEI CDs was only quenched by $Cu^{2+}$, as expected from the literature [257], so the PEI CDs can be used to selectively detect $Cu^{2+}$ among the other ions studied.

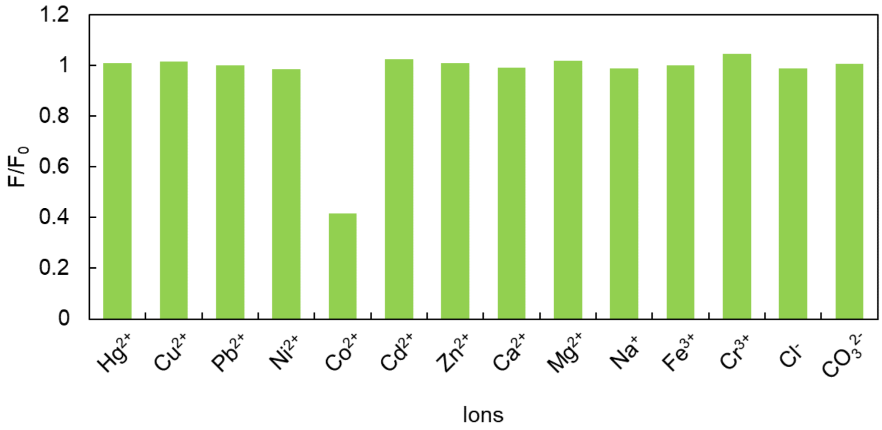

Figure 4.9: Ratio between the fluorescence after the addition of different ions to the ACR CDs and the fluorescence of the ACR CDs

In Figure 4.9, it can be observed that the fluorescence of the ACR CDs was only quenched by $Co^{2+}$, as expected from the literature [334], so it can be concluded that the ACR CDs can be used to selectively detect this heavy metal ion among the other ions studied.

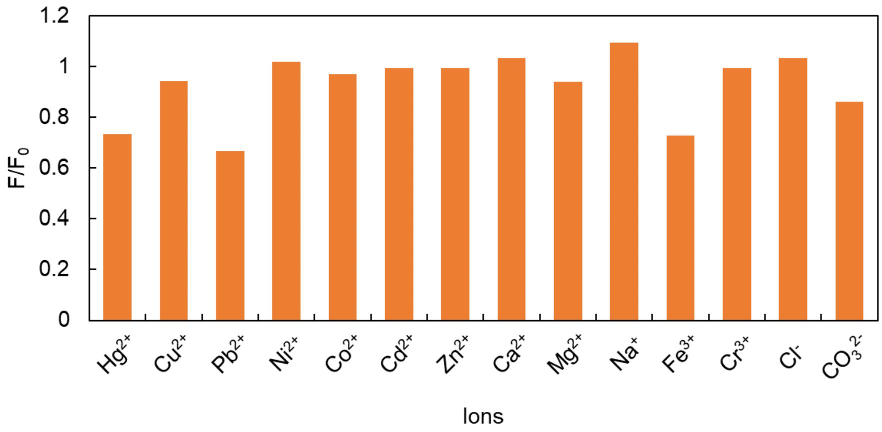

Figure 4.10: Ratio between the fluorescence after the addition of different ions to the MET CDs and the fluorescence of the MET CDs

In this case, as can be seen in Figure 4.10, the fluorescence of the MET CDs was quenched by $Fe^{3+}$, as expected from the literature [335], but the quenching effect was weak. Moreover, other ions like $Hg^{2+}$ or $Pb^{2+}$ produce quenching of fluorescence, making the CDs not suitable for selective determination $Fe^{3+}$ ions. In addition to that, these CDs present a very low QY. Thus, they were discarded for subsequent experiments.

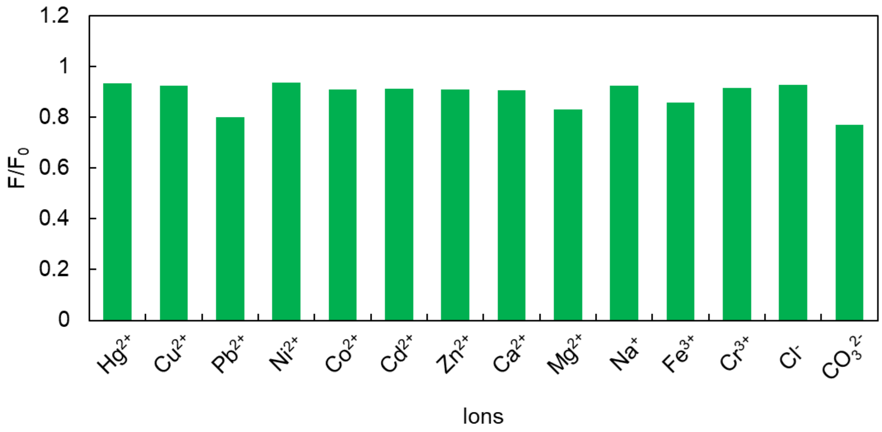

Figure 4.11: Ratio between the fluorescence after the addition of different ions to the PA CDs and the fluorescence of the PA CDs

As can be seen in Figure 4.11, the fluorescence of the PA CDs was not significantly quenched by any of the studied ions. A slight decrease in the fluorescence was observed in the presence of $Pb^{2+}$, as expected from the literature [264], but it was also observed in the presence of other ions. So, these CDs were not suitable for selectively detecting $Pb^{2+}$ ions.

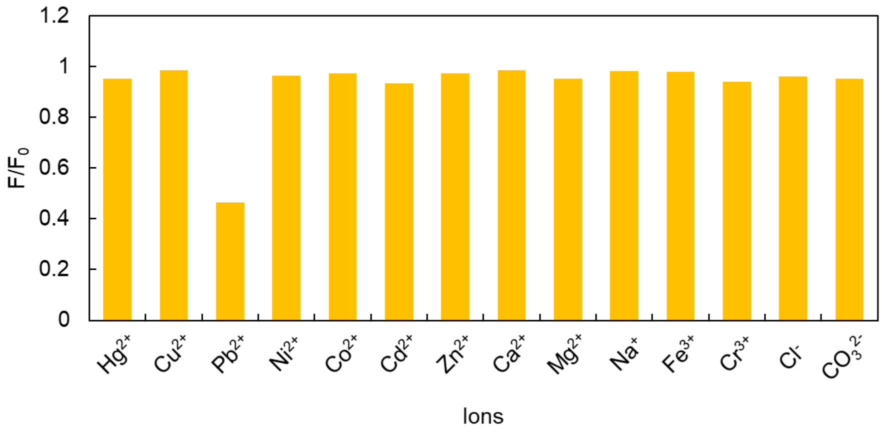

Figure 4.12: Ratio between the fluorescence after the addition of different ions to the EA CDs and the fluorescence of the EA CDs

In Figure 4.12, it can be clearly seen that the fluorescence of the EA CDs was only quenched in the presence of $Pb^{2+}$, as expected from the literature [336], therefore, these CDs were used for the selective determination of $Pb^{2+}$ in subsequent experiments.

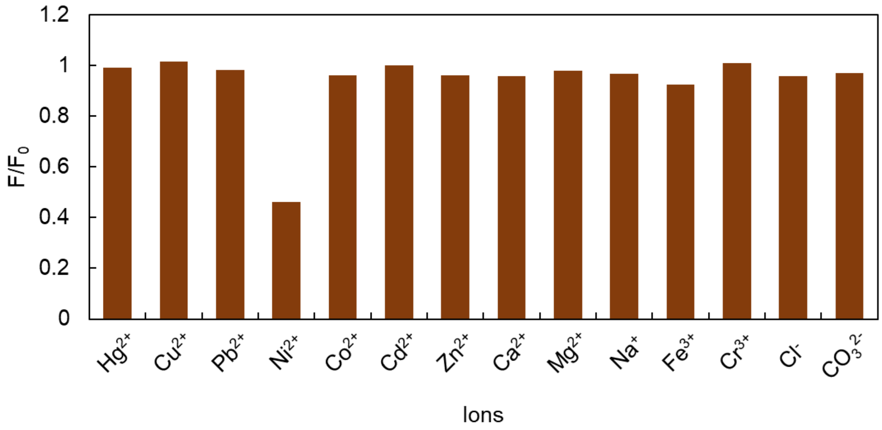

Figure 4.13: Ratio between the fluorescence after the addition of different ions to the UREA CDs and the fluorescence of the UREA CDs

As can be seen in Figure 4.13, the fluorescence of the UREA CDs was only quenched by $Ni^{2+}$, as expected from the literature [337] so the UREA CDs can be used to selectively detect $Ni^{2+}$ among the other ions studied.

So, to conclude this section, taking into consideration the selectivity towards the different heavy metal ions and also the QY, the CDs selected for the development of the miniaturized heavy metal analyzer were ED CDs (selective to $Hg^{2+}$), PEI CDs (selective to $Cu^{2+}$), ACR CDs (selective to $Co^{2+}$), EA CDs (selective to $Pb^{2+}$), and UREA CDs (selective to $Ni^{2+}$).

### 4.1.1.3 Optimization of the analytical system

Once the CDs were completely characterized and their selectivity was assessed, they were tested as fluorescence probes in the miniaturized analyzer based on a rFIA protocol.

First of all, different chemical and hydrodynamic parameters of the FIA system affecting the analytical quality parameters of the analyzer for the determination of heavy metal ions were optimized using a univariate optimization procedure and taking as compromise the fluorescence emission intensity, the signal-to-noise ratio, the sensitivity, response time and reagents saving.

The first variable optimized was the buffer pH and concentration. As mentioned, a citric/citrate buffer was used with an approximate buffer capacity from 3-6. The three different concentrations tested were 0.01, 0.1 and 1 M, being 0.1 M enough to buffer the CDs dispersion as well as very low pH samples as those from acidic extracts, which were intended to be analyzed in further experiments. Moreover, four different pH values (3, 4, 5, 6) were tested to obtain the maximum fluorescence signal and ensure that the heavy metal species are free in solution.

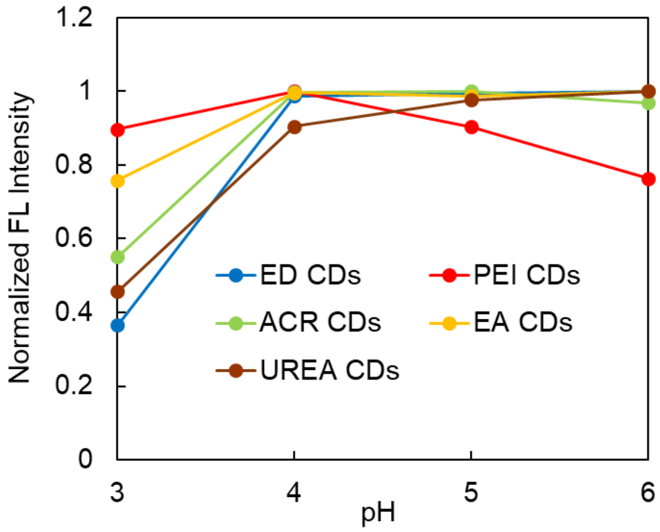

Figure 4.14: Normalized fluorescence intensity obtained by injecting the five CDs into 0.1 M citric/citrate buffer solutions of different pH values

Figure 4.14 shows the normalized fluorescence intensity of the CDs in buffer solutions of different pH values. This parameter is crucial to control the optical properties of CDs since they present ionizable functional groups on their surface, which are responsible for their selective interaction to the analyte and determine the fluorescence efficiency that depends on the surface quantum effects. Moreover, fluorescence of CDs is reduced at extreme pH values, acidic or alkaline [344,345]. Taking all these aspects into account, pH 4 was chosen as the optimal one since all the CDs had almost maximum fluorescence emission at this pH value.

Once the pH and the concentration of the buffer were optimized, some hydrodynamic parameters affecting the FIA measurements were also optimized, starting with the flow rate. Four different flow rates were tested, and the effect on the signal can be observed when a volume of 0.5 mL of the dispersion of the 100-times diluted ED CDs was injected into a 0.1 M citric/citrate buffer at pH 4 in Figure 4.15.

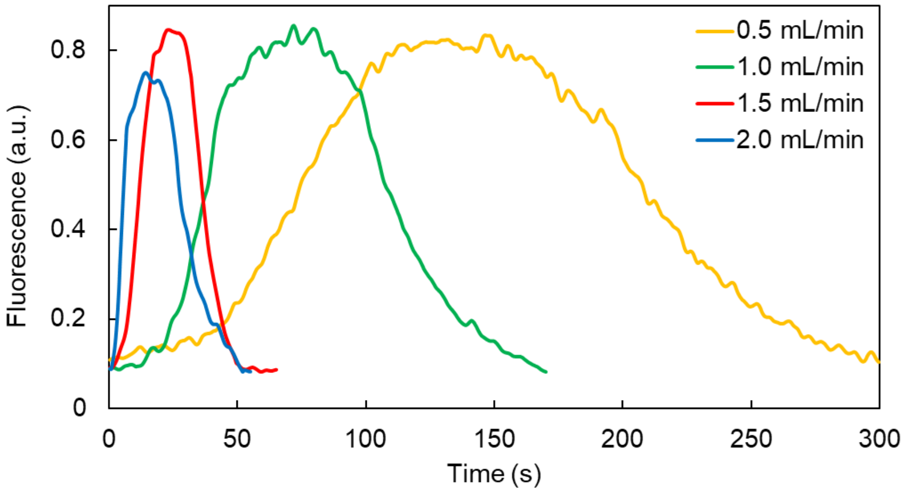

Figure 4.15: Effect of flow rate into the obtained signal for an injection of 0.5 mL of 100-times diluted ED CDs into the 0.1 M citric/citrate buffer solution at pH 4

As can be seen, faster flow rates implied more rapid analysis and therefore, higher sample throughput, which is desirable. However, slightly less intense peaks were obtained in the case of the highest flow rate tested (2 mL/min) because the carrier solution (samples or standard solutions) is less time in contact with the injected volume of CDs. As expected, the slower the flow rate is, the wider are the obtained peaks. As for the 0.5, 1.0, and 1.5 mL/min the peak height almost did not change, a 1.5 mL/min flow rate was chosen as the optimal one for subsequent experiments achieving a response time of approximately 50 s.

Injection volume also impacts the signal. Four different injection volumes were tested by injecting 100-times diluted ED CDs at a flow rate of 1.5 mL/min. Results can be observed in Figure 4.16.

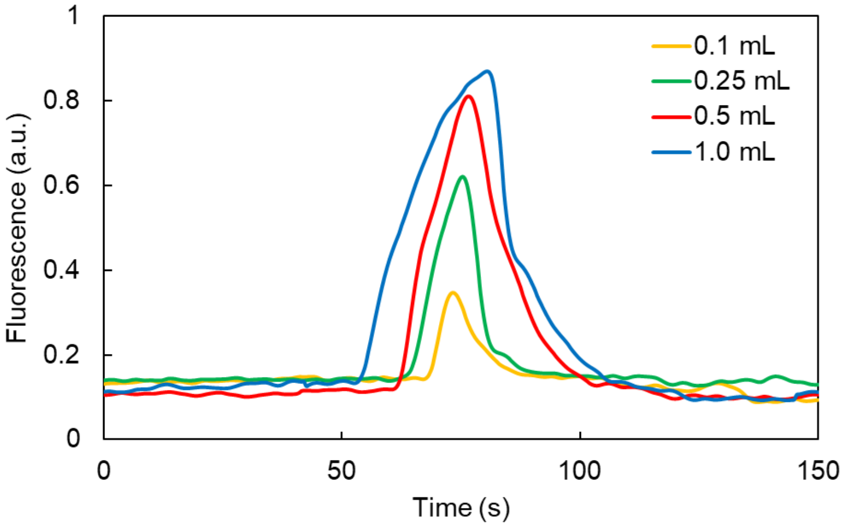

Figure 4.16: Transitory signal obtained for different injection volumes of 100-times diluted ED CDs into the 0.1 M citric/citrate buffer at pH 4

As can be seen, as a general tendency, the higher injection volume, the higher intensity signal. However, the analysis time slightly increased. The intensity signal difference between a 0.5 mL and a 1.0 mL injection volume was not significant, so it was decided to take 0.5 mL as the optimal injection volume with enough signal and a smaller number of CDs as the optical probe.

Finally, the CDs dilution factor was optimized. As mentioned in Section 3.1.6, 10, 50, 100, 500, and 1000 dilution factors were tested for the five CDs used for the heavy metals' determination. For this optimization, dispersions of CDs were injected into citric/citrate buffer, 0.1, 0.5 and 1 ppm solutions of the heavy metal ion for which each type of CD was selective to, and then the fluorescence quenching was related to the concentration of the heavy metal by means of the Stern-Volmer equation explained in Section 1.5.3.2 and the sensitivities were compared. The transient response of the microsystem by injecting the ED CDs into the mentioned solutions (Figure 4.17A) and the Stern-Volmer representation of quenching effect of ED CDs with the different dilution factors (Figure 4.17B) are shown below as an example.

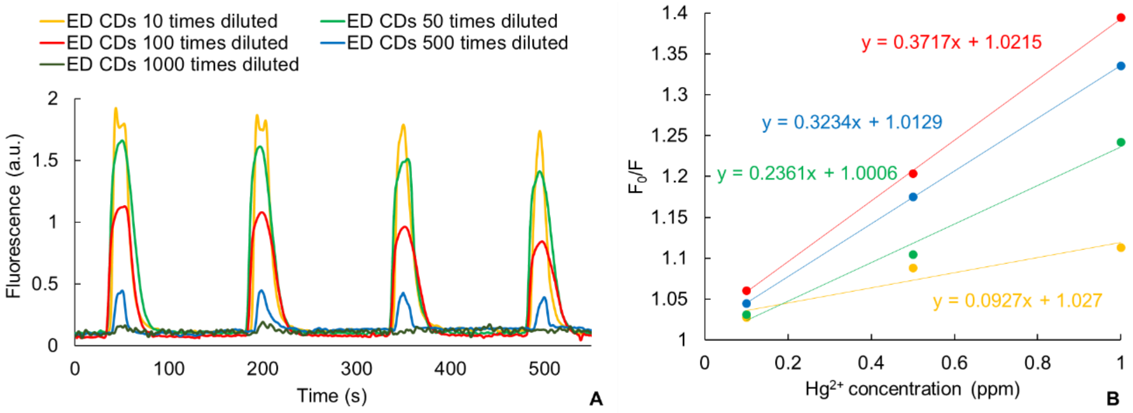

Figure 4.17: A) Transient response of the microsystem by injecting ED CDs of different dilution factors into the buffer and into 0.1, 0.5, and 1 ppm $Hg^{2+}$ solutions and B) Stern-Volmer representation of quenching effect of ED CDs with different dilution factors

As it can be seen in Figure 4.17A, with the 1000-times diluted ED CDs the signal was almost indistinguishable from the background noise and the Stern-Volmer representation could not be made. As can be seen in Figure 4.17B the higher sensitivity was obtained with the 100-times diluted ED CDs. Moreover, at lower dilution factors (higher concentrations of CDs), it was observed the appearance of double peaks due to improper mixing of the CDs and the carrier that caused repeatability issues. The reduction of the sensitivity in this case could also be caused by the saturation of the detector. In the case of the 500 times dilution factor the sensitivity was also high but the signal-to-noise ratio was much better for the 100-times diluted ED CDs. Another aspect to consider was that the limiting reagent in this analysis was the CDs probe, so less quantity of them was preferred. In the case of the other four CDs the procedure followed to optimize the dilution factor was the same. The optimal dilution factors for the other four CDs can be seen in Table 4.6.

After the hydrodynamic parameters were optimized, other operational variables determining the optical signal obtained with the customized optical detection system were evaluated. These were the signal amplification modulated by the electronic circuitry and the integration time (the parameter input that tells the detector how long to collect data before giving the signal).

As explained in Section 3.1.6, ED CDs were injected per triplicate into the 0.1 M buffer solution at pH 4 and into 0.01 ppm $Hg^{2+}$ standard solution to evaluate the signal-to-noise ratio. Three different signal amplification factors (1, 10, and 100) and three different integration times (0.1, 0.5 and 1.0 s) were tested. 100-times diluted ED CDs were used for these experiments. To establish the optimal conditions, the difference between the mean of the peak height of the three injections made into the buffer and the mean of the peak height of the three injections made into the 0.01 ppm $Hg^{2+}$ solution was divided by the noise of the measurement. Figure 4.18A, B, and C show the transient signals of the system to the injection of ED CDs into the mentioned solutions with the three integration times and signal amplifications of 1, 10, and 100, respectively. Results obtained are summarized in Table 4.5.

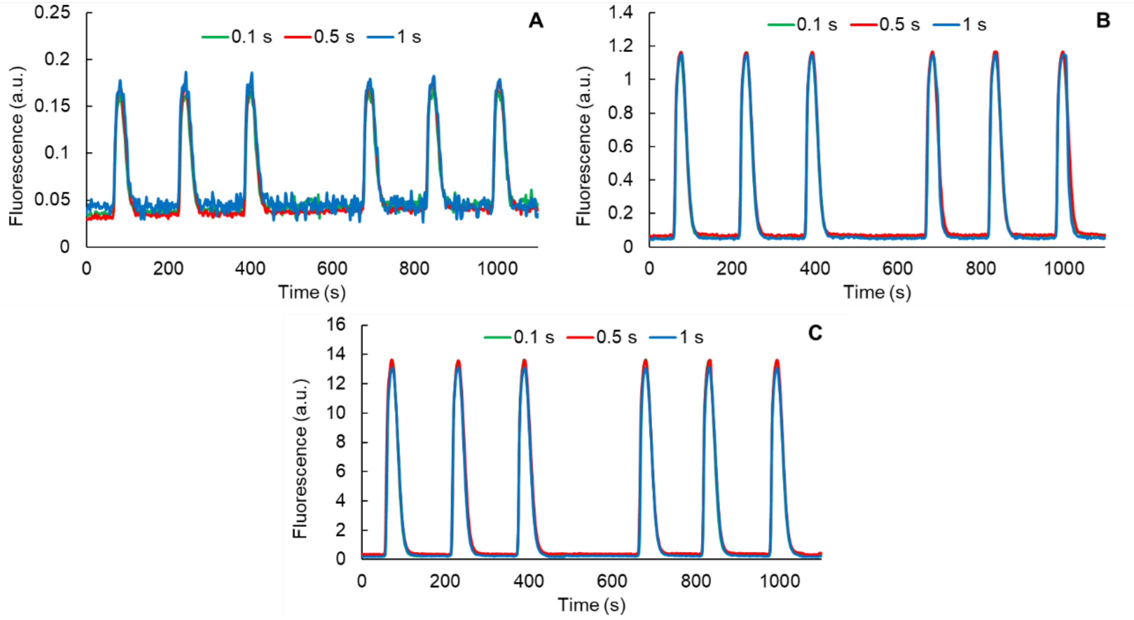

Figure 4.18: Transient signals of the miniaturized optical system to the injection of ED CDs into citric/citrate buffer and into the 0.01 ppm $Hg^{2+}$ solution with the three integration times and signal amplifications of: A) 1, B) 10, and C) 100

Table 4.5: Table with the different signal-to-noise ratio values obtained

| **Signal amplification factor** | **Integration time (s)** | **Difference between the means of the peak heights** | **Noise of the measurement** | **Signal-to-noise ratio** |
|---|---|---|---|---|
| 1 | 0.1 | $4.22 \times 10^{-4}$ | $1.21 \times 10^{-2}$ | **$3.49 \times 10^{-2}$** |
|  | 0.5 | $2.67 \times 10^{-4}$ | $5.50 \times 10^{-3}$ | **$4.85 \times 10^{-2}$** |
|  | 1.0 | $2.60 \times 10^{-3}$ | $1.03 \times 10^{-2}$ | **$2.52 \times 10^{-1}$** |
| 10 | 0.1 | $4.43 \times 10^{-3}$ | $8.10 \times 10^{-3}$ | **$5.47 \times 10^{-1}$** |
|  | 0.5 | $1.20 \times 10^{-3}$ | $9.40 \times 10^{-3}$ | **$1.28 \times 10^{-1}$** |
|  | 1.0 | $2.87 \times 10^{-3}$ | $7.00 \times 10^{-3}$ | **$4.09 \times 10^{-1}$** |
| 100 | 0.1 | $2.99 \times 10^{-2}$ | $8.12 \times 10^{-2}$ | **$3.68 \times 10^{-1}$** |
|  | 0.5 | $2.92 \times 10^{-2}$ | $8.88 \times 10^{-2}$ | **$3.29 \times 10^{-1}$** |
|  | 1.0 | $1.79 \times 10^{-2}$ | $7.50 \times 10^{-2}$ | **$2.39 \times 10^{-1}$** |

From the data obtained, it seemed that the different integration times had a random effect on the signal-to-noise ratio and did not follow any clear trend. Regarding the signal amplification factor, an amplification factor of 1, showed a smaller difference between the mean of the peak height than the other signal amplification factors, thus giving a worse signal-to-noise ratio. For a signal amplification factor of 10, the difference between the mean of the peak height was higher than for the signal amplification factor of 1 and the noise of the measurement was similar, thus the signal-to-noise ratio was higher. For the signal amplification factor of 100, the difference between the means of the peak heights increased compared to the other two signal amplification factors, but the variability of the baseline leaded to a noise increase, thus causing that the signal-to-noise ratio values were lower. Taking all these factors into account and considering the results of Table 4.5, it could be concluded that the best conditions were a signal amplification factor of 10 and an integration time of 0.1 s.

To summarize, in this section, different parameters affecting the fluorescent signal in the customized miniaturized optical detection system were optimized. These optimal values, that were used for all the subsequent experiments, can be seen in Table 4.6.

Table 4.6: Summary of the optimization of chemical, operational and hydrodynamic parameters

| Parameter | Tested interval | Optimal value |
|---|---|---|
| Buffer concentration (M) | 0.01 – 1.00 | 0.10 |
| Buffer pH | 3 – 6 | 4 |
| Carrier flow rate (mL/min) | 0.5 – 2.0 | 1.5 |
| Injection volume (mL) | 0.1 – 1.0 | 0.5 |
| Signal amplification | 1 – 100 | 10 |
| Integration time (s) | 0.1 – 1.0 | 0.1 |
| ED CDs dilution factor | 10 – 1000 | 100 |
| PEI CDs dilution factor | 10 – 1000 | 50 |
| ACR CDs dilution factor | 10 – 1000 | 100 |
| EA CDs dilution factor | 10 – 1000 | 10 |
| UREA CDs dilution factor | 10 – 1000 | 50 |

#### 4.1.1.4 Analytical quality parameters

Once the different parameters affecting the determination of heavy metal ions were optimized, the different analytical quality parameters were calculated from calibration plots obtained performing the separate analysis of each heavy metal. As explained in Section 3.1.7.2, calibration plots were obtained by injecting per triplicate each type of CDs synthesized in batch into the 0.1 M citric/citrate buffer at pH 4 (from which a maximum signal should be obtained ($F_0$)), and into standard solutions containing increasing concentrations of the heavy metal studied in each case (from which quenched signals should be obtained (F)). The transient signals of the five measurements performed can be seen in Figure 4.19 to Figure 4.23, and the Stern-Volmer representation of the data is shown in Figure 4.24. Some analytical quality parameters like sensitivity ($K_{SV}$), LOD, and repeatability are also summarized in Table 4.7.

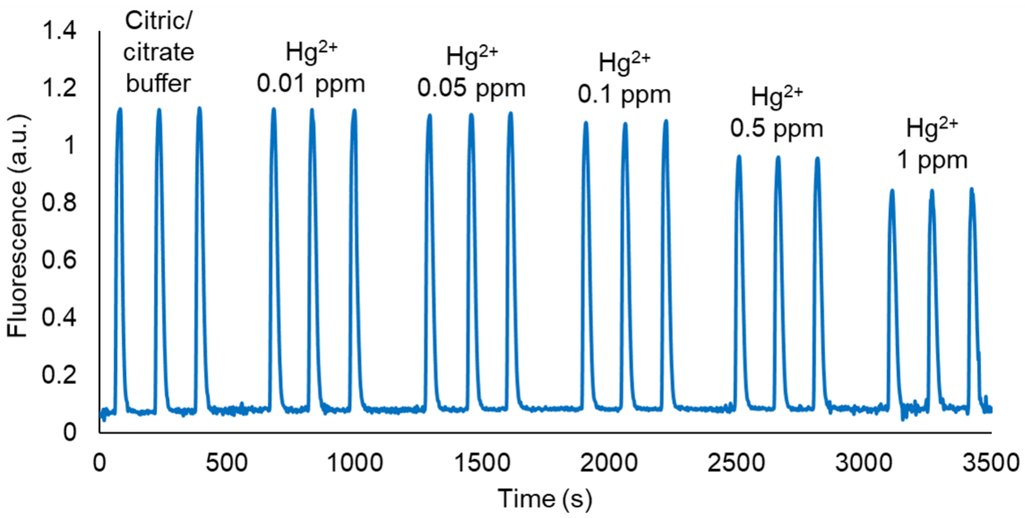

Figure 4.19: Transient fluorescence intensity signal of the microsystem by injecting the 100-times diluted ED CDs into 0.1 M citric/citrate buffer solution pH 4 and solutions of different concentrations of $Hg^{2+}$

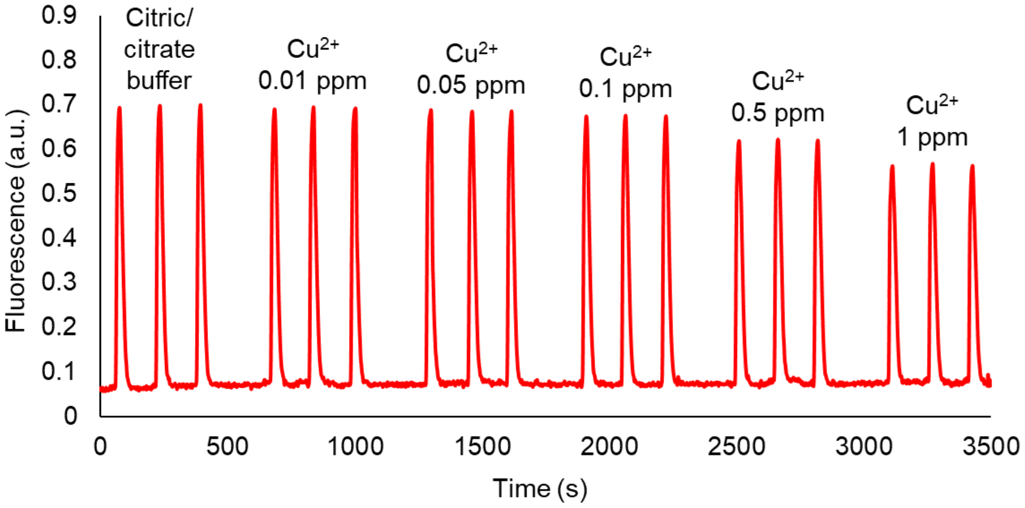

Figure 4.20: Transient fluorescence intensity signal of the microsystem by injecting the 50-times diluted PEI CDs into 0.1 M citric/citrate buffer solution pH 4 and solutions of different concentrations of $Cu^{2+}$

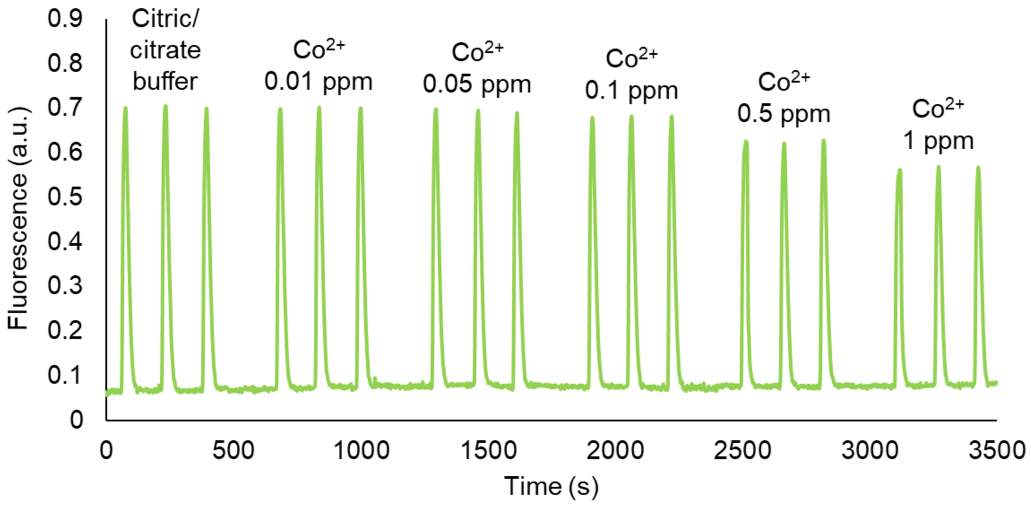

Figure 4.21: Transient fluorescence intensity signal of the microsystem by injecting the 100-times diluted ACR CDs into 0.1 M citric/citrate buffer solution pH 4 and solutions of different concentrations of $Co^{2+}$

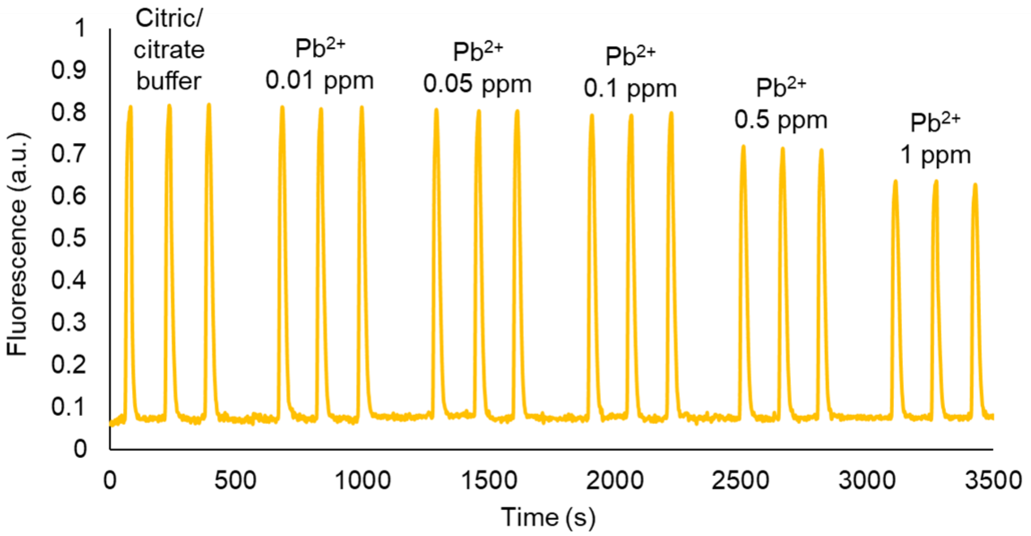

Figure 4.22: Transient fluorescence intensity signal of the microsystem by injecting the 10-times diluted EA CDs into 0.1 M citric/citrate buffer solution pH 4 and solutions of different concentrations of $Pb^{2+}$

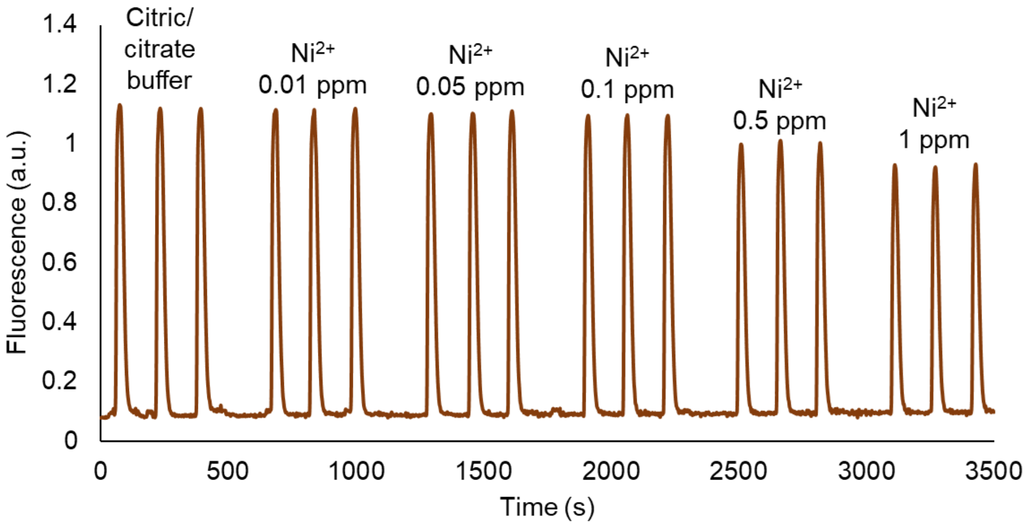

Figure 4.23: Transient fluorescence intensity signal of the microsystem by injecting the 50-times diluted UREA CDs into 0.1 M citric/citrate buffer solution pH 4 and solutions of different concentrations of $Ni^{2+}$

As can be seen in the different transient measurements, the fluorescence signal quickly returned to the baseline after each signal peak and there was not any significant signal drift of the baseline, demonstrating the robustness of the miniaturized optical system for the determination of heavy metal ions.

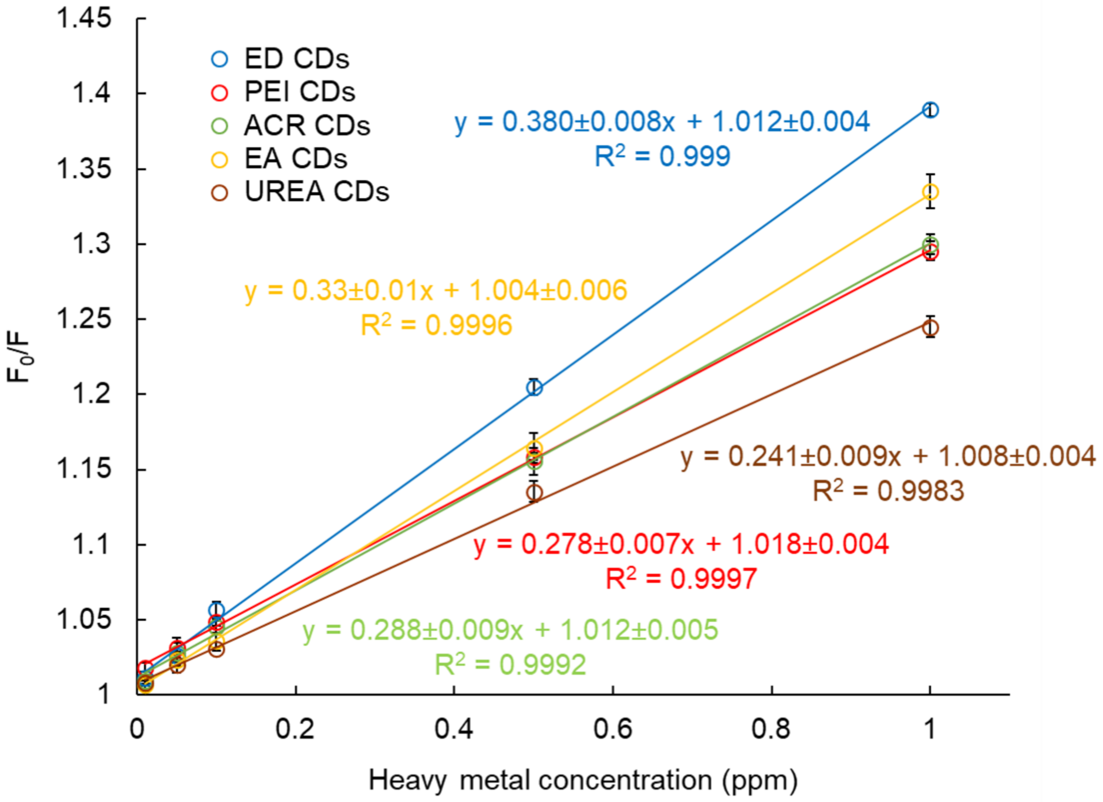

Figure 4.24: Stern-Volmer representation of the quenching effect of the target heavy metals on the fluorescence of the different CDs synthesized in batch

Calibration plots showed a good linear correlation in the studied range ($R^2 > 0.99$), as can be seen in Figure 4.24. Moreover, the values of the intercept were approximately 1 in all cases, indicating that the calibration plots fit the Stern-Volmer equation and that a single quenching mechanism was occurring between the different heavy metal ions and the CDs at the evaluated concentration range.

Table 4.7: Analytical performance of the miniaturized analyzer for the determination of heavy metals with the CDs synthesized in batch

| **Type of CDs** | **$K_{SV}$ (ppm$^{-1}$)** | **LOD (ppb)** | **Repeatability (%RSD)** |
|---|---|---|---|
| ED CDs | 0.380 ± 0.008 | 5.9 ± 0.8 | 0.5 |
| PEI CDs | 0.278 ± 0.007 | 11.7 ± 0.7 | 1.2 |
| ACR CDs | 0.288 ± 0.009 | 3.9 ± 0.5 | 0.9 |
| EA CDs | 0.33 ± 0.01 | 8.8 ± 0.8 | 1.1 |
| UREA CDs | 0.241 ± 0.009 | 2.5 ± 0.3 | 0.4 |

From this data, it could be concluded that all the measurements had good repeatability (below 1.2%), and the LODs obtained for four of the five heavy metals studied were below the limits set by different organizations (EU, US EPA, and WHO), that are listed in Table 1.1 (Section 1.1.1) for drinking water. Only in the case of $Hg^{2+}$, the limits set were below the LOD obtained with the microanalyzer.

#### 4.1.1.5 Analysis of synthetic and real samples

As it is explained in Section 3.1.7.3, to assess the applicability of the miniaturized analyzer for the determination of heavy metal ions, spiked tap water samples and extracts of polluted soil samples were analyzed with the CDs synthesized in batch. For the tap water samples, they were spiked with different concentrations of the heavy metal studied in each case, and the recovery rates were calculated. Results are shown in Table 4.8.

Table 4.8: Recovery rates obtained for the determination of the heavy metals studied in spiked tap water samples

| | | **Analyte recovery rates** | | | | |
|---|---|---|---|---|---|---|
| **Sample** | **Concentration of the analyte in the sample (ppm)** | **$Hg^{2+}$** | **$Cu^{2+}$** | **$Co^{2+}$** | **$Pb^{2+}$** | **$Ni^{2+}$** |
| Spiked tap water | 0.03 | 129% | 131% | 120% | 134% | 123% |
| | 0.06 | 116% | 112% | 111% | 120% | 110% |
| | 0.1 | 105% | 103% | 105% | 105% | 104% |
| | 0.4 | 101% | 100% | 100% | 102% | 100% |
| | 0.8 | 99% | 99% | 98% | 101% | 99% |

From the data obtained, it can be extracted that, in general, an overestimation is noticed for the less concentrated samples, the ones that are near the LODs. However, despite that for some of the heavy metal ions studied the results obtained at their limits set in drinking water are overestimated ($Hg^{2+}$, $Ni^{2+}$, and $Pb^{2+}$), for the other two ($Cu^{2+}$ and $Co^{2+}$), the results of recovery rates obtained at concentrations lower than the limits set for drinking water are around 100%. Therefore, the developed strategy and the automatic miniaturized analyzer has the potential to be employed as a multiparametric warning system for heavy metals pollution in water samples.

In addition to these spiked tap water samples, nitric acid extracts of polluted soil samples containing high concentrations of four of the five heavy metals studied ($Cu^{2+}$, $Co^{2+}$, $Ni^{2+}$, and $Pb^{2+}$), as well as other metallic ions were analyzed. To carry out these measurements, previously, calibration plots were performed with standard solutions at higher concentrations (different concentration ranges depending on the analyte). The Stern-Volmer representations of this calibration plots are shown in Figure 4.25.

Continuous flow techniques (such as FIA) can be adapted easily to the sample by changing or adding different operations. For instance, in the case that the sample was too acid/basic for the buffer capacity, or that the concentration of the sample felt outside the linear range, the sample/buffer ratio could be modified to tune pH or dilution, respectively. Another possibility for future prototypes is to automatically prepare the standard solutions for calibration by dilution of a concentrated stock solution.

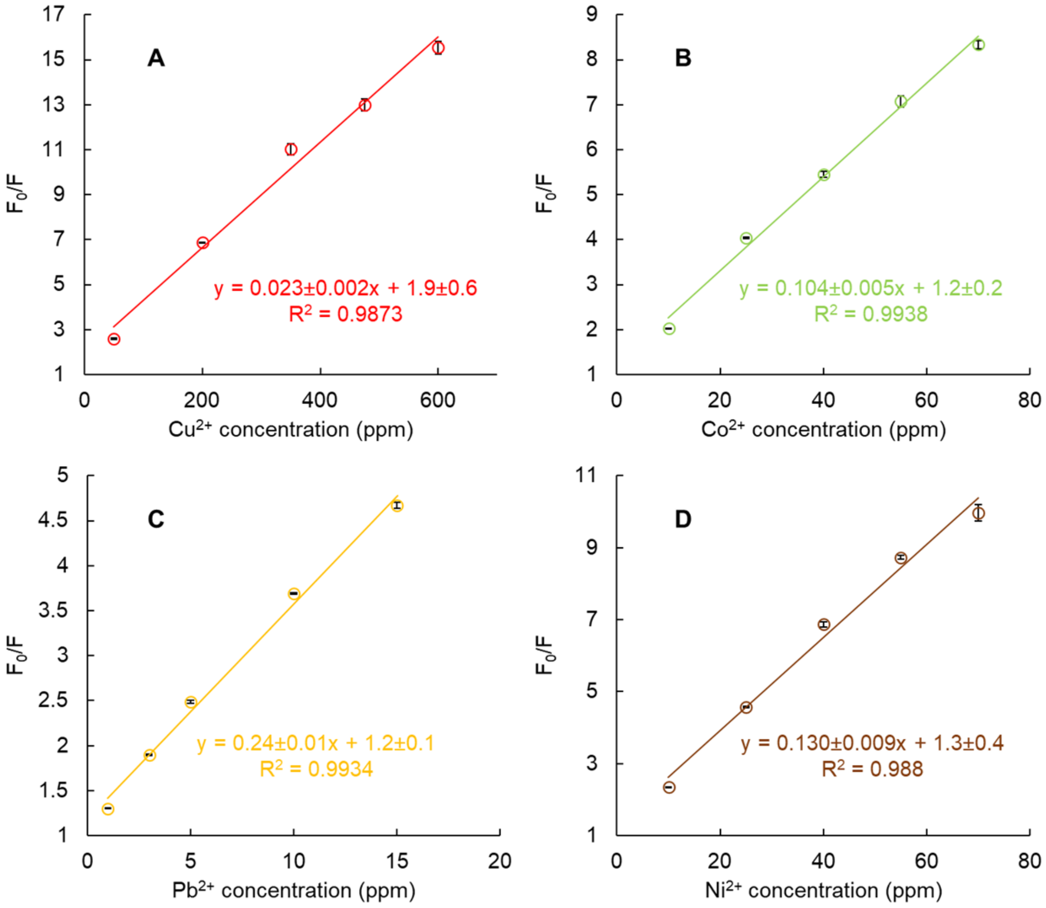

Figure 4.25: Stern-Volmer representation of the quenching effect of the heavy metal ion studied in each case on the fluorescence of A) ED CDs, B) ACR CDs, C) EA CDs, and D) UREA CDs

From these Stern-Volmer representations, it could be noticed that measurements had lower sensitivity at higher concentrations, even though the linear correlation was good. This is because the Stern-Volmer model has some limitations that affect the accuracy, caused by deviations at high concentrations [346].

In Table 4.9, the concentration of the heavy metals studied in 8 polluted soil samples, determined by the reference method (ICP-OES) and with the developed microanalyzer, and accuracies expressed as % error are shown.

Table 4.9: Concentration of the heavy metals studied in polluted soil samples determined by the reference method (ICP-OES) and with the developed microanalyzer, and % error between the two methods

| **Sample number** | **[Cu$^{2+}$] ICP-OES (ppm)** | **[Cu$^{2+}$] developed microanalyzer (ppm)** | **% error** | **[Co$^{2+}$] ICP-OES (ppm)** | **[Co$^{2+}$] developed microanalyzer (ppm)** | **% error** |
|---|---|---|---|---|---|---|
| **1** | 576.2 | 587.0 | 1.9 | 49.4 | 49.1 | 0.5 |
| **2** | 255.7 | 251.1 | 1.8 | 34.2 | 36.0 | 5.1 |
| **3** | 511.7 | 507.3 | 0.9 | 61.3 | 63.9 | 4.3 |
| **4** | 119.7 | 116.2 | 2.9 | 24.8 | 26.0 | 4.8 |
| **5** | 231.9 | 236.5 | 2.0 | 39.1 | 37.9 | 3.1 |
| **6** | 458.3 | 477.9 | 4.3 | 43.3 | 41.4 | 4.4 |
| **7** | 90.5 | 92.2 | 1.9 | 13.6 | 14.3 | 4.5 |
| **8** | 95.7 | 92.4 | 3.4 | 19.9 | 21.0 | 5.7 |

| **Sample number** | **[Pb$^{2+}$] ICP-OES (ppm)** | **[Pb$^{2+}$] developed microanalyzer (ppm)** | **% error** | **[Ni$^{2+}$] ICP-OES (ppm)** | **[Ni$^{2+}$] developed microanalyzer (ppm)** | **% error** |
|---|---|---|---|---|---|---|
| **1** | 11.5 | 12.0 | 4.8 | 42.3 | 42.8 | 1.0 |
| **2** | 4.8 | 4.9 | 2.1 | 31.8 | 31.6 | 0.7 |
| **3** | 5.3 | 5.2 | 1.7 | 61.3 | 61.9 | 1.0 |
| **4** | 3.7 | 3.9 | 7.4 | 35.8 | 35.9 | 0.3 |
| **5** | 4.0 | 4.0 | 1.0 | 57.9 | 58.7 | 1.4 |
| **6** | 7.1 | 7.0 | 1.3 | 33.4 | 32.9 | 1.4 |
| **7** | 0.8 | 0.8 | 4.0 | 25.7 | 26.4 | 3.1 |
| **8** | 2.2 | 2.3 | 7.5 | 33.9 | 35.4 | 4.4 |

As can be appreciated, accuracy depends on the analyte as well as the concentration, the mean of the errors being less than 3%. At low concentrations the error is bigger and four samples from the 32 analyses gave an error over 5%, therefore we can conclude that the system can operate with acidic extracts of polluted soils with different heavy metals and other ions at different concentration levels. Moreover, a comparative study between the results obtained for the four heavy metals determined in the polluted soil samples with the two methods (the reference method (ICP-OES) and the developed miniaturized analyzer) is presented in Figure 4.26.

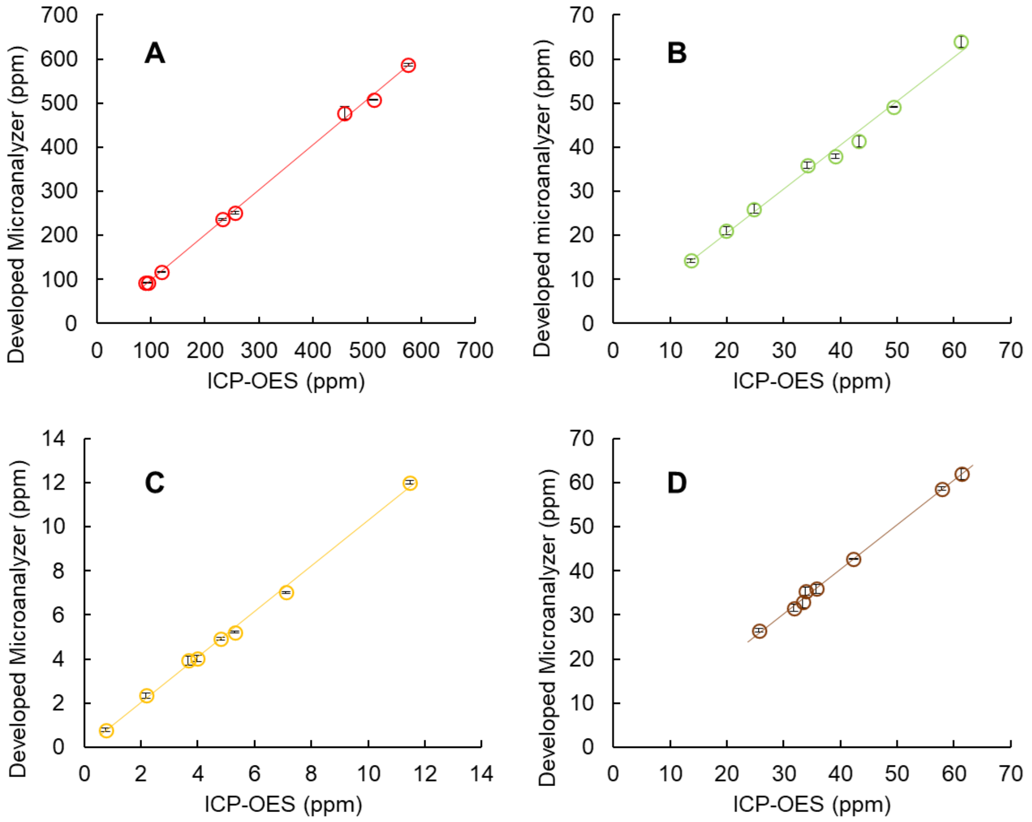

Figure 4.26: Comparative study between results for the analysis of (A) $Cu^{2+}$, (B) $Co^{2+}$, (C) $Pb^{2+}$, and (D) $Ni^{2+}$ in polluted soil samples (n=8)

Regression equations of the comparison tests (intercept, slope, and correlation coefficient) for the four heavy metal ions studied as well as $t_{calc}$ (95% of confidence) values obtained with the paired t-test are shown in Table 4.10.

Table 4.10: Data obtained from the statistical data treatment of the comparative studies

| | **Analyte** | | | |
|---|---|---|---|---|
| | **$Cu^{2+}$** | **$Co^{2+}$** | **$Pb^{2+}$** | **$Ni^{2+}$** |
| Slope (b) | 1.02 ± 0.02 | 1.00 ± 0.04 | 1.03 ± 0.04 | 1.01 ± 0.04 |
| Intercept (a) | -4 ± 4 | 0.5 ± 0.5 | -0.03 ± 0.06 | 0.02 ± 0.08 |
| Correlation coefficient ($R^2$) | 0.9986 | 0.9908 | 0.9971 | 0.9978 |
| $t_{calc}$ | 0.851 | 0.911 | 1.639 | 1.994 |

From the statistical data treatment, it can be concluded that the results obtained with the developed microanalyzer were not significantly different from the ones measured with the reference method (ICP-OES) according to the paired t-test (as $t_{calc} < t_{tab}$) for the four heavy metals analyzed. Taking this into account, it has been demonstrated that the developed microanalyzer can be used for determining different heavy metal ions in different types of samples with good accuracy and precision, proving the reliability of the miniaturized analyzer as a warning system.

### 4.1.2 Optical detection of heavy metal ions with CDs synthesized in LTCC microreactors

#### 4.1.2.1 Synthesis and optimization

Different CDs were synthesized following the methods described in Section 3.1.4.2. The solutions obtained from the synthesis in the LTCC microreactors had different colors and viscosities, very similar to the analogues synthesized in batch. A brief description of the synthesized CDs follows as: ED CDs (dark brown suspension), PEI CDs (light brown suspension), ACR CDs (dark brown suspension), and EA CDs (dark brown suspension). As mentioned in Section 3.1.4.2, for the four syntheses, two fractions were separated, one that was dialyzed (D) and another one that was not dialyzed (ND). Some experiments were performed using both fractions, where they are identified with D or ND, and in some other experiments only the D fraction was used.

As explained in Section 3.1.4.2, two of the synthesis processes were adapted and reproduced to characterize the analytical response of the resulting CDs (ED CDs and PEI CDs). Moreover, two other synthesis processes performed in batch were adapted to be done in the LTCC microreactor (ACR CDs and EA CDs). In this process some parameters affecting the QY of the final product were optimized. On the one hand, the concentration of the nitrogen precursor (ED for the two synthetic processes) and on the other hand, temperature. Pressure was another important parameter affecting the synthesis. It was fixed at 17 bar as for the two previous syntheses. In Figure 4.27A and B a comparison of the QYs obtained by varying the two parameters is shown.

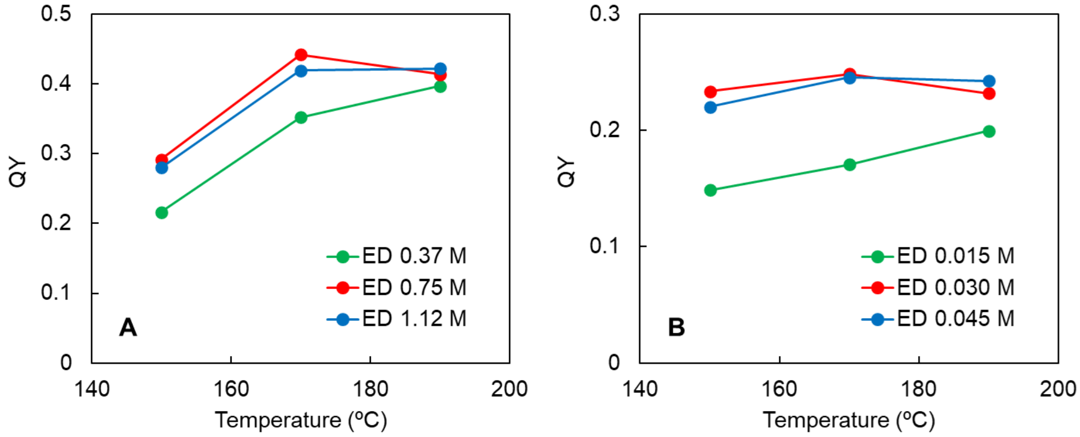

Figure 4.27: Comparison of the QYs of (A) D ACR CDs, and (B) D EA CDs under different temperatures and different amounts of nitrogen precursor

As can be seen in the previous figure, the temperature of the synthesis had an important effect on the QY of the CDs obtained, showing a maximum at 170 °C in both cases. As mentioned in Section 4.1.1.1, performing the synthesis at higher temperatures could increase the carbonization degree, obtaining a carbon core-based product, which is more photostable but has a lower QY [340]. The effect of the concentration of the nitrogen precursor (ED) was also noticeable. With the three concentrations tested in the two cases, the smallest one led to lower QY values due to the incomplete reaction between the two precursors, while when the concentration of the ED solution was the highest tested, the QY was lower than that obtained with the solution of medium concentration, which could mean that an excess of ED in solution was affecting the final CDs QY. Therefore, the optimal synthetic conditions to obtain the highest QY were using a solution containing 0.75 M of ED in the case of the ACR CDs, and a solution containing 0.030 M of ED in the case of the EA CDs and performing the syntheses at 170 ºC.

#### 4.1.2.2 Characterization

As for the CDs synthesized in batch, the four CDs synthesized with the LTCC microreactor showed blue PL upon irradiation with a UV lamp. All of them present similar absorbance spectra, as can be seen in Figure 4.28. As mentioned earlier, the CDs were diluted until an approximate absorption of 0.05 a.u. was reached, to avoid possible self-attenuation effects.

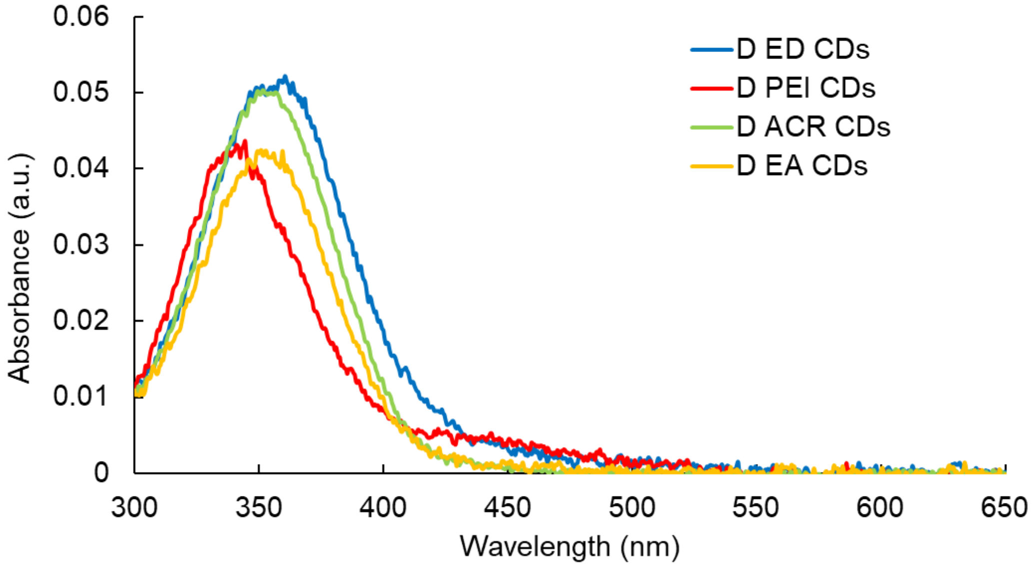

Figure 4.28: UV-Vis spectra of the different D CDs synthesized in the LTCC microreactor

In Table 4.11 the wavelengths at which the maximum absorbance of the different synthesized CDs appears, can be seen.

Table 4.11: Wavelengths for the SPR band of the CDs synthesized in the LTCC microreactor

| **Type of CDs** | **Wavelength of the maximum absorbance (nm)** |
|---|---|
| D ED CDs | 360 |
| D PEI CDs | 345 |
| D ACR CDs | 352 |
| D EA CDs | 353 |

As can be seen in the table, maxima of the absorption bands are located between 345 and 360 nm in all cases, therefore, they are suited to be used with the developed analyzer, which employs a LED emitting at 365 nm as excitation source.

After characterizing the absorbance of the CDs, the PL was also evaluated by registering their emission and excitation spectra, that can be observed in Figure 4.29.

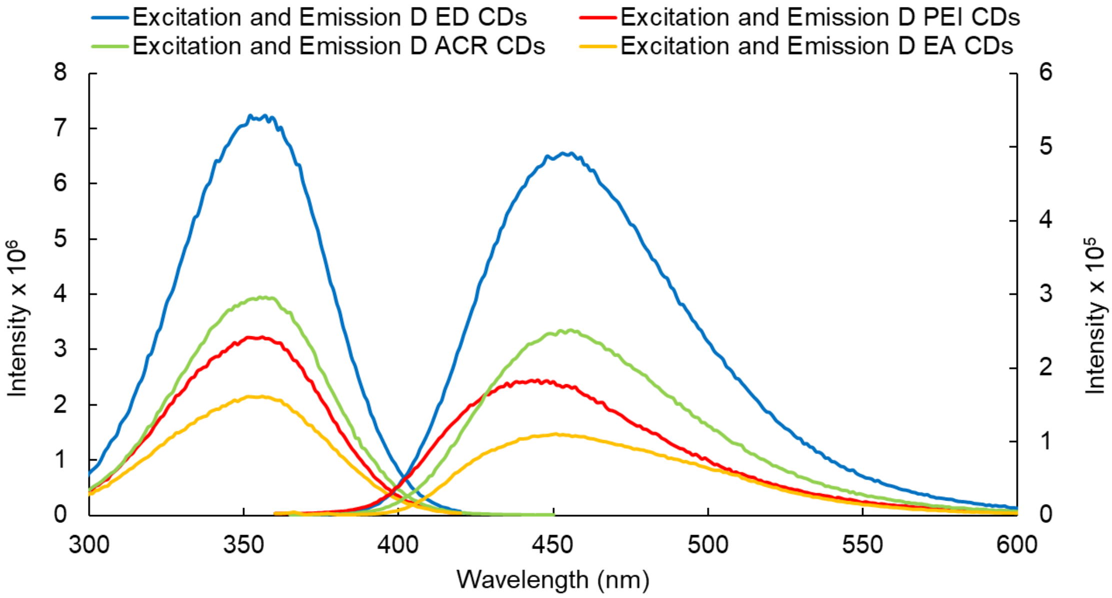

Figure 4.29: Excitation and emission spectra of the CDs synthesized in the LTCC microreactor

The different CDs dispersions show, as well as for the ones previously synthesized in batch, wide excitation bands with maxima around 350 nm and wide emission bands with maxima around 450 nm. The Stokes shifts were also calculated obtaining values around 100 nm in all cases, as it can be seen in Table 4.12.

Table 4.12: Maximum emission and excitation wavelengths and Stokes shifts of the CDs synthesized in the LTCC microreactor

| Type of CDs | Maximum emission wavelength (nm) | Maximum excitation wavelength (nm) | Stokes shift (nm) |
|---|---|---|---|
| D ED CDs | 456 | 352 | 104 |
| D PEI CDs | 443 | 350 | 93 |
| D ACR CDs | 456 | 355 | 101 |
| D EA CDs | 450 | 355 | 95 |

QYs were also calculated with the optically dilute method using quinine sulfate in 0.1 M sulfuric acid as a reference. In this case, for comparison purposes, we calculated QY of both fractions of each type of CD synthesized in the LTCC microreactor. In this way, we would identify if the purification process was essential or not and assess whether CDs could be directly employed after their synthesis. Obtained results are presented in Table 4.13.

Table 4.13: QY values of the CDs synthesized in the LTCC microreactor

| Type of CDs | QY (%) | Type of CDs | QY (%) |
|---|---|---|---|
| D ED CDs | 80 | ND ED CDs | 72 |
| D PEI CDs | 35 | ND PEI CDs | 31 |
| D ACR CDs | 46 | ND ACR CDs | 44 |
| D EA CDs | 24 | ND EA CDs | 20 |

In general, and compared to batch synthesis, QYs are higher when the synthesis is performed in the microreactors. Moreover, the D fractions had slightly higher QYs than the ND fractions, indicating that without purification the presence of some unreacted precursors or other by-products formed in the synthesis quench the fluorescence of the CDs. However, QYs obtained with the ND fractions were high enough, compared to other luminophores, to be employed as PL probes. DLS measurements were performed to determine the size distribution of the CDs. The measurements acquired for the four different CDs synthesized can be seen in Figure 4.30, and the results of the particle size distributions are shown in Table 4.14.

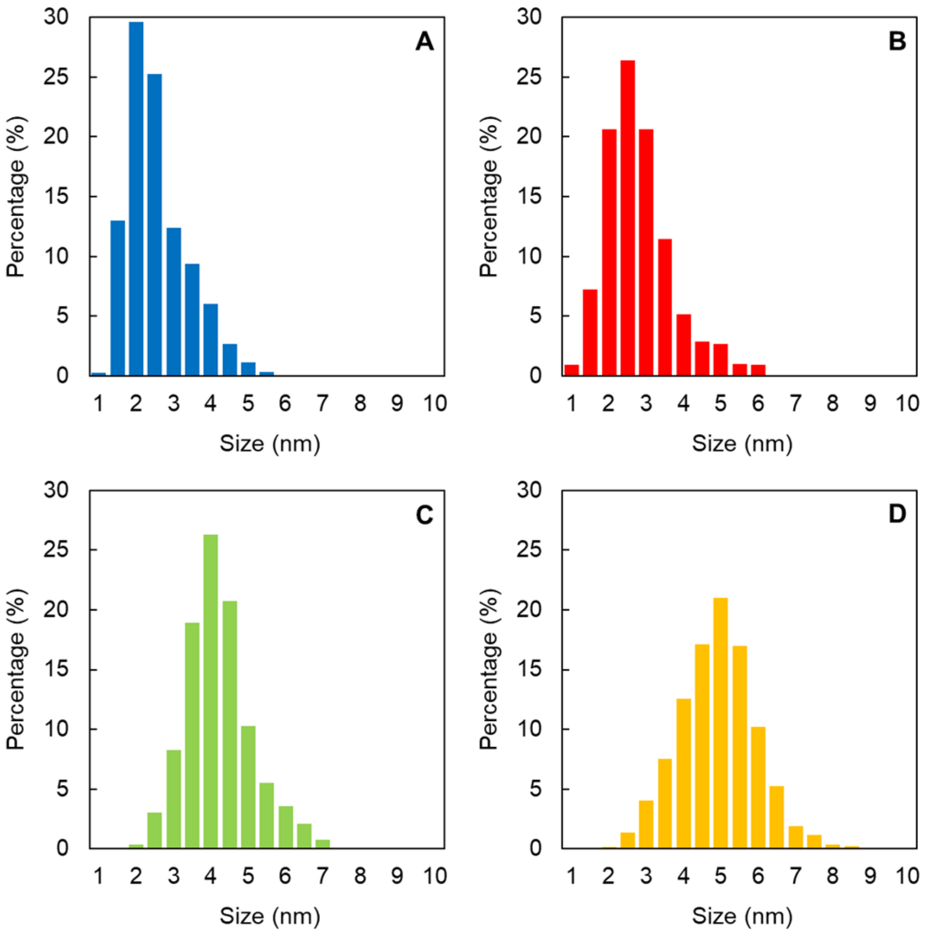

Figure 4.30: Size distribution of the CDs synthesized in the LTCC microreactor: D ED CDs (A), D PEI CDs (B), D ACR CDs (C), and D EA CDs (D)

Table 4.14: Particle size of the CDs synthesized in the LTCC microreactor

| Type of CDs | Particle size (nm) |
|---|---|
| D ED CDs | 2.6 ± 0.9 |
| D PEI CDs | 2.8 ± 1.1 |
| D ACR CDs | 4.2 ± 0.8 |
| D EA CDs | 4.9 ± 1.5 |

Results showed that the CDs have average sizes between 2 and 5 nm, as for the CDs synthesized in batch. However, the size distribution is narrower in the case of using the LTCC microreactor as a consequence of the better control of temperature and mixture of precursors.

As commented in Section 4.1.1.1, it was very challenging to obtain HRTEM images of the CDs with high contrast. In Figure 4.31A, a HRTEM image of the ACR CDs can be seen. Some D ACR CDs have been identified thanks to the diffraction planes after the treatment with the ImageJ software. D ACR CDs had a quasi-spherical shape and an approximate size of 3-5 nm, that was similar to the one obtained with the DLS measurement. Figure 4.31B also shows a Scanning Transmission Electron Microscopy (STEM) image obtained from this CDs sample. In this case, the electron beam is focused on a small spot and the surrounding is scanned [347]. This technique allowed to observe the CDs with better contrast (white dots in Figure 4.31B), but the beam cannot be focused on the same spot of the sample for a long time because it is burned.

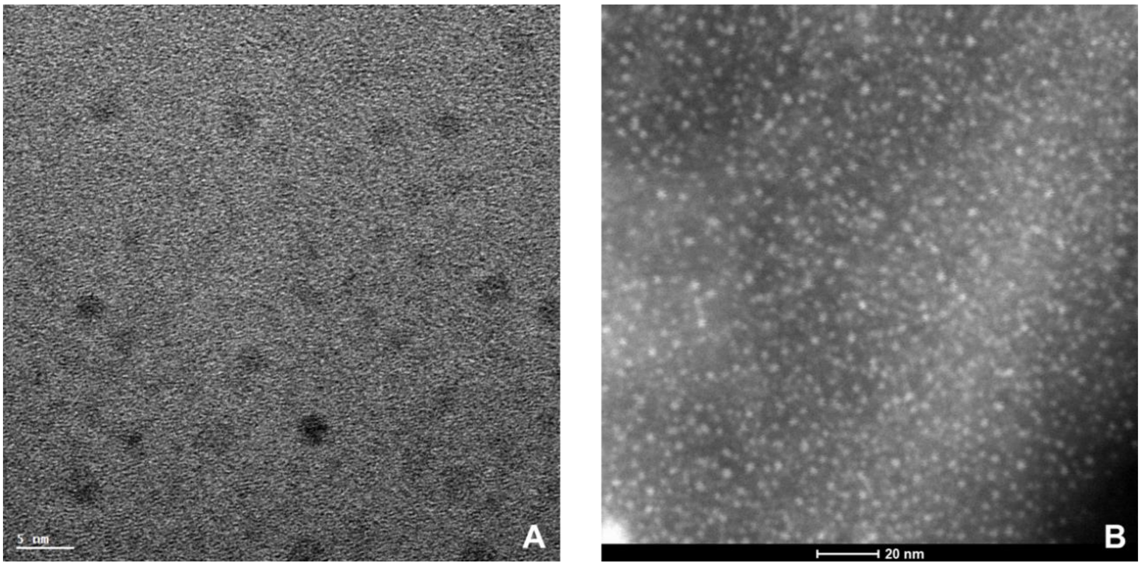

Figure 4.31: (A) HRTEM image and (B) STEM image of the D ACR CDs

Finally, FTIR spectra of the CDs synthesized in the LTCC microreactor were acquired to know the functional groups present in their surface. The results obtained are the following.

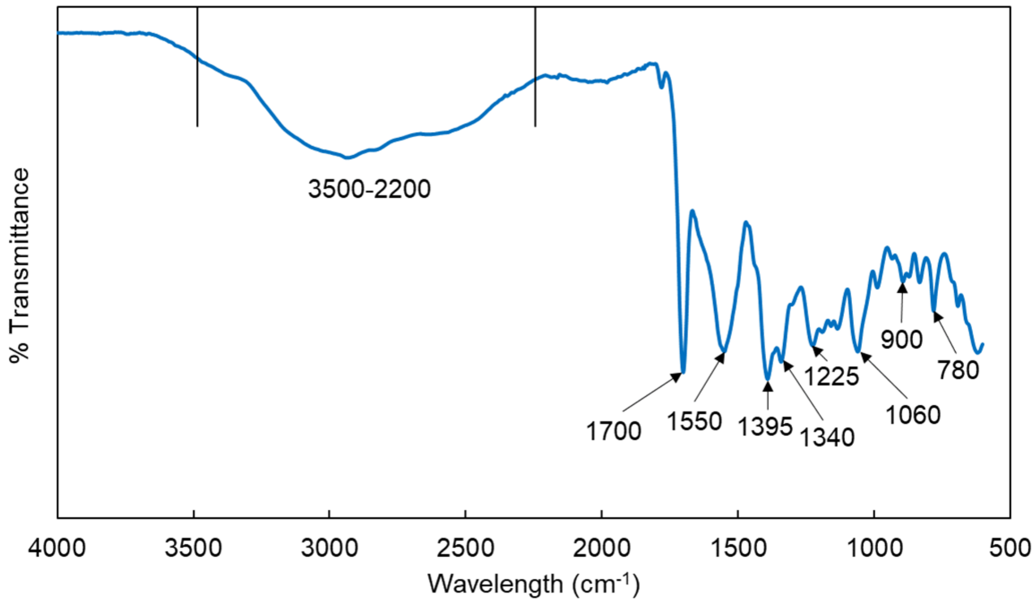

Figure 4.32: FTIR spectrum of the D ED CDs

For ED CDs, it can be observed a broad band ranging from 3500 to 2200 cm$^{-1}$, which could be attributed to the presence of water in the sample. The peak at 1700 cm$^{-1}$ corresponds to C=O stretching, the peak at 1550 cm$^{-1}$ to the C=C stretching, the peak at 1395 to N-H bending vibration, the peak at 1340 cm$^{-1}$ to the C-N stretching, the peak at 1225 cm$^{-1}$ to the C=O aromatic stretching, and the one at 1060 cm$^{-1}$ can be ascribed to the O-H stretching vibration. The peak at 900 cm$^{-1}$ is attributed to the O-H of the carboxyl group and the peak at 780 cm$^{-1}$ to C-H deformation vibration.

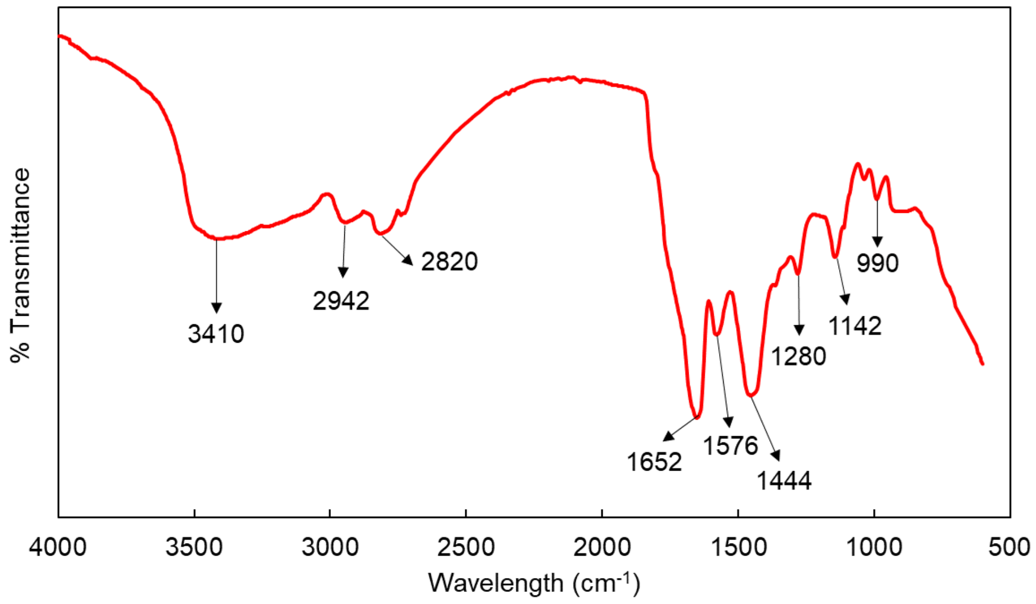

Figure 4.33: FTIR spectrum of the D PEI CDs

For PEI CDs, it can be observed a peak at 3410 cm$^{-1}$, that can be associated with O-H stretching vibrations, and the peaks at 2942 and 2820 cm$^{-1}$, correspond to C-H stretching vibrations. The peak at 1652 cm$^{-1}$ is attributed to C=O stretching vibration, the one at 1576 cm$^{-1}$ to the C=C stretching, and the one at 1444 cm$^{-1}$ to the N-H bending vibration. Finally, the peaks located at 1280, 1142, and 990 cm$^{-1}$ correspond to asymmetric stretch of a C-N bond, to C=C stretching, and to C-O aromatic stretching, respectively.

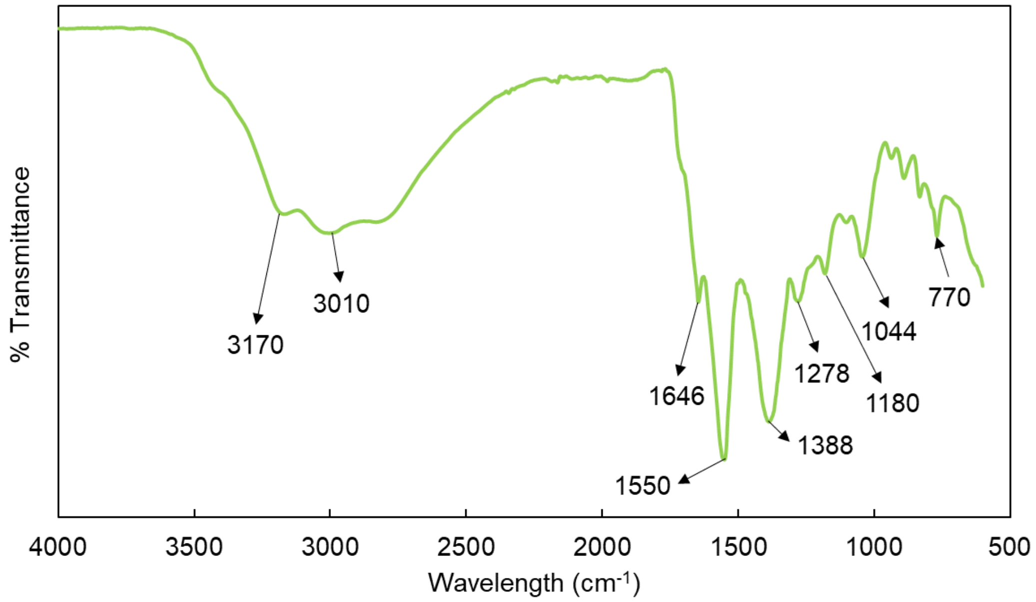

Figure 4.34: FTIR spectrum of D ACR CDs

For ACR CDs, the following peaks can be observed, which can be assigned to different functional groups: the broad peak in the 3500-2500 cm$^{-1}$ area could come from stretching vibrations of O-H groups. Moreover, bands at 3170 cm$^{-1}$ and 3010 cm$^{-1}$ correspond with N-H of an amide group and with C-H stretching vibrations, respectively. The peak at 1646 cm$^{-1}$ could be assigned to the stretching vibration of C=O, the peak at 1550 cm$^{-1}$ to the C=C stretching vibration, the peak at 1388 cm$^{-1}$ belongs to the bending vibration of N-H, the one at 1278 cm$^{-1}$ is from the asymmetric stretch of C-N, and finally, the peak at 1044 cm$^{-1}$ is attributed to C-O aromatic stretching, and the one at 770 cm$^{-1}$ that is associated with the deformation vibration of C-H.

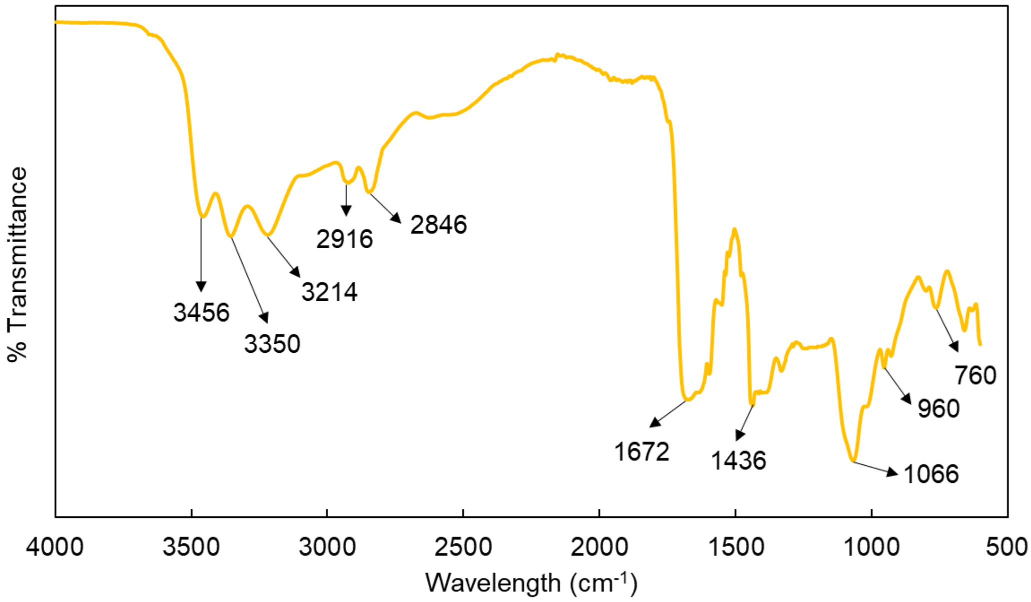

Figure 4.35: FTIR spectrum of the D EA CDs

Finally, for the EA CDs the main peaks that can be observed are: a peak at 3456 cm$^{-1}$ and another one at 3350 cm$^{-1}$ that correspond to the stretching vibration of O-H, the peak at 3214 cm$^{-1}$ that is associated with the N-H of an amide, the peaks at 2916 cm$^{-1}$ and at 2846 cm$^{-1}$ correspond to C-H stretching vibrations. The peak at 1672 cm$^{-1}$ comes from C=O stretching vibrations, the one at 1436 cm$^{-1}$ from N-H bending vibration, and the one at 1066 cm$^{-1}$ from the O-H stretching vibrations. Finally, the peaks located at 960 and 760 cm$^{-1}$ correspond to the O-H of a carboxyl group, and to the deformation vibration of C-H bonds, respectively.

The results obtained from the FTIR spectra of the CDs indicated that nitrogen functionalization was successful in all cases and that different carboxyl, hydroxyl, amino, and amide bonds exist on the surface of the CDs, which confer the CDs their water solubility and allow the selective interaction with different heavy metal ions [218].

The main differences between the CDs based on their FTIR spectra were: for ED CDs the bands associated with O-H stretching vibrations, C-H stretching vibrations, and N-H of an amide were not detected probably due to the presence of water in the sample, for PEI CDs the band associated with an N-H bond of an amide could not be observed, for ACR CDs the band associated with C=O stretching vibrations was found to be less intense than for the other CDs analyzed, for EA CDs the band associated with C=C stretching could not be observed (it could be overlapped with other bands) and in the case of PEI CDs this band is less intense than for the other two CDs. Moreover, for EA CDs the band associated with C=O aromatic stretching could not be observed. These differences in the results obtained for CDs surface functional groups could be the responsible of the different selectivity of the synthesized CDs.

There is not much information in the literature about the functionalization of CDs and their selectivity. -COOH, -OH, or -CONH- functional groups are Lewis bases that can interact with Lewis acids such as heavy metal ions, and this interaction, and thus selectivity, may depend on many factors related with coordination chemistry.

### 4.1.2.3 Selectivity tests

Selectivity of the obtained CDs was also assessed and to evaluate it, emission spectra of the CDs dispersions in the presence of different heavy metal ion solutions ($Cd^{2+}$, $Co^{2+}$, $Cu^{2+}$, $Cr^{3+}$, $Fe^{3+}$, $Hg^{2+}$, $Ni^{2+}$, $Pb^{2+}$, $Zn^{2+}$) at a concentration of 10 ppm, and other potentially interfering ions present in water ($Na^+$, $Mg^{2+}$, $Ca^{2+}$, $Cl^-$, $CO_3^{2-}$) at a concentration of 1000 ppm, were registered in the spectrofluorometer. The ratio between the fluorescence after the addition of the studied ions to the CDs dispersion and the fluorescence of the CDs ($F/F_0$) is represented for each type of CDs synthesized in the LTCC microreactor.

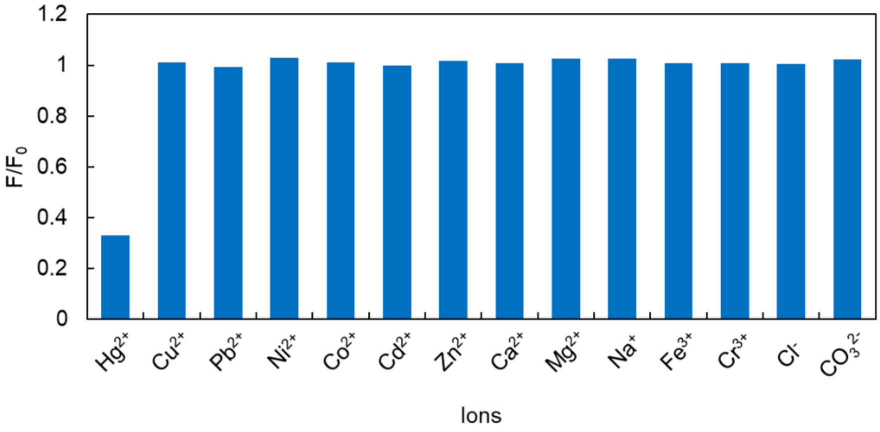

Figure 4.36: Ratio between the fluorescence after the addition of different ions to the D ED CDs and the fluorescence of the D ED CDs synthesized in the LTCC microreactor

As can be seen in Figure 4.36, the fluorescence of the ED CDs was strongly quenched by $Hg^{2+}$, as in CDs synthesized in batch. None of the other ions studied induced a significant quenching effect.

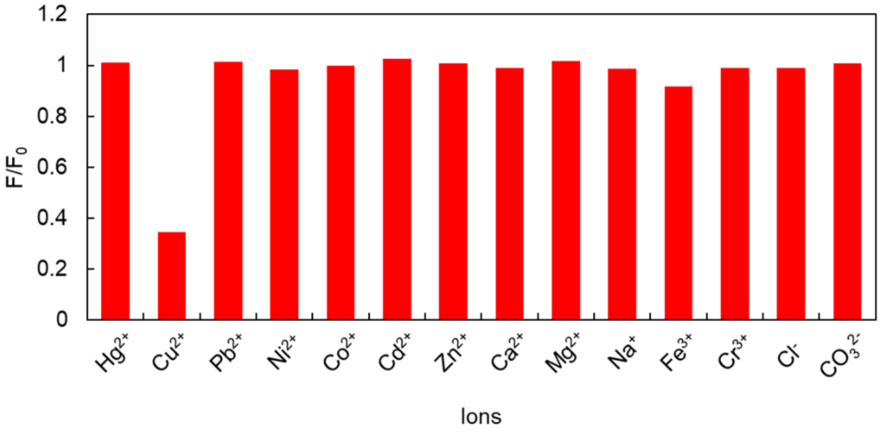

Figure 4.37: Ratio between the fluorescence after the addition of different ions to the D PEI CDs and the fluorescence of the D PEI CDs synthesized in the LTCC microreactor

In Figure 4.37, it can be clearly seen that the fluorescence of the PEI CDs was quenched by $Cu^{2+}$ and was slightly quenched by $Fe^{3+}$ as their analogous synthesized in batch, but it was not significant, as it could be demonstrated in the selective detection of Cu$^{2+}$ with the developed microanalyzer under solutions containing Fe$^{3+}$ as well (acidic extracts of polluted samples). The other ions studied did not present any quenching effect on the fluorescence of PEI CDs.

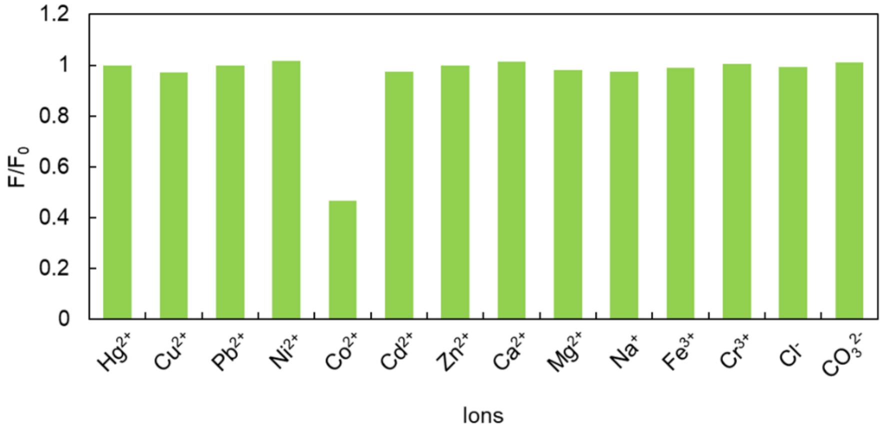

Figure 4.38: Ratio between the fluorescence after the addition of different ions to the D ACR CDs and the fluorescence of the D ACR CDs synthesized in the LTCC microreactor

For ACR CDs, as can be seen in Figure 4.38, the only ion that produced a significant quenching effect was Co$^{2+}$, as in ACR CDs synthesized in batch.

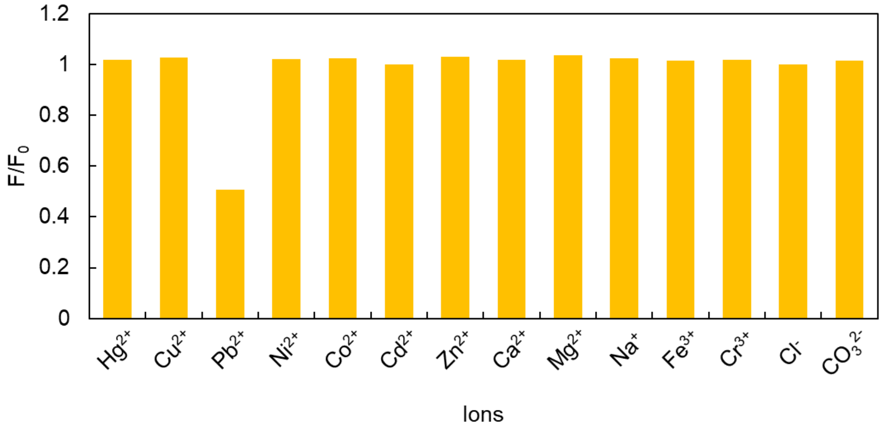

Figure 4.39: Ratio between the fluorescence after the addition of different ions to the D EA CDs and the fluorescence of the D EA CDs synthesized in the LTCC microreactor

Finally, in Figure 4.39, it can be clearly seen that the fluorescence of the EA CDs was only quenched in the presence of Pb$^{2+}$, as in EA CDs synthesized in batch.

To sum up, the use of the microreactor improves the homogeneity of the obtained CDs in terms of size distribution but did not alter their selectivity because this property is mainly attributed to the employed precursors, which were the same. Therefore, selectivity was the following: ED CDs were selective to Hg$^{2+}$, PEI CDs were selective to Cu$^{2+}$, ACR CDs were selective to Co$^{2+}$, and EA CDs were selective to Pb$^{2+}$.

### 4.1.2.4 Analytical quality parameters

The synthesized nanomaterials were afterwards employed as fluorescent probes to determine the four heavy metals in water using the developed analytical system. As in Section 4.1.1.4, four calibration plots for the separate analysis of each heavy metal studied were obtained to calculate different analytical quality parameters. In this case the calibration plots for both fractions of each type of CDs were obtained to compare the analytical quality parameters. They were acquired in the same way, injecting per triplicate each type of CDs dispersion into the 0.1 M citric/citrate buffer at pH 4 (from which a maximum signal should be obtained ($F_0$)), and into standard solutions containing increasing concentrations of the heavy metal studied (from which quenched signals could be obtained (F)). In Figure 4.40, the four Stern-Volmer plots can be seen.

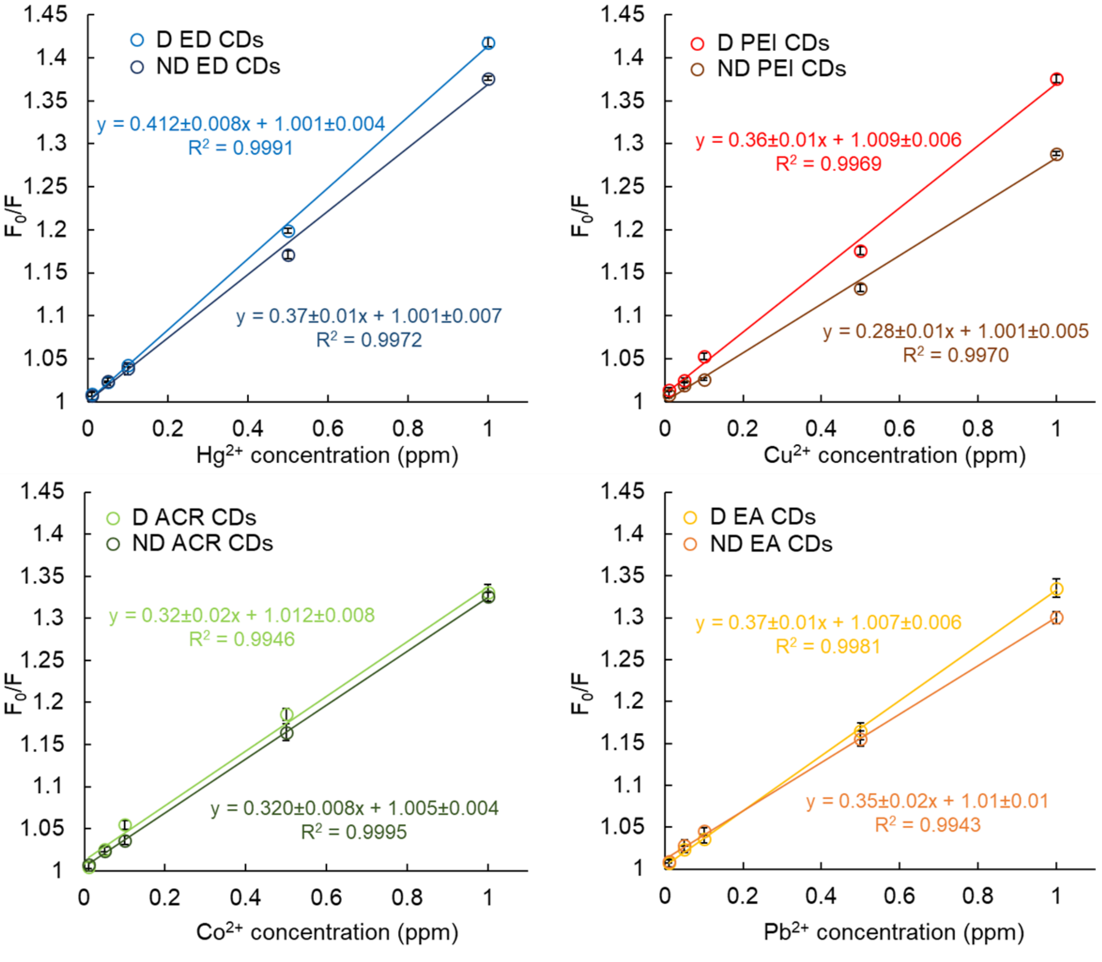

Figure 4.40: Calibration curves represented as the Stern-Volmer plot for the target heavy metals

Calibration plots showed a good linear correlation in the studied range ($R^2$ > 0.99). From the plots, the sensitivity ($K_{SV}$) and the LOD could be obtained. Repeatability was also calculated, and these three parameters are summarized in Table 4.15. As well as for the CDs synthesized in batch, the values of the intercept were approximately 1 in all cases, indicating that the calibration plots fit the Stern-Volmer equation and that a single quenching mechanism was occurring between the different heavy metal ions and the CDs.

Table 4.15: Analytical performance of the miniaturized analyzer for the determination of heavy metals with the CDs synthesized in the LTCC microreactor

| **Type of CDs** | **$K_{SV}$ ($ppm^{-1}$)** | **LOD (ppb)** | **Repeatability (%RSD)** |
|---|---|---|---|
| D ED CDs | 0.412 ± 0.008 | 6.3 ± 0.9 | 1.8 |
| ND ED CDs | 0.37 ± 0.01 | 6.6 ± 0.8 | 1.7 |
| D PEI CDs | 0.36 ± 0.01 | 9.7 ± 0.7 | 1.3 |
| ND PEI CDs | 0.28 ± 0.01 | 11.2 ± 1.0 | 1.5 |
| D ACR CDs | 0.32 ± 0.02 | 6.0 ± 1.0 | 1.5 |
| ND ACR CDs | 0.320 ± 0.008 | 6.7 ± 0.9 | 1.6 |
| D EA CDs | 0.37 ± 0.01 | 8.4 ± 0.6 | 0.8 |
| ND EA CDs | 0.35 ± 0.02 | 7.5 ± 1.2 | 2.1 |

All measurements have a good repeatability (with a maximum RSD value of 2.1%), and as in the case of the CDs synthesized in batch the LODs obtained for three of the four heavy metals studied were below the limits set listed in Table 1.1 for drinking water. In the case of $Hg^{2+}$, the limits set are below the LOD obtained with the microanalyzer. As a general trend, the D fractions showed higher sensitivity than the ND fractions. As already stated, this effect could be caused by the unreacted precursors and by-products formed that interfere in the CDs/heavy metal interaction. However, in all the cases, sensitivity was high enough to conclude that the different CDs synthesized in the LTCC microreactor could be used for the analysis of heavy metals without further purification, thus enabling the integration of the synthesis and the optical detection, as it was performed afterwards and that can be seen in Section 4.1.3.

#### 4.1.2.5 Analysis of synthetic and real samples

To demonstrate the applicability of the system for the analysis of water samples, spiked tap and river water samples were analyzed. Recovery rates and %RSD were calculated for the tap and river water samples, that can be seen in Table 4.16 and 4.17 respectively.

Table 4.16: Recovery rates and %RSD obtained with spiked tap water samples (n=3)

| **Concentration of Hg$^{2+}$ spiked in the sample (ppm)** | **Recovery rate (%)** | **RSD (%)** | **Concentration of Cu$^{2+}$ spiked in the sample (ppm)** | **Recovery rate (%)** | **RSD (%)** |
|---|---|---|---|---|---|
| 0.10 | 107 | 3.6 | 0.10 | 99 | 4.7 |
| 0.25 | 99 | 2.8 | 0.25 | 100 | 5.6 |
| 0.50 | 98 | 2.5 | 0.50 | 100 | 2.0 |
| 0.75 | 101 | 1.4 | 0.75 | 102 | 2.2 |
| **Concentration of Co$^{2+}$ spiked in the sample (ppm)** | **Recovery rate (%)** | **RSD (%)** | **Concentration of Pb$^{2+}$ spiked in the sample (ppm)** | **Recovery rate (%)** | **RSD (%)** |
| 0.10 | 101 | 2.5 | 0.10 | 102 | 3.4 |
| 0.25 | 99 | 2.7 | 0.25 | 100 | 2.3 |
| 0.50 | 97 | 1.9 | 0.50 | 99 | 3.0 |
| 0.75 | 102 | 1.7 | 0.75 | 100 | 2.0 |

Table 4.17: Recovery rates and %RSD obtained with spiked river water samples (n=3)

| **Concentration of Hg$^{2+}$ spiked in the sample (ppm)** | **Recovery rate (%)** | **RSD (%)** | **Concentration of Cu$^{2+}$ spiked in the sample (ppm)** | **Recovery rate (%)** | **RSD (%)** |
|---|---|---|---|---|---|
| 0.10 | 103 | 4.5 | 0.10 | 100 | 5.3 |
| 0.25 | 100 | 3.7 | 0.25 | 102 | 4.5 |
| 0.50 | 98 | 1.5 | 0.50 | 99 | 3.8 |
| 0.75 | 103 | 2.7 | 0.75 | 101 | 1.1 |
| **Concentration of Co$^{2+}$ spiked in the sample (ppm)** | **Recovery rate (%)** | **RSD (%)** | **Concentration of Pb$^{2+}$ spiked in the sample (ppm)** | **Recovery rate (%)** | **RSD (%)** |
| 0.10 | 102 | 4.6 | 0.10 | 104 | 3.0 |
| 0.25 | 100 | 1.4 | 0.25 | 102 | 3.8 |
| 0.50 | 102 | 3.9 | 0.50 | 101 | 2.9 |
| 0.75 | 102 | 1.1 | 0.75 | 99 | 2.3 |

From the results obtained, the calculated recovery rates are between 97% and 107%, showing good accuracy. Precision depends on the analyte as well as the concentration, but the mean of the RSD for three measurements was calculated to be less than 3% in the case of the spiked tap water samples and less than 4% in the case of spiked river water samples. The slightly higher value of RSD found in the case of spiked river water samples can be attributed to a more complex matrix. As can be seen, in general, at low concentrations the RSD is higher, but only one of the spiked tap water samples and one of the spiked river water samples exceeded 5% of RSD. With these results it can be concluded that the microanalyzer was able to determine four heavy metal ions with good precision and accuracy with the CDs synthesized in the LTCC microreactor.

#### 4.1.2.6 Comparison of the performance with CDs synthesized in batch

Some of the most important features regarding the performance of the CDs are compared in this section for the four synthesis processes that were adapted to be performed in the fabricated LTCC microreactor. In Table 4.18, QYs, LODs and sensitivities ($K_{SV}$) for the same CDs synthesized in batch and in the LTCC microreactor can be seen.

Table 4.18: Comparison between some features for the same CDs synthesized in batch and in the LTCC microreactor

| **CDs synthesized in batch** | **QY (%)** | **LOD (ppb)** | **Sensitivity ($K_{SV}$) ($ppm^{-1}$)** |
|---|---|---|---|
| ED CDs | 78 | 5.9 ± 0.8 | 0.380 ± 0.008 |
| PEI CDs | 32 | 11.7 ± 0.7 | 0.278 ± 0.007 |
| ACR CDs | 25 | 3.9 ± 0.5 | 0.288 ± 0.009 |
| EA CDs | 16 | 8.8 ± 0.8 | 0.33 ± 0.01 |
| **CDs synthesized in the LTCC microreactor** | **QY (%)** | **LOD (ppb)** | **Sensitivity ($K_{SV}$) ($ppm^{-1}$)** |
| ED CDs | 80 | 6.3 ± 0.9 | 0.412 ± 0.008 |
| PEI CDs | 35 | 9.7 ± 0.7 | 0.36 ± 0.01 |
| ACR CDs | 46 | 6.0 ± 1.0 | 0.32 ± 0.02 |
| EA CDs | 24 | 8.4 ± 0.6 | 0.37 ± 0.01 |

As seen previously, one parameter that improved with the synthesis in the LTCC microreactors was homogeneity of the CDs size distribution as can be seen from the narrower particle size distribution obtained. From data in Table 4.18 it can be noticed that QY are higher for the CDs synthesized in the microreactor, thus indicating the formation of a greater quantity of amorphous nanoparticles (polymer dots) that have more molecular fluorophore moieties embedded, causing the enhancement of the QY. Sensitivity was also slightly enhanced, and it could also be the result of more fluorescence moieties capable of interacting with the analyte. Regarding the LODs, as this parameter is calculated from the baseline, and it is limited from the instrumental noise no clear tendency was observed from the comparison of both synthesizing methods. However, as can be seen in the table, except in the case of $Hg^{2+}$, LODs were below the legal limits set for drinking water in all cases. Moreover, the use of LTCC microreactors for the synthesis of CDs allow the automation of the syntheses.

### 4.1.3 Coupling of the synthesis of CDs and the determination of cobalt

#### 4.1.3.1 Synthesis and characterization

The final goal of this thesis regarding the development of an automatic analyzer for the multiparametric monitoring of heavy metals in water and, after demonstrating that CDs obtained from the microreactor could be directly used without a purification step as optical probes, was to couple their synthesis with the heavy metals' determination. In this way, it would be possible to control the quantity of nanomaterials to be used and avoid degradation processes of these, which although it is known that their photostability is much higher than that of any organic luminophore, the chemical stability of dispersed nanoparticles could be a limitation for their application in water quality monitoring with low reagent maintenance requirements. Therefore, we developed an automated system capable of synthesizing the CDs in the LTCC microreactor and directly use them to determine the concentration of heavy metal ions in water with the miniaturized optical detection system without the need for any intervention. As demonstrator, ACR CDs were synthesized and directly used to determine the $Co^{2+}$ concentration on the same tap water and river water samples analyzed in Section 4.1.2.5. In this case, CDs dispersions were used directly as obtained without further purification steps.

The ACR CDs synthesized showed blue PL upon irradiation with a UV lamp. Their SPR band can be seen in Figure 4.41, and the emission and excitation spectra in Figure 4.42.

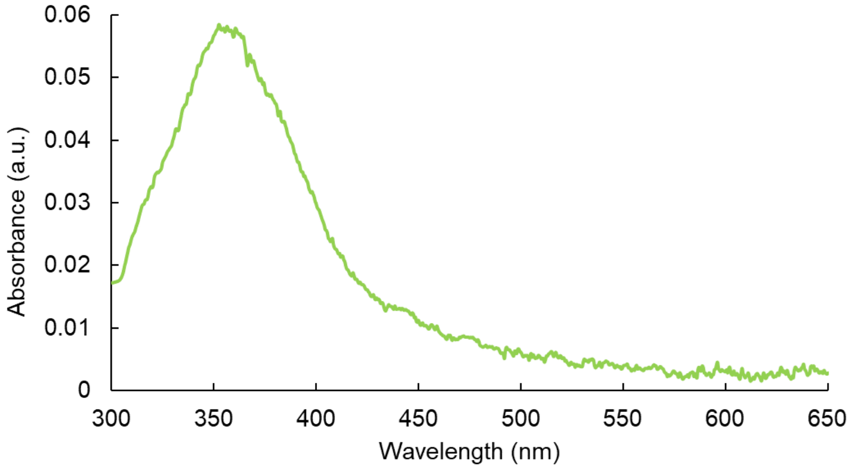

Figure 4.41: UV-Vis spectra of ACR CDs synthesized in the integrated microanalyzer

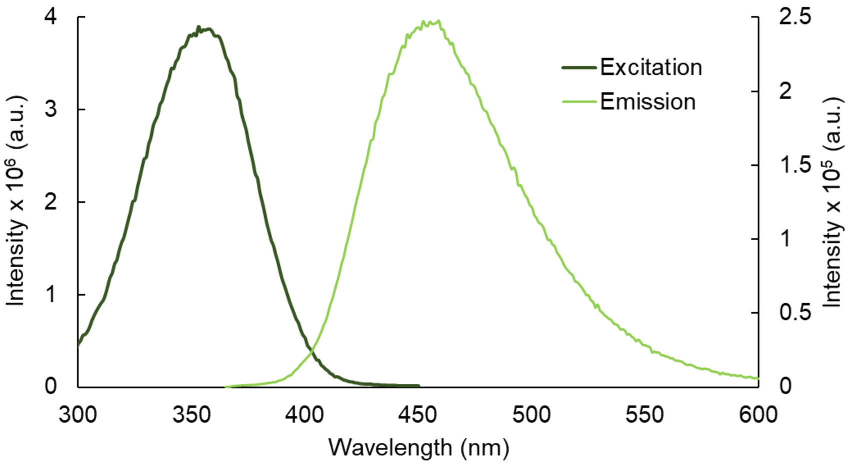

Figure 4.42: Excitation and emission spectra of ACR CDs synthesized in the integrated microanalyzer

Spectra shows the wavelength of the SPR band at 353 nm, and an excitation and emission maxima located at 358 nm and 452 nm respectively. The Stokes shift was of 94 nm and QY was 44%. These results were very similar to those obtained for the ND ACR CDs that can be seen in Section 4.1.2.2, indicating that the ACR CDs synthesized with the integrated system were very similar to ND ACR CDs, as expected. As for the other CDs synthesized, these CDs are suited to be used with the developed analyzer, which employs an LED emitting at 365 nm as excitation source.

Moreover, a DLS measurement was performed to determine the size distribution of the ACR CDs synthesized with the integrated system, that can be seen in Figure 4.43.

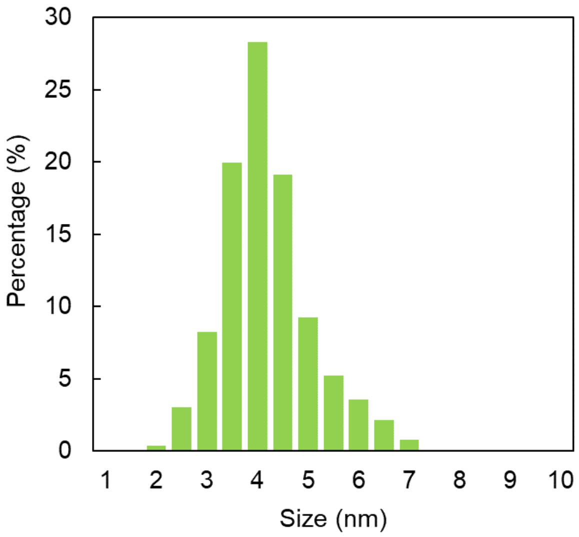

Figure 4.43: Size distribution of ACR CDs synthesized in the integrated microanalyzer

Obtained results show that the particle size distribution of the ACR CDs was 4.2 ± 0.9 nm, very similar to the D ACR CDs (4.2 ± 0.8), thus indicating that these CDs without being purified presented good homogeneity of sizes. Moreover, differences between these CDs synthesized in the integrated system and synthesized with only the LTCC microreactor were negligible, as expected.

Also, HRTEM images and an FTIR spectrum of these CDs can be observed in Section 4.1.2.2, as these techniques required that the CDs were dialyzed. Briefly, from the results presented it can be concluded that the ACR CDs have quasi-spherical shapes and that the functional groups of the surface of the CDs (-COOH, -OH, -CONH) allow their selective interaction with $Co^{2+}$ ions, producing the quenching of fluorescence of the ACR CDs [15,348].

### 4.1.3.2 Analytical quality parameters

To remember, once ACR CDs are automatically synthesized following a programmable protocol, a volume of 500 µL, 100-times automatically diluted ACR CDs, is injected in the carrier solution per triplicate (citric/citrate buffer (from which a maximum signal should be obtained ($F_0$)), and into standard solutions) to obtain the calibration plot. The obtained Stern-Volmer plot can be seen in Figure 4.44.

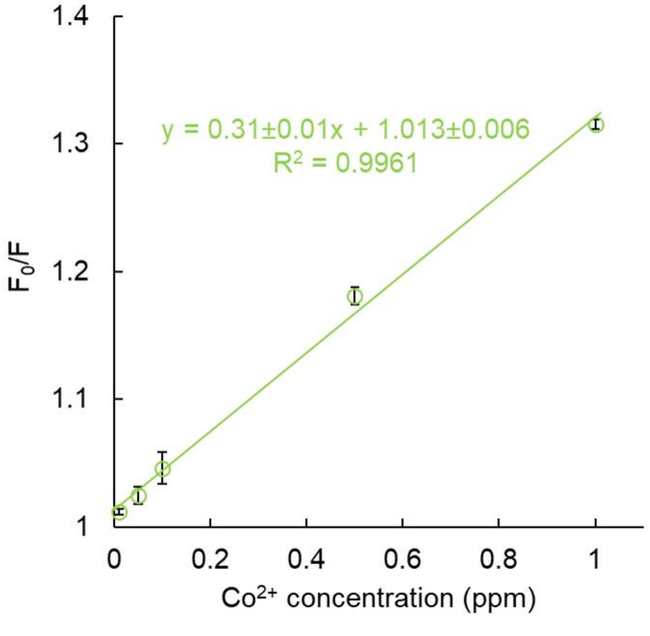

Figure 4.44: Stern-Volmer plot of quenching effect of $Co^{2+}$ on the fluorescence of ACR CDs synthesized in the integrated microanalyzer

Calibration plot showed a good linear correlation in the 0.02 to 1 ppm range ($R^2 > 0.99$) and the sensitivity ($K_{SV}$) (0.31 ± 0.01 $ppm^{-1}$) and LOD (6.9 ± 0.9 ppb) obtained were very similar to those obtained with the ND ACR CDs ($K_{SV}$ = 0.320 ± 0.008 $ppm^{-1}$ and LOD = 6.7 ± 0.9 ppb), and with the D ACR CDs ($K_{SV}$ = 0.32 ± 0.02 $ppm^{-1}$ and LOD = 6.0 ± 1.0 ppb), thus indicating that purification was not critical, as already stated in Section 4.1.2.4, and that CDs could be used directly in the integrated automatic analyzer without losing the properties of the analytical system. Repeatability was also calculated to be 1.3%.

For comparison purposes, some analytical features of other reported CDs-based optical methods to determine $Co^{2+}$ are summarized in Table 4.19. As it can be seen, these methods reach slightly lower LODs and wider linear ranges. However, the method presented in this part of the thesis, allows obtaining CDs with the highest QY, which ensures a strong signal even in case of possible reagent decomposition and as optical probes in the developed analyzer, they procure a LOD that is well below the reference value for $Co^{2+}$ set by the US EPA for drinking water (Table 1.1).

Table 4.19: An overview on recently reported CDs-based optical methods for the determination of $Co^{2+}$ ions

| **Precursors** | **QY (%)** | **LOD (ppb)** | **Linear range (ppm)** | **Reference** |
|---|---|---|---|---|
| Pyridoxal 5-phosphate and ethanediamine | 15 | 3 | 0-3.5 | [349] |
| L-cysteine | 27 | 2 | 0.06-2.9 | [350] |
| p-phenylenediamine and asparagine | 16 | 1 | 0.02-3.8 | [351] |
| Carbopol 934 and diethylenetriamine | 39 | 27 | 0-2.4 | [15] |
| Citric acid and L-cysteine | - | 5 | 0.005-5.9 | [352] |
| Acrylic acid and ethylenediamine | 23 | 15 | 0.06-3.5 | [334] |
| Acrylic acid and ethylenediamine | 44 | 7 | 0.02-1.0 | This work |

Regarding the Stern-Volmer quenching constant ($K_{SV}$), it has been doubled (0.31 ± 0.01 $ppm^{-1}$) compared with the synthetic method in batch (0.14 $ppm^{-1}$) [334] indicating an improvement in the sensitivity.

### 4.1.3.3 Analysis of synthetic and real samples

To confirm the applicability of the totally integrated system, the same spiked tap water and river water samples analyzed in Section 4.1.2.5, were analyzed. Results obtained are summarized in Table 4.20.

Table 4.20: Recovery rates and %RSD obtained with spiked tap and river water samples (n=3)

| **Sample** | **[$Co^{2+}$] added (ppm)** | **[$Co^{2+}$] found (ppm)** | **Recovery (%)** | **RSD (%)** |
|---|---|---|---|---|
| Tap water | 0.10 | 0.104 ± 0.007 | 104 | 2.8 |
| | 0.25 | 0.25 ± 0.02 | 101 | 2.5 |
| | 0.50 | 0.50 ± 0.02 | 100 | 1.6 |
| | 0.75 | 0.77 ± 0.05 | 102 | 2.5 |
| River water | 0.10 | 0.10 ± 0.01 | 102 | 3.8 |
| | 0.25 | 0.24 ± 0.02 | 98 | 2.9 |
| | 0.50 | 0.49 ± 0.02 | 99 | 2.0 |
| | 0.75 | 0.75 ± 0.04 | 100 | 2.0 |

The calculated recovery rates ranged from 98-104%, indicating a good accuracy. Regarding precision, the mean of the RSD for three replicates was calculated to be 2.4% in the case of the spiked tap water samples and 2.7% in the case of spiked river water samples. The mean of the RSD for three replicates obtained with the separated system was 2.2% for spiked tap water samples and 2.8% for spiked river water samples. Moreover, as can be seen in Table 4.20, all the samples presented an RSD below 4%. These results show that no significant differences between the performance of the integrated automatic analyzer and the separated system exist, thus validating the applicability of the integrated automatic analyzer for the determination of heavy metals in water samples.

## 4.2 Electrochemical detection of cadmium with CDs-modified SPCEs

This part of the work was performed during my research stay in the group Analytical Development LAQV Requimte from the Universidade do Porto, and the main goal was to study the effect of modifying SPCEs with CDs to determine heavy metal ions in water by voltammetry.

### 4.2.1 Synthesis and characterization

As it has been explained in Section 3.2.2, the CDs to electrochemically determine $Cd^{2+}$ ions were synthesized from citric acid and urea as the precursors in batch using a hydrothermal process. The CDs were dialyzed against MilliQ water for their purification.

The synthesized CDs were first optically characterized because the intensity and the position of the bands provides valuable information about the nanoparticles. The SPR band provide information about the sizes of the CDs and about the size particle dispersion. Moreover, the PL performance of the CDs allow the comparison of the synthesized CDs with other CDs presented in the literature. As the CDs synthesized for the optical detection of heavy metals, these CDs showed blue PL upon irradiation with a UV lamp. Their UV-Vis spectrum can be seen in Figure 4.45, and the emission and excitation spectra in Figure 4.46.

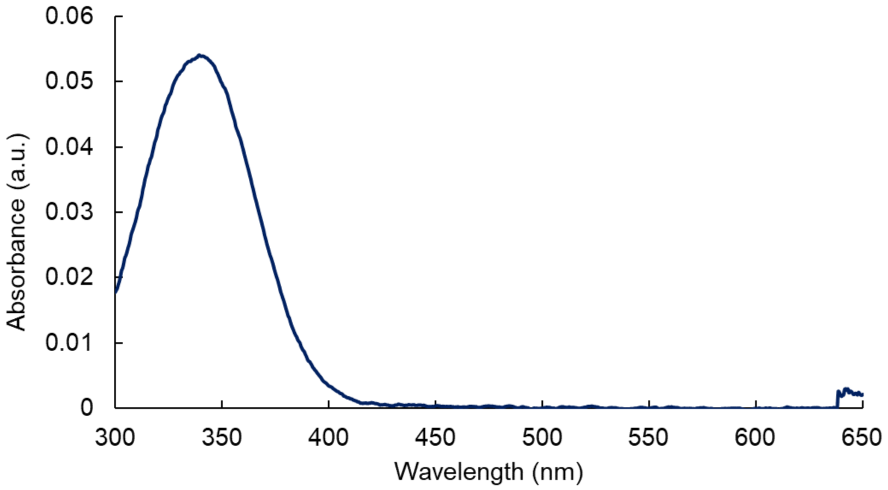

Figure 4.45: UV-Vis spectrum of the synthesized CDs

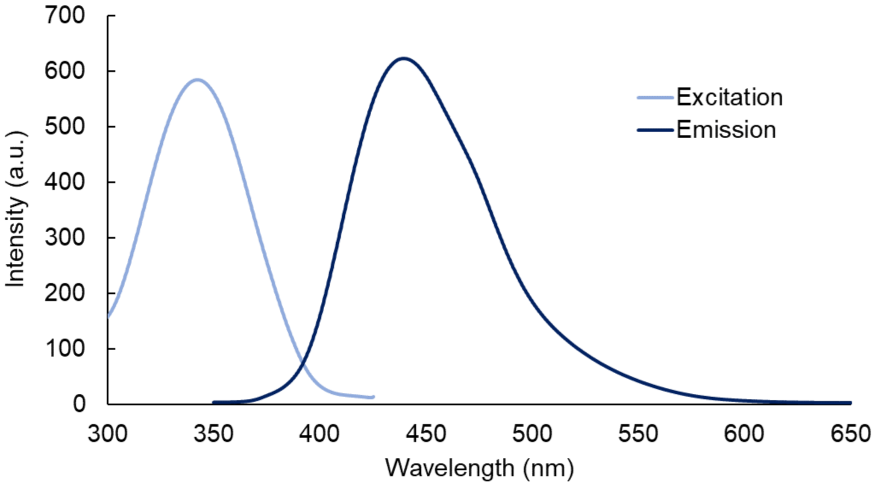

Figure 4.46: Excitation and emission spectra of synthesized CDs

From the absorbance and PL spectra of the CDs it can be extracted that the SPR band appears at 340 nm, and that the synthesized CDs show a wide excitation band with a maximum value at 342 nm and a wide emission band with a maximum value at 440 nm, thus obtaining a Stokes shift of 98 nm. The width of the bands and the Stokes shift obtained were similar to those obtained for the CDs synthesized in batch and used for the optical detection of heavy metals. The QY was also calculated in the same way as for the CDs used for the optical detection of heavy metals, obtaining a value of 32%.

The size distribution of the CDs dispersion was also studied by acquiring a DLS measurement, and the result can be observed in Figure 4.47. From the measurement an average particle size of 3.0 ± 1.1 nm was obtained.

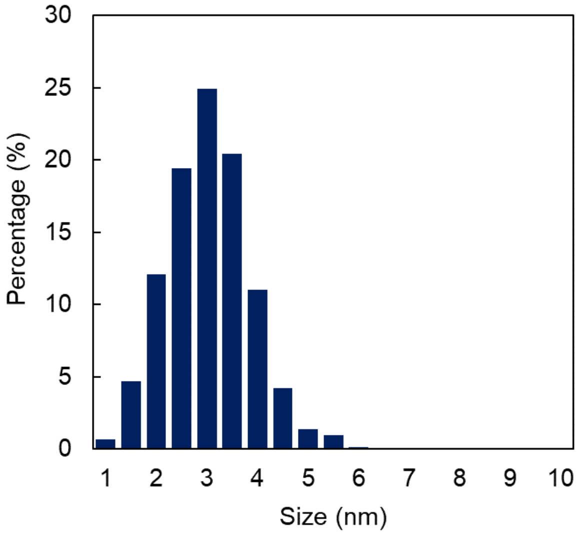

Figure 4.47: Size distribution of synthesized CDs

Finally, the FTIR spectrum of the CDs was registered to elucidate the functional groups present in their surface. The spectrum can be seen in Figure 4.48.

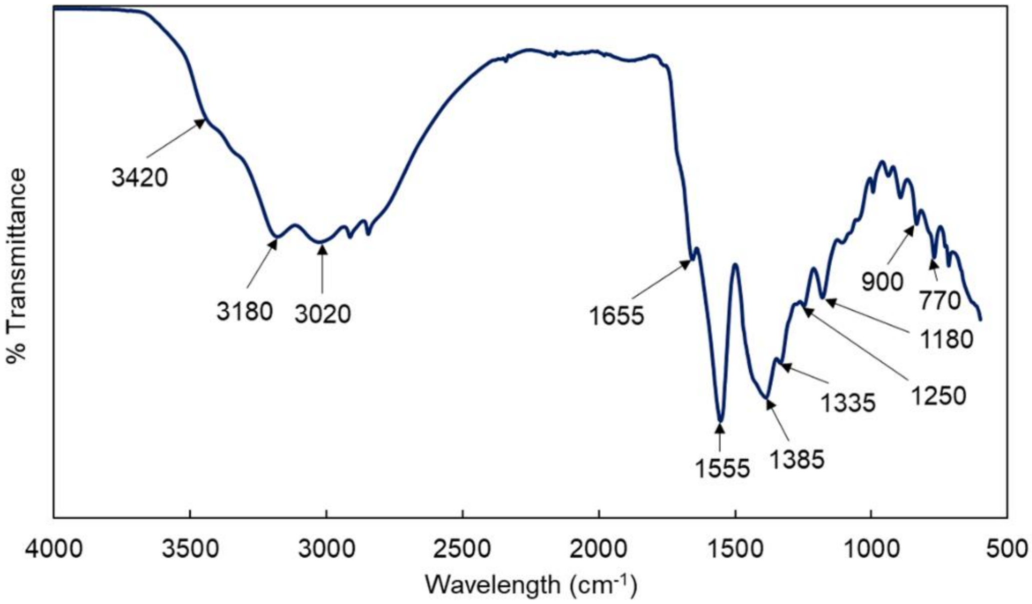

Figure 4.48: FTIR spectrum of the synthesized CDs

In the spectrum the following peaks can be observed: 3420 cm$^{-1}$ is from the stretching vibration of O-H, 3180 cm$^{-1}$ from the stretching vibration of N-H of an amide group, 3020 cm$^{-1}$ from the stretching vibration of C-H of methylene. The peak at 1655 cm$^{-1}$ is from the stretching vibration of C=O, the peak at 1555 cm$^{-1}$ from the C=C stretching vibration, the peak at 1385 cm$^{-1}$ belongs to the bending vibration of N-H, and the one at 1335 cm$^{-1}$ is from the asymmetric stretch of C-N. The peak at 1250 cm$^{-1}$ is attributed to C=O aromatic stretching, the peak at 1180 cm$^{-1}$ belongs to C=C stretching, the peak at 900 cm$^{-1}$ is attributed to the bending vibration from O-H of the carboxyl group and the out-of-plane deformation vibration of C-H is at 770 cm$^{-1}$. The results indicated that carboxyl, hydroxyl, amino and amide bonds exist on the surface of the synthesized

CDs, which can act as anchor sites to adsorb more $Cd^{2+}$ on CDs surface to improve the analysis sensitivity. This FTIR spectra can be compared with the ones registered for the CDs synthesized in the LTCC microreactor that can be seen in Section 4.1.2.2. Briefly, in the FTIR spectrum of this CDs the band associated with C=O stretching vibration is less intense, as for the D ACR CDs, but in this case the band associated with C=O aromatic stretching could be identified.

### 4.2.2 Optimization

As mentioned in Section 3.2.3, different methods were tested to determine $Cd^{2+}$ ions. The aim was to improve the sensitivity of the working electrode of the SPCE by surface modification with carbonaceous nanomaterials. MWCNT-COOH, SWCNT-amine, and GO were used as modifiers. First of all, we checked the current enhancement depending on the modifier by performing square wave voltammograms of a solution containing 1 ppb of $Cd^{2+}$. They can be seen in Figure 4.49.

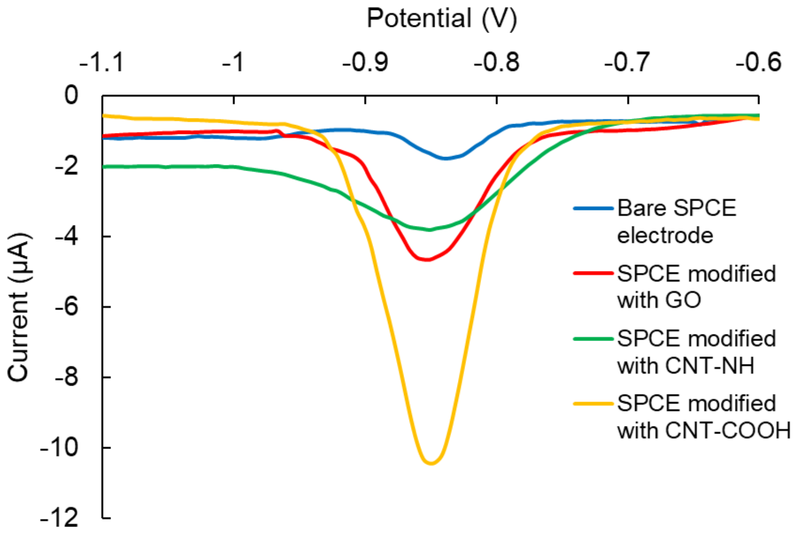

Figure 4.49: Anodic current signals obtained with different working electrode modifications

A signal enhancement was obtained with the different modifications with carbonaceous nanomaterials tested, but the greater signal was obtained with the MWCNT-COOH, so it was decided to use them to modify the electrodes for subsequent experiments.

For the previous modification optimization CDs diluted 10 times were used. As mentioned in Section 3.2.3 modification of electrodes with CDs provides fast electron transfer kinetics due to the high electrical conductivity and an increased surface area due to the high surface-to-volume ratio. Also, the hydroxyl, carboxyl, carbonyl, and other functional groups present in the surface of the CDs provide different selectivity depending on the precursors used for their synthesis. Even though the volume used for the modification of the electrodes is very low, CDs with different dilution factors were also tested to compare the response. In Figure 4.50, square wave stripping voltammograms obtained with three different CDs dilution factors with SPCEs modified with MWCNTs, can be seen.

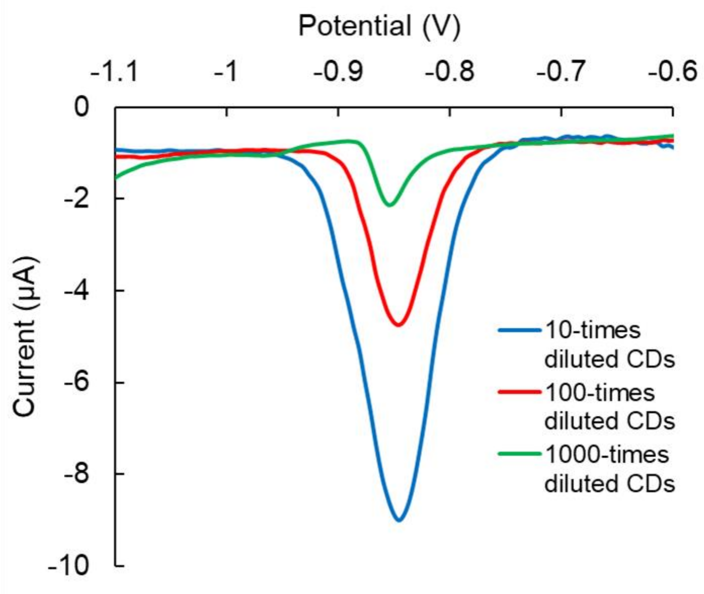

Figure 4.50: Effect of the CDs dilution factor on the stripping peak currents of $Cd^{2+}$

As the concentration of the CDs increased (expressed as dilution factor from 1000-times to 10-times diluted dispersions of CDs), the electrochemical response to $Cd^{2+}$ increased gradually. Considering that the quantity of the synthesized CDs is a limiting factor in this application and that only 6 µL were consumed in each analysis, a 10-dilution factor was selected for the preparation of the SPCEs with CDs to obtain a higher signal.

In SWSV, a symmetrical square-wave pulse is superimposed to a staircase wave resulting in a square wave. Once the working electrode modification process was stated, different experimental parameters affecting the SWSV measurements were systematically optimized. These were: deposition time, deposition potential, amplitude, and frequency. Different values for all these parameters were tested to try to improve stripping peak currents of $Cd^{2+}$.

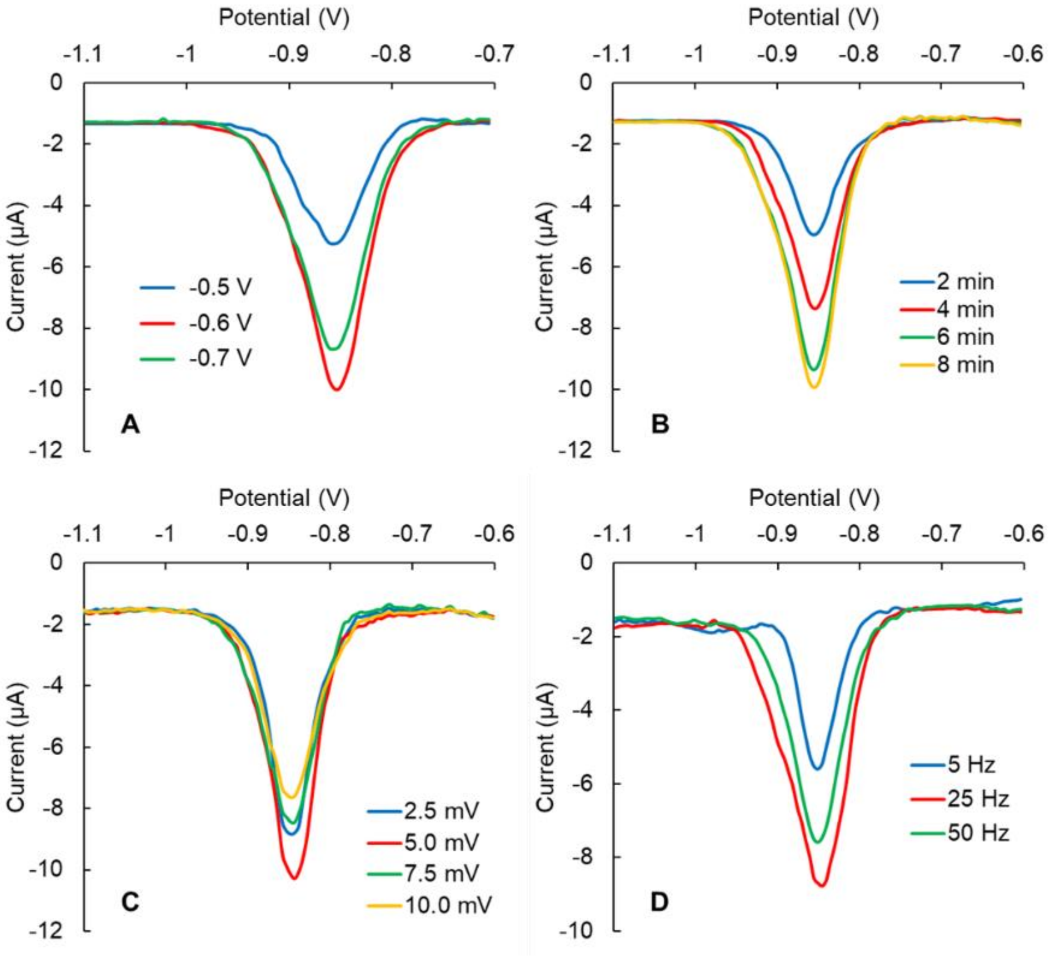

Figure 4.51: Effect of (A) deposition potential, (B) deposition time, (C) amplitude, and (D) frequency on the stripping peak currents of $Cd^{2+}$

The applied potential plays an important role in the sensitivity of SWSV measurements. As can be seen in Figure 4.51A, the maximum peak current was observed at -0.6 V so it was chosen as the deposition potential for further determination. The influence of the deposition time was then investigated (Figure 4.51B) by increasing the time from 2 to 8 min. The electrochemical response increased linearly with deposition time from 2 min to 6 min, and when the time was prolonged, the linear trend became insignificant due to the saturated load on the electrode surface. Therefore, 6 min was enough to achieve the highest sensitivity and the faster response time. Concerning the amplitude, 2.5 mV, 5 mV, 7.5 mV, and 10 mV were tested (Figure 4.51C). Amplitude is the height of a single pulse. The peak current increased as the amplitude decreased reaching a maximum value at 5 mV and decreasing again at 2.5 mV. So, 5 mV was chosen as the optimal value for the amplitude. Finally, frequencies ranging from 5 Hz to 50 Hz were tested (Figure 4.51D). Frequency can be understood as the number of potential cycles in a unit of time. In this case, the maximum peak current was obtained with a frequency of 25 Hz, so it was chosen as the optimal value.

### 4.2.3 Analytical quality parameters

To study the selectivity of the developed electrodes, some other metal ions were analyzed to assess their possible interference effects on the detection of $Cd^{2+}$. Different heavy metal ions ($Co^{2+}$, $Cu^{2+}$, $Fe^{3+}$, $Hg^{2+}$, $Ni^{2+}$, $Pb^{2+}$ and $Zn^{2+}$) at a concentration of 1 ppm and other metal ions present in water ($Ca^{2+}$, $Mg^{2+}$, and $Na^{+}$) at a concentration of 100 ppm were individually added to standard solutions containing 1 ppb of $Cd^{2+}$.

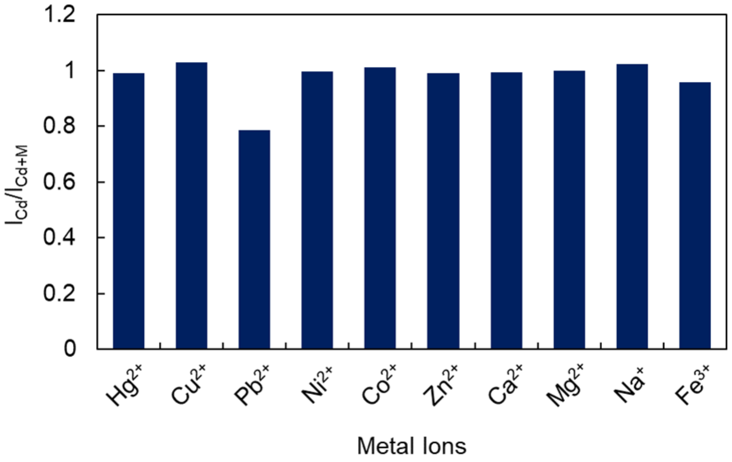

Figure 4.52: Interference of metal ions on the stripping peak current of $Cd^{2+}$ detection. The dark blue columns represent the $I_{Cd}/I_{Cd+M}$, being M the different metal ions tested

As can be seen in Figure 4.52, the metal ions analyzed, had little influence on the signals, except for $Pb^{2+}$, that showed a significant interference on the $Cd^{2+}$ detection. This effect can appear due to their close standard reduction potentials, and it is noticeable even using the synthesized CDs that should be selective to $Cd^{2+}$. This effect should be studied in more detail, however $Cd^{2+}$ could be successfully determined. Moreover, it has to be taken into account that for this experiment the concentration of $Pb^{2+}$ was 1000 times higher than the concentration of $Cd^{2+}$.

Finally, a calibration plot was performed at the previously specified optimal conditions to determine sensitivity and LOD of the studied method. The stripping voltammograms for different concentrations of $Cd^{2+}$ at MWCNT-COOH/CDs/SPCEs, as well as the calibration plot are shown in Figure 4.53.

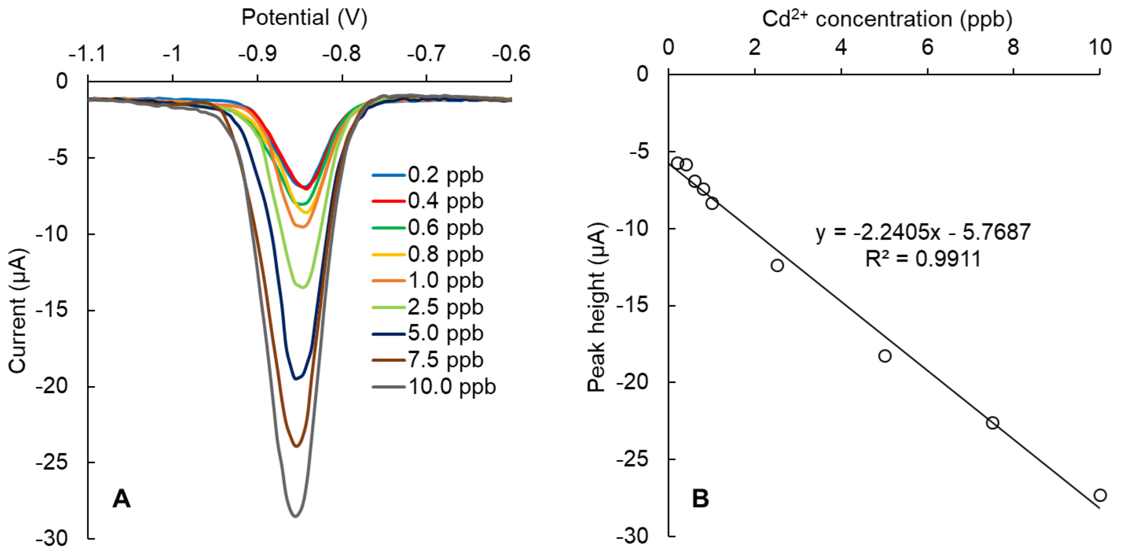

Figure 4.53: (A) Square wave stripping voltammograms for $Cd^{2+}$ increasing concentrations. (B) Calibration plot of the peak currents to the concentration of $Cd^{2+}$

The regression equation of the calibration plot obtained was: $I_p$ (μA) = -2.240 [$Cd^{2+}$] (ppb) - 5.769 ($R^2$ = 0.991). The LOD, as mentioned in Section 3.2.5, was calculated from 3SD/S (SD being the standard deviation of 1 ppb $Cd^{2+}$ measurements (n=10)). LOD was found to be 0.09 ppb, which is below the maximum concentration of cadmium in drinking water set by the EU, the US EPA and the WHO. With the obtained data, it can be concluded that the developed setup containing MWCNT-COOH/CDs modified SPCEs was capable of determining $Cd^{2+}$ with high sensitivity and with an LOD low enough to apply this system for the control of $Cd^{2+}$ in drinking water.

# 5 Conclusions and future perspectives

The results obtained along this thesis demonstrated the advantages of using nanomaterials, CDs in this case, for the improvement of analytical features in terms of sensitivity and selectivity in different techniques (fluorescence spectroscopy and voltammetry). On the other hand, it was demonstrated that miniaturization brings advantages to analytical chemistry regarding the use of chemical sensors (electrochemical and optical), as well as the use of microfluidic platforms to develop automatic multiparametric analyzers.

In a first approach, CDs were employed as optical probes taking advantage of the excellent properties that these nanomaterials present. First, different types of CDs were synthesized in batch. Five of them were used to selectively determine different heavy metal ions ($Co^{2+}$, $Cu^{2+}$, $Hg^{2+}$, $Ni^{2+}$, and $Pb^{2+}$). Spiked tap water samples and extracts of soil samples (that did not contain $Hg^{2+}$) were analyzed using an optimized multiparametric µTAS. In the case of the extracts of soil samples, the microanalyzer performance was compared with a reference method (ICP-OES) showing that the proposed approach could be used for the determination of heavy metals with accuracy and precision. Moreover, detection limits were below the limits set in drinking water except for $Hg^{2+}$, so we can conclude that the microanalyzer developed could be used as a reliable warning system for heavy metals monitoring in water.

Some advantages to remark of this developed system are related to the reduced dimensions of the COC microfluidic platform and the fluidic system. For instance, the consumption of reagents, the production of wastes and the analysis time, which were greatly reduced. The use of a rFIA protocol also diminished the volume of CDs needed. However, the synthesis processes performed were time-consuming and the control over reaction variables like temperature and pressure was very poor.

In this sense, microreactor technology brought some advantages like the easy automation of the synthetic processes and the enhanced temperature and mass transfer, enabling a better control of the synthesis conditions. Thus, more homogeneous nanoparticles were obtained and the reproducibility between batches was also enhanced. The comparison between the results obtained with CDs synthesized in batch and in the LTCC microreactor showed that the homogeneity of CDs sizes improved with the microreactor, and QYs increased due to the formation of more quantity of amorphous polymer dots. Sensitivity was also slightly enhanced, which could be the result of the presence of more fluorescence moieties capable of interacting with the heavy metal ions.

Four of the five synthesis protocols previously followed, were adapted to the synthesis in the LTCC microreactors. The results obtained showed good selectivity of the synthesized nanomaterials, with which it was possible to determine four different heavy metal ions ($Co^{2+}$, $Cu^{2+}$, $Hg^{2+}$, and $Pb^{2+}$). As in the case of the CDs synthesized in batch, except for $Hg^{2+}$ the obtained LODs were below the limits set for drinking water. To evaluate the effect of the purification of the CDs, each type of CDs synthesized in the LTCC microreactor was divided into two fractions, one that was dialyzed (D) and the other that was not (ND). The comparison of the results obtained with both fractions showed that the D fractions presented slightly higher sensitivity than the ND fractions.

Despite that, the sensitivity was high enough to state that the effect of the purification over the CDs was not critical, and they could be used directly from the synthesis. Furthermore, spiked tap water and spiked river water samples were also analyzed with the CDs synthesized in the LTCC microreactor, showing good results in terms of accuracy and precision.

Finally, to demonstrate the applicability of the microanalyzer for on-site monitoring of heavy metals in water, the goal was to couple the synthesis of CDs in the LTCC microreactor with the heavy metals analysis. As a proof of concept, ACR CDs were synthesized in the microreactor, automatically diluted, and buffered, and directly used without further purification for the selective determination of $Co^{2+}$ in the customized miniaturized optical detection system. This represents an advantage not only in terms of automation of the synthesis but also in terms of the use of a fresh optical material that has not undergone any degradation prior to analysis. Sensitivity and LOD obtained were very similar to those obtained with the ACR CDs synthesized in the separated system demonstrating the potential of the integrated automatic analyzer. Good accuracy and precision were also obtained with the spiked tap water and spiked river water samples, proving the reliability of the developed integrated microanalyzer for the analysis of water samples.

Despite the potential of the system, some future work must be conducted to finally validate the real applicability of the proposed methodology, such as long-term studies, to assess the stability of the CDs, the good performance with real river water samples that contain a lot of particles in suspension, the possible interferences associated with the presence of organic material, etc. Also, it will be necessary to compare results with a reference method and analyze certified reference materials. Further miniaturization and integration of the different modular parts could also be achieved by using computer-controlled micropumps and microvalves to perform fluidic management.

In a second approach, CDs were also used to improve the selectivity and sensitivity of SWSV to determine $Cd^{2+}$. A simple method using modified SPCEs with MWCNT-COOH, and CDs synthesized from citric acid and urea was established. In addition to assess the working electrode modification process, different experimental parameters affecting the SWSV measurements were also optimized. The effect of the presence of other metal ions showed that $Pb^{2+}$, produced a significant interference on the $Cd^{2+}$ detection, but it has to be taken into account that for this experiment the concentration of $Pb^{2+}$ was 1000 times higher than the concentration of $Cd^{2+}$. Considering this, $Cd^{2+}$ could be successfully determined with high sensitivity and a LOD below the maximum concentration of $Cd^{2+}$ permitted in drinking water.

Due to the lack of time, real samples could not be analyzed to demonstrate the real applicability of the designed methodology. Moreover, other CDs synthesized from different precursors could be synthesized to test their selectivity to other heavy metal ions or other contaminants present in water, and with this, a multiparametric system could be developed.

# 6 References

[1] Singh, P., Singh, R., Singh, V.K., & Bhadouria, R. (2021). *Pollutants and Water Management: Resources, Strategies and Scarcity* (1st ed.). Wiley Blackwell.

[2] Madhav, S., & Singh, P. (2021). *Groundwater Geochemistry: Pollution and Remediation Methods* (1st ed.). Wiley Blackwell.

[3] National Institute of Environmental Health Sciences. (2022). *Water-related Illnesses*. https://www.niehs.nih.gov/research/programs/climatechange/health_impacts/waterborne_diseases/index.cfm#:~:text=Some%20common%20water%2Drelated%20illnesses,have%20long%2Dlasting%20health%20impacts. Accessed 25 February 2023.

[4] World Health Organization. (2022). *Guidelines for drinking-water quality* (4th ed.). World Health Organization.

[5] Jaishankar, M., Tseten, T., Anbalagan, N., Mathew, B.B., & Beeregowda, K.N. (2014). Toxicity, mechanism and health effects of some heavy metals. *Interdisciplinary Toxicology, 7*(2), 60-72). https://doi.org/10.2478/intox-2014-0009

[6] Lichtfouse, E., Schwarzbauer, J., & Robert, D. (2005). *Environmental chemistry: green chemistry and pollutants in ecosystems* (1st ed.). Springer.

[7] Lace, A., & Cleary, J. (2021). A review of microfluidic detection strategies for heavy metals in water. *Chemosensors, 9*(4), 60, 1-27. https://doi.org/10.3390/chemosensors9040060

[8] Hussain, A., Priyadarshi, M., Qureshi, F., & Ahmed, S. (2021). Risk Assessment on Human Health with Effect of Heavy Metals. In: Inamuddin (Ed.), M.I. Ahamed (Ed.), R. Boddula (Ed.), & T.A. Rangreez (Ed.), *Applied Water Science Volume 1: Fundamentals and Applications* (1st ed., pp 401-419). Wiley-Scrivener.

[9] Sharma, A., Grewal, A.S., Sharma, D., & Srivastav, A.L. (2023). Heavy metal contamination in water: consequences on human health and environment. In: S.K. Shukla (Ed.), S. Kumar (Ed.), S. Madhav (Ed.), & P.K. Mishra (Ed.), *Metals in Water: Global Sources, Significance, and Treatment* (1st ed., pp 39-52). Elsevier.

[10] Witkowska, D., Słowik, J., & Chilicka, K. (2021). Heavy Metals and Human Health: Possible Exposure Pathways and the Competition for Protein Binding Sites. *Molecules, 26*(19), 6060, 1-16. https://doi.org/10.3390/molecules26196060

[11] Mohammed Abdul, K.S., Jayasinghe, S.S., Chandana, E.P.S., Jayasumana, C., & De Silva, P.M.C.S. (2015). Arsenic and human health effects: A review. *Environmental Toxicology and Pharmacology, 40*(3), 828-846. https://doi.org/10.1016/j.etap.2015.09.016

[12] Godt, J., Scheidig, F., Grosse-Siestrup, C., Esche, V., Brandenburg, P., Reich, A., & Groneberg, D.A. (2006). The toxicity of cadmium and resulting hazards for human health. *Journal of Occupational Medicine and Toxicology, 1*(22), 1-6. https://doi.org/10.1186/1745-6673-1-22

[13] Achmad, R.T., Budiawan, & Auerkari, E.I. (2017). Effects of Chromium on Human Body. *Annual Research & Review in Biology, 17*(2), 1-8. https://doi.org/10.9734/ARRB/2017/33462

[14] Alkian, I., Sutanto, H., Hadiyanto, B., Prasetio, A., & Aprimanti Utami, B. (2022). Facile synthesized carbon dots for simple and selective detection of cobalt ions in aqueous media. *Cogent Engineering, 9*(1), 2033467, 1-12. https://doi.org/10.1080/23311916.2022.2033467

[15] Kong, D., Yan, F., Han, Z., Xu, J., Guo, X., & Chen, L. (2016). Cobalt(II) ions detection using carbon dots as an sensitive and selective fluorescent probe. *RSC Advances, 6*(72), 67481-67487. https://doi.org/10.1039/c6ra12986b

[16] Uriu-Adams, J.Y., & Keen, C.L. (2005). Copper, oxidative stress, and human health. *Molecular Aspects of Medicine, 26*(4-5), 268-298. https://doi.org/10.1016/j.mam.2005.07.015

[17] Papanikolaou, G., & Pantopoulos, K. (2005). Iron metabolism and toxicity. *Toxicology and Applied Pharmacology, 202*(2), 199–211. https://doi.org/10.1016/j.taap.2004.06.021

[18] Matta, G., & Gjyli, L. (2016). Mercury, lead and arsenic: impact on environment and human health. *Journal of Chemical and Pharmaceutical Sciences, 9*(2), 718-725.

[19] Genchi, G., Carocci, A., Lauria, G., Sinicropi, M.S., & Catalano, A. (2020). Nickel: Human health and environmental toxicology. *International Journal of Environmental Research and Public Health, 17*(3), 679, 1-21. https://doi.org/10.3390/ijerph17030679

[20] Punia, P., Bharti, M.K., Dhar, R., Thakur, P., & Thakur, A. (2022). Recent Advances in Detection and Removal of Heavy Metals from Contaminated Water. *ChemBioEng Reviews, 9*(4), 351-369. https://doi.org/10.1002/cben.202100053

[21] Singh, E., Kumar, A., Mishra, R., Singh, A.K., Madhav, S., Shukla, S.K., & Kumar, S. (2023). Measurement techniques for detection of metals in water resources. In S.K. Shukla (Ed.), S. Kumar (Ed.), S. Madhav (Ed.), & P.K. Mishra (Ed.), *Metals in Water: Global Sources, Significance, and Treatment* (1st ed., pp 1-20). Elsevier.

[22] Malik, L.A., Bashir, A., Qureashi, A., & Pandith, A.H. (2019). Detection and removal of heavy metal ions: a review. *Environmental Chemistry Letters, 17*, 1495-1521. https://doi.org/10.1007/s10311-019-00891-z

[23] Wang, T., Wu, J., Hartman, R., Jia, X., & Egan, R.S. (2000). A multi-element ICP-MS survey method as an alternative to the heavy metals limit test for pharmaceutical materials. *Journal of Pharmaceutical and Biomedical Analysis, 23*(5), 867-890. https://doi.org/10.1016/s0731-7085(00)00361-7

[24] Yuan, C.G., Shi, J.B., He, B., Liu, J.F., Liang, L.N., & Jiang, G.B. (2004). Speciation of heavy metals in marine sediments from the East China Sea by ICP-MS with sequential extraction. *Environment International, 30*(6), 769-783. https://doi.org/10.1016/j.envint.2004.01.001

[25] Chand, V., & Prasad, S. (2013). ICP-OES assessment of heavy metal contamination in tropical marine sediments: A comparative study of two digestion

techniques. *Microchemical Journal, 111*, 53-61. https://doi.org/10.1016/j.microc.2012.11.007

[26] Feist, B., Mikula, B., Pytlakowska, K., Puzio, B., & Buhl, F. (2008). Determination of heavy metals by ICP-OES and F-AAS after preconcentration with 2,2′-bipyridyl and erythrosine. *Journal of Hazardous Materials, 152*(3), 1122-1129. https://doi.org/10.1016/j.jhazmat.2007.07.095

[27] Gomez, M.R., Cerutti, S., Sombra, L.L., Silva, M.F., & Martínez, L.D. (2007). Determination of heavy metals for the quality control in argentinian herbal medicines by ETAAS and ICP-OES. *Food and Chemical Toxicology, 45*(6), 1060-1064. https://doi.org/10.1016/j.fct.2006.12.013

[28] Liu, Y., & Xiong, W. (2022). Controllable synthesis of phenolic resin-based carbon nanospheres for simultaneous detection of heavy-metal ions. *Journal of Materials Science: Materials in Electronics, 33*(3), 1542-1554. https://doi.org/10.1007/s10854-021-07669-6

[29] Lu, M., Deng, Y., Luo, Y., Lv, J., Li, T., Xu, J., Chen, S.W., & Wang, J. (2019). Graphene Aerogel-Metal-Organic Framework-Based Electrochemical Method for Simultaneous Detection of Multiple Heavy-Metal Ions. *Analytical Chemistry, 91*(1), 888-895. https://doi.org/10.1021/acs.analchem.8b03764

[30] Shi, H., Zhu, F., Zhou, X., Li, H., Yang, F., Zhang, X., & Liu, J. (2019). Large scale fabrication of disposable carbon cloth electrochemical sensors for simultaneous determination of heavy metal ion. *Journal of Electroanalytical Chemistry, 840*, 328-337. https://doi.org/10.1016/j.jelechem.2019.04.001

[31] Xu, Z., Liu, Z., Xiao, M., Jiang, L., & Yi, C. (2020). A smartphone-based quantitative point-of-care testing (POCT) system for simultaneous detection of multiple heavy metal ions. Chemical Engineering Journal, 394, 124966, 1-9. https://doi.org/10.1016/j.cej.2020.124966

[32] Tan, Z., Wu, W., Feng, C., Wu, H., & Zhang, Z. (2020). Simultaneous determination of heavy metals by an electrochemical method based on a nanocomposite consisting of fluorinated graphene and gold nanocage. *Microchimica Acta, 187*(7), 414, 1-9. https://doi.org/10.1007/s00604-020-04393-6

[33] Zhang, X., An, D., Bi, Z., Shan, W., Zhu, B., Zhou, L., Yu, L., Zhang, H., Xia, S., & Qiu, M. (2022). Ti3C2-MXene@N-doped carbon heterostructure-based electrochemical sensor for simultaneous detection of heavy metals. *Journal of Electroanalytical Chemistry, 911*, 116239, 1-12. https://doi.org/10.1016/j.jelechem.2022.116239

[34] Zhao, D., Guo, X., Wang, T., Alvarez, N., Shanov, V.N., & Heineman, W.R. (2014). Simultaneous Detection of Heavy Metals by Anodic Stripping Voltammetry Using Carbon Nanotube Thread. *Electroanalysis, 26*(3), 488-496. https://doi.org/10.1002/elan.201300511

[35] Youngvises, N., Suwannasaroj, K., Jakmunee, J., & AlSuhaimi, A. (2017). Multi-reverse flow injection analysis integrated with multi-optical sensor for simultaneous determination of Mn(II), Fe(II), Cu(II) and Fe(III) in natural waters. *Talanta, 166*, 369-374. https://doi.org/10.1016/j.talanta.2016.01.052

[36] Páscoa, R.N.M.J., Tóth, I.V., & Rangel, A.O.S.S. (2011). Spectrophotometric determination of zinc and copper in a multi-syringe flow injection analysis system using a liquid waveguide capillary cell: Application to natural waters. *Talanta, 84*(5), 1267-1272. https://doi.org/10.1016/j.talanta.2011.01.023

[37] Chowdhury, S., Rooj, B., Dutta, A., & Mandal, U. (2018). Review on Recent Advances in Metal Ions Sensing Using Different Fluorescent Probes. *Journal of Fluorescence, 28*(4), 999-1021. https://doi.org/10.1007/s10895-018-2263-y

[38] He, X., Jia, K., Bai, Y., Chen, Z., Liu, Y., Huang, Y., & Liu, X. (2021). Quantum dots encoded white-emitting polymeric superparticles for simultaneous detection of multiple heavy metal ions. *Journal of Hazardous Materials, 405*, 124263, 1-11. https://doi.org/10.1016/j.jhazmat.2020.124263

[39] Felix, F.S., & Angnes, L. (2015). Flow-Injection Analysis with Electrochemical Detection. In: A. Escarpa (Ed.), M.C. González (Ed.), & M.A. López (Ed.), *Agricultural and Food Electroanalysis* (1st ed., pp 49-72). Wiley Blackwell.

[40] Martínez, L.D., Cerutti, S., & Gil, R.A. (2012). Green Analytical Chemistry and Flow Injection Methodologies. In: M. de la Guardia (Ed.), & S. Garrigues (Ed.), *Handbook of Green Analytical Chemistry* (1st ed., pp 321-338). Wiley. https://doi.org/10.1002/9781119940722.ch16

[41] Ružička, J., Hansen E.H. (1975). Flow injection analyses: Part I. A new concept of fast continuous flow analysis. *Analytica Chimica Acta, 78*(1), 145-157. https://doi.org/10.1016/S0003-2670(01)84761-9

[42] Trojanowicz, M., & Kołacińska, K. (2016). Recent advances in flow injection analysis. *Analyst, 141*(7), 2085-2139. https://doi.org/10.1039/c5an02522b

[43] Mansour, F.R., & Danielson, N.D. (2012). Reverse flow-injection analysis. *TrAC - Trends in Analytical Chemistry, 40*, 1-14. https://doi.org/10.1016/j.trac.2012.06.006

[44] Feng, S., Zhang, M., Huang, Y., Yuan, D., & Zhu, Y. (2013). Simultaneous determination of nanomolar nitrite and nitrate in seawater using reverse flow injection analysis coupled with a long path length liquid waveguide capillary cell. *Talanta, 117*, 456-462. https://doi.org/10.1016/j.talanta.2013.09.042

[45] Lin, K., Li, P., Wu, Q., Feng, S., Ma, J., & Yuan, D. (2018). Automated determination of ammonium in natural waters with reverse flow injection analysis based on the indophenol blue method with o-phenylphenol. *Microchemical Journal, 138*, 519-525. https://doi.org/10.1016/j.microc.2018.02.004

[46] Bezerra, M.A., Santelli, R.E., Lemos, V.A., dos Santos Alves, J.P., Braz, B.F., & Santos, L.B. (2020). Strategies to Make Methods Based on Flow Injection Analysis Greener. *Clean - Soil, Air, Water, 48*(7-8), 2000007, 1-11. https://doi.org/10.1002/clen.202000007

[47] Huang, Y., Yuan, D., Dai, M., & Liu, Y. (2012). Reverse flow injection analysis method for catalytic spectrophotometric determination of iron in estuarine and coastal waters: A comparison with normal flow injection analysis. *Talanta, 93*, 86-93. https://doi.org/10.1016/j.talanta.2012.01.050

[48] Manz, A., Graber, N., & Widmer, H.M. (1990). Miniaturized total chemical analysis systems: A novel concept for chemical sensing. *Sensors and Actuators B: Chemical, 1*(1-6), 244-248. https://doi.org/10.1016/0925-4005(90)80209-I

[49] Lin, B. (2011). *Microfluidics Technologies and Applications* (1st ed.). Springer.

[50] Pfaffl, M.W. (2023). *Lab on Chip PCR (1)*. https://www.gene-quantification.de/lab-on-chip.html

[51] Dincer, C., Bruch, R., Costa-Rama, E., Fernández-Abedul, M.T., Merkoçi, A., Manz, A., Urban, G.A., & Güder, F. (2019). Disposable Sensors in Diagnostics, Food, and Environmental Monitoring. *Advanced Materials, 31*(30), 1806739, 1-28. https://doi.org/10.1002/adma.201806739

[52] Shang, Y., Xiang, X., Ye, Q., Wu, Q., Zhang, J., & Lin, J.M. (2022). Advances in nanomaterial-based microfluidic platforms for on-site detection of foodborne bacteria. *TrAC - Trends in Analytical Chemistry, 147*, 116509, 1-20. https://doi.org/10.1016/j.trac.2021.116509

[53] Auroux, P.A., Iossifidis, D., Reyes, D.R., & Manz, A. (2002). Micro total analysis systems. 2. Analytical standard operations and applications. *Analytical Chemistry, 74*(12), 2637-2652). https://doi.org/10.1021/ac020239t

[54] Afsaneh, H., & Mohammadi, R. (2022). Microfluidic platforms for the manipulation of cells and particles. *Talanta Open, 5*, 100092, 1-14. https://doi.org/10.1016/j.talo.2022.100092

[55] Coluccio, M.L., Perozziello, G., Malara, N., Parrotta, E., Zhang, P., Gentile, F., Limongi, T., Raj, P.M., Cuda, G., Candeloro, P., & Di Fabrizio, E. (2019). Microfluidic platforms for cell cultures and investigations. *Microelectronic Engineering, 208*, 14-28. https://doi.org/10.1016/j.mee.2019.01.004

[56] Xiong, B., Ren, K., Shu, Y., Chen, Y., Shen, B., & Wu, H. (2014). Recent developments in microfluidics for cell studies. *Advanced Materials, 26*(31), 5525-5532. https://doi.org/10.1002/adma.201305348

[57] Schuster, B., Junkin, M., Kashaf, S.S., Romero-Calvo, I., Kirby, K., Matthews, J., Weber, C.R., Rzhetsky, A., White, K.P., & Tay, S. (2020). Automated microfluidic platform for dynamic and combinatorial drug screening of tumor organoids. *Nature Communications, 11*(1), 5271, 1-12. https://doi.org/10.1038/s41467-020-19058-4

[58] Tomazelli Coltro, W.K., Cheng, C.M., Carrilho, E., & de Jesus, D.P. (2014). Recent advances in low-cost microfluidic platforms for diagnostic applications. *Electrophoresis, 35*(16), 2309-2324. https://doi.org/10.1002/elps.201400006

[59] Chassaing, P. (2022). *Fundamentals of Fluid Mechanics* (1st ed.). Springer.

[60] Kakaç, S., Kosoy, B., & Li, D. (2010). *Microfluidics Based Microsystems: Fundamentals and Applications* (1st ed.). Springer.

[61] The Constructor. (2021). *Laminar Flow and Turbulent Flow*. https://theconstructor.org/fluid-mechanics/laminar-turbulent-flow/559432/. Accessed 3 March 2023.

[62] Janasek, D., Franzke, J., & Manz, A. (2006). Scaling and the design of miniaturized chemical-analysis systems. *Nature, 442*(7101), 374-380. https://doi.org/10.1038/nature05059

[63] Ríos, A., Escarpa, A., & Simonet, B. (2009). *Miniaturization of Analytical Systems: Principles, Designs and Applications* (1st ed.). Wiley.

[64] Dyer, O.T., & Ball, R.C. (2021). Influence of thermal fluctuations on active diffusion at large Péclet numbers. *Physics of Fluids, 33*(5), 051904, 1-14. https://doi.org/10.1063/5.0049386

[65] Shamshuddin, M.D., Mabood, F., Khan, W.A., & Rajput, G.R. (2023). Exploration of thermal Péclet number, vortex viscosity, and Reynolds number on two-dimensional flow of micropolar fluid through a channel due to mixed convection. *Heat Transfer, 52*(1), 854-873. https://doi.org/10.1002/htj.22719

[66] Haeberle, S., & Zengerle, R. (2007). Microfluidic platforms for lab-on-a-chip applications. *Lab on a Chip, 7*(9), 1094-1110. https://doi.org/10.1039/b706364b

[67] Lynn, N.S., & Dandy, D.S. (2009). Passive microfluidic pumping using coupled capillary/evaporation effects. *Lab on a Chip, 9*(23), 3422-3429. https://doi.org/10.1039/b912213c

[68] Mark, D., Haeberle, S., Roth, G., von Stetten, F., & Zengerle, R. (2010). Microfluidic lab-on-a-chip platforms: Requirements, characteristics and applications. *Chemical Society Reviews, 39*(3), 1153-1182. https://doi.org/10.1039/b820557b

[69] Oh, K.W., Lee, K., Ahn, B., & Furlani, E.P. (2012). Design of pressure-driven microfluidic networks using electric circuit analogy. Lab on a Chip, 12(3), 515-545. https://doi.org/10.1039/c2lc20799k

[70] Strohmeier, O., Keller, M., Schwemmer, F., Zehnle, S., Mark, D., von Stetten, F., Zengerle, R., & Paust, N. (2015). Centrifugal microfluidic platforms: advanced unit operations and applications. *Chemical Society Reviews, 44*(17), 6187-6229. https://doi.org/10.1039/c4cs00371c

[71] Gomez-Quiñones, J., Moncada-Hernandez, H., Rossetto, O., Martinez-Duarte, R., Lapizco-Encinas, B.H., Madou, M., & Martinez-Chapa, S.O. (2011). An application specific multi-channel stimulator for electrokinetically-driven microfluidic devices. *IEEE 9th International New Circuits and Systems Conference, NEWCAS 2011*, 350-353. https://doi.org/10.1109/NEWCAS.2011.5981242

[72] Sonker, M., Knob, R., Sahore, V., & Woolley, A.T. (2017). Integrated electrokinetically driven microfluidic devices with pH-mediated solid-phase extraction coupled to microchip electrophoresis for preterm birth biomarkers. *Electrophoresis, 38*(13-14), 1743-1754. https://doi.org/10.1002/elps.201700054

[73] Guttenberg, Z., Müller, H., Habermüller, H., Geisbauer, A., Pipper, J., Felbel, J., Kielpinski, M., Scriba, J., & Wixforth, A. (2005). Planar chip device for PCR and hybridization with surface acoustic wave pump. *Lab on a Chip, 5*(3), 308-317. https://doi.org/10.1039/b412712a

[74] Whitesides, G.M., & Stroock, A.D. (2001). Flexible methods for microfluidics. *Physics Today, 54*(6), 42-48. https://doi.org/10.1063/1.1387591

[75] Hessel, V., Löwe, H., & Schönfeld, F. (2005). Micromixers - A review on passive and active mixing principles. *Chemical Engineering Science, 60*(8-9), 2479-2501. https://doi.org/10.1016/j.ces.2004.11.033

[76] Nguyen, N.T., & Wu, Z. (2005). Micromixers - A review. *Journal of Micromechanics and Microengineering, 15*(2), 1-16. https://doi.org/10.1088/0960-1317/15/2/R01

[77] Kotz, K.T., Noble, K.A., & Faris, G.W. (2004). Optical microfluidics. *Applied Physics Letters, 85*(13), 2658-2660. https://doi.org/10.1063/1.1797538

[78] Arora, A., Simone, G., Salieb-Beugelaar, G.B., Kim, J.T., & Manz, A. (2010). Latest developments in micro total analysis systems. *Analytical Chemistry, 82*(12), 4830-4847. https://doi.org/10.1021/ac100969k

[79] Raj, A., Suthanthiraraj, P.P.A., & Sen, A.K. (2018). Pressure-driven flow through PDMS-based flexible microchannels and their applications in microfluidics. *Microfluidics and Nanofluidics, 22*(11), 128, 1-25. https://doi.org/10.1007/s10404-018-2150-5

[80] Brennan, M.D., Rexius-Hall, M.L., Elgass, L.J., & Eddington, D.T. (2014). Oxygen control with microfluidics. *Lab on a Chip, 14*(22), 4305-4318. https://doi.org/10.1039/c4lc00853g

[81] Perez-Toralla, K., Champ, J., Mohamadi, M.R., Braun, O., Malaquin, L., Viovy, J.L., & Descroix, S. (2013). New non-covalent strategies for stable surface treatment of thermoplastic chips. *Lab on a Chip, 13*(22), 4409-4418. https://doi.org/10.1039/c3lc50888a

[82] Franssila, S. (2004). *Introduction to Microfabrication* (2nd ed.). Wiley.

[83] Becker, H., & Gärtner, C. (2008). Polymer microfabrication technologies for microfluidic systems. *Analytical and Bioanalytical Chemistry, 390*(1), 89-111. https://doi.org/10.1007/s00216-007-1692-2

[84] Damodara, S., Shahriari, S., Wu, W.I., Rezai, P., Hsu, H.H., & Selvaganapathy, R. (2021). Materials and methods for microfabrication of microfluidic devices. In: X.J. Li (Ed.), & Y. Zhou (Ed.), Microfluidic Devices for Biomedical Applications (2nd ed., pp 1-78). Woodhead Publishing.

[85] Rötting, O., Röpke, W., Becker, H., & Gärtner, C. (2002). Polymer microfabrication technologies. *Microsystem Technologies, 8*(1), 32-36. https://doi.org/10.1007/s00542-002-0106-9

[86] Mohammadzadeh, A., Fox-Robichaud, A.E., & Selvaganapathy, P.R. (2019). Rapid and inexpensive method for fabrication of multi-material multi-layer microfluidic devices. Journal of Micromechanics and Microengineering, 29(1), 015013. https://doi.org/10.1088/1361-6439/aaf25a

[87] Shin, J.U.Y., Park, J.I.Y., Liu, C., He, J., & Kim, S.C. (2005). Chemical structure and physical properties of cyclic olefin copolymers. *Pure and Applied Chemistry, 77*(5), 801-814. https://doi.org/10.1351/pac200577050801

[88] Lamonte, R.R., & McNally, D. (2001). Cyclic Olefin Copolymers. *Advanced Materials and Processes, 159*(3), 33-36.

[89] Bruijns, B., Veciana, A., Tiggelaar, R., & Gardeniers, H. (2019). Cyclic olefin copolymer microfluidic devices for forensic applications. *Biosensors, 9*(3), 85, 1-14. https://doi.org/10.3390/bios9030085

[90] Agha, A., Waheed, W., Alamoodi, N., Mathew, B., Alnaimat, F., Abu-Nada, E., Abderrahmane, A., & Alazzam, A. (2022). A Review of Cyclic Olefin Copolymer Applications in Microfluidics and Microdevices. Macromolecular Materials and Engineering, 307(8), 2200053, 1-34. https://doi.org/10.1002/mame.202200053

[91] Ben Azouz, A., Murphy, S., Karazi, S., Vázquez, M., & Brabazon, D. (2014). Fast Fabrication Process of Microfluidic Devices Based on Cyclic Olefin Copolymer. Materials and Manufacturing Processes, 29(2), 93-99. https://doi.org/10.1080/10426914.2013.811739

[92] Jena, R.K., Yue, C.Y., & Lam, Y.C. (2012). Micro fabrication of cyclic olefin copolymer (COC) based microfluidic devices. *Microsystem Technologies, 18*(2), 159-166. https://doi.org/10.1007/s00542-011-1366-z

[93] Steigert, J., Haeberle, S., Brenner, T., Müller, C., Steinert, C.P., Koltay, P., Gottschlich, N., Reinecke, H., Rühe, J., Zengerle, R., & Ducrée, J. (2007). Rapid prototyping of microfluidic chips in COC. *Journal of Micromechanics and Microengineering, 17*(2), 333-341. https://doi.org/10.1088/0960-1317/17/2/020

[94] Denz, M., Brehm, G., Hémonnot, C.Y.J., Spears, H., Wittmeier, A., Cassini, C., Saldanha, O., Perego, E., Diaz, A., Burghammer, M., & Köster, S. (2018). Cyclic olefin copolymer as an X-ray compatible material for microfluidic devices. *Lab on a Chip, 18*(1), 171-178. https://doi.org/10.1039/c7lc00824d

[95] Li, H., Chen, H., Chen, H., Yan, M., Xue, Q., & Che, W. (2022). Implementation of cyclic olefin copolymer-based microwave circuit and the performance comparison. *Microwave and Optical Technology Letters, 64*(3), 515-519. https://doi.org/10.1002/mop.33153

[96] Fink, J.K. (2010). *Handbook of Engineering and Speciality Thermoplastics* (1st ed.). Wiley-Scrivener.

[97] Imanaka, Y. (2005). *Multilayered Low Temperature Cofired Ceramics (LTCC) Technology* (1st ed.). Springer.

[98] Sebastian, M.T., & Jantunen, H. (2017). High Temperature Cofired Ceramic (HTCC), Low Temperature Cofired Ceramic (LTCC), and Ultralow Temperature Cofired Ceramic (ULTCC) Materials. In: M.T. Sebastian (Ed.), R. Ubic (Ed.), H. Jantunen (Ed.), *Microwave Materials and Applications* (1st ed., pp 355-425). Wiley.

[99] Zhou, J. (2012). Towards rational design of low-temperature co-fired ceramic (LTCC) materials. *Journal of Advanced Ceramics, 1*(2), 89-99. https://doi.org/10.1007/s40145-012-0011-3

[100] Ibanez-Garcia, N., Mercader, M.B., Mendes Da Rocha, Z., Seabra, C.A., Góngora-Rubio, M.R., & Alonso-Chamarro, J. (2006). Continuous flow analytical

microsystems based on low-temperature co-fired ceramic technology. Integrated potentiometric detection based on solvent polymeric ion-selective electrodes. *Analytical Chemistry, 78*(9), 2985-2992. https://doi.org/10.1021/ac051994k

[101] Ibañez-Garcia, N., Gonçalves, R.D.M., da Rocha, Z.M., Góngora-Rubio, M.R., Seabra, A.C., & Alonso-Chamarro, J. (2006). LTCC meso-analytical system for chloride ion determination in drinking waters. *Sensors and Actuators B: Chemical, 118*(1-2), 67-72. https://doi.org/10.1016/j.snb.2006.04.063

[102] Jurków, D., Maeder, T., Dąbrowski, A., Zarnik, M.S., Belavič, D., Bartsch, H., & Müller, J. (2015). Overview on low temperature co-fired ceramic sensors. *Sensors and Actuators A: Physical, 233*, 125-146. https://doi.org/10.1016/j.sna.2015.05.023

[103] Couceiro, P., Gómez-de Pedro, S., & Alonso-Chamarro, J. (2015). All-ceramic analytical microsystems with monolithically integrated optical detection microflow cells. *Microfluidics and Nanofluidics, 18*(4), 649-656. https://doi.org/10.1007/s10404-014-1463-2

[104] Couceiro, P., & Alonso-Chamarro, J. (2017). Microfabrication of Monolithic Microfluidic Platforms Using Low Temperature Co-Fired Ceramics Suitable for Fluorescence Imaging. *Analytical Chemistry, 89*(17), 9147-9153. https://doi.org/10.1021/acs.analchem.7b01889

[105] Vasudev, A., Kaushik, A., Jones, K., & Bhansali, S. (2013). Prospects of low temperature co-fired ceramic (LTCC) based microfluidic systems for point-of-care biosensing and environmental sensing. *Microfluidics and Nanofluidics, 14*(3-4), 683-702). https://doi.org/10.1007/s10404-012-1087-3

[106] Almeida, S.A.A., Arasa, E., Puyol, M., Martinez-Cisneros, C.S., Alonso-Chamarro, J., Montenegro, M.C.B.S.M., & Sales, M.G.F. (2011). Novel LTCC-potentiometric microfluidic device for biparametric analysis of organic compounds carrying plastic antibodies as ionophores: Application to sulfamethoxazole and trimethoprim. *Biosensors and Bioelectronics, 30*(1), 197-203. https://doi.org/10.1016/j.bios.2011.09.011

[107] Gómez-De Pedro, S., Puyol, M., & Alonso-Chamarro, J. (2010). Continuous flow synthesis of nanoparticles using ceramic microfluidic devices. *Nanotechnology, 21*(41), 415603. https://doi.org/10.1088/0957-4484/21/41/415603

[108] Llopis, X., Ibáñez-García, N., Alegret, S., & Alonso, J. (2007). Pesticide determination by enzymatic inhibition and amperometric detection in a low-temperature cofired ceramics microsystem. *Analytical Chemistry, 79*(10), 3662-3666. https://doi.org/10.1021/ac062390z

[109] Ibáñez-García, N., Martínez-Cisneros, C.S., Valdés, F., & Alonso, J. (2008). Green-tape ceramics. New technological approach for integrating electronics and fluidics in microsystems. *TrAC - Trends in Analytical Chemistry, 27*(1), 24-33. https://doi.org/10.1016/j.trac.2007.11.002

[110] Martínez-Cisneros, C.S., Ibáñez-García, N., Valdés, F., & Alonso, J. (2007). LTCC microflow analyzers with monolithic integration of thermal control. *Sensors and Actuators A: Physical, 138*(1), 63-70. https://doi.org/10.1016/j.sna.2007.04.059

[111] Thelemann, T., Thust, H., & Hintz, M. (2002). Using LTCC for microsystems. *Microelectronics International, 19*(3), 19-23. https://doi.org/10.1108/13565360210445505

[112] Bhushan, B. (2010). *Springer Handbook of Nanotechnology* (3rd ed.). Springer.

[113] Kanchi, S. (2014). Nanotechnology for Water Treatment. *International Journal of Environmental Analytical Chemistry, 1*(2), 1-3. https://doi.org/10.4172/jreac.1000e102

[114] Passos, M.L.C., Pinto, P.C.A.G., Santos, J.L.M., Saraiva, M.L.M.F.S., & Araujo, A.R.T.S. (2015). Nanoparticle-based assays in automated flow systems: A review. *Analytica Chimica Acta, 889*, 22-34. https://doi.org/10.1016/j.aca.2015.05.052

[115] Valcárcel, M., Simonet, B.M., & Cárdenas, S. (2008). Analytical nanoscience and nanotechnology today and tomorrow. *Analytical and Bioanalytical Chemistry, 391*(5), 1881-1887. https://doi.org/10.1007/s00216-008-2130-9

[116] De Mello Donegá, C. (2014). *Nanoparticles: Workhorses of nanoscience* (1st ed.). Springer.

[117] Hussain, C.M., & Kharisov, B. (2017). *Advanced Environmental Analysis: Applications of Nanomaterials* (1st ed.). The Royal Society of Chemistry.

[118] WichLab. (2022). *Size-comparison-Bio-nanoparticles nanometer scale comparison nanoparticle size comparison nanotechnology chart ruler*. https://www.wichlab.com/nanometer-scale-comparison-nanoparticle-size-comparison-nanotechnology-chart-ruler-2/. Accessed 11 March 2023.

[119] Zeng, S., Baillargeat, D., Ho, H.P., & Yong, K.T. (2014). Nanomaterials enhanced surface plasmon resonance for biological and chemical sensing applications. *Chemical Society Reviews, 43*(10), 3426-3452). https://doi.org/10.1039/c3cs60479a

[120] Bahru, T.B., & Ajebe, E.G. (2019). A Review on Nanotechnology: Analytical Techniques Use and Applications. *International Research Journal of Pure and Applied Chemistry, 19*(4), 1-10. https://doi.org/10.9734/irjpac/2019/v19i430117

[121] Alegret, S. (1995). *Els Sensors químics: un nou concepte en instrumentació analítica* (1st ed.). Institut d'Estudis Catalans.

[122] Alegret, S. (2003). *Integrated Analytical Systems* (1st ed.). Elsevier.

[123] Galán-Vidal, C.A., Muñoz, J., Domínguez, C., Alegret, S. (1995). Chemical sensors, biosensors and thick-film technology. TrAC - Trends in Analytical Chemistry, 14(5), 225-231. https://doi.org/10.1016/0165-9936(95)91375-3

[124] Gründler, P. (2007). Chemical sensors: An introduction for scientists and engineers (1st ed.). Springer.

[125] Gómez-de Pedro, S. (2014). (Bio)analytical Microsystems based on the use of Nanoparticles. Microreactors for the Synthesis of Nanoparticles [Doctoral Thesis, Universitat Autònoma de Barcelona].

[126] Ding, Q., Li, C., Wang, H., Xu, C., & Kuang, H. (2021). Electrochemical detection of heavy metal ions in water. *Chemical Communications, 57*(59), 7215-7231. https://doi.org/10.1039/d1cc00983d

[127] Luo, X., Morrin, A., Killard, A.J., & Smyth, M.R. (2006). Application of nanoparticles in electrochemical sensors and biosensors. *Electroanalysis, 18*(4), 319-326. https://doi.org/10.1002/elan.200503415

[128] Sawan, S., Maalouf, R., Errachid, A., & Jaffrezic-Renault, N. (2020). Metal and metal oxide nanoparticles in the voltammetric detection of heavy metals: A review. *TrAC - Trends in Analytical Chemistry, 131*, 116014, 1-17. https://doi.org/10.1016/j.trac.2020.116014

[129] Welch, C.M., & Compton, R.G. (2006). The use of nanoparticles in electroanalysis: A review. *Analytical and Bioanalytical Chemistry, 384*(3), 601-619. https://doi.org/10.1007/s00216-005-0230-3

[130] Zhang, G. (2013). Functional gold nanoparticles for sensing applications. *Nanotechnology Reviews, 2*(3), 269-288. https://doi.org/10.1515/ntrev-2012-0088

[131] Liu, H., Wang, D., Song, Z., & Shang, S. (2011). Preparation of silver nanoparticles on cellulose nanocrystals and the application in electrochemical detection of DNA hybridization. *Cellulose, 18*(1), 67-74. https://doi.org/10.1007/s10570-010-9464-0

[132] Sepunaru, L., Plowman, B.J., Sokolov, S.V., Young, N.P., & Compton, R.G. (2016). Rapid electrochemical detection of single influenza viruses tagged with silver nanoparticles. *Chemical Science, 7*(6), 3892-3899. https://doi.org/10.1039/c6sc00412a

[133] Gloag, L., Mehdipour, M., Chen, D., Tilley, R.D., & Gooding, J.J. (2019). Advances in the Application of Magnetic Nanoparticles for Sensing. *Advanced Materials, 31*(48), 1904385, 1-26. https://doi.org/10.1002/adma.201904385

[134] Radhakrishnan, S., Krishnamoorthy, K., Sekar, C., Wilson, J., & Kim, S.J. (2014). A highly sensitive electrochemical sensor for nitrite detection based on $Fe_2O_3$ nanoparticles decorated reduced graphene oxide nanosheets. *Applied Catalysis B: Environmental, 148-149*, 22-28. https://doi.org/10.1016/j.apcatb.2013.10.044

[135] Asadian, E., Ghalkhani, M., & Shahrokhian, S. (2019). Electrochemical sensing based on carbon nanoparticles: A review. *Sensors and Actuators B: Chemical, 293*, 183-209. https://doi.org/10.1016/j.snb.2019.04.075

[136] Li, Y., Wang, Z., Sun, L., Liu, L., Xu, C., & Kuang, H. (2019). Nanoparticle-based sensors for food contaminants. *TrAC - Trends in Analytical Chemistry 113*, 74-83. Elsevier B.V. https://doi.org/10.1016/j.trac.2019.01.012

[137] Chah, S., Hammond, M.R., & Zare, R.N. (2005). Gold nanoparticles as a colorimetric sensor for protein conformational changes. *Chemistry and Biology, 12*(3), 323-328. https://doi.org/10.1016/j.chembiol.2005.01.013

[138] Lee, K.S., & El-Sayed, M.A. (2006). Gold and silver nanoparticles in sensing and imaging: Sensitivity of plasmon response to size, shape, and metal composition. *Journal of Physical Chemistry B, 110*(39), 19220-19225. https://doi.org/10.1021/jp062536y

[139] Medley, C.D., Smith, J.E., Tang, Z., Wu, Y., Bamrungsap, S., & Tan, W. (2008). Gold nanoparticle-based colorimetric assay for the direct detection of cancerous cells. *Analytical Chemistry, 80*(4), 1067-1072. https://doi.org/10.1021/ac702037y

[140] Prosposito, P., Burratti, L., & Venditti, I. (2020). Silver nanoparticles as colorimetric sensors for water pollutants. *Chemosensors, 8*(2), 26, 1-29. https://doi.org/10.3390/CHEMOSENSORS8020026

[141] Kailasa, S.K., Koduru, J.R., Desai, M.L., Park, T.J., Singhal, R.K., & Basu, H. (2018). Recent progress on surface chemistry of plasmonic metal nanoparticles for colorimetric assay of drugs in pharmaceutical and biological samples. *TrAC - Trends in Analytical Chemistry, 105*, 106-120. https://doi.org/10.1016/j.trac.2018.05.004

[142] Sabela, M., Balme, S., Bechelany, M., Janot, J.M., & Bisetty, K. (2017). A Review of Gold and Silver Nanoparticle-Based Colorimetric Sensing Assays. *Advanced Engineering Materials, 19*(12), 1700270, 1-24. https://doi.org/10.1002/adem.201700270

[143] Bigdeli, A., Ghasemi, F., Golmohammadi, H., Abbasi-Moayed, S., Nejad, M.A.F., Fahimi-Kashani, N., Jafarinejad, S., Shahrajabian, M., & Hormozi-Nezhad, M.R. (2017). Nanoparticle-based optical sensor arrays. *Nanoscale, 9*(43), 16546-16563. https://doi.org/10.1039/c7nr03311g

[144] Liu, D., Wang, Z., & Jiang, X. (2011). Gold nanoparticles for the colorimetric and fluorescent detection of ions and small organic molecules. *Nanoscale, 3*(4), 1421-1433. https://doi.org/10.1039/c0nr00887g

[145] Kumar Thiyagarajan, S., Raghupathy, S., Palanivel, D., Raji, K., & Ramamurthy, P. (2016). Fluorescent carbon nano dots from lignite: Unveiling the impeccable evidence for quantum confinement. *Physical Chemistry Chemical Physics, 18*(17), 12065-12073. https://doi.org/10.1039/c6cp00867d

[146] Zhu, S., Song, Y., Wang, J., Wan, H., Zhang, Y., Ning, Y., & Yang, B. (2017). Photoluminescence mechanism in graphene quantum dots: Quantum confinement effect and surface/edge state. *Nano Today, 13*, 10-14. https://doi.org/10.1016/j.nantod.2016.12.006

[147] Reisch, A., & Klymchenko, A.S. (2016). Fluorescent Polymer Nanoparticles Based on Dyes: Seeking Brighter Tools for Bioimaging. *Small, 12*(15), 1968-1992. https://doi.org/10.1002/smll.201503396

[148] Emam, A.N., Loutfy, S.A., Mostafa, A.A., Awad, H., & Mohamed, M.B. (2017). Cyto-toxicity, biocompatibility and cellular response of carbon dots-plasmonic based nano-hybrids for bioimaging. *RSC Advances, 7*(38), 23502-23514. https://doi.org/10.1039/c7ra01423f

[149] Kaur, A., & Dhakal, S. (2020). Recent applications of FRET-based multiplexed techniques. *TrAC - Trends in Analytical Chemistry, 123*, 115777, 1-10. https://doi.org/10.1016/j.trac.2019.115777

[150] Ouyang, Q., Yang, Y., Ali, S., Wang, L., Li, H., & Chen, Q. (2021). Upconversion nanoparticles-based FRET system for sensitive detection of Staphylococcus aureus.

Spectrochimica Acta Part A: Molecular and Biomolecular Spectroscopy, 255, 119734, 1-9. https://doi.org/10.1016/j.saa.2021.119734

[151] Suárez, P.L., García-Cortés, M., Fernández-Argüelles, M.T., Encinar, J.R., Valledor, M., Ferrero, F.J., Campo, J.C., & Costa-Fernández, J.M. (2019). Functionalized phosphorescent nanoparticles in (bio)chemical sensing and imaging - A review. *Analytica Chimica Acta, 1046*, 16-31. https://doi.org/10.1016/j.aca.2018.08.018

[152] Chen, L.Y., Wang, C.W., Yuan, Z., & Chang, H.T. (2015). Fluorescent gold nanoclusters: Recent advances in sensing and imaging. *Analytical Chemistry, 87*(1), 216-229. https://doi.org/10.1021/ac503636j

[153] Coto-García, A.M., Sotelo-González, E., Fernández-Argüelles, M.T., Pereiro, R., Costa-Fernández, J.M., & Sanz-Medel, A. (2011). Nanoparticles as fluorescent labels for optical imaging and sensing in genomics and proteomics. *Analytical and Bioanalytical Chemistry, 399*(1), 29-42. https://doi.org/10.1007/s00216-010-4330-3

[154] Elevathoor Vikraman, A., Rosin Jose, A., Jacob, M., & Girish Kumar, K. (2015). Thioglycolic acid capped CdS quantum dots as a fluorescent probe for the nanomolar determination of dopamine. *Analytical Methods, 7*(16), 6791-6798. https://doi.org/10.1039/c5ay01412c

[155] Zhang, Y., Xiao, J.Y., Zhu, Y., Tian, L.J., Wang, W.K., Zhu, T.T., Li, W.W., & Yu, H.Q. (2020). Fluorescence Sensor Based on Biosynthetic CdSe/CdS Quantum Dots and Liposome Carrier Signal Amplification for Mercury Detection. *Analytical Chemistry, 92*(5), 3990-3997. https://doi.org/10.1021/acs.analchem.9b05508

[156] Jiang, L., Liu, H., Li, M., Xing, Y., & Ren, X. (2016). Surface molecular imprinting on CdTe quantum dots for fluorescence sensing of 4-nitrophenol. *Analytical Methods, 8*(10), 2226-2232. https://doi.org/10.1039/c5ay03160e

[157] Sahu, A., & Kumar, D. (2022). Core-shell quantum dots: A review on classification, materials, application, and theoretical modeling. *Journal of Alloys and Compounds, 924*, 166508, 1-22. https://doi.org/10.1016/j.jallcom.2022.166508

[158] Vasudevan, D., Gaddam, R.R., Trinchi, A., & Cole, I. (2015). Core-shell quantum dots: Properties and applications. *Journal of Alloys and Compounds, 636*, 395-404. https://doi.org/10.1016/j.jallcom.2015.02.102

[159] Liu, M.L., Chen, B.B., Li, C.M., & Huang, C.Z. (2019). Carbon dots: Synthesis, formation mechanism, fluorescence origin and sensing applications. *Green Chemistry, 21*(3), 449-471. https://doi.org/10.1039/c8gc02736f

[160] Zheng, X.T., Ananthanarayanan, A., Luo, K.Q., & Chen, P. (2015). Glowing graphene quantum dots and carbon dots: Properties, syntheses, and biological applications. *Small, 11*(14), 1620-1636). https://doi.org/10.1002/smll.201402648

[161] Mintz, K.J., Bartoli, M., Rovere, M., Zhou, Y., Hettiarachchi, S.D., Paudyal, S., Chen, J., Domena, J.B., Liyanage, P.Y., Sampson, R., Khadka, D., Pandey, R.R., Huang, S., Chusuei, C.C., Tagliaferro, A., & Leblanc, R.M. (2021). A deep investigation into the structure of carbon dots. *Carbon, 173*, 433-447. https://doi.org/10.1016/j.carbon.2020.11.017

[162] Yu, J., Yong, X., Tang, Z., Yang, B., & Lu, S. (2021). Theoretical Understanding of Structure-Property Relationships in Luminescence of Carbon Dots. *Journal of Physical Chemistry Letters, 12*(32), 7671-7687. https://doi.org/10.1021/acs.jpclett.1c01856

[163] Zhu, S., Song, Y., Zhao, X., Shao, J., Zhang, J., & Yang, B. (2015). The photoluminescence mechanism in carbon dots (graphene quantum dots, carbon nanodots, and polymer dots): current state and future perspective. *Nano Research, 8*(2), 355-381. https://doi.org/10.1007/s12274-014-0644-3

[164] Yat, Y.D., Foo, H.C.Y., Tan, I.S., Lam, M.K., & Lim, S. (2022). Carbon dots and miniaturizing fabrication of portable carbon dot-based devices for bioimaging, biosensing, heavy metal detection and drug delivery applications. *Journal of Materials Chemistry C, 10*(41), 15277-15300. https://doi.org/10.1039/d2tc03230a

[165] Ge, G., Li, L., Wang, D., Chen, M., Zeng, Z., Xiong, W., Wu, X., & Guo, C. (2021). Carbon dots: Synthesis, properties and biomedical applications. *Journal of Materials Chemistry B, 9*(33), 6553-6575. https://doi.org/10.1039/d1tb01077h

[166] Lim, S.Y., Shen, W., & Gao, Z. (2015). Carbon quantum dots and their applications. *Chemical Society Reviews, 44*(1), 362-381. https://doi.org/10.1039/c4cs00269e

[167] Anwar, S., Ding, H., Xu, M., Hu, X., Li, Z., Wang, J., Liu, L., Jiang, L., Wang, D., Dong, C., Yan, M., Wang, Q., & Bi, H. (2019). Recent Advances in Synthesis, Optical Properties, and Biomedical Applications of Carbon Dots. *ACS Applied Bio Materials, 2*(6), 2317-2338. https://doi.org/10.1021/acsabm.9b00112

[168] Chen, B.B., Liu, M.L., Li, C.M., & Huang, C.Z. (2019). Fluorescent carbon dots functionalization. *Advances in Colloid and Interface Science, 270*, 165-190. https://doi.org/10.1016/j.cis.2019.06.008

[169] Roy, P., Chen, P.C., Periasamy, A.P., Chen, Y.N., & Chang, H.T. (2015). Photoluminescent carbon nanodots: Synthesis, physicochemical properties and analytical applications. *Materials Today, 18*(8), 447-458. https://doi.org/10.1016/j.mattod.2015.04.005

[170] Cayuela, A., Soriano, M.L., Carrillo-Carrión, C., & Valcárcel, M. (2016). Semiconductor and carbon-based fluorescent nanodots: The need for consistency. *Chemical Communications, 52*(7), 1311-1326. https://doi.org/10.1039/c5cc07754k

[171] Zhao, Q., Song, W., Zhao, B., & Yang, B. (2020). Spectroscopic studies of the optical properties of carbon dots: Recent advances and future prospects. Materials Chemistry Frontiers, 4(2), 472-488. https://doi.org/10.1039/c9qm00592g

[172] Xu, X., Ray, R., Gu, Y., Ploehn, H.J., Gearheart, L., Raker, K., & Scrivens, W.A. (2004). Electrophoretic analysis and purification of fluorescent single-walled carbon nanotube fragments. *Journal of the American Chemical Society, 126*(40), 12736-12737. https://doi.org/10.1021/ja040082h

[173] Sun, Y.P., Zhou, B., Lin, Y., Wang, W., Fernando, K.A.S., Pathak, P., Meziani, M.J., Harruff, B.A., Wang, X., Wang, H., Luo, P.G., Yang, H., Kose, M.E., Chen, B., Veca, L.M., & Xie, S.Y. (2006). Quantum-sized carbon dots for bright and colorful

photoluminescence. *Journal of the American Chemical Society, 128*(24), 7756-7757. https://doi.org/10.1021/ja062677d

[174] Yang, N., Jiang, X., & Pang, D.W. (2016). *Carbon Nanoparticles and Nanostructures* (1st ed.). Springer.

[175] Edinburgh Instruments. (2023). Photoluminescence Spectroscopy of Carbon Dots. https://www.edinst.com/photoluminescence-spectroscopy-of-carbon-dots/. Accessed 21 March 2023.

[176] Bottini, M., Balasubramanian, C., Dawson, M.I., Bergamaschi, A., Bellucci, S., & Mustelin, T. (2006). Isolation and characterization of fluorescent nanoparticles from pristine and oxidized electric arc-produced single-walled carbon nanotubes. *Journal of Physical Chemistry B, 110*(2), 831-836. https://doi.org/10.1021/jp055503b

[177] Kaczmarek, A., Hoffman, J., Morgiel, J., Moscicki, T., Stobinski, L., Szymanski, Z., & Małolepszy, A. (2021). Luminescent Carbon Dots Synthesized by the Laser Ablation of Graphite in Polyethylenimine and Ethylenediamine. *Materials, 14*(4), 729, 1-13. https://doi.org/10.3390/ma14040729

[178] Zuo, P., Lu, X., Sun, Z., Guo, Y., & He, H. (2016). A review on syntheses, properties, characterization and bioanalytical applications of fluorescent carbon dots. Microchimica Acta, 183(2), 519-542. https://doi.org/10.1007/s00604-015-1705-3

[179] Yan, Z., Shu, J., Yu, Y., Zhang, Z., Liu, Z., & Chen, J. (2015). Preparation of carbon quantum dots based on starch and their spectral properties. *Luminescence, 30*(4), 388-392. https://doi.org/10.1002/bio.2744

[180] Xia, C., Zhu, S., Feng, T., Yang, M., & Yang, B. (2019). Evolution and Synthesis of Carbon Dots: From Carbon Dots to Carbonized Polymer Dots. Advanced Science, 6(23), 1901316, 1-23. https://doi.org/10.1002/advs.201901316

[181] Zhou, J., Booker, C., Li, R., Zhou, X., Sham, T.K., Sun, X., & Ding, Z. (2007). An electrochemical avenue to blue luminescent nanocrystals from multiwalled carbon nanotubes (MWCNTs). *Journal of the American Chemical Society, 129*(4), 744-745. https://doi.org/10.1021/ja0669070

[182] Lin, L., Wang, Y., Xiao, Y., & Liu, W. (2019). Hydrothermal synthesis of carbon dots codoped with nitrogen and phosphorus as a turn-on fluorescent probe for cadmium(II). *Microchimica Acta, 186*(3), 147, 1-7. https://doi.org/10.1007/s00604-019-3264-5

[183] Wang, Y., Zhu, Y., Yu, S., & Jiang, C. (2017). Fluorescent carbon dots: Rational synthesis, tunable optical properties and analytical applications. *RSC Advances, 7*(65), 40973-40989. https://doi.org/10.1039/c7ra07573a

[184] Zhao, P., Li, X., Baryshnikov, G., Wu, B., Ågren, H., Zhang, J., & Zhu, L. (2018). One-step solvothermal synthesis of high-emissive amphiphilic carbon dots: Via rigidity derivation. *Chemical Science, 9*(5), 1323-1329. https://doi.org/10.1039/c7sc04607c

[185] De Medeiros, T.V., Manioudakis, J., Noun, F., Macairan, J.R., Victoria, F., & Naccache, R. (2019). Microwave-assisted synthesis of carbon dots and their

applications. *Journal of Materials Chemistry C, 7*(24), 7175-7195. https://doi.org/10.1039/c9tc01640f

[186] Ng, H.K.M., Lim, G.K., & Leo, C.P. (2021). Comparison between hydrothermal and microwave-assisted synthesis of carbon dots from biowaste and chemical for heavy metal detection: A review. *Microchemical Journal, 165*, 106116, 1-13. https://doi.org/10.1016/j.microc.2021.106116

[187] Cui, L., Ren, X., Sun, M., Liu, H., & Xia, L. (2021). Carbon dots: Synthesis, properties and applications. *Nanomaterials, 11*(12), 3419, 1-38. https://doi.org/10.3390/nano11123419

[188] Tan, X.W., Romainor, A.N.B., Chin, S.F., & Ng, S.M. (2014). Carbon dots production via pyrolysis of sago waste as potential probe for metal ions sensing. *Journal of Analytical and Applied Pyrolysis, 105*, 157-165. https://doi.org/10.1016/j.jaap.2013.11.001

[189] Hebbar, A., Selvaraj, R., Vinayagam, R., Varadavenkatesan, T., Kumar, P.S., Duc, P.A., & Rangasamy, G. (2023). A critical review on the environmental applications of carbon dots. *Chemosphere, 313*, 137308, 1-17. https://doi.org/10.1016/j.chemosphere.2022.137308

[190] Martínez-Cisneros, C.S., Gómez-de Pedro, S., Puyol, M., García-García, J., & Alonso-Chamarro, J. (2012). Design, fabrication and characterization of microreactors for high temperature syntheses. *Chemical Engineering Journal, 211-212*, 432-441. https://doi.org/10.1016/j.cej.2012.09.101

[191] Lu, Y., Zhang, L., & Lin, H. (2014). The use of a microreactor for rapid screening of the reaction conditions and investigation of the photoluminescence mechanism of carbon dots. *Chemistry - A European Journal, 20*(15), 4246-4250. https://doi.org/10.1002/chem.201304358

[192] Shao, M., Yu, Q., Jing, N., Cheng, Y., Wang, D., Wang, Y.D., & Xu, J.H. (2019). Continuous synthesis of carbon dots with full spectrum fluorescence and the mechanism of their multiple color emission. *Lab on a Chip, 19*(23), 3974-3978. https://doi.org/10.1039/c9lc00683d

[193] Cheng, Y., Chen, Z., Wang, Y., & Xu, J. (2022). Continuous synthesis of N, S co-coped carbon dots for selective detection of CD (II) ions. *Journal of Photochemistry and Photobiology A: Chemistry, 429*, 113910, 1-8. https://doi.org/10.1016/j.jphotochem.2022.113910

[194] Uriarte, D., Gómez, N., Canals, A., Domini, C., & Garrido, M. (2023). On-line carbon dots synthesis using flow injection analysis. Application to aluminium determination in water samples. *Talanta Open, 7*, 100192, 1-8. https://doi.org/10.1016/j.talo.2023.100192

[195] Rao, L., Tang, Y., Li, Z., Ding, X., Liang, G., Lu, H., Yan, C., Tang, K., & Yu, B. (2017). Efficient synthesis of highly fluorescent carbon dots by microreactor method and their application in Fe3+ ion detection. *Materials Science and Engineering C, 81*, 213-223. https://doi.org/10.1016/j.msec.2017.07.046

[196] Rao, L., Tang, Y., Lu, H., Yu, S., Ding, X., Xu, K., Li, Z., & Zhang, J.Z. (2018). Highly photoluminescent and stable n-doped carbon dots as nanoprobes for Hg2+ detection. *Nanomaterials, 8*(11), 900, 1-18. https://doi.org/10.3390/nano8110900

[197] Tang, Y., Rao, L., Li, Z., Lu, H., Yan, C., Yu, S., Ding, X., & Yu, B. (2018). Rapid synthesis of highly photoluminescent nitrogen-doped carbon quantum dots via a microreactor with foamy copper for the detection of Hg2+ ions. *Sensors and Actuators B: Chemical, 258*, 637-647. https://doi.org/10.1016/j.snb.2017.11.140

[198] Groß, G.A., Thelemann, T., Schneider, S., Boskovic, D., & Köhler, J.M. (2008). Fabrication and fluidic characterization of static micromixers made of low temperature cofired ceramic (LTCC). *Chemical Engineering Science, 63*(10), 2773-2784. https://doi.org/10.1016/j.ces.2008.02.030

[199] Gómez-de Pedro, S., Martínez-Cisneros, C.S., Puyol, M., & Alonso-Chamarro, J. (2012). Microreactor with integrated temperature control for the synthesis of CdSe nanocrystals. *Lab on a Chip, 12*(11), 1979-1986. https://doi.org/10.1039/c2lc00011c

[200] Gómez-de Pedro, S., Puyol, M., Izquierdo, D., Salinas, I., De La Fuente, J.M., & Alonso-Chamarro, J. (2012). A ceramic microreactor for the synthesis of water soluble CdS and CdS/ZnS nanocrystals with on-line optical characterization. *Nanoscale, 4*(4), 1328-1335. https://doi.org/10.1039/c2nr11525e

[201] Berenguel-Alonso, M., Ortiz-Gómez, I., Fernández, B., Couceiro, P., Alonso-Chamarro, J., Capitán-Vallvey, L.F., Salinas-Castillo, A., & Puyol, M. (2019). An LTCC monolithic microreactor for the synthesis of carbon dots with photoluminescence imaging of the reaction progress. *Sensors and Actuators B: Chemical, 296*, 126613, 1-8. https://doi.org/10.1016/j.snb.2019.05.090

[202] Gómez-de Pedro, S., Salinas-Castillo, A., Ariza-Avidad, M., Lapresta-Fernández, A., Sánchez-González, C., Martínez-Cisneros, C.S., Puyol, M., Capitan-Vallvey, L.F., & Alonso-Chamarro, J. (2014). Microsystem-assisted synthesis of carbon dots with fluorescent and colorimetric properties for pH detection. *Nanoscale, 6*(11), 6018-6024. https://doi.org/10.1039/c4nr00573b

[203] Liu, M. (2020). Optical Properties of Carbon Dots: A Review. *Nanoarchitectonics, 1*(1), 1-12. https://doi.org/10.37256/nat.112020124.1-12

[204] Jiang, K., Zhang, L., Lu, J., Xu, C., Cai, C., & Lin, H. (2016). Triple-Mode Emission of Carbon Dots: Applications for Advanced Anti-Counterfeiting. *Angewandte Chemie, 128*(25), 7347-7351. https://doi.org/10.1002/ange.201602445

[205] Liu, J., Li, R., & Yang, B. (2020). Carbon Dots: A New Type of Carbon-Based Nanomaterial with Wide Applications. *ACS Central Science, 6*(12), 2179-2195. https://doi.org/10.1021/acscentsci.0c01306

[206] Liu, R., Wu, D., Liu, S., Koynov, K., Knoll, W., & Li, Q. (2009). An aqueous route to multicolor photoluminescent carbon dots using silica spheres as carriers. *Angewandte Chemie - International Edition, 48*(25), 4598-4601. https://doi.org/10.1002/anie.200900652

[207] Javed, N., & O’Carroll, D.M. (2021). Carbon Dots and Stability of Their Optical Properties. *Particle and Particle Systems Characterization, 38*(4), 2000271, 1-12. https://doi.org/10.1002/ppsc.202000271

[208] Kang, Z., & Lee, S.T. (2019). Carbon dots: Advances in nanocarbon applications. *Nanoscale, 11*(41), 19214-19224. https://doi.org/10.1039/c9nr05647e

[209] Xia, J., Chen, S., Zou, G.Y., Yu, Y.L., & Wang, J.H. (2018). Synthesis of highly stable red-emissive carbon polymer dots by modulated polymerization: From the mechanism to application in intracellular pH imaging. *Nanoscale, 10*(47), 22484-22492. https://doi.org/10.1039/c8nr08208a

[210] Bao, L., Zhang, Z.L., Tian, Z.Q., Zhang, L., Liu, C., Lin, Y., Qi, B., & Pang, D.W. (2011). Electrochemical tuning of luminescent carbon nanodots: From preparation to luminescence mechanism. *Advanced Materials, 23*(48), 5801-5806. https://doi.org/10.1002/adma.201102866

[211] Bao, L., Liu, C., Zhang, Z.L., & Pang, D.W. (2015). Photoluminescence-tunable carbon nanodots: Surface-state energy-gap tuning. *Advanced Materials, 27*(10), 1663-1667. https://doi.org/10.1002/adma.201405070

[212] Chen, D., Wu, W., Yuan, Y., Zhou, Y., Wan, Z., & Huang, P. (2016). Intense multi-state visible absorption and full-color luminescence of nitrogen-doped carbon quantum dots for blue-light-excitable solid-state-lighting. *Journal of Materials Chemistry C, 4*(38), 9027-9035. https://doi.org/10.1039/c6tc02853e

[213] Zhang, Y., Yuan, R., He, M., Hu, G., Jiang, J., Xu, T., Zhou, L., Chen, W., Xiang, W., & Liang, X. (2017). Multicolour nitrogen-doped carbon dots: Tunable photoluminescence and sandwich fluorescent glass-based light-emitting diodes. *Nanoscale, 9*(45), 17849-17858. https://doi.org/10.1039/c7nr05363k

[214] Li, H., He, X., Kang, Z., Huang, H., Liu, Y., Liu, J., Lian, S., Tsang, C.H.A., Yang, X., & Lee, S.T. (2010). Water-soluble fluorescent carbon quantum dots and photocatalyst design. *Angewandte Chemie - International Edition, 49*(26), 4430-4434. https://doi.org/10.1002/anie.200906154

[215] Wang, B., & Lu, S. (2022). The light of carbon dots: From mechanism to applications. *Matter, 5*(1), 110-149. https://doi.org/10.1016/j.matt.2021.10.016

[216] Song, Y., Zhu, S., Zhang, S., Fu, Y., Wang, L., Zhao, X., & Yang, B. (2015). Investigation from chemical structure to photoluminescent mechanism: A type of carbon dots from the pyrolysis of citric acid and an amine. *Journal of Materials Chemistry C, 3*(23), 5976-5984. https://doi.org/10.1039/c5tc00813a

[217] Zhou, J., Liu, Q., Feng, W., Sun, Y., & Li, F. (2015). Upconversion luminescent materials: Advances and applications. *Chemical Reviews, 115*(1), 395-465. https://doi.org/10.1021/cr400478f

[218] Song, Y., Zhu, S., Xiang, S., Zhao, X., Zhang, J., Zhang, H., Fu, Y., & Yang, B. (2014). Investigation into the fluorescence quenching behaviors and applications of carbon dots. *Nanoscale, 6*(9), 4676-4682. https://doi.org/10.1039/c4nr00029c

[219] Lakowicz, J.R. (2006). *Principles of Fluorescence Spectroscopy* (3rd ed.). Springer.

[220] Gehlen, M.H. (2020). The centenary of the Stern-Volmer equation of fluorescence quenching: From the single line plot to the SV quenching map. *Journal of Photochemistry and Photobiology C: Photochemistry Reviews, 42*, 100338, 1-14. https://doi.org/10.1016/j.jphotochemrev.2019.100338

[221] Sun, X., & Lei, Y. (2017). Fluorescent carbon dots and their sensing applications. *TrAC - Trends in Analytical Chemistry, 89*, 163-180. https://doi.org/10.1016/j.trac.2017.02.001

[222] Mintz, K.J., Guerrero, B., & Leblanc, R.M. (2018). Photoinduced Electron Transfer in Carbon Dots with Long-Wavelength Photoluminescence. *Journal of Physical Chemistry C, 122*(51), 29507-29515. https://doi.org/10.1021/acs.jpcc.8b06868

[223] Zu, F., Yan, F., Bai, Z., Xu, J., Wang, Y., Huang, Y., & Zhou, X. (2017). The quenching of the fluorescence of carbon dots: A review on mechanisms and applications. *Microchimica Acta, 184*(7), 1899-1914. https://doi.org/10.1007/s00604-017-2318-9

[224] Wang, B., Sun, Z., Yu, J., Waterhouse, G.I.N., Lu, S., & Yang, B. (2022). Cross-linking enhanced room-temperature phosphorescence of carbon dots. *SmartMat, 3*(2), 337-348. https://doi.org/10.1002/smm2.1123

[225] Li, Q., Zhou, M., Yang, Q., Wu, Q., Shi, J., Gong, A., & Yang, M. (2016). Efficient room-temperature phosphorescence from nitrogen-doped carbon dots in composite matrices. *Chemistry of Materials, 28*(22), 8221-8227. https://doi.org/10.1021/acs.chemmater.6b03049

[226] Li, Q., Zhou, M., Yang, M., Yang, Q., Zhang, Z., & Shi, J. (2018). Induction of long-lived room temperature phosphorescence of carbon dots by water in hydrogen-bonded matrices. *Nature Communications, 9*(1), 734, 1-8. https://doi.org/10.1038/s41467-018-03144-9

[227] Tang, G., Wang, C., Zhang, K., Wang, Y., & Yang, B. (2021). Deep-Blue Room-Temperature Phosphorescent Carbon Dots/Silica Microparticles from a Single Raw Material. *Langmuir, 37*(45), 13187-13193. https://doi.org/10.1021/acs.langmuir.1c01264

[228] Zhao, L., Di, F., Wang, D., Guo, L.H., Yang, Y., Wan, B., & Zhang, H. (2013). Chemiluminescence of carbon dots under strong alkaline solutions: A novel insight into carbon dot optical properties. *Nanoscale, 5*(7), 2655-2658. https://doi.org/10.1039/c3nr00358b

[229] Wang, D.M., Lin, K.L., & Huang, C.Z. (2019). Carbon dots-involved chemiluminescence: Recent advances and developments. *Luminescence, 34*(1), 4-22. https://doi.org/10.1002/bio.3570

[230] Shen, C.L., Lou, Q., Liu, K.K., Dong, L., & Shan, C.X. (2020). Chemiluminescent carbon dots: Synthesis, properties, and applications. *Nano Today, 35*, 100954, 1-23. https://doi.org/10.1016/j.nantod.2020.100954

[231] Lin, Z., Xue, W., Chen, H., & Lin, J.M. (2012). Classical oxidant induced chemiluminescence of fluorescent carbon dots. *Chemical Communications, 48*(7), 1051-1053. https://doi.org/10.1039/c1cc15290d

[232] Lin, Z., Xue, W., Chen, H., & Lin, J.M. (2011). Peroxynitrous-acid-induced chemiluminescence of fluorescent carbon dots for nitrite sensing. *Analytical Chemistry, 83*(21), 8245-8251. https://doi.org/10.1021/ac202039h

[233] Xu, Y., Liu, J., Gao, C., & Wang, E. (2014). Applications of carbon quantum dots in electrochemiluminescence: A mini review. *Electrochemistry Communications, 48*, 151-154. https://doi.org/10.1016/j.elecom.2014.08.032

[234] Zhang, R., Adsetts, J.R., Nie, Y., Sun, X., & Ding, Z. (2018). Electrochemiluminescence of nitrogen- and sulfur-doped graphene quantum dots. *Carbon, 129*, 45-53. https://doi.org/10.1016/j.carbon.2017.11.091

[235] Yang, S., Liang, J., Luo, S., Liu, C., & Tang, Y. (2013). Supersensitive detection of chlorinated phenols by multiple amplification electrochemiluminescence sensing based on carbon quantum dots/graphene. *Analytical Chemistry, 85*(16), 7720-7725. https://doi.org/10.1021/ac400874h

[236] Dong, Y., Chen, C., Lin, J., Zhou, N., Chi, Y., & Chen, G. (2013). Electrochemiluminescence emission from carbon quantum dot-sulfite coreactant system. *Carbon, 56*, 12-17. https://doi.org/10.1016/j.carbon.2012.12.086

[237] Lu, J., Yan, M., Ge, L., Ge, S., Wang, S., Yan, J., & Yu, J. (2013). Electrochemiluminescence of blue-luminescent graphene quantum dots and its application in ultrasensitive aptasensor for adenosine triphosphate detection. *Biosensors and Bioelectronics, 47*, 271-277. https://doi.org/10.1016/j.bios.2013.03.039

[238] Yang, H., Liu, W., Ma, C., Zhang, Y., Wang, X., Yu, J., & Song, X. (2014). Gold-silver nanocomposite-functionalized graphene based electrochemiluminescence immunosensor using graphene quantum dots coated porous PtPd nanochains as labels. *Electrochimica Acta, 123*, 470-476. https://doi.org/10.1016/j.electacta.2014.01.014

[239] Chen, B.B., Liu, M.L., & Huang, C.Z. (2020). Carbon dot-based composites for catalytic applications. *Green Chemistry, 22*(13), 4034-4054. https://doi.org/10.1039/d0gc01014f

[240] Rosso, C., Filippini, G., & Prato, M. (2020). Carbon dots as nano-organocatalysts for synthetic applications. *ACS Catalysis, 10*(15), 8090-8105. https://doi.org/10.1021/acscatal.0c01989

[241] Zhai, Y., Zhang, B., Shi, R., Zhang, S., Liu, Y., Wang, B., Zhang, K., Waterhouse, G.I.N., Zhang, T., & Lu, S. (2022). Carbon Dots as New Building Blocks for Electrochemical Energy Storage and Electrocatalysis. *Advanced Energy Materials, 12*(6), 2103426, 1-36. https://doi.org/10.1002/aenm.202103426

[242] Campuzano, S., Yáñez-Sedeño, P., & Pingarrón, J.M. (2019). Carbon dots and graphene quantum dots in electrochemical biosensing. *Nanomaterials, 9*(4) 634, 1-18. https://doi.org/10.3390/nano9040634

[243] Shin, J., Guo, J., Zhao, T., & Guo, Z. (2019). Functionalized Carbon Dots on Graphene as Outstanding Non-Metal Bifunctional Oxygen Electrocatalyst. *Small, 15*(16), 1900296, 1-9. https://doi.org/10.1002/smll.201900296

[244] Zhang, E., Jia, X., Wang, B., Wang, J., Yu, X., & Lu, B. (2020). Carbon Dots@rGO Paper as Freestanding and Flexible Potassium-Ion Batteries Anode. *Advanced Science, 7*(15), 2000470, 1-8. https://doi.org/10.1002/advs.202000470

[245] Sinha, R., Roy, N., & Mandal, T.K. (2022). SWCNT/ZnO nanocomposite decorated with carbon dots for photoresponsive supercapacitor applications. *Chemical Engineering Journal, 431*, 133915, 1-13. https://doi.org/10.1016/j.cej.2021.133915

[246] Zhao, Z., & Xie, Y. (2017). Enhanced electrochemical performance of carbon quantum dots-polyaniline hybrid. *Journal of Power Sources, 337*, 54-64. https://doi.org/10.1016/j.jpowsour.2016.10.110

[247] Bonet-San-Emeterio, M., Algarra, M., Petković, M., & del Valle, M. (2020). Modification of electrodes with N-and S-doped carbon dots. Evaluation of the electrochemical response. *Talanta, 212*, 120806, 1-8. https://doi.org/10.1016/j.talanta.2020.120806

[248] Mansuriya, B.D., & Altintas, Z. (2021). Carbon Dots: Classification, Properties, Synthesis, Characterization, and Applications in Health Care - An Updated Review (2018-2021). *Nanomaterials, 11*(10), 2525, 1-55. https://doi.org/10.3390/nano11102525

[249] Sharma, V., Tiwari, P., & Mobin, S.M. (2017). Sustainable carbon-dots: Recent advances in green carbon dots for sensing and bioimaging. *Journal of Materials Chemistry B, 5*(45), 8904-8924. https://doi.org/10.1039/c7tb02484c

[250] Wei, W., Huang, J., Gao, W., Lu, X., & Shi, X. (2021). Carbon dots fluorescence-based colorimetric sensor for sensitive detection of aluminum ions with a smartphone. *Chemosensors, 9*(2), 25, 1-13. https://doi.org/10.3390/chemosensors9020025

[251] Jiao, Y., Gao, Y., Meng, Y., Lu, W., Liu, Y., Han, H., Shuang, S., Li, L., & Dong, C. (2019). One-Step Synthesis of Label-Free Ratiometric Fluorescence Carbon Dots for the Detection of Silver Ions and Glutathione and Cellular Imaging Applications. ACS *Applied Materials and Interfaces, 11*(18), 16822-16829. https://doi.org/10.1021/acsami.9b01319

[252] Jin, J.C., Wang, B.B., Xu, Z.Q., He, X.H., Zou, H.F., Yang, Q.Q., Jiang, F.L., & Liu, Y. (2018). A novel method for the detection of silver ions with carbon dots: Excellent selectivity, fast response, low detection limit and good applicability. *Sensors and Actuators B: Chemical, 267*, 627-635. https://doi.org/10.1016/j.snb.2018.04.036

[253] Huang, Z.Y., Wu, W.Z., Li, Z.X., Wu, Y., Wu, C.B., Gao, J., Guo, J., Chen, Y., Hu, Y., & Huang, C. (2022). Solvothermal production of tea residue derived carbon dots by the pretreatment of choline chloride/urea and its application for cadmium detection. *Industrial Crops and Products, 184*, 115085, 1-9. https://doi.org/10.1016/j.indcrop.2022.115085

[254] Li, C.L., Huang, C.C., Periasamy, A.P., Roy, P., Wu, W.C., Hsu, C.L., & Chang, H.T. (2015). Synthesis of photoluminescent carbon dots for the detection of cobalt ions. *RSC Advances, 5*(3), 2285-2291. https://doi.org/10.1039/c4ra11704b

[255] Ma, Y., Chen, Y., Liu, J., Han, Y., Ma, S., & Chen, X. (2018). Ratiometric fluorescent detection of chromium(VI) in real samples based on dual emissive carbon dots. *Talanta, 185*, 249-257. https://doi.org/10.1016/j.talanta.2018.03.081

[256] Gedda, G., Lee, C.Y., Lin, Y.C., & Wu, H.F. (2016). Green synthesis of carbon dots from prawn shells for highly selective and sensitive detection of copper ions. *Sensors and Actuators B: Chemical, 224*, 396-403. https://doi.org/10.1016/j.snb.2015.09.065

[257] Salinas-Castillo, A., Ariza-Avidad, M., Pritz, C., Camprubí-Robles, M., Fernández, B., Ruedas-Rama, M.J., Megia-Fernández, A., Lapresta-Fernández, A., Santoyo-Gonzalez, F., Schrott-Fischer, A., & Capitan-Vallvey, L.F. (2013). Carbon dots for copper detection with down and upconversion fluorescent properties as excitation sources. *Chemical Communications, 49*(11), 1103-1105. https://doi.org/10.1039/c2cc36450f

[258] Wang, C., Hu, T., Wen, Z., Zhou, J., Wang, X., Wu, Q., & Wang, C. (2018). Concentration-dependent color tunability of nitrogen-doped carbon dots and their application for iron(III) detection and multicolor bioimaging. *Journal of Colloid and Interface Science, 521*, 33-41. https://doi.org/10.1016/j.jcis.2018.03.021

[259] Zhang, X.Y., Li, Y., Wang, Y.Y., Liu, X.Y., Jiang, F.L., Liu, Y., & Jiang, P. (2022). Nitrogen and sulfur co-doped carbon dots with bright fluorescence for intracellular detection of iron ion and thiol. *Journal of Colloid and Interface Science, 611*, 255-264. https://doi.org/10.1016/j.jcis.2021.12.069

[260] Ma, Y., Zhang, Z., Xu, Y., Ma, M., Chen, B., Wei, L., & Xiao, L. (2016). A bright carbon-dot-based fluorescent probe for selective and sensitive detection of mercury ions. *Talanta, 161*, 476-481. https://doi.org/10.1016/j.talanta.2016.08.082

[261] Yan, F., Zou, Y., Wang, M., Mu, X., Yang, N., & Chen, L. (2014). Highly photoluminescent carbon dots-based fluorescent chemosensors for sensitive and selective detection of mercury ions and application of imaging in living cells. *Sensors and Actuators B: Chemical, 192*, 488-495. https://doi.org/10.1016/j.snb.2013.11.041

[262] Li, Y., Liu, C., Chen, M., An, Y., Zheng, Y., Tian, H., Shi, R., He, X., & Lin, X. (2022). Solvent-Free Preparation of Tannic Acid Carbon Dots for Selective Detection of Ni2+ in the Environment. *International Journal of Molecular Sciences, 23*(12), 6681, 1-13. https://doi.org/10.3390/ijms23126681

[263] Bandi, R., Dadigala, R., Gangapuram, B.R., & Guttena, V. (2018). Green synthesis of highly fluorescent nitrogen - Doped carbon dots from Lantana camara berries for effective detection of lead(II) and bioimaging. *Journal of Photochemistry and Photobiology B: Biology, 178*, 330-338. https://doi.org/10.1016/j.jphotobiol.2017.11.010

[264] Liu, Y., Zhou, Q., Yuan, Y., & Wu, Y. (2017). Hydrothermal synthesis of fluorescent carbon dots from sodium citrate and polyacrylamide and their highly

selective detection of lead and pyrophosphate. *Carbon, 115*, 550-560. https://doi.org/10.1016/j.carbon.2017.01.035

[265] da Silva Júnior, A.H., Macuvele, D.L.P., Gracher Riella, H., Soares, C., & Padoin, N. (2021). Novel carbon dots for zinc sensing from Campomanesia phaea. *Materials Letters, 283*, 128813, 1-5. https://doi.org/10.1016/j.matlet.2020.128813

[266] Yang, M., Kong, W., Li, H., Liu, J., Huang, H., Liu, Y., & Kang, Z. (2015). Fluorescent carbon dots for sensitive determination and intracellular imaging of zinc(II) ion. *Microchimica Acta, 182*(15-16), 2443-2450. https://doi.org/10.1007/s00604-015-1592-7

[267] Guo, J., Ye, S., Li, H., Song, J., & Qu, J. (2020). Novel fluorescence probe based on bright emitted carbon dots for ClO− detection in real water samples and living cells. *Spectrochimica Acta Part A: Molecular and Biomolecular Spectroscopy, 240*, 118592, 1-7. https://doi.org/10.1016/j.saa.2020.118592

[268] Zhang, J., Dong, L., & Yu, S.H. (2015). A selective sensor for cyanide ion (CN−) based on the inner filter effect of metal nanoparticles with photoluminescent carbon dots as the fluorophore. *Science Bulletin, 60*(8), 785-791. https://doi.org/10.1007/s11434-015-0764-5

[269] Tang, X., Yu, H., Bui, B., Wang, L., Xing, C., Wang, S., Chen, M., Hu, Z., & Chen, W. (2021). Nitrogen-doped fluorescence carbon dots as multi-mechanism detection for iodide and curcumin in biological and food samples. *Bioactive Materials, 6*(6), 1541-1554. https://doi.org/10.1016/j.bioactmat.2020.11.006

[270] Liu, S., Liu, Z., Li, Q., Xia, H., Yang, W., Wang, R., Li, Y., Zhao, H., & Tian, B. (2021). Facile synthesis of carbon dots from wheat straw for colorimetric and fluorescent detection of fluoride and cellular imaging. *Spectrochimica Acta Part A: Molecular and Biomolecular Spectroscopy, 246*, 118964, 1-8. https://doi.org/10.1016/j.saa.2020.118964

[271] Zhang, X., Tan, X., & Hu, Y. (2021). Blue/yellow emissive carbon dots coupled with curcumin: a hybrid sensor toward fluorescence turn-on detection of fluoride ion. *Journal of Hazardous Materials, 411*, 125184, 1-7. https://doi.org/10.1016/j.jhazmat.2021.125184

[272] Zhao, H.X., Liu, L.Q., Liu, Z.D., Wang, Y., Zhao, X.J., & Huang, C.Z. (2011). Highly selective detection of phosphate in very complicated matrixes with an off–on fluorescent probe of europium-adjusted carbon dots. *Chemical Communications, 47*(9), 2604-2606. https://doi.org/10.1039/c0cc04399k

[273] Chen, J., Li, Y., Lv, K., Zhong, W., Wang, H., Wu, Z., Yi, P., & Jiang, J. (2016). Cyclam-functionalized carbon dots sensor for sensitive and selective detection of copper(II) ion and sulfide anion in aqueous media and its imaging in live cells. *Sensors and Actuators B: Chemical, 224*, 298-306. https://doi.org/10.1016/j.snb.2015.10.046

[274] Hou, X., Zeng, F., Du, F., & Wu, S. (2013). Carbon-dot-based fluorescent turn-on sensor for selectively detecting sulfide anions in totally aqueous media and imaging inside live cells. *Nanotechnology, 24*(33), 335502, 1-9. https://doi.org/10.1088/0957-4484/24/33/335502

[275] Wang, T., Luo, H., Jing, X., Yang, J., Huo, M., & Wang, Y. (2021). Synthesis of fluorescent carbon dots and their application in ascorbic acid detection. *Molecules, 26*(5), 1246, 1-11. https://doi.org/10.3390/molecules26051246

[276] Wang, L., Jana, J., Chung, J.S., & Hur, S.H. (2021). Glutathione modified N-doped carbon dots for sensitive and selective dopamine detection. *Dyes and Pigments, 186*, 109028, 1-8. https://doi.org/10.1016/j.dyepig.2020.109028

[277] Yang, Z., Liu, Y., Lu, C., Yue, G., Wang, Y., Rao, H., Zhang, W., Lu, Z., & Wang, X. (2021). One-pot synthesis of CeO2-carbon dots with enhanced peroxidase-like activity and carbon dots for ratiometric fluorescence detection of H2O2 and cholesterol. *Journal of Alloys and Compounds, 862*, 158323, 1-9. https://doi.org/10.1016/j.jallcom.2020.158323

[278] Ji, H., Zhou, F., Gu, J., Shu, C., Xi, K., & Jia, X. (2016). Nitrogen-doped carbon dots as a new substrate for sensitive glucose determination. *Sensors, 16*(5), 630, 1-10. https://doi.org/10.3390/s16050630

[279] Nie, H., Li, M., Li, Q., Liang, S., Tan, Y., Sheng, L., Shi, W., & Zhang, S.X.A. (2014). Carbon dots with continuously tunable full-color emission and their application in ratiometric pH sensing. *Chemistry of Materials, 26*(10), 3104-3112. https://doi.org/10.1021/cm5003669

[280] Zhong, D., Miao, H., Yang, K., & Yang, X. (2016). Carbon dots originated from carnation for fluorescent and colorimetric pH sensing. *Materials Letters, 166*, 89-92. https://doi.org/10.1016/j.matlet.2015.12.061

[281] Guo, R., Chen, B., Li, F., Weng, S., Zheng, Z., Chen, M., Wu, W., Lin, X., & Yang, C. (2018). Positive carbon dots with dual roles of nanoquencher and reference signal for the ratiometric fluorescence sensing of DNA. *Sensors and Actuators B: Chemical, 264*, 193-201. https://doi.org/10.1016/j.snb.2018.02.175

[282] Lee, H.N., Ryu, J.S., Shin, C., & Chung, H.J. (2017). A Carbon-Dot-Based Fluorescent Nanosensor for Simple Visualization of Bacterial Nucleic Acids. *Macromolecular Bioscience, 17*(9), 1700086, 1-9. https://doi.org/10.1002/mabi.201700086

[283] Liu, G., Zhao, J., Wang, S., Lu, S., Sun, J., & Yang, X. (2020). Enzyme-induced in situ generation of polymer carbon dots for fluorescence immunoassay. *Sensors and Actuators B: Chemical, 306*, 127583, 1-8. https://doi.org/10.1016/j.snb.2019.127583

[284] Zhu, L., Cui, X., Wu, J., Wang, Z., Wang, P., Hou, Y., & Yang, M. (2014). Fluorescence immunoassay based on carbon dots as labels for the detection of human immunoglobulin G. *Analytical Methods, 6*(12), 4430-4436. https://doi.org/10.1039/c4ay00717d

[285] Xu, D., Lin, Q., & Chang, H.T. (2020). Recent Advances and Sensing Applications of Carbon Dots. *Small Methods, 4*(4), 1900387, 1-17. https://doi.org/10.1002/smtd.201900387

[286] Du, J., Xu, N., Fan, J., Sun, W., & Peng, X. (2019). Carbon Dots for In Vivo Bioimaging and Theranostics. *Small, 15*(32), 1805087, 1-16. https://doi.org/10.1002/smll.201805087

[287] Malina, T., Poláková, K., Skopalík, J., Milotová, V., Holá, K., Havrdová, M., Tománková, K.B., Čmiel, V., Šefc, L., & Zbořil, R. (2019). Carbon dots for in vivo fluorescence imaging of adipose tissue-derived mesenchymal stromal cells. *Carbon, 152*, 434-443. https://doi.org/10.1016/j.carbon.2019.05.061

[288] Algarra, M., Pérez-Martín, M., Cifuentes-Rueda, M., Jiménez-Jiménez, J., Esteves Da Silva, J.C.G., Bandosz, T.J., Rodríguez-Castellón, E., López Navarrete, J.T., & Casado, J. (2014). Carbon dots obtained using hydrothermal treatment of formaldehyde. Cell imaging in vitro. *Nanoscale, 6*(15), 9071-9077. https://doi.org/10.1039/c4nr01585a

[289] Ramanan, V., Thiyagarajan, S.K., Raji, K., Suresh, R., Sekar, R., & Ramamurthy, P. (2016). Outright green synthesis of fluorescent carbon dots from eutrophic algal blooms for in vitro imaging. *ACS Sustainable Chemistry and Engineering, 4*(9), 4724-4731. https://doi.org/10.1021/acssuschemeng.6b00935

[290] Vasimalai, N., Vilas-Boas, V., Gallo, J., Cerqueira, M. de F., Menéndez-Miranda, M., Costa-Fernández, J.M., Diéguez, L., Espiña, B., & Fernández-Argüelles, M.T. (2018). Green synthesis of fluorescent carbon dots from spices for in vitro imaging and tumour cell growth inhibition. *Beilstein Journal of Nanotechnology, 9*(1), 530-544. https://doi.org/10.3762/bjnano.9.51

[291] Calabrese, G., De Luca, G., Nocito, G., Rizzo, M.G., Lombardo, S.P., Chisari, G., Forte, S., Sciuto, E.L., & Conoci, S. (2021). Carbon dots: An innovative tool for drug delivery in brain tumors. *International Journal of Molecular Sciences, 22*(21), 11783, 1-17. https://doi.org/10.3390/ijms222111783

[292] Dou, Q., Fang, X., Jiang, S., Chee, P.L., Lee, T.C., & Loh, X.J. (2015). Multi-functional fluorescent carbon dots with antibacterial and gene delivery properties. *RSC Advances, 5*(58), 46817-46822. https://doi.org/10.1039/c5ra07968c

[293] Liu, C., Zhang, P., Zhai, X., Tian, F., Li, W., Yang, J., Liu, Y., Wang, H., Wang, W., & Liu, W. (2012). Nano-carrier for gene delivery and bioimaging based on carbon dots with PEI-passivation enhanced fluorescence. *Biomaterials, 33*(13), 3604-3613. https://doi.org/10.1016/j.biomaterials.2012.01.052

[294] Wu, Y.F., Wu, H.C., Kuan, C.H., Lin, C.J., Wang, L.W., Chang, C.W., & Wang, T.W. (2016). Multi-functionalized carbon dots as theranostic nanoagent for gene delivery in lung cancer therapy. *Scientific Reports, 6*, 21170, 1-12. https://doi.org/10.1038/srep21170

[295] Zeng, Q., Shao, D., He, X., Ren, Z., Ji, W., Shan, C., Qu, S., Li, J., Chen, L., & Li, Q. (2016). Carbon dots as a trackable drug delivery carrier for localized cancer therapy in vivo. *Journal of Materials Chemistry B, 4*(30), 5119-5126. https://doi.org/10.1039/c6tb01259k

[296] Chen, S., Sun, T., Zheng, M., & Xie, Z. (2020). Carbon Dots Based Nanoscale Covalent Organic Frameworks for Photodynamic Therapy. *Advanced Functional Materials, 30*(43), 2004680, 1-8. https://doi.org/10.1002/adfm.202004680

[297] Li, Y., Zheng, X., Zhang, X., Liu, S., Pei, Q., Zheng, M., & Xie, Z. (2017). Porphyrin-Based Carbon Dots for Photodynamic Therapy of Hepatoma. *Advanced Healthcare Materials, 6*(1), 1600924, 1-6. https://doi.org/10.1002/adhm.201600924

[298] Li, Y., Wu, S., Zhang, J., Zhou, R., & Cai, X. (2020). Sulphur doped carbon dots enhance photodynamic therapy via PI3K/Akt signalling pathway. *Cell Proliferation, 53*(5), 12821, 1-10. https://doi.org/10.1111/cpr.12821

[299] Li, Y., Bai, G., Zeng, S., & Hao, J. (2019). Theranostic Carbon Dots with Innovative NIR-II Emission for in Vivo Renal-Excreted Optical Imaging and Photothermal Therapy. *ACS Applied Materials and Interfaces, 11*(5), 4737-4744. https://doi.org/10.1021/acsami.8b14877

[300] Shen, Y., Zhang, X., Liang, L., Yue, J., Huang, D., Xu, W., Shi, W., Liang, C., & Xu, S. (2020). Mitochondria-targeting supra-carbon dots: Enhanced photothermal therapy selective to cancer cells and their hyperthermia molecular actions. *Carbon, 156*, 558-567. https://doi.org/10.1016/j.carbon.2019.09.079

[301] Zhao, S., Yan, L., Cao, M., Huang, L., Yang, K., Wu, S., Lan, M., Niu, G., & Zhang, W. (2021). Near-Infrared Light-Triggered Lysosome-Targetable Carbon Dots for Photothermal Therapy of Cancer. *ACS Applied Materials and Interfaces, 13*(45), 53610-53617. https://doi.org/10.1021/acsami.1c15926

[302] Benetti, D., Jokar, E., Yu, C.H., Fathi, A., Zhao, H., Vomiero, A., Wei-Guang Diau, E., & Rosei, F. (2019). Hole-extraction and photostability enhancement in highly efficient inverted perovskite solar cells through carbon dot-based hybrid material. *Nano Energy, 62*, 781-790. https://doi.org/10.1016/j.nanoen.2019.05.084

[303] Ghann, W., Sharma, V., Kang, H., Karim, F., Richards, B., Mobin, S.M., Uddin, J., Rahman, M.M., Hossain, F., Kabir, H., & Uddin, N. (2019). The synthesis and characterization of carbon dots and their application in dye sensitized solar cell. *International Journal of Hydrogen Energy, 44*(29), 14580-14587. https://doi.org/10.1016/j.ijhydene.2019.04.072

[304] Han, M., Zhu, S., Lu, S., Song, Y., Feng, T., Tao, S., Liu, J., & Yang, B. (2018). Recent progress on the photocatalysis of carbon dots: Classification, mechanism and applications. *Nano Today, 19*, 201-218. https://doi.org/10.1016/j.nantod.2018.02.008

[305] Cheng, Y., Song, H., Yu, J., Chang, J., Waterhouse, G.I.N., Tang, Z., Yang, B., & Lu, S. (2022). Carbon dots-derived carbon nanoflowers decorated with cobalt single atoms and nanoparticles as efficient electrocatalysts for oxygen reduction. *Chinese Journal of Catalysis, 43*(9), 2443-2452. https://doi.org/10.1016/S1872-2067(22)64146-9

[306] Ding, P., Song, H., Chang, J., & Lu, S. (2022). N-doped carbon dots coupled NiFe-LDH hybrids for robust electrocatalytic alkaline water and seawater oxidation. *Nano Research, 15*(8), 7063-7070. https://doi.org/10.1007/s12274-022-4377-4

[307] Mohideen, M.M., Liu, Y., & Ramakrishna, S. (2020). Recent progress of carbon dots and carbon nanotubes applied in oxygen reduction reaction of fuel cell for transportation. *Applied Energy, 257*, 114027, 1-19. https://doi.org/10.1016/j.apenergy.2019.114027

[308] Zhong, H., Sa, R., Lv, H., Yang, S., Yuan, D., Wang, X., & Wang, R. (2020). Covalent Organic Framework Hosting Metalloporphyrin-Based Carbon Dots for Visible-Light-Driven Selective CO2 Reduction. *Advanced Functional Materials, 30*(35), 2002654, 1-8. https://doi.org/10.1002/adfm.202002654

[309] Zhu, C., Liu, C., Zhou, Y., Fu, Y., Guo, S., Li, H., Zhao, S., Huang, H., Liu, Y., & Kang, Z. (2017). Carbon dots enhance the stability of CdS for visible-light-driven overall water splitting. *Applied Catalysis B: Environmental, 216*, 114-121. https://doi.org/10.1016/j.apcatb.2017.05.049

[310] Da, X., Han, Z., Yang, Z., Zhang, D., Hong, R., Tao, C., Lin, H., & Huang, Y. (2022). Preparation of multicolor carbon dots with high fluorescence quantum yield and application in white LED. *Chemical Physics Letters, 794*, 139497, 1-8. https://doi.org/10.1016/j.cplett.2022.139497

[311] Liu, X., Zheng, J., Yang, Y., Chen, Y., & Liu, X. (2018). Preparation of N-doped carbon dots based on starch and their application in white LED. *Optical Materials, 86*, 530-536. https://doi.org/10.1016/j.optmat.2018.10.057

[312] Williams, D.B., & Barry Carter, C. (2009). *Transmission Electron Microscopy. Part 1: Basics* (2nd ed.). Springer.

[313] Wang, Z.L. (2000). Transmission electron microscopy of shape-controlled nanocrystals and their assemblies. *Journal of Physical Chemistry B, 104*(6), 1153-1175. https://doi.org/10.1021/jp993593c

[314] Encyclopædia Britannica. (2023). *Transmission Electron Microscope*. https://www.britannica.com/technology/transmission-electron-microscope. Accessed 2 April 2023.

[315] Alexander, M., & Dalgleish, D.G. (2006). Dynamic light scattering techniques and their applications in food science. *Food Biophysics, 1*(1), 2-13. https://doi.org/10.1007/s11483-005-9000-1

[316] Mcneil, S.E. (2018). *Characterization of Nanoparticles Intended for Drug Delivery* (2nd ed.). Humana Press.

[317] Berne, B.J., Pecora, R. (2000). *Dynamic Light Scattering with Applications to Chemistry, Biology and Physics* (2nd ed.). Dover Publications.

[318] Falke, S., & Betzel, C. (2019). Dynamic Light Scattering (DLS): Principles, Perspectives, Applications to Biological Samples. In: A.S. Pereira (Ed.), P. Tavares (Ed.), & P. Limão-Vieira (Ed.), *Radiation in Bioanalysis: Spectroscopic Techniques and Theoretical Methods* (1st ed., pp 173-193). Springer.

[319] Berthomieu, C., & Hienerwadel, R. (2009). Fourier transform infrared (FTIR) spectroscopy. *Photosynthesis Research, 101*(2-3), 157-170. https://doi.org/10.1007/s11120-009-9439-x

[320] Schmitt, J., & Flemming, H.C. (1998). FTIR-spectroscopy in microbial and material analysis. *International Biodeterioration and Biodegradation, 41*(1), 1-11. https://doi.org/10.1016/S0964-8305(98)80002-4

[321] Korin, E., Froumin, N., & Cohen, S. (2017). Surface Analysis of Nanocomplexes by X-ray Photoelectron Spectroscopy (XPS). *ACS Biomaterials Science and Engineering, 3*(6), 882-889. https://doi.org/10.1021/acsbiomaterials.7b00040

[322] Stevie, F.A., & Donley, C.L. (2020). Introduction to x-ray photoelectron spectroscopy. *Journal of Vacuum Science & Technology A, 38*(6), 063204, 1-20. https://doi.org/10.1116/6.0000412

[323] Scimeca, M., Bischetti, S., Lamsira, H.K., Bonfiglio, R., & Bonanno, E. (2018). Energy dispersive X-ray (EDX) microanalysis: A powerful tool in biomedical research and diagnosis. *European Journal of Histochemistry, 62*(1), 89-99. https://doi.org/10.4081/ejh.2018.2841

[324] Lee, H.C. (2018). Review of inductively coupled plasmas: Nano-applications and bistable hysteresis physics. Applied Physics Reviews, 5(1), 011108, 1-26. https://doi.org/10.1063/1.5012001

[325] Skoog, D.A. (2008). *Principios de análisis instrumental* (6th ed.). Cengage Learning Editores S.A.

[326] Berenguel-Alonso, M. (2017). *Lab on a Chip Systems for Biochemical Analysis, Biology and Synthesis: Towards Simple, Scalable Microfabrication Technologies Based on COC and LTCC* [Doctoral Thesis, Universitat Autònoma de Barcelona].

[327] Puigmartí-Luis, J. (2014). Microfluidic platforms: A mainstream technology for the preparation of crystals. *Chemical Society Reviews, 43*(7), 2253-2271. https://doi.org/10.1039/c3cs60372e

[328] Hu, R., Liu, C., Xuan, J., Xu, Y., Li, T., Liu, B.F., Li, Y., & Yang, Y. (2019). 3D hydrodynamic flow focusing-based micromixer enables high-resolution imaging for studying the early folding kinetics of G-quadruplex. *Sensors and Actuators B: Chemical, 293*, 312-320. https://doi.org/10.1016/j.snb.2019.05.026

[329] TOPAS Advanced Polymers. (2023). *TOPAS COC polymers*. https://www.topas.com/products/topas-coc-polymers. Accessed 26 February 2023.

[330] Ymbern, O., Berenguel-Alonso, M., Calvo-López, A., Gómez-De Pedro, S., Izquierdo, D., & Alonso-Chamarro, J. (2015). Versatile lock and key assembly for optical measurements with microfluidic platforms and cartridges. *Analytical Chemistry, 87*(3), 1503-1508. https://doi.org/10.1021/ac504255t

[331] Pascual-Esco, A., Alonso-Chamarro, J., & Puyol, M. (2022). Rapid warning microanalyzer for heavy metals monitoring in natural waters. *Sensors and Actuators B: Chemical, 368*, 132180, 1-8. https://doi.org/10.1016/j.snb.2022.132180

[332] Du, F., Zeng, F., Ming, Y., & Wu, S. (2013). Carbon dots-based fluorescent probes for sensitive and selective detection of iodide. *Microchimica Acta, 180*(5-6), 453-460. https://doi.org/10.1007/s00604-013-0954-2

[333] Zhu, S., Meng, Q., Wang, L., Zhang, J., Song, Y., Jin, H., Zhang, K., Sun, H., Wang, H., & Yang, B. (2013). Highly Photoluminescent Carbon Dots for Multicolor Patterning, Sensors, and Bioimaging. *Angewandte Chemie, 125*(14), 4045-4049. https://doi.org/10.1002/ange.201300519

[334] Jing, N., Tian, M., Wang, Y., & Zhang, Y. (2019). Nitrogen-doped carbon dots synthesized from acrylic acid and ethylenediamine for simple and selective determination of cobalt ions in aqueous media. *Journal of Luminescence, 206*, 169-175. https://doi.org/10.1016/j.jlumin.2018.10.059

[335] Cui, X., Wang, Y., Liu, J., Yang, Q., Zhang, B., Gao, Y., Wang, Y., & Lu, G. (2017). Dual functional N- and S-co-doped carbon dots as the sensor for temperature and Fe3+ ions. *Sensors and Actuators B: Chemical, 242*, 1272-1280. https://doi.org/10.1016/j.snb.2016.09.032

[336] Jiang, Y., Wang, Y., Meng, F., Wang, B., Cheng, Y., & Zhu, C. (2015). N-doped carbon dots synthesized by rapid microwave irradiation as highly fluorescent probes for Pb2+ detection. *New Journal of Chemistry, 39*(5), 3357-3360. https://doi.org/10.1039/c5nj00170f

[337] Wang, X., Wang, D., Guo, Y., Yang, C., Iqbal, A., Liu, W., Qin, W., Yan, D., & Guo, H. (2015). Imidazole derivative-functionalized carbon dots: Using as a fluorescent probe for detecting water and imaging of live cells. *Dalton Transactions, 44*(12), 5547-5554. https://doi.org/10.1039/c5dt00128e

[338] Demas, J.N., & Crosby, G.A. (1971). The Measurement of Photoluminescence Quantum Yields: A Review. *Journal of Physical Chemistry, 75*(8), 991-1024. https://doi.org/10.1021/j100678a001

[339] Qu, S., Wang, X., Lu, Q., Liu, X., & Wang, L. (2012). A biocompatible fluorescent ink based on water-soluble luminescent carbon nanodots. *Angewandte Chemie - International Edition, 51*(49), 12215-12218. https://doi.org/10.1002/anie.201206791

[340] Wang, J., Zhang, P., Huang, C., Liu, G., Leung, K.C.F., & Wáng, Y.X.J. (2015). High Performance Photoluminescent Carbon Dots for in Vitro and in Vivo Bioimaging: Effect of Nitrogen Doping Ratios. *Langmuir, 31*(29), 8063-8073. https://doi.org/10.1021/acs.langmuir.5b01875

[341] De Carlo, S., & Harris, J.R. (2011). Negative staining and cryo-negative staining of macromolecules and viruses for TEM. *Micron, 42*(2), 117-131. https://doi.org/10.1016/j.micron.2010.06.003

[342] Papp, I., Sieben, C., Ludwig, K., Roskamp, M., Böttcher, C., Schlecht, S., Herrmann, A., & Haag, R. (2010). Inhibition of influenza virus infection by multivalent sialic-acid-functionalized gold nanoparticles. *Small, 6*(24), 2900-2906. https://doi.org/10.1002/smll.201001349

[343] Postis, V., Rawson, S., Mitchell, J.K., Lee, S.C., Parslow, R.A., Dafforn, T.R., Baldwin, S.A., & Muench, S.P. (2015). The use of SMALPs as a novel membrane protein scaffold for structure study by negative stain electron microscopy. *Biochimica et Biophysica Acta - Biomembranes, 1848*(2), 496-501. https://doi.org/10.1016/j.bbamem.2014.10.018

[344] Dutta Choudhury, S., Chethodil, J.M., Gharat, P.M., Praseetha, P.K., & Pal, H. (2017). pH-Elicited Luminescence Functionalities of Carbon Dots: Mechanistic Insights. *Journal of Physical Chemistry Letters, 8*(7), 1389-1395. https://doi.org/10.1021/acs.jpclett.7b00153

[345] Ehtesabi, H., Hallaji, Z., Najafi Nobar, S., & Bagheri, Z. (2020). Carbon dots with pH-responsive fluorescence: a review on synthesis and cell biological applications. *Microchimica Acta, 187*(2), 150, 2-18. https://doi.org/10.1007/s00604-019-4091-4

[346] Htun, T. (2004). A Negative Deviation from Stern-Volmer Equation in Fluorescence Quenching. *Journal of Fluorescence, 14*(2), 217-222. https://doi.org/10.1023/B:JOFL.0000016294.96775.fd

[347] Muller, D.A. (2009). Structure and bonding at the atomic scale by scanning transmission electron microscopy. *Nature Materials, 8*(4), 263-270. https://doi.org/10.1038/nmat2380

[348] Xu, O., Liu, W., Li, J., Wan, S., & Zhu, X. (2022). A Novel Surfactant Sensitized Fluorescent Sensor for Co(II) Based on Nitrogen Doped Carbon Quantum Dots. *Photonic Sensors, 12*(2), 152-163. https://doi.org/10.1007/s13320-021-0642-5

[349] Liao, S., Zhu, F., Zhao, X., Yang, H., & Chen, X. (2018). A reusable P, N-doped carbon quantum dot fluorescent sensor for cobalt ion. *Sensors and Actuators B: Chemical, 260*, 156-164. https://doi.org/10.1016/j.snb.2017.12.206

[350] Sun, L., Liu, Y., Wang, Y., Xu, J., Xiong, Z., Zhao, X., & Xia, Y. (2021). Nitrogen and sulfur Co-doped carbon dots as selective and visual sensors for monitoring cobalt ions. *Optical Materials, 112*, 110787, 1-7. https://doi.org/10.1016/j.optmat.2020.110787

[351] Tian, M., Liu, Y., Wang, Y., & Zhang, Y. (2019). Facile synthesis of yellow fluorescent carbon dots for highly sensitive sensing of cobalt ions and biological imaging. *Analytical Methods, 11*(32), 4077-4083. https://doi.org/10.1039/c9ay01244c

[352] Chen, Y., Shang, P., Dong, Y., & Chi, Y. (2017). Regulating the overlap between the absorption spectrum of metal ion-chromogenic agent and the emission spectrum of carbon-based dots to improve the sensing performance for metal ions. *Sensors and Actuators B: Chemical, 242*, 1210-1215. https://dx.doi.org/10.1016/j.snb.2016.09.102

# Annex: Publications

The work presented in this thesis contributed to the publication of the following articles in peer-reviewed journals:

1. Pascual-Esco, A., Alonso-Chamarro, J., & Puyol, M. (2022). Rapid warning microanalyzer for heavy metals monitoring in natural waters. *Sensors and Actuators B: Chemical, 368*, 132180, 1-8. https://doi.org/10.1016/j.snb.2022.132180

2. Pascual-Esco, A., Lleonart, P., Calvo-López, A., Alonso-Chamarro, J., & Puyol, M. (2023). Live synthesis of selective Carbon Dots as fluorescent probes for cobalt determination in water with an automatic microanalyzer. *Microchimica Acta, 190*, 400, 1-11. https://doi.org/10.1007/s00604-023-05975-w

# Rapid warning microanalyzer for heavy metals monitoring in natural waters

Alex Pascual-Esco, Julián Alonso-Chamarro, and Mar Puyol

Sensors and Actuators B: Chemical, 368, 132180, 1-8.
https://doi.org/10.1016/j.snb.2022.132180

Sensors & Actuators: B. Chemical 368 (2022) 132180

Contents lists available at ScienceDirect

Sensors and Actuators: B. Chemical

journal homepage: www.elsevier.com/locate/snb

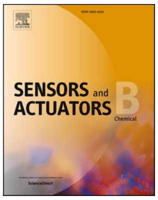

# Rapid warning microanalyzer for heavy metals monitoring in natural waters

Alex Pascual-Esco, Julián Alonso-Chamarro, Mar Puyol [*]

*Group of Sensors and Biosensors, Department of Chemistry, Faculty of Sciences, Universitat Autònoma de Barcelona, Carrer dels Til·lers s/n, Bellaterra, 08193 Cerdanyola del Vallès, Spain*

ARTICLE INFO

*Keywords:*
Carbon Dots
Heavy metals
Fluorescence quenching
Microfluidics

ABSTRACT

A warning microanalyzer for the rapid monitoring of different heavy metals in water using Carbon Dots (CDs) as selective optical reagents is presented. The synthesized CDs have different surface functionalization and exhibit selective fluorescence quenching by heavy metal ions, that combined with the use of microfluidics, provide sensitivity, ease of automation and reproducibility to the method. Moreover, they present maximum excitation wavelengths around 350 nm, allowing multiparametric analysis with a single light source. Although quantum yields range from 16 % to 78 % depending on the type of CDs, enough sensitivity is achieved for each heavy metal using the same measurement conditions of the optical detection system (lock-in modulating frequency, signal amplitude and measurement frequency). The microanalyzer is composed of a Cyclic Olefin Copolymer (COC) analytical microsystem, a flow management system, and a miniaturized customized optical detection system. In this paper, we demonstrate that our proposed system can be used as a toxicity control system by selectively measuring five different heavy metal ions ($Co^{2+}$, $Cu^{2+}$, $Hg^{2+}$, $Ni^{2+}$, and $Pb^{2+}$) with detection limits ranging from 2 to 12 ppb. Spiked tap water samples were analyzed, giving recoveries from 98 % to 134 %. Polluted samples containing four of the five heavy metal ions studied ($Co^{2+}$, $Cu^{2+}$, $Ni^{2+}$, and $Pb^{2+}$) were also analyzed with no significant differences observed between both methods, the proposed microanalyzer and the reference method (ICP-OES).

## 1. Introduction

Contamination of water by heavy metals, coming from human activities like mining or industrial wastes, has been a critical environmental concern for decades. One of the main preoccupations is their toxicity caused by the non-biodegradability and potential of bioaccumulation in different tissues and organs. The commonly employed techniques for heavy metals detection (mainly atomic absorption spectrometry (AAS) and inductively coupled plasma mass spectroscopy (ICP-MS)) require complex and expensive instrumentation and are not suitable for on-site analysis [1–5]. Currently, it is very difficult to analyze simultaneously several heavy metal ions in water with low detection limits without using these techniques and it is still a challenge to develop a sensor for on-site and real-time monitoring of various heavy metal ions with high selectivity and sensitivity [6]. There is consequently great demand for regular water quality monitoring to identify and assess heavy metal pollution in water [5].

The tendency towards on-site analysis requires new approaches and new instrumentation capable of procuring analytical information rapidly and with high sensitivity. The miniaturization of analytical procedures brings some important advantages for environmental continuous monitoring like enhanced portability and reduced reagents consumption and waste generation [7,8]. In this sense, microfluidic devices are broadly used because of the increase in surface area to volume ratio that improves process-control, reproducibility, allows the integration of different processes and yields faster reaction times [5, 9–12]. In the area of environmental pollution control and early warning systems, the combination of microelectronics and microfluidics with optical sensors is gaining importance, because of the simplicity of the integration [12,13].

Photoluminescent nanoparticles have attracted a lot of interest in recent years due to their potential applications in optical sensing [14, 15], as well as in medical and biological fields [16,17]. The use of these nanoparticles as analytical reagents enhances sensitivity, improves detection limits, and improves the stability of optical reagents [18]. Carbon Dots (CDs) show unique characteristics as optical reagents

---

[*] Corresponding author.
*E-mail address:* mariadelmar.puyol@uab.cat (M. Puyol).

https://doi.org/10.1016/j.snb.2022.132180
Received 15 March 2022; Received in revised form 6 May 2022; Accepted 6 June 2022
Available online 8 June 2022
0925-4005/© 2022 The Author(s). Published by Elsevier B.V. This is an open access article under the CC BY-NC-ND license (http://creativecommons.org/licenses/by-nc-nd/4.0/).

because of their excellent optical properties (tuneable fluorescence emission properties, high quantum yields, and photochemical stability) [19–21] and other outstanding properties like their solubility in water, chemical inertness [22], ease of functionalization, and good biocompatibility [23]. Additionally, CDs' low toxicity highlights them as an alternative to other luminescent nanoparticles as quantum dots [24,25]. Regarding the aim of this work, N-modified CDs have also been demonstrated to provide sensitivity to heavy metals, and an easy synthesis based on cheap precursors [26,27].

In this sense, we propose an automated microanalyzer for the determination of heavy metal ions as an on-site warning system based on the fluorescence quenching effect of these ions on the emission of CDs. For the multiparametric determination and as demonstrators of heavy metal pollution, we selected five different types of CDs from the bibliography with proven selectivity to $Co^{2+}$, $Cu^{2+}$, $Hg^{2+}$, $Ni^{2+}$, and $Pb^{2+}$. Hydrothermal and microwave-assisted bottom-up methods [28–32] were performed to synthesize five types of CDs as reagent demonstrators of heavy metals pollution. The microanalyzer is composed of a microfluidic platform and a customized miniaturized optical detection system. The platform is fabricated in cyclic olefin copolymer (COC), which is ideal for optical detection methods because of its high transparency in near-ultraviolet and visible regions compared to other polymers [9,33] and suited to multi-layered microfabrication techniques. Signal acquisition is computer controlled and the analytical method is based on a continuous flow strategy, specifically reverse Flow Injection Analysis (rFIA). The sample is continuously flowing as a carrier, into which a specific volume of the different CDs is periodically injected [34]. In this way, a transient signal is obtained with maximum emission when the sample does not contain heavy metals, and fluorescent quenched signal when heavy metals are present in the sample [35–38]. Fluorescence (measured as the peak height) is related to the analyte concentration following the Stern-Volmer equation. Finally, FIA systems procure reproducibility and automatic baseline recovery [39].

Chemical and hydrodynamic parameters of the developed microanalyzer have been optimized to achieve the lowest limit of detection of all the heavy metals and the highest repeatability by analyzing standard solutions. Finally, its applicability has been demonstrated by measuring heavy metals in spiked tap water and extracts of polluted soil samples from areas near a lead-zinc metal smelter, increasing confidence in the accuracy and validity of the results.

## 2. Material and methods

### 2.1. Chemicals and materials

Acrylic acid, citric acid, ethylenediamine, glycerol, imidazole-2-carboxylic acid, quinine sulphate, sodium citrate, urea, the metal salts mercury (II) nitrate, nickel (II) nitrate, cobalt (II) nitrate, lead (II) nitrate, copper nitrate, zinc nitrate, cadmium nitrate, sodium nitrate, calcium nitrate, magnesium nitrate, potassium chloride and potassium carbonate were purchased from Sigma-Aldrich (Barcelona, Spain). Polyethyleneimine, branched, was purchased from Fisher Scientific (Madrid, Spain). All the CDs synthesized were purified by dialysis against MilliQ water using a Pur-A-Lyzer Mega 1000 dialysis kit with a cut-off of 1 kDa.

Dispersions for the CDs syntheses and citric/citrate buffer were prepared in MilliQ water. All solutions for the microanalyzer characterization and the metal ion sensing were buffered at pH 4 with a 0.1 M citric/citrate buffer.

Cyclic Olefin Copolymer (COC) sheets were supplied from TOPAS Advanced Polymers GmbH (Florence, KY, USA).

### 2.2. Apparatus

A Labolan IDL.AI36 oven (Navarra, Spain) was used for the hydrothermal synthesis processes and a Bifinett KH 1106 domestic microwave oven for the microwave-assisted processes.

Absorption spectra were acquired with a Shimadzu UV-3101PC UV-Vis-NIR double beam spectrophotometer (Kyoto, Japan) and fluorescence spectra were registered with a Horiba Jobin Yvon Fluorolog FL3–11 spectrofluorometer (Longjumeau, France). Dynamic Light Scattering (DLS) measurements were performed in a Microtrac Nanotrac Flex nanoparticle size analyzer (Krefeld, Germany). High-Resolution Transmission Electron Microscopy (HR-TEM) images were taken on a high-resolution JEOL JEM-2011 Microscope (Tokyo, Japan).

### 2.3. Microfluidic platform and experimental setup

The fabrication process of the microfluidic platform starts with the design of the different layers with Computer-Aided Design (CAD) software. Every COC layer substrate was machined on an LPKF Laser and Electronics Protomat S63 Computer Numerical Control (CNC) micromilling machine (Garbsen, Germany). The different layers were thermolaminated using a Talleres Francisco Camps hydraulic press (Granollers, Spain). The microfluidic platform is formed by a structural layer of TOPAS 5013, which was previously laminated with two films of lower glass transition temperature (TOPAS 8007) acting as sealing layers [40], and two outer layers of TOPAS 5013. Once overlapped and aligned, COC tapes were laminated to obtain the final device. As it can be seen in Fig. 1A, the microfluidic platform (30 mm wide, 50 mm height, and 2 mm depth) has two inlets, a two-dimensional meander micromixer (0.8 mm wide and 1 mm depth), an optical flow cell (4.5 mm diameter and 1 mm depth), and an outlet.

The experimental setup is based on a rFIA, where CDs are sequentially injected into a blank (buffer solution) and samples (standard solutions, spiked tap water and soil extracts). The microfluidic set-up allows the pre-buffering of the samples by an in-line T connector mixer (sample/buffer solution in 1:1 proportion). For continuous flow injection, the microfluidic platform was connected with 0.8 mm internal diameter Teflon tubing (Tecnyfluor, Barcelona, Spain), to a Gilson Minipuls 2 peristaltic pump (Middleton, WI, USA) fitted with 1.14 mm internal diameter Tygon tubing (Ismatec, Wertheim, Germany). Connections were secured with O-rings FPM75 (Epidor, Barcelona, Spain). A Hamilton MVP TMI-6116 six-port injection valve (Bonaduz, Switzerland) was used to inject the CDs.

The microfluidic platform is inserted in a customized miniaturized optical detection system (Fig. 1B) by using an Optical Lock and Key Reader approach [8]. It consists of a LED emitting at 365 nm (OSA Opto Light GmbH EOLD-365–525), a Thorlabs 460/60 25 mm band-pass filter (Munich, Germany), and a PIN photodetector (Hamamatsu S1337–66BR) with 33 $mm^2$ of active area mounted and integrated on a printed circuit board (PCB). The optical detection system is modulated

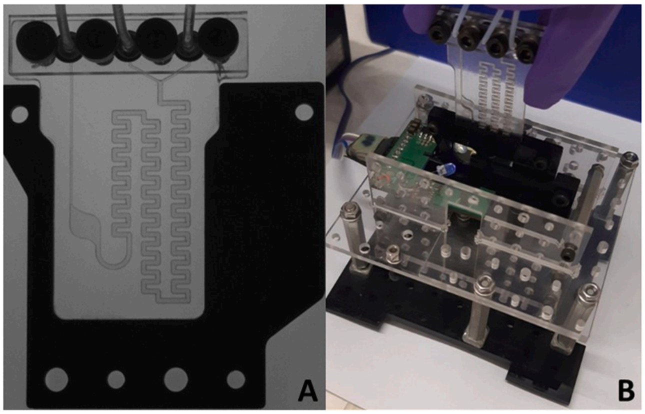

**Fig. 1.** (A) Microfluidic platform fabricated for the heavy metal ions detection. (B) Customized miniaturized optical detection system with the microfluidic platform inserted.

with a digital lock-in amplifier to avoid light interferences and the signal is obtained with a NI USB-6211 Data Acquisition Card (National Instruments, Austin, TX, USA).

### 2.4. CDs synthesis and optical characterization

Five different CDs were synthesized following published synthesis procedures: CDs synthesized with citric acid and ethylenediamine (ED CDs) [28], CDs synthesized with citric acid and polyethyleneimine (PEI CDs) [29], CDs synthesized with glycerol and ethylenediamine (EA CDs) [30], CDs synthesized with citric acid, urea, and imidazole (UREA CDs) [31], CDs synthesized with acrylic acid and ethylenediamine (ACR CDs) [32]. All batches were dialyzed against MilliQ water using a dialysis membrane with a cut-off of 1 kDa for their purification and kept in a refrigerator. Since the concentration of the CDs is unknown, dilution factors in citric/citrate buffer are used as an approximate measurement.

Absorption spectra and photoluminescence spectra (excitation and emission) of CDs' water dispersions were obtained. Quantum Yields (QYs) were calculated with the optically dilute measurement method [41] using quinine sulphate in 0.1 M sulphuric acid as a standard.

### 2.5. Optimization of the chemical and hydrodynamic parameters of the microanalyzer

Some chemical and hydrodynamic parameters were optimized using a univariate optimization procedure taking as compromise signal to noise ratio and sensitivity for all the five target heavy metals.

Citric/citrate buffer solutions prepared at four different pH values (3, 4, 5, and 6) and four different concentration levels (0.001, 0.01, 0.1 and 1 M) were tested to obtain the maximum fluorescence signal and taking into account the solubility of the different heavy metal ions.

Regarding hydrodynamic parameters, the flow rate of the sample (carrier) was tested from 0.5 to 2 mL/min and CDs injection volume from 0.1 to 1 mL. Moreover, some operational parameters of the optical detection system like signal amplification and integration time were optimized. In this case, CDs were injected into buffer solution and 0.01 ppm heavy metal standard solutions to evaluate the signal to noise ratio and detection limit.

Finally, different dilution factors of the CDs dispersions were also tested. For the five types of CDs, 10, 50, 100, 500 and 1000 dilutions in buffer solution, were prepared.

### 2.6. Characterization of CDs selectivity

Before performing photoluminescence studies of the synthesized CDs, a dilution was done to obtain an absorption of 0.05 a.u. and avoid possible self-absorption effects.

Selectivity of the different CDs was firstly tested in batch against different heavy metal ion solutions ($Cd^{2+}$, $Co^{2+}$, $Cu^{2+}$, $Hg^{2+}$, $Ni^{2+}$, $Pb^{2+}$, $Zn^{2+}$), and other potentially interfering ions present in water ($Na^{+}$, $Mg^{2+}$, $Ca^{2+}$, $Cl^{-}$, $CO_3^{2-}$). Emission spectra of 0.5 mL of the corresponding CD dispersion at the optimized dilution factor showing an absorption of 0.05 a.u. with the addition of 2.5 mL of citric/citrate buffer at pH 4 were compared with the same CDs dispersion with the addition of 2.5 mL of a buffered solution containing a specific ion at a concentration of 10 ppm (in the case of the heavy metal ions) or at a concentration of 1000 ppm (for other potentially interfering ions) after the dilution in the cuvette.

### 2.7. Analytical quality parameters of the microanalyzer

Selectivity was tested in the microfluidic system using several standard solutions with a 0.5 ppm concentration of the target heavy metal ($Co^{2+}$, $Cu^{2+}$, $Hg^{2+}$, $Ni^{2+}$, and $Pb^{2+}$ in each case). Every standard solution also contained the rest of the heavy metal ions tested at a concentration of 10 ppm and the other potentially interfering ions tested at a concentration of 1000 ppm.

Limit of detection was evaluated from the calibration curves obtained by injecting per triplicate each type of CDs in standard solutions containing increasing concentrations of the five heavy metals studied (0.01, 0.05, 0.1, 0.5, and 1 ppm) and the other interfering ions. Fluorescence quenching of the CDs was studied through the Stern-Volmer equation [42].

Repeatability of the analytical system was evaluated by performing ten injections of each CD into a standard solution containing 0.5 ppm of each target heavy metal and the other studied ions.

### 2.8. Samples analysis

To assess the applicability of this method, spiked tap water samples and extracts of polluted soil samples were tested. Tap water samples were spiked to obtain concentrations of 0.03, 0.06, 0.1, 0.4, and 0.8 ppm of the target heavy metals. They were also spiked with the rest of the heavy metal ions tested at a concentration of 10 ppm and the other potentially interfering ions tested at a concentration of 1000 ppm.

Nitric acid extracts of polluted soil samples coming from the neighbourhood of a smelter plant (located in Torreon, Mexico) and containing high concentrations of four of the five heavy metals studied ($Hg^{2+}$ is not present), were directly supplied, and analyzed by the reference method ICP-OES and the proposed microanalyzer, for comparison purposes. 0.5 g of the samples were digested with 10 mL of nitric acid in a Milestone Ultrawave microwave digestion system at 175ºC for 15 min. Samples were filtered with a 0.45 μm filter, diluted to 50 mL with MilliQ water, and finally analyzed with a Perkin-Elmer Optima 4300DV spectrometer.

Calibration curves were performed with standard solutions at higher concentrations (different concentration ranges depending on the analyte). As stated, to avoid pH changes of these acid extracts, samples were automatically buffered in the system before the injection of the CDs. Moreover, an exhaustive cleaning of the microsystem consisting of flowing buffer solution for 2 min was necessary between samples.

## 3. Results and discussion

### 3.1. CDs characterization

As reproducibility and characteristics of the synthesized CDs will impact directly on the analytical results and reproducibility of the analytical method, CDs were fully characterized. Regarding optical properties, they show similar absorbance and photoluminescence spectra, with a wide absorption band around 350 nm and a wide emission band around 450 nm, obtaining Stokes' shifts of approximately 100 nm in all cases, as it can be seen in Fig. 2. Therefore, all of them could be used as optical reagents with the same miniaturized optical setup.

QYs were calculated, obtaining values of 78 % for ED CDs, 32 % for PEI CDs, 16 % for EA CDs, 44 % for UREA CDs, and 25 % for ACR CDs.

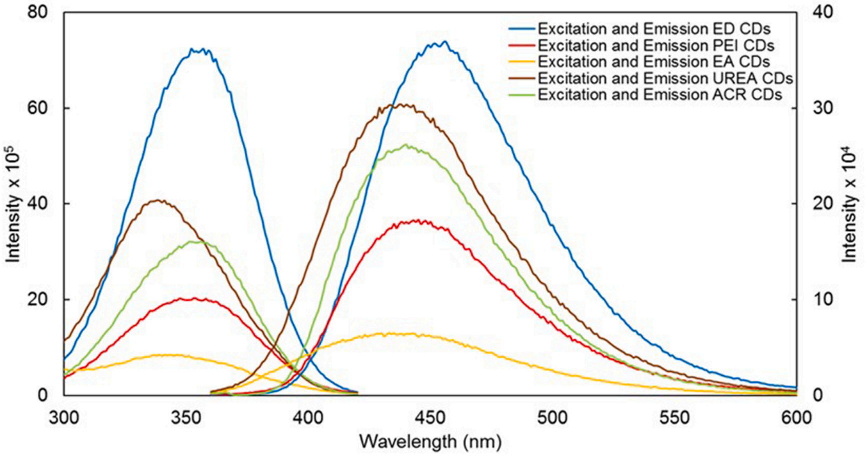

**Fig. 2.** Excitation and emission spectra of the five synthesized CDs.

Size and shape were obtained with HR-TEM images and DLS measurements. Results showed spherical shape nanoparticles with sizes ranging from 2 to 4 nm. Although high-quality contrast images are difficult to obtain with CDs with HR-TEM, we observed two populations of CDs, one with a crystalline structure, where the diffraction planes could be distinguished and the other amorphous one.

### *3.2. CDs selectivity tests in batch*

First, the quenching effect of different heavy metals, and other potentially interfering ions present in water was investigated in batch. A great number of publications demonstrate that different types of N-modified CDs present very strong interactions towards different heavy metal ions through the surface functional groups (-COOH, -OH, -CONH-) [28–32]. According to the bibliography and as shown in the supplementary information (Fig. S2A-E), each CD dispersion was selective to a specific heavy metal. ED CDs show good selectivity to $Hg^{2+}$, PEI CDs to $Cu^{2+}$, EA CDs to $Pb^{2+}$, UREA CDs to $Ni^{2+}$, and ACR CDs to $Co^{2+}$. The quenching effect of all the other tested ions was not significant. In these experiments, it could also be noticed the different sensitivity of the synthesized CDs to the target heavy metal, which would affect the optimization of the measurement conditions of the optical detection system of the microanalyzer for multiparametric measurements.

### *3.3. Optimization of the microanalyzer*

Different chemical, hydrodynamic and optical measuring variables of the microanalyzer were optimized to make possible the multiparametric detection of heavy metals in water, as a compromise between the best S/N, limits of detection, response time and reagents saving. Tested values intervals and the final optimal selected values are shown in Table 1.

**Table 1**
Optimization of chemical, operational and hydrodynamic parameters.

| Parameter | Tested interval | Optimal value |
|---|---|---|
| Buffer concentration (M) | 0.001 – 1.000 | 0.100 |
| Buffer pH | 3 – 6 | 4 |
| Injection volume (mL) | 0.1 – 1.0 | 0.5 |
| Carrier flow rate (mL/min) | 0.5 – 2.0 | 1.5 |
| Signal amplification | 1 – 100 | 10 |
| Integration time (s) | 0.1 – 1.0 | 0.1 |
| ED CDs dilution factor | 10–1000 | 100 |
| PEI CDs dilution factor | 10–1000 | 50 |
| EA CDs dilution factor | 10–1000 | 10 |
| UREA CDs dilution factor | 10–1000 | 50 |
| ACR CDs dilution factor | 10–1000 | 10 |

As an example, Fig. 3A shows optimization of the buffer pH. The optical properties of CDs are sensitive to pH due to the ionizable functional groups on the surface. Therefore, the analytical system must operate at a constant pH. In general, the higher the pH, the higher the fluorescence of the CDs. However, the selected pH must ensure to have heavy metal species free in solution. As it can be seen, the highest fluorescence intensity is obtained at pH 4 for all the different CDs. On the other hand, the effect of the flow rate on the measured signal can be seen in Fig. 3B with the injection of 0.5 mL of a dilution of 100 of ED CDs into a 0.1 M citric/citrate buffer at pH 4 as an example. A faster flow rate implies a more rapid analysis and therefore, higher sample throughput, which are desirable. However, slightly less intense peaks are obtained because the sample is less time in contact with the CDs. The lower is the flow rate, the wider and more intense are the obtained peaks until achieving the steady-state signal. Therefore, a 1.5 mL/min sample flow rate was chosen as the optimal one for subsequent experiments. At this flow rate, response time is calculated in 50 s

### *3.4. Analytical quality parameters of the microanalyzer*

Analytical quality parameters were calculated from calibration curves obtained performing the separate analysis of each heavy metal at the optimized operational values. Fig. 4A show the transient response of the microsystem by injecting the five optimized CDs dispersions into buffer solution and into 0.5 ppm standard solutions of the target heavy metal ($Co^{2+}$, $Cu^{2+}$, $Hg^{2+}$, $Ni^{2+}$, and $Pb^{2+}$) which also contained the rest of the heavy metal ions tested at a concentration of 10 ppm and the other potentially interfering ions tested at a concentration of 1000 ppm. Results obtained confirm the selectivity of the different CDs tested in batch. The fluorescence signal quickly returned to the baseline after each signal peak and there was not any significant signal drift of the baseline. This demonstrates the robustness of the microanalyzer for the proposed application.

Calibration curves showed a good linear correlation between 0.01 and 1 ppm, as can be seen in Fig. 4B. And even though the Stern-Volmer model has some limitations that affect the accuracy, caused by deviations at high concentrations [43,44], concentration ranges as high as 50–600 ppm were tested for real polluted samples, showing also good linear correlation but lower sensitivity.

Detection limits, LODs (Table 2) were calculated as 3 SD/$K_{SV}$ (where SD is the standard deviation of the blank and $K_{SV}$ (Stern-Volmer constant) is the slope of the linear fit near to unity).

Repeatability was calculated as relative standard deviation (RSD) obtained with 10 repeated injections of the same CDs into the 0.5 ppm heavy metal standard solutions. Data is detailed in Table 2, showing values under 1.2%.

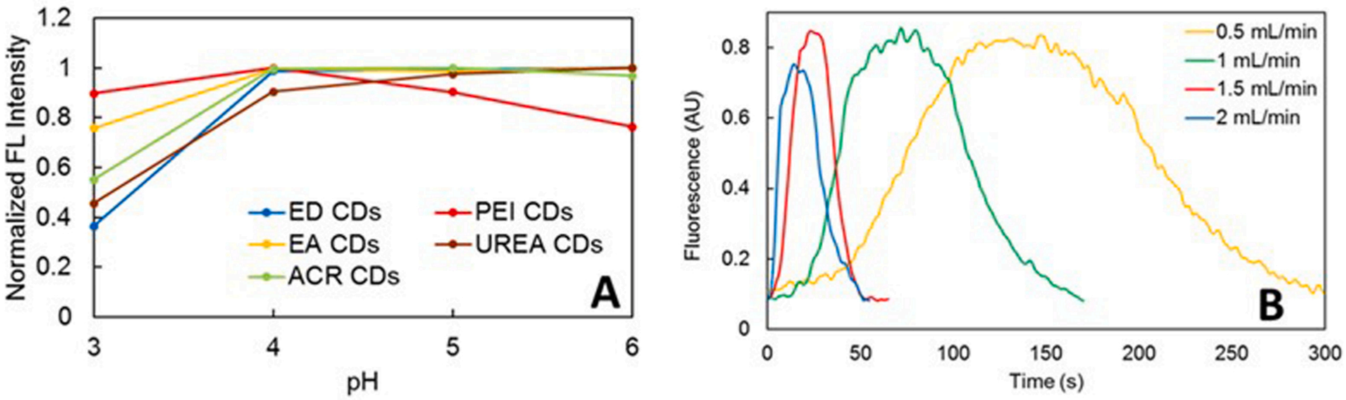

**Fig. 3.** (A) Normalized fluorescence intensity obtained by injecting the five CDs at their optimal dilution factor into 0.1 M citric/citrate buffer solutions of different pH values. (B) Effect of flow rate into the obtained signal for an injection of 0.5 mL of ED CDs (100 dilution factor) into buffer solution.

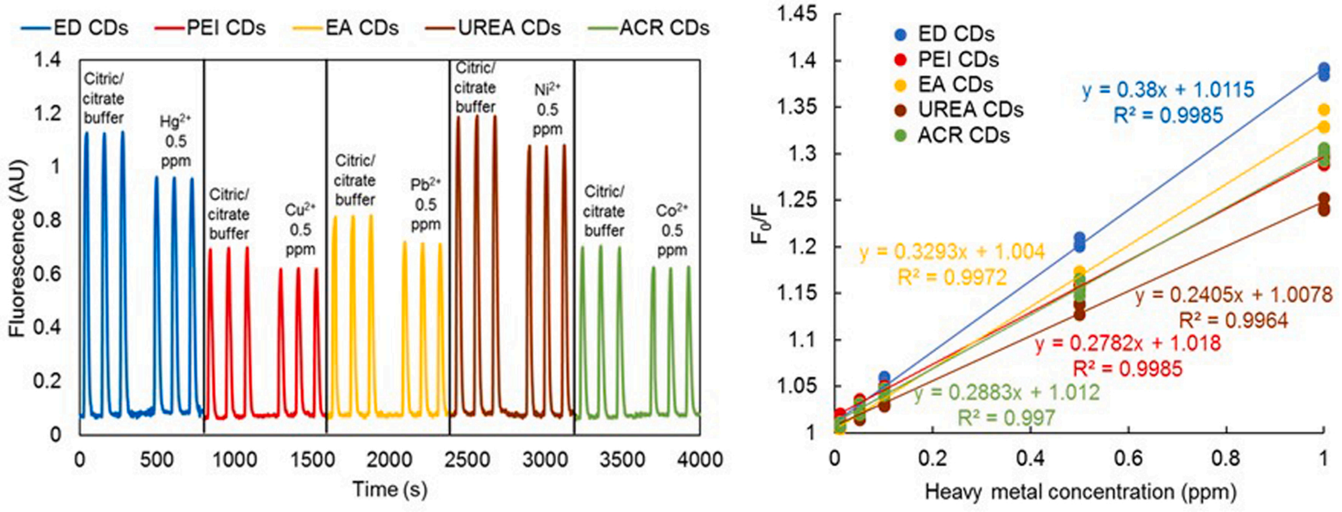

**Fig. 4.** (A) Transient response of the microsystem by injecting the CDs into buffer solution (as intensity value with no quencher) and to different standard solutions of heavy metals containing potential interferents ($Zn^{2+}$, $Cd^{2+}$, $Na^{+}$, $Mg^{2+}$, $Ca^{2+}$, $Cl^{-}$, $CO_3^{2-}$). (B) Stern-Volmer representation of quenching effect of the target heavy metals on the fluorescence of the five types of CDs.

**Table 2**
Results summarizing the analytical performance of the proposed microanalyzer for the monitoring of heavy metals in water samples.

| Type of CDs | Selectivity | $K_{SV}$ ($ppm^{-1}$) | Detection Limit (ppb) | RSD (%) |
|---|---|---|---|---|
| ED CDs | $Hg^{2+}$ | 0.3800 | 5.9 ± 0.8 | 0.5 |
| PEI CDs | $Cu^{2+}$ | 0.2782 | 11.7 ± 0.7 | 1.2 |
| EA CDs | $Pb^{2+}$ | 0.3293 | 8.8 ± 0.8 | 1.1 |
| UREA CDs | $Ni^{2+}$ | 0.2405 | 2.5 ± 0.3 | 0.4 |
| ACR CDs | $Co^{2+}$ | 0.2883 | 3.9 ± 0.5 | 0.9 |

### 3.5. *Samples analysis*

Spiked tap water samples were analyzed at the optimized conditions and after performing a calibration experiment for each heavy metal. Table 3 shows recovery rates. In general, an overestimation is noticed for the less concentrated samples near the limit of detection. At this concentration level, results are also less precise because the error of the interpolated signal is higher at lower concentrations. However, as a warning system, results allow determining the estimated value of heavy metals as indicators of pollution.

To validate the usability of the developed microanalyzer, real polluted soil samples taken from areas surrounding a metallurgic industry were analyzed. Nitric acid extracts were prepared and analyzed by a reference method (ICP-OES) and the proposed microanalyzer. Fig. 5 shows, as an example, the calibration curve for $Co^{2+}$ at a higher concentration range (10–70 ppm) where it can be noticed from the slope of the calibration curve a lower sensitivity. Fig. 6 shows the comparative test for the measurement of $Co^{2+}$ in 8 different samples. Regression equations of the comparison test (intercept, slope, and correlation coefficient) for the five heavy metal ions as well as $t_{calc}$ values obtained

**Table 3**
Determination of the heavy metals studied in spiked tap water samples.

| | | Analyte recovery rates | | | | |
|---|---|---|---|---|---|---|
| **Sample** | **Concentration of the analyte in the sample (ppm)** | **$Hg^{2+}$** | **$Cu^{2+}$** | **$Pb^{2+}$** | **$Ni^{2+}$** | **$Co^{2+}$** |
| Spiked tap water | 0.03 | 129 % | 131 % | 134 % | 123 % | 120 % |
| | 0.06 | 116 % | 112 % | 120 % | 110 % | 111 % |
| | 0.1 | 105 % | 103 % | 105 % | 104 % | 105 % |
| | 0.4 | 101 % | 100 % | 102 % | 100 % | 100 % |
| | 0.8 | 99.1 % | 99.0 % | 101 % | 98.8 % | 98.2 % |

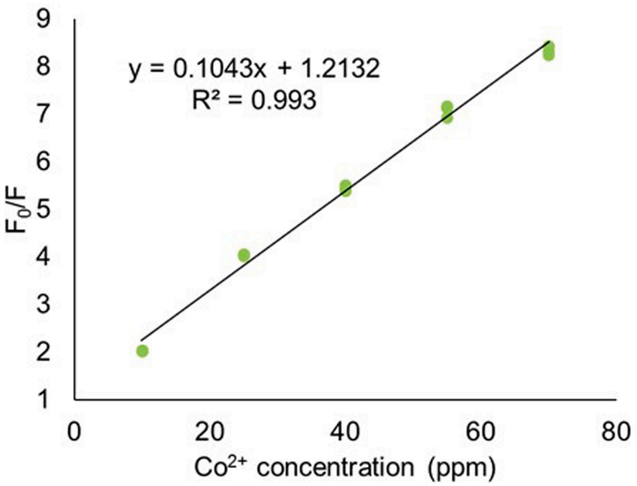

**Fig. 5.** Stern-Volmer representation of quenching effect of $Co^{2+}$ on the fluorescence of ACR CDs in a higher concentration range (10–70 ppm).

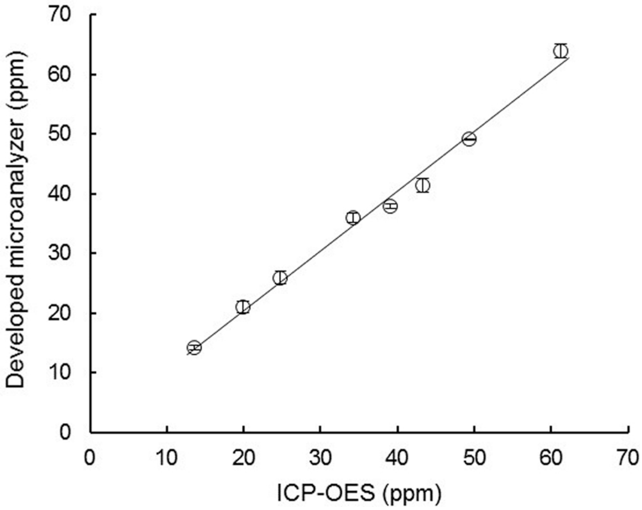

**Fig. 6.** Comparative study between the results for the analysis of $Co^{2+}$ in polluted soil samples (n = 8) obtained by the developed microanalyzer and the reference method (ICP-OES).

**Table 4**
Concentration of the heavy metals studied in polluted soil samples determined by the reference method (ICP-OES) and with the proposed method, and accuracy expressed as (% error).

| Sample number | $[Cu^{2+}]$ ICP-OES (ppm) | $[Cu^{2+}]$ proposed method (ppm) | % error | $[Pb^{2+}]$ ICP-OES (ppm) | $[Pb^{2+}]$ proposed method (ppm) | % error |
|---|---|---|---|---|---|---|
| **1** | 576.2 | 587.0 | 1.9 | 11.5 | 12.0 | 4.8 |
| **2** | 255.7 | 251.1 | 1.8 | 4.8 | 4.9 | 2.1 |
| **3** | 511.7 | 507.3 | 0.9 | 5.3 | 5.2 | 1.7 |
| **4** | 119.7 | 116.2 | 2.9 | 3.7 | 3.9 | 7.4 |
| **5** | 231.9 | 236.5 | 2.0 | 4.0 | 4.0 | 1.0 |
| **6** | 458.3 | 477.9 | 4.3 | 7.1 | 7.0 | 1.3 |
| **7** | 90.5 | 92.2 | 1.9 | 0.8 | 0.8 | 4.0 |
| **8** | 95.7 | 92.4 | 3.4 | 2.2 | 2.3 | 7.5 |

| Sample number | $[Ni^{2+}]$ ICP-OES (ppm) | $[Ni^{2+}]$ proposed method (ppm) | % error | $[Co^{2+}]$ ICP-OES (ppm) | $[Co^{2+}]$ proposed method (ppm) | % error |
|---|---|---|---|---|---|---|
| **1** | 42.3 | 42.8 | 1.0 | 49.4 | 49.1 | 0.5 |
| **2** | 31.8 | 31.6 | 0.7 | 34.2 | 36.0 | 5.1 |
| **3** | 61.3 | 61.9 | 1.0 | 61.3 | 63.9 | 4.3 |
| **4** | 35.8 | 35.9 | 0.3 | 24.8 | 26.0 | 4.8 |
| **5** | 57.9 | 58.7 | 1.4 | 39.1 | 37.9 | 3.1 |
| **6** | 33.4 | 32.9 | 1.4 | 43.3 | 41.4 | 4.4 |
| **7** | 25.7 | 26.4 | 3.1 | 13.6 | 14.3 | 4.5 |
| **8** | 33.9 | 35.4 | 4.4 | 19.9 | 21.0 | 5.7 |

with the paired t-test are shown in the Supplementary Information (Table S1). From the statistical data treatment, it can be concluded results obtained with the developed microanalyzer were not significantly different from the ones measured with the reference method according to the paired t-test ($t_{calc} < t_{tab}$) for the four heavy metals analyzed.

Table 4 shows accuracy expressed as % error for the differences between results obtained with both methods. As it can be seen, accuracy is different for each heavy metal and, as it is more affected at lower concentrations, the determination of $Pb^{2+}$ is less accurate. However, a maximum value of 7.5% error is calculated.

## 4. Conclusions

In this paper we have developed a new multiparametric microanalyzer as a warning system for heavy metals pollution monitoring. Thanks to the reduced dimensions of the fluidic system, it consumes small volumes of reagents and has a fast analysis time. Although sample treatment (buffering) must be performed, which for acid extracts was crucial, this is performed by the same flow management systems before CDs are injected. Performance of the microanalyzer, tested with standard solutions, spiked tap water and real samples, combined with the stability of the luminescent reagents (N-modified CDs) demonstrates its potential application for long-term and continuous monitoring of heavy metals in water. Five different heavy metals ($Co^{2+}$, $Cu^{2+}$, $Hg^{2+}$, $Ni^{2+}$ and $Pb^{2+}$) have been selectively detected. However, it is possible to expand the analytes to determine, as far as other selective CDs (with absorption bands around 350 nm) could be synthesized. In most of the cases, LODs comply with the regulation [5] concerning heavy metal pollution in water (between 2 and 12 ppb) but in the case of $Hg^{2+}$, the established LOD is still lower. Some future work must be conducted in order to finally validate the real applicability of the proposed methodology for heavy metals monitoring, such as long-term studies. Despite current maintenance criteria of quality control stations is approximately every 15 days and no critical issues are expected regarding the stability of CDs, this should be assessed. Taking into account results for repeatability, selectivity, recoveries of spiked tap water samples and accuracy of real polluted samples, we demonstrate its applicability as an on-site warning system of heavy metals contamination.

Although the presented set-up requires bulky components for flow management in continuous mode, such as a peristaltic pump, the equipment can be further miniaturized, and it is easily automatable. We are currently working on the development of an automatic and computer-controlled microanalyzer based on the use of solenoid peristaltic micro-pumps and three-way solenoid valves, enabling automation of the whole analytical procedure.

## CRediT authorship contribution statement

**Alex Pascual-Esco:** Methodology Development, Investigation, Data analysis, Statistical analysis, Validation and Writing – original draft. **Julián Alonso-Chamarro:** Resources, Project administration, Funding acquisition, and Writing – review & editing. Mar Puyol: Research Conceptualization, Resources, Supervision, Project administration, Funding acquisition, and Writing – original draft.

## Declaration of Competing Interest

The authors declare that they have no known competing financial interests or personal relationships that could have appeared to influence the work reported in this paper.

## Acknowledgements

We gratefully thank the Instituto Tecnológico de la Laguna (Torreón, México) for soil samples supply and Dr. Eva Arasa for the soil extracts preparation. This work has been financially supported by the Spanish Ministry of Science and Innovation (MICINN) through project CTQ2017-85011-R and project PID2020-117216RB-I00, co-funded by FEDER (Fondo Europeo de Desarrollo Regional), and the Catalonia Government through 2017SGR-220. The support of Met-Mex Peñoles for the development of this work was also gratefully acknowledged.

## Appendix A. Supporting information

Supplementary data associated with this article can be found in the online version at doi:10.1016/j.snb.2022.132180.

## References

[1] Z. Wang, C. Xu, Y. Lu, X. Chen, H. Yuan, G. Wei, G. Ye, J. Chen, Fluorescence sensor array based on amino acid derived carbon dots for pattern-based detection of toxic metal ions, Sens. Actuators B Chem. 241 (2017) 1324–1330, https://doi.org/10.1016/j.snb.2016.09.186.

[2] C.Y. Wang, C.C. Hsu, Online, continuous, and interference-free monitoring of trace heavy metals in water using plasma spectroscopy driven by actively modulated pulsed power, Environ. Sci. Technol. 53 (2019) 10888–10896, https://doi.org/10.1021/acs.est.9b02970.

[3] N. Ullah, M. Mansha, I. Khan, A. Qurashi, Nanomaterial-based optical chemical sensors for the detection of heavy metals in water: recent advances and challenges, Trends Anal. Chem. 100 (2018) 155–166, https://doi.org/10.1016/j.trac.2018.01.002.

[4] J.P. Devadhasan, J. Kim, A chemically functionalized paper-based microfluidic platform for multiplex heavy metal detection, Sens. Actuators B Chem. 273 (2018) 18–24, https://doi.org/10.1016/j.snb.2018.06.005.

[5] A. Lace, J. Cleary, A review of microfluidic detection strategies for heavy metals in water, Chemosensors 9 (60) (2021) 1–26, https://doi.org/10.3390/chemosensors9040060.

[6] X. Liu, Y. Wang, Y. Song, Visually multiplexed quantitation of heavy metal ions in water using volumetric bar-chart chip, Biosens. Bioelectron. 117 (2018) 644–650, https://doi.org/10.1016/j.bios.2018.06.046.

[7] Ö. Biçen Ünlüer, F. Ghorbani-Bidkorbeh, R. Keçili, C. Mustansar Hussain, Future of the modern age of analytical chemistry: Nanominiaturization, in: C. Mustansar Hussain (Ed.), Handbook on Miniaturization in Analytical Chemistry: Application of Nanotechnology, Elsevier, Amsterdam, 2020, pp. 277–296.

[8] O. Ymbern, M. Berenguel-Alonso, A. Calvo-López, S. Gómez-de Pedro, D. Izquierdo, J. Alonso-Chamarro, Versatile lock and key assembly for optical measurements with microfluidic platforms and cartridges, Anal. Chem. 87 (2015) 1503–1508, https://doi.org/10.1021/ac504255t.

[9] R.K. Jena, C.Y. Yue, Y.C. Lam, Micro fabrication of cyclic olefin copolymer (COC) based microfluidic devices, Microsyst. Technol. 18 (2012) 159–166, https://doi.org/10.1007/s00542-011-1366-z.

[10] N. Yogarajaha, S.S.H. Tsai, Detection of trace arsenic in drinking water: challenges and opportunities for microfluidics, Environ. Sci.: Water Res. Technol. 1 (2015) 426–447, https://doi.org/10.1039/c5ew00099h.

[11] L. Lin, Y. Yin, S.A. Starostin, H. Xu, C. Li, K. Wu, C. He, V. Hessel, Microfluidic fabrication of fluorescent nanomaterials: a review, Chem. Eng. J. 425 (131511) (2021) 1–15, https://doi.org/10.1016/j.cej.2021.131511.

[12] H. Gai, Y. Li, E.S. Yeung, Optical detection systems on microfluidic chips, in: B. Lin (Ed.), Microfluidics: Technologies and Applications, Springer, Berlin, 2011, pp. 171–201.

[13] K.A. Lukyanenko, I.A. Denisov, V.V. Sorokin, A.S. Yakimov, E.N. Esimbekova, P. I. Belobrov, Handheld enzymatic luminescent biosensor for rapid detection of heavy metals in water samples, Chemosensors 7 (2019) 1–10, https://doi.org/10.3390/chemosensors7010016.

[14] M. Berenguel-Alonso, I. Ortiz-Gómez, B. Fernández, P. Couceiro, J. Alonso-Chamarro, L.F. Capitán-Vallvey, A. Salinas-Castillo, M. Puyol, An LTCC monolithic microreactor for the synthesis of carbon dots with photoluminescence imaging of the reaction progress, Sens. Actuators B Chem. 296 (126613) (2019) 1–8, https://doi.org/10.1016/j.snb.2019.05.090.

[15] F. Copur, N. Bekar, E. Zor, S. Alpaydin, H. Bingol, Nanopaper-based photoluminescent enantioselective sensing of L-Lysine by L-Cysteine modified carbon quantum dots, Sens. Actuators B Chem. 279 (2019) 305–312, https://doi.org/10.1016/j.snb.2018.10.026.

[16] M.L.C. Passos, P.C.A.G. Pinto, J.L.M. Santos, M.L.M.F.S. Saraiva, A.R.T.S. Araujo, Nanoparticle-based assays in automated flow systems: a review, Anal. Chim. Acta 889 (2015) 22–34, https://doi.org/10.1016/j.aca.2015.05.052.

[17] Y. Liu, F. Seidi, C. Deng, R. Li, T. Xu, H. Xiao, Porphyrin derived dual-emissive carbon quantum dots: customizable synthesis and application for intracellular Cu2 + quantification, Sensors Actuators B Chem. 343 (2021), 130072, https://doi.org/10.1016/j.snb.2021.130072.

[18] T. Chen, S. Yin, J. Wu, Nanomaterials meet microfluidics: improved analytical methods and high-throughput synthetic approaches, Trends Anal. Chem. 142 (116309) (2021) 1–19, https://doi.org/10.1016/j.trac.2021.116309.

[19] K.J. Mintz, Y. Zhou, R.M. Leblanc, Recent development of carbon quantum dots regarding their optical properties, photoluminescence mechanism, and core structure, Nanoscale 11 (2019) 4634–4652, https://doi.org/10.1039/c8nr10059d.

[20] A. Simpson, R.R. Pandey, C.C. Chusuei, K. Ghosh, R. Patel, A.K. Wanekaya, Fabrication characterization and potential applications of carbon nanoparticles in the detection of heavy metal ions in aqueous media, Carbon 127 (2018) 122–130, https://doi.org/10.1016/j.carbon.2017.10.086.

[21] R. Jelinek, Carbon Quantum Dots: Synthesis, Properties and Applications, electronic ed, Springer, Cham (Switzerland), 2017.

[22] Y. Wang, A. Hu, Carbon quantum dots: synthesis, properties and applications, J. Mater. Chem. C. 2 (2014) 6921–6939, https://doi.org/10.1039/c4tc00988f.

[23] S. Anwar, H. Ding, M. Xu, X. Hu, Z. Li, J. Wang, L. Liu, L. Jiang, D. Wang, C. Dong, M. Yan, Q. Wang, H. Bi, Recent advances in synthesis, optical properties, and biomedical applications of carbon dots, ACS Appl. Bio Mater. 2 (6) (2019) 2317–2338, https://doi.org/10.1021/acsabm.9b00112.

[24] M.L. Liu, B.B. Chen, C.M. Li, C.Z. Huang, Carbon dots: synthesis, formation mechanism, fluorescence origin and sensing applications, Green. Chem. 21 (2019) 449–471, https://doi.org/10.1039/c8gc02736f.

[25] J.H. Liu, Y. Wang, G.H. Yan, F. Yang, H. Gao, Y. Huang, H. Wang, P. Wang, L. Yang, Y. Tang, L.R. Teisl, Y.P. Sun, Systematic toxicity evaluations of high-performance carbon "Quantum" dots, J. Nanosci. Nanotechnol. 19 (4) (2019) 2130–2137, https://doi.org/10.1166/jnn.2019.15807.

[26] X. Sun, Y. Lei, Fluorescent carbon dots and their sensing applications, Trends Anal. Chem. 89 (2017) 163–180, https://doi.org/10.1016/j.trac.2017.02.001.

[27] P. Li, S.F.Y. Li, Recent advances in fluorescence probes based on carbon dots for sensing and speciation of heavy metals, Nanophotonics 10 (2) (2020) 877–908, https://doi.org/10.1515/nanoph-2020-0507.

[28] F. Du, F. Zeng, Y. Ming, S. Wu, Carbon dots-based fluorescent probes for sensitive and selective detection of iodide, Microchim. Acta 180 (2013) 453–460, https://doi.org/10.1007/s00604-013-0954-2.

[29] A. Salinas-Castillo, M. Ariza-Avidad, C. Pritz, M. Camprubí-Robles, B. Fernández, M.J. Ruedas-Rama, A. Megia-Fernández, A. Lapresta-Fernández, F. Santoyo-Gonzalez, A. Schrott-Fischer, L.F. Capitan-Vallvey, Carbon dots for copper detection with down and upconversion fluorescent properties as excitation sources, Chem. Commun. 49 (2013) 1103–1105, https://doi.org/10.1039/c2cc36450f.

[30] Y. Jiang, Y. Wang, F. Meng, B. Wang, Y. Cheng, C. Zhu, N-doped carbon dots synthesized by rapid microwave irradiation as highly fluorescent probes for Pb2+ detection, N. J. Chem. 39 (2015) 3357–3360, https://doi.org/10.1039/c5nj00170f.

[31] X. Wang, D. Wang, Y. Guo, C. Yang, A. Iqbal, W. Liu, W. Qin, D. Yan, H. Guo, Imidazole derivative-functionalized carbon dots: using as a fluorescent probe for detecting water and imaging of live cells, Dalton Trans. 44 (2015) 5547–5554, https://doi.org/10.1039/c5dt00128e.

[32] N. Jing, M. Tian, Y. Wang, Y. Zhang, Nitrogen-doped carbon dots synthesized from acrylic acid and ethylenediamine for simple and selective determination of cobalt ions in aqueous media, J. Lumin. 206 (2019) 169–175, https://doi.org/10.1016/j.jlumin.2018.10.059.

[33] M. Denz, G. Brehm, C.Y.J. Hémonnot, H. Spears, A. Wittmeier, C. Cassini, O. Saldanha, E. Perego, A. Diaz, M. Burghammerd, S. Köster, Cyclic olefin copolymer as an X-ray compatible material for microfluidic devices, Lab Chip 18 (2018) 171–178, https://doi.org/10.1039/c7lc00824d.

[34] L. Chen, J. Xu, T. Wang, Y. Huang, D. Yuan, Z. Gong, Toward a versatile flow technique: Development and application of reverse flow dual-injection analysis (rFDIA) for determining dissolved iron redox species and soluble reactive phosphorus in seawater, Talanta 232 (122404) (2021) 1–9, https://doi.org/10.1016/j.talanta.2021.122404.

[35] C. Hu, T.J. Lin, Y.C. Huang, Y.Y. Chen, K.H. Wang, K.Y.A. Lin, Photoluminescence quenching of thermally treated waste-derived carbon dots for selective metal ion sensing, Environ. Res. 197 (111008) (2021) 1–10, https://doi.org/10.1016/j.envres.2021.111008.

[36] F. Zu, F. Yan, Z. Bai, J. Xu, Y. Wang, Y. Huang, X. Zhou, The quenching of the fluorescence of carbon dots: a review on mechanisms and applications, Microchim. Acta 184 (2017) 1899–1914, https://doi.org/10.1007/s00604-017-2318-9.

[37] H. Lee, Y.C. Su, H.H. Tang, Y.S. Lee, J.Y. Lee, C.C. Hu, T.C. Chiu, One-Pot hydrothermal synthesis of carbon dots as fluorescent probes for the determination of mercuric and hypochlorite ions, Nanomaterials 11 (1831) (2021) 1–11, https://doi.org/10.3390/nano11071831.

[38] C. Zhang, S. Wu, Y. Yu, F. Chen, Determination of thiourea based on the reversion of fluorescence quenching of nitrogen doped carbon dots by Hg2+, Spectrochim, Acta A 227 (117666) (2020) 1–6, https://doi.org/10.1016/j.saa.2019.117666.

[39] S. Karada, E.M. Görüsük, E. Çetinkaya, S. Deveci, K.B. Dönmez, E. Uncuoglu, M. Dogu, Development of an automated flow injection analysis system for determination of phosphate in nutrient solutions, J. Sci. Food Agric. 98 (2018) 3926–3934, https://doi.org/10.1002/jsfa.8911.

[40] TOPAS Advanced Polymers. http://www.topas.com, 2021 (Accessed October 28, 2021).

[41] G.A. Crosby, J.N. Demas, The measurement of photoluminescence quantum yields. A review, J. Phys. Chem. 75 (1971) 991–1024, https://doi.org/10.1021/j100678a001.

[42] Y. Song, S. Zhu, S. Xiang, X. Zhao, J. Zhang, H. Zhang, Y. Fu, B. Yang, Investigation into the fluorescence quenching behaviours and applications of carbon dots, Nanoscale 6 (2014) 4676–4682, https://doi.org/10.1039/c4nr00029c.

[43] A. de la Torre, S. Medina-Rodríguez, J.C. Segura, J.F. Fernández-Sánchez, A polynomial-exponent model for calibrating the frequency response of photoluminescence-based sensors, Sensors 20 (2020) 4635, https://doi.org/10.3390/s20164635.

[44] T. Htun, A negative deviation from stern–volmer equation in fluorescence quenching, J. Fluoresc. 14 (2004) 217–222, https://doi.org/10.1023/B:JOFL.0000016294.96775.fd.

**Alex Pascual-Esco** received a degree in Chemistry from Universitat Autònoma de Barcelona (UAB) in 2017. In 2018 obtained a Master's degree in Analytical Chemistry form Universitat de Barcelona (UB). Since October 2018, he is a Ph.D. candidate at the Sensors and Biosensors Group under the supervision of Dr. Mar Puyol. His research interests include the design and fabrication of microsystems for water quality monitoring (µTAS) based on LTCC and polymer technologies, microfluidic platforms for the synthesis of nanomaterials and optical sensors.

**Julián Alonso-Chamarro** received his Ph.D. in Analytical Chemistry in 1987 at the Autonomous University of Barcelona. He is Professor of Analytical Chemistry at the same university. He has co-authored more than 140 research papers on (Bio)chemical sensors and automated flow systems and is author of different patents about sensors and analytical instrumentation for environmental monitoring. His research interests include the design and fabrication of microsystems for chemical analysis (µTAS) based on LTCC, polymer and IC technologies, microfluidic platforms for the synthesis of nanomaterials and optical and electrochemical microsensors. Most of these developments were applied in the environmental and industrial control fields.

**Mar Puyol** completed her Ph.D. in Analytical Chemistry in 2002 from the Autonomous University of Barcelona. She was working as a researcher for two years in the Applied Physics Department of the Universidad de Zaragoza until 2006. She is author of more than 40 papers related on the field. Her research interests include the study and characterization of new chromo(fluoro)ionophores and its integration as recognition elements in miniaturized optochemical sensors, the development of microsystems for chemical analysis (µTAS) based on LTCC, polymer and IC technologies and its application in environmental, agri-food, space and biomedical fields, and the design and fabrication of microfluidic platforms for the synthesis of nanomaterials and for the development of (bio)chemical miniaturized analyzers based on the use of nanostructured materials.

# Live synthesis of selective Carbon Dots as fluorescent probes for cobalt determination in water with an automatic microanalyzer

Alex Pascual-Esco, Pere Lleonart, Antonio Calvo-López, Julián Alonso-Chamarro, and Mar Puyol

Microchimica Acta, 190, 400, 1-11.
https://doi.org/10.1007/s00604-023-05975-w

Microchimica Acta (2023) 190:400
https://doi.org/10.1007/s00604-023-05975-w

ORIGINAL PAPER

# Live synthesis of selective carbon dots as fluorescent probes for cobalt determination in water with an automatic microanalyzer

Alex Pascual-Esco[1] · Pere Lleonart[1] · Antonio Calvo-López[1] · Julián Alonso-Chamarro[1] · Mar Puyol[1]

Received: 13 June 2023 / Accepted: 28 August 2023
© The Author(s) 2023

## Abstract

A new strategy integrating the straight synthesis of carbon dots (CDs) and their direct use for the determination of heavy metals by means of fluorescence quenching is presented. The proposal consists of a modular analyzer, which includes a low temperature co-fired ceramics (LTCC) microreactor for the synthesis of CDs and a cyclic olefin copolymer (COC) microfluidic platform, which automatically performs a reverse flow injection analysis (rFIA) protocol for the determination of heavy metal ions in water by CD fluorescence quenching. As a proof of concept, nitrogen-doped CDs were synthesized from acrylic acid and ethylenediamine (ED) with quantum yields (QYs) of up to 44%, which are selective to cobalt. With the described system, we synthesized homogeneous CDs without the need for further purification and with the minimum consumption of reagents, and optimized fluorescence measurements can be performed with freshly obtained luminescent nanomaterials that have not undergone decomposition processes. They have an average hydrodynamic diameter of 4.2 ± 0.9 nm and maximum excitation and emission wavelengths at 358 nm and 452 nm, respectively. The system allows the automatic dilution and buffering of the synthesized CDs and the sample prior to the determination of cobalt. The concentration of cobalt was determined with good sensitivity and a limit of detection of 7 $\mu g \cdot L^{-1}$ with a linear range of 0.02–1 $mg \cdot L^{-1}$ of $Co^{2+}$. Spiked tap water and river water samples were analyzed, obtaining recovery from 98 to 104%. This demonstrates the potential of the equipment as an efficient on-site control system for heavy metal monitoring in water.

**Keywords** Microreactor · Carbon dots · Fluorescence quenching · Microfluidics · Cobalt determination

## Introduction

Environmental pollution is receiving more attention in the last decades. One of the most critical polluting agents are heavy metals, considering that they are not biodegradable and tend to accumulate in the ecosystem and different tissues of living beings [1]. Different heavy metals can be found naturally in the environment, but the rise of some human activities like mining, manufacturing, smelting, and the improper disposal of industrial wastes is contributing to an increase in their negative environmental and health impact [2–5]. The most common techniques used to analyze heavy metals include inductively coupled plasma mass spectrometry (ICP-MS), inductively coupled plasma optical emission spectrometry (ICP-OES), and atomic absorption spectrometry (AAS) [6, 7]. These techniques offer high analytical features in terms of sensitivity, accuracy, and precision but show some disadvantages for on-site monitoring because of the complexity and dimensions of the instrumentation, which hinders the possibility of carrying out measurements outside a laboratory and the need for specialized personnel [4]. In this sense, the miniaturization of analytical procedures through microfluidic devices solves some of the mentioned problems, increasing the portability and enabling the on-site continuous monitoring of a wide variety of analytes, including heavy metals [5, 8, 9].

Currently, with the fast expansion of nanotechnology, different photoluminescent nanoparticles have been investigated due to their potential applicability in sensing [10] and bioimaging [11], to list just a few fields. Their use as fluorescent probes for heavy metals analysis has proven to lead to better sensitivity and selectivity, improved detection limits, and faster response time [3, 12]. One type of

✉ Mar Puyol
mariadelmar.puyol@uab.cat

[1] Group of Sensors and Biosensors, Department of Chemistry, Faculty of Sciences, Universitat Autònoma de Barcelona, Carrer dels Til·lers s/n, Bellaterra, 08193 Cerdanyola del Vallès, Spain

Published online: 19 September 2023

photoluminescent nanoparticles that have recently drawn great attention from the scientific community are carbon dots (CDs). They are carbon nanoparticles with sizes below 10 nm [13] and have different characteristics to highlight as optical probes like their distinctive photoluminescence (strong fluorescence with tunable emission) [14] and good biocompatibility [15]. Compared to other luminescent molecules, CDs do not suffer from photobleaching, which is one of the major drawbacks of the formers, and compared to other luminescent nanomaterials such as quantum dots (QDs), CDs are water soluble directly from a one-pot synthesis [13], so it is not necessary to proceed with solubilization steps before its use. Due to their carbonaceous nature, they present lower toxicity than QDs [16, 17], which is in accordance with green chemistry. Finally, CDs have been successfully used to selectively detect different heavy metal ions in water by easy methods of preparation and functionalization [18, 19]. CDs can be easily modified by element doping [1]. More specifically, nitrogen doping originates an increase in fluorescence intensity of CDs, caused by changes in the electronic structure, and also leads to the formation of active sites [2, 20], which are useful for further surface functionalization in order to provide them with selectivity. However, the main bottom-up synthetic methods of CDs (hydrothermal synthesis and microwave-assisted synthesis) [1, 21] lack the required reproducibility to produce materials for analytical applications [21], which will directly impact the reliability of the final analytical result.

In order to face this issue, microreactor technology arises for synthesis process intensification [22–24]. It allows for enhancing reagents mixing and heat and mass transfer efficiency. In consequence, better control over the particle size distribution and a reduction in the consumption of energy and reagents are achieved. From the different substrate materials for microreactor fabrication, low temperature co-fired ceramics (LTCC) technology has some advantages like the capability to withstand harsh temperature and pressure conditions, chemical inertness, and compatibility with screen printing technology, which enables the easy integration of electrical components [11, 25, 26].

Taking this context into account, our proposal was the development of a modular automatic analyzer consisting of a cyclic olefin copolymer (COC) microfluidic system, which was optimized for the determination of heavy metals in water, and an LTCC microreactor for the direct synthesis of CDs and their use as fluorescent probes, without the need of any purification steps. The synthetic strategy used, an adaptation of a hydrothermal batch method, based on the use of a microreactor, takes profit of the advantages of a microfluidic continuous strategy that allows much better control of the chemical variables of the reaction (minimizing temperature gradients, increasing the speed of mixing, and controlling the reaction times), which improves the reproducibility of the synthesis processes. As an example of the integration of the optical probe synthesis and the water quality parameter analysis in a single unit, the microreactor was optimized to synthesize N-doped CDs, which were selective to cobalt(II), from two precursors, acrylic acid and ethylenediamine (ED) [27]. Therefore, the analytical microsystem was optimized to determine cobalt(II) in water samples, taking advantage of its fluorescence quenching effect on the CDs. Cobalt, which at trace levels is an essential element in the human body [28], is harmful at high concentrations, causing asthma, rhinitis, gastritis, and, in severe cases, cardiomyopathy [28, 29]. Although it is not a heavy metal that causes great concern, its determination in water served us perfectly as a model to validate our proposal.

## Experimental

### Reagents, materials, and preparation of precursors

All reagents, namely acrylic acid (99%), ethylenediamine (99%), citric acid (99%), sodium citrate tribasic (99%), quinine sulfate (90%), sulfuric acid (95%), and the metal salts $Co(NO_3)_2 \cdot 6H_2O$, $Hg(NO_3)_2 \cdot H_2O$, $Pb(NO_3)_2$, $FeCl_3 \cdot 6H_2O$, $Cu(NO_3)_2 \cdot 3H_2O$, $Ni(NO_3)_2 \cdot 6H_2O$, $Cd(NO_3)_2 \cdot 4H_2O$, $Zn(NO_3)_2 \cdot 6H_2O$, $NaNO_3$, $CaCl_2 \cdot 2H_2O$, $MgCl_2 \cdot 6H_2O$, and $Cr(NO_3)_3 \cdot 9H_2O$ (> 98% for all the metal salts) were supplied from Merck Sigma-Aldrich (Barcelona, Spain) (https://www.sigmaaldrich.com/ES/en).

Solutions of the precursors for the CD synthesis and 0.1 M citric/citrate (pH 4) buffer were prepared in MilliQ water. The solutions used for the CD characterization, selectivity, and cobalt ion determination were prepared in the mentioned buffer.

For the different syntheses of N-doped CDs, 1.6 mL of acrylic acid (99%, density 1.05 $g \cdot mL^{-1}$) was dissolved in 10 mL of MilliQ water (2.33 M) and loaded in a glass syringe (Hamilton series Gastight 1000 TLL). Three different concentrations of the nitrogen source precursor were prepared: 0.5 mL, 1.0 mL, and 1.5 mL of ED (99%, density 0.9 $g \cdot mL^{-1}$) were dissolved in 20 mL of MilliQ water in each case (0.37, 0.75, and 1.12 M, respectively). For each synthesis process, two glass syringes were loaded with the same nitrogen source precursor.

LTCC 951 green tapes with various thicknesses were supplied by DuPont Corporation (Wilmington, DE, USA) (https://www.dupont.es/) and used to fabricate the microreactor: 254 µm thick DuPont 951PX green tapes and 114 µm thick DuPont 951PT green tapes. DuPont 5742 gold co-fireable conductor paste was used to print the gold resistor, and DuPont 6141 silver co-fireable paste was used to print the contact pads.

The microfluidic platform was fabricated with COC sheets of diverse thicknesses and grades, which were purchased from TOPAS Advanced Polymers GmbH (Florence, KY, USA) (https://www.topas.com/): 400 µm Topas 5013 COC and 25 µm Topas 8007 COC layers.

## Fabrication of the low temperature co-fired ceramics (LTCC) and cyclic olefin copolymer (COC) microfluidic platform

The LTCC microreactor was fabricated by a procedure previously developed by our research group [11]. Briefly, the different layers of the microreactor were designed with computer-aided design (CAD) software. The microfluidic channels and other elements were cut in the LTCC green tapes using a Nd:YAG Protolaser 200 (LPKF Laser and Electronics, Garbsen, Germany) (https://www.lpkf.com/en/). Then, the processed layers were aligned and thermolaminated with a hydraulic press (Talleres Francisco Camps, Granollers, Spain) (http://www.tallerescamp.com/). Fluidics comprises three inlets for the introduction of the synthesis precursors, a spiral-shaped microfluidic channel, and an outlet. The cross-section dimensions of the channel are 525 µm width and 290 µm height, while the total length is 630 mm. With this, the total volume of the microreactor channel is approximately 100 µL.

The heating resistor, which occupies the same area as the microfluidic channel to reduce energy consumption, was screen-printed on the reverse of the fluidic inlets and outlet. Another LTCC green tape was laminated on top of the resistor, where the connecting pads were also screen-printed. The device with all the layers laminated was then sintered in a CBCWF11/23P16 programmable box furnace (Carbolite Gero, Hope Valley, England) (https://www.carbolite-gero.com/) following a two-step thermal profile, including a 1 h organic burnout at 350 °C and 1 h firing at 850 °C. Finally, a PT100 temperature sensor (Innovative Sensor Technology, Ebnat-Kappel, Switzerland) (https://www.ist-ag.com/en) was adhered to the microreactor using EPO-TEK H20E epoxy paste (Epoxy Technology, Billerica, MA, USA) (https://www.epotek.com/). The final device (Fig. 1b) has a thickness of 3 mm and a diameter of 6 cm.

The COC microfluidic platform that can be seen in Fig. 1b is 30 mm wide, 50 mm high, and 2 mm deep and has two inlets, a two-dimensional meander micromixer (0.8 mm wide and 1 mm deep), an optical flow cell (4.5 mm diameter and 1 mm deep), and an outlet. It was fabricated with a multilayered approach in the same way as the LTCC

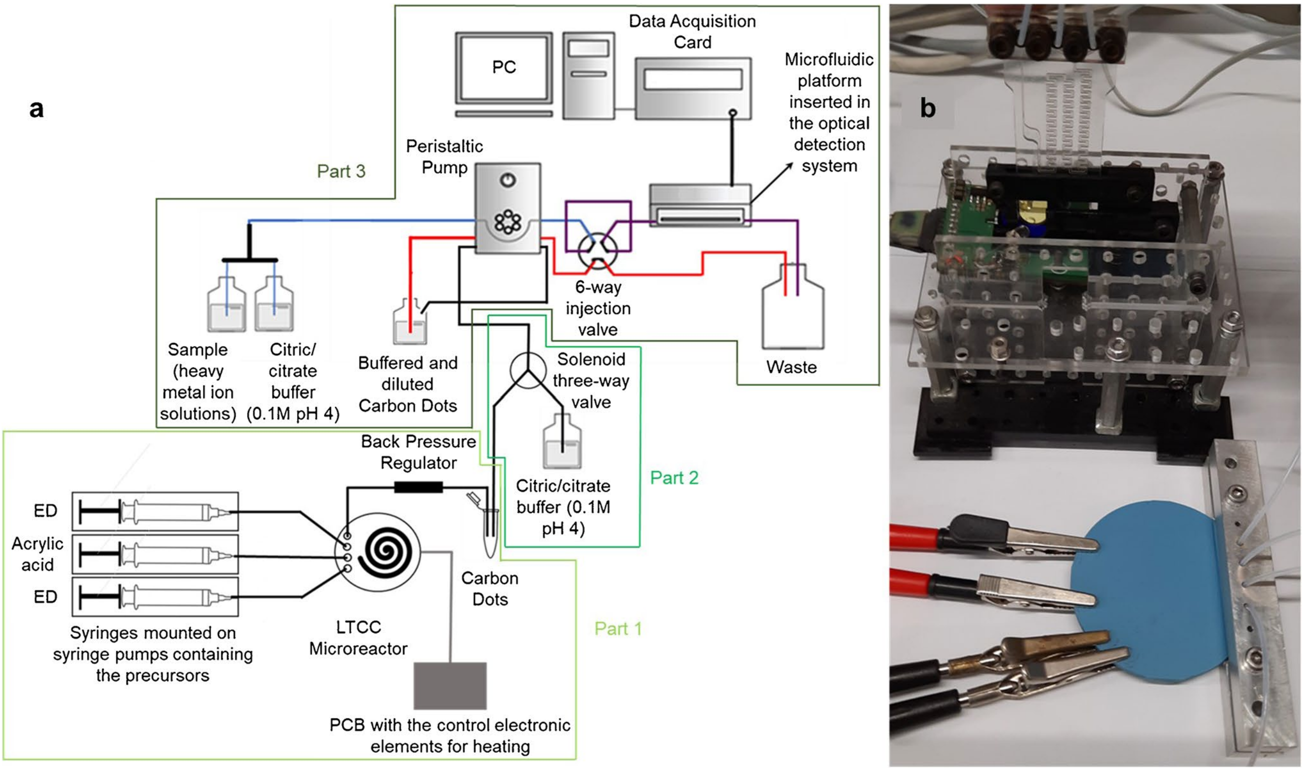

**Fig. 1** (**a**) Experimental setup used, including the synthesis of the CDs (part 1), their automated dilution (part 2), and the determination of $Co^{2+}$ (part 3). The fluidic management equipment is also depicted. (**b**) Detailed image including the microreactor with fluidics (secured with a custom-built aluminum connector) and electrical connections, and the custom-made miniaturized optical detection system with an inserted microfluidic platform

microreactor was. The process was also developed in our research group [8, 30], and the first step was the CAD design of the layers. Then, the different layers were micromachined on a Protomat S63 Computer Numerical Control (CNC) micromilling machine (LPKF Laser and Electronics Garbsen, Germany). As for the LTCC microreactor, when microfluidics were integrated into the COC substrate, the different layers were thermolaminated with the hydraulic press to obtain the final device.

## Carbon dots characterization and selectivity test

Absorption spectra of the synthesized CDs were registered with a UV-3101PC UV-Vis-NIR double beam spectrophotometer (Shimadzu, Kyoto, Japan) (https://www.shimadzu.com/), and fluorescence excitation and emission spectra were obtained with a Fluorolog FL3-11 spectrofluorometer (Horiba Jobin Yvon, Longjumeau, France) (https://www.horiba.com/int/scientific/). QY values were determined by applying the optically dilute measurement method [31] using quinine sulfate in 0.1 M sulfuric acid as a reference as follows:

$$\varphi_x = \varphi_{st} \times \frac{I_x}{I_{st}} \times \frac{A_{st}}{A_x} \times \frac{\eta_x^2}{\eta_{st}^2}$$

where $\varphi$ is the photoluminescence QY, $I$ is the integrated area of the corrected emission spectrum, $A$ is the absorbance, and $\eta$ is the refractive index of the solvent. The subindexes $x$ and $st$ refer to the sample and the reference standard, respectively. Considering that both the standard and sample were dissolved in water, the last term of the equation was ignored.

Fourier transform infrared (FTIR) spectra of the CDs were acquired with a Tensor 27 FTIR spectrophotometer (Bruker, Billerica, MA, USA) (https://www.bruker.com/en.html). High-resolution transmission electron microscopy (HR-TEM) images were collected using a Tecnai G2 F20 HR(S)TEM (Field Electron and Ion Company, Hillsboro, OR, USA) (https://www.fei.com), and dynamic light scattering (DLS) measurements were carried out in a Zetasizer Nano ZS (Malvern Panalytical, London, England) (https://www.malvernpanalytical.com/en) to check morphology and particle size distribution of the CDs.

To test the selectivity of the CDs, their emission spectra in the presence of different heavy metal ion solutions ($Cd^{2+}$, $Co^{2+}$, $Cu^{2+}$, $Cr^{3+}$, $Fe^{3+}$, $Hg^{2+}$, $Ni^{2+}$, $Pb^{2+}$, $Zn^{2+}$) at a concentration of 10 mg·L$^{-1}$ and other metal ions normally present in water ($Na^{+}$, $Mg^{2+}$, $Ca^{2+}$) at a concentration of 1000 mg·L$^{-1}$ were acquired per triplicate.

Emission spectra were recorded by mixing in a cuvette 0.5 mL of CD dispersion at the optimized dilution factor (to have an approximate absorption of 0.05 a.u. and avoid possible self-absorption effects) and 2.5 mL of citric/citrate buffer as reference emission value and with 2.5 mL of buffered solutions containing the mentioned metallic ions.

## Experimental setup

The complete system setup (Fig. 1a) is computer-controlled and consists of three main parts: (1) an automatic system for the synthesis of CDs (containing a fluidic management system and a temperature-controlled microreactor), (2) an interface (including the automated dilution of the CDs), and (3) the determination system of $Co^{2+}$ (containing a fluidic management system and the COC microfluidic platform integrated into a miniaturized optical detection system).

Part 1): For the synthesis of the CDs, three syringes were filled with the precursors. The syringes were mounted on three NE-500 OEM syringe pumps (New Era Pump Systems Inc., Farmingdale, NY, USA) (https://www.newerainstruments.com/) and connected to the microreactor using 0.8 mm internal diameter Teflon tubing (Tecnyfluor, Barcelona, Spain) (https://www.tecnyfluor.com/). The connections were secured with FPM75 O-rings (Epidor, Barcelona, Spain) (https://epidor-srt.com/) and a custom-built aluminum connector. To improve mixing, acrylic acid (the carbon source) was introduced through the central inlet, while ED (the nitrogen source) was introduced through the other two inlets, as can be seen in Fig. 1a. The pressure inside the microreactor was regulated by a back-pressure regulator connected to the outlet. A pressure of 17 bars was applied to all the syntheses, and three different working temperatures were tested (150 °C, 170 °C, and 190 °C). The synthesis precursors were pumped at a flow rate of 3.33 μL·min$^{-1}$ for each inlet (total flow rate of 10 μL·min$^{-1}$), and considering that the internal volume of the microreactor is about 100 μL, the residence time of the reagents is of approximately 10 min. The temperature was controlled by means of a proportional-integral-derivative (PID) system implemented on a PIC18F4431 microcontroller (Microchip Technology Inc., Chandler, AZ, USA) (https://www.microchip.com/), receiving the sensor input [32].

Part 2): CDs from the synthesis were automatically diluted and buffered at pH 4 with the help of a 161T031 three-way solenoid valve (NResearch, West Caldwell, NJ, USA) (https://www.nresearch.com/). They were diluted 100 times with 0.1 M citric/citrate buffer; 0.8 mm internal diameter Teflon tubing was used for fluidic connections. A FlowTest automated controller (BioTray, Villeurbanne, France) (https://www.biotray.fr) controlled the operation of the solenoid valve. It was programmed through the dedicated CosDesigner software.

Part 3): For the determination of $Co^{2+}$, a reverse flow injection analysis (rFIA) strategy was applied [30]. The diluted CDs were sequentially injected into the buffer (blank) and different $Co^{2+}$-containing solutions. The microfluidic setup includes a pre-buffering step of samples that is automatically performed by using an in-line T connector mixer, through which the sample and the buffer are introduced in a 1:1 ratio. The flow management is performed with a Gilson Minipuls 2 peristaltic pump (Middleton, WI, USA) (https://es.gilson.com/), 0.8 mm internal diameter Teflon tubing, and 1.14 mm internal diameter Tygon tubing (Ismatec, Wertheim, Germany) (https://heidolph-instruments.com/es/start). An MVP six-port injection valve (Hamilton Company, Bonaduz, Switzerland) (https://www.hamiltoncompany.com/) was used to inject the CDs, and the connections with the microfluidic platform are secured with FPM75 O-rings. The microfluidic platform is introduced in a custom-made miniaturized optical detection system previously reported [8, 30]. Briefly, it contains an LED emitting at 365 nm, a bandpass filter, and a PIN photodetector integrated into a printed circuit board (PCB). The insertion of the platform is based on a “lock-and-key” concept [8] that allows a reproducible positioning of the device with respect to the LED and the photodetector. The signal is obtained with a data acquisition card. Some parameters affecting signal-to-noise ratio were previously optimized [30]. To summarize, for this specific work, the following conditions were applied: CD injection volume of 500 μL, flow rate of 1.5 $mL \cdot min^{-1}$, signal amplification of 10, and integration time of 0.1 s.

With this method, a continuous photoluminescent signal was established, with a maximum value when CDs were injected into a solution without cobalt, and quenched values when the solution contained cobalt. The fluorescence intensity, which is obtained as the peak height, was correlated with the $Co^{2+}$ concentration using the Stern–Volmer equation [33].

### Analytical characterization for $Co^{2+}$ determination in water

The relative fluorescence intensity can be plotted against the quencher concentration (in this case, cobalt), according to the Stern–Volmer equation.

$$\frac{F_0}{F} = 1 + K_{SV} \times [Q]$$

where $F_0$ is the fluorescence intensity of the CDs in the absence of the quencher, $F$ is the fluorescence intensity of the CDs in the presence of the quenching species Q ($Co^{2+}$), and $K_{SV}$ is the Stern–Volmer quenching constant, which indicates the sensitivity of the method. According to the literature, the CD quenching mechanism of $Co^{2+}$ can be associated with static quenching [27].

Calibration plots were obtained by injecting per triplicate 100-time diluted CDs in standard solutions with different concentrations of cobalt, namely 0.01 $mg \cdot L^{-1}$, 0.05 $mg \cdot L^{-1}$, 0.1 $mg \cdot L^{-1}$, 0.5 $mg \cdot L^{-1}$, and 1 $mg \cdot L^{-1}$. This CD dilution ensures a good signal-to-noise ratio and avoids the inner filter effect (the absorbance is less than 0.04 at the maximum excitation wavelength of 365 nm). The repeatability of the measurement, calculated as relative standard deviation (RSD), was checked by performing ten injections of CDs into a solution containing 0.05 $mg \cdot L^{-1}$ of $Co^{2+}$. The limit of detection (LOD) and limit of quantification (LOQ) were calculated as three times and ten times the standard deviation of the blank signal (citric/citrate buffer) divided by the slope of the calibration plot ($K_{SV}$), respectively.

To assess the practical applicability of the synthesized CDs to determine $Co^{2+}$, spiked tap water and river water (Besòs river, Spain) samples were evaluated. The spiking process was done to undiluted samples prior to their analysis, and the concentration range was chosen, taking into consideration the maximum admissible limit of cobalt in drinking water set at 0.1 $mg \cdot L^{-1}$ by the US EPA. Therefore, four spiked concentrations of $Co^{2+}$ (0.10 $mg \cdot L^{-1}$, 0.25 $mg \cdot L^{-1}$, 0.50 $mg \cdot L^{-1}$, and 0.75 $mg \cdot L^{-1}$) were tested. Recovery rates and % RSD were calculated for three measurements, considering these concentrations as the true value because the concentration of $Co^{2+}$ in tap and river water samples was under the LOD (1 $\mu g \cdot L^{-1}$) determined by ICP-OES.

## Results and discussion

### Synthesis of carbon dots optimization

The modification of the reaction conditions such as temperature, pressure, reaction time, and molar fraction of the precursors allows modulating QYs because different proportions of the two fractions of CDs (crystalline and amorphous) can be obtained, but these do not affect significantly the maximum excitation and emission wavelengths. The effect of the concentration of the nitrogen precursor and the temperature over the resulting CDs were evaluated by comparing the corresponding QYs; 17 bars were the pressure chosen for all the syntheses due to channel occlusion observed at lower pressures [11].

As can be seen in Fig. 2, the temperature of the synthesis had an important effect on the QY of the CDs obtained, showing a maximum at 170 °C. Performing the reaction at higher temperatures can increase the carbonization, obtaining a carbon core-based product, which is more photostable

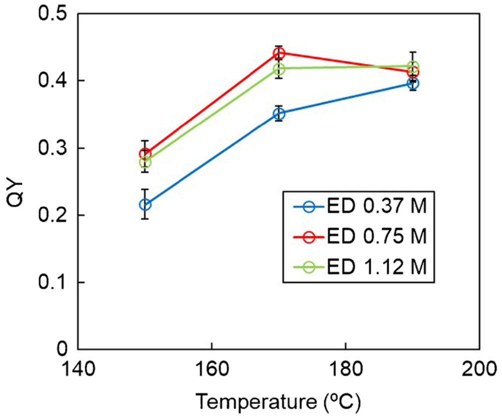

**Fig. 2** Comparison of the QYs of the CDs under different temperatures and different concentrations of nitrogen precursor (ED). All the syntheses were performed at 17 bars and with a solution of 2.33 M of carbon precursor (acrylic acid)

but has a lower QY [34]. Additionally, the effect of the precursor concentration was also noticeable. When the concentration of the ED solution was 0.37 M, lower QY values were obtained, indicating that the reaction was incomplete, while when the concentration of the ED solution was 1.12 M, the QY was lower than that obtained with the solution containing 0.75 M of ED, which means that an excess of ED in solution was affecting the final CDs QY.

Therefore, the optimal synthetic conditions to obtain the highest QY (44%) were using a solution containing 0.75 M of the nitrogen precursor and performing the synthesis at 170 °C and 17 bars.

## Characterization of carbon dots and selectivity tests

To follow the optical performance of the synthesized CDs, fluorescence emission and excitation spectra were examined (Fig. 3a). CDs showed wide excitation and emission bands with maximum intensities at 358 nm and 452 nm, respectively, obtaining a Stokes shift of approximately 100 nm.

An FTIR spectrum (Fig. 3b) was taken to characterize the functional groups present on the surface of the CDs. The following peaks can be observed, which can be assigned to different functional groups: the broad peak in the 3500–2500 cm$^{-1}$ area comes from stretching vibrations of O-H groups. Bands at 3170 cm$^{-1}$ and 3010 cm$^{-1}$ correspond with N-H of an amide group and with C-H stretching vibrations, respectively. The peak at 1646 cm$^{-1}$ can be assigned to the stretching vibration of C=O, the peak at 1550 cm$^{-1}$ to the C=C stretching vibration, the peak at 1388 cm$^{-1}$ belongs to the bending vibration of N-H, the one at 1278 cm$^{-1}$ is

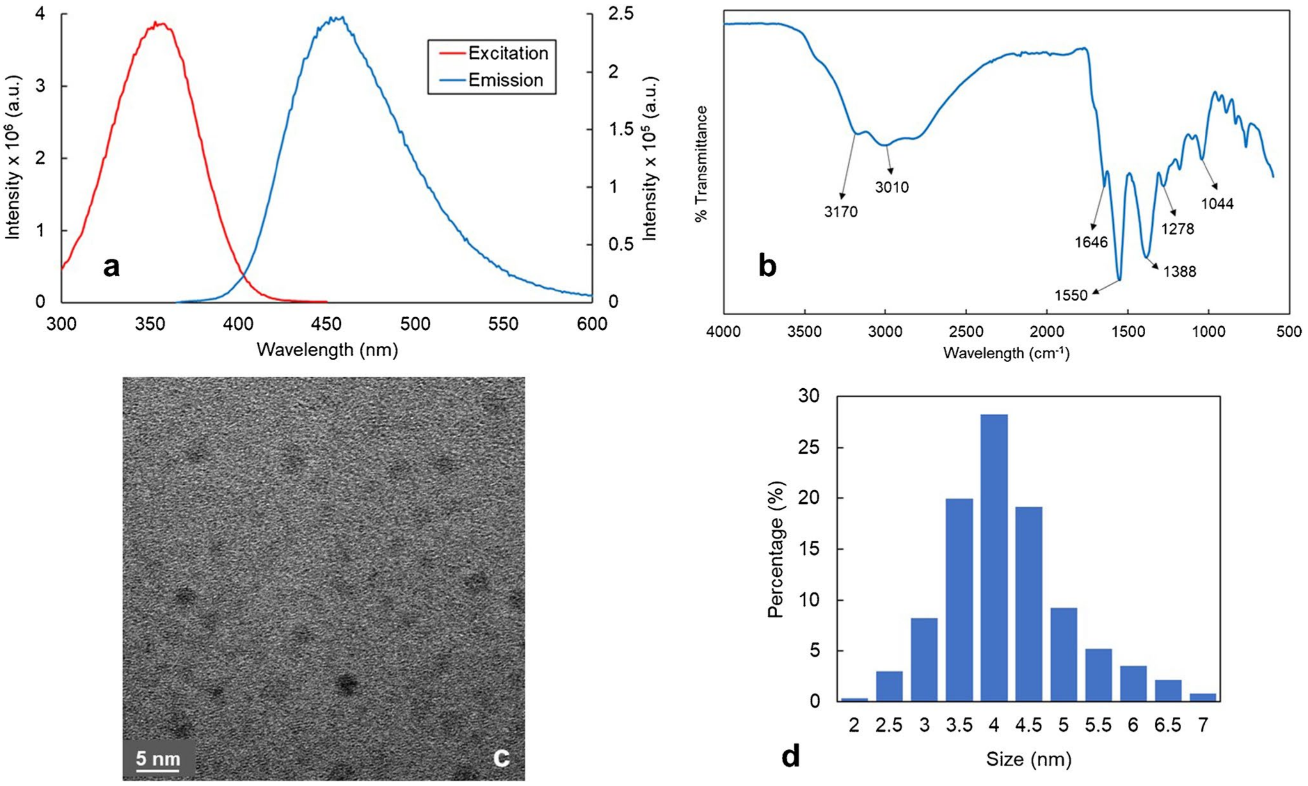

**Fig. 3** (**a**) Photoluminescence spectra of the synthesized CDs diluted 100 times to have an approximate absorption of 0.04 a.u; (**b**) FTIR spectrum of the undiluted CDs; (**c**) HR-TEM image of the undiluted CDs; and (**d**) DLS measurement of the undiluted CDs

from the asymmetric stretch of C-N, and, finally, the peak at 1044 cm$^{-1}$ is attributed to C-O aromatic stretching [35].

Results indicated that nitrogen functionalization was successful and that carboxyl, hydroxyl, amino, and amide bonds exist on the surface of the CDs, which can act as anchor sites to adsorb more Co$^{2+}$ on the CDs' surface to enhance the analysis sensitivity [27].

The morphology and size distribution of the CDs were studied through HR-TEM images and DLS measurements (Fig. 3c, d, respectively). Results show that the CDs have a quasi-spherical shape and an average hydrodynamic diameter of 4.2 ± 0.9 nm. However, it was very difficult to obtain high-quality contrast TEM images due to the formation of two fractions of CDs, one with a crystalline structure (carbon core particles) that can be identified thanks to the observation of the diffraction planes and another one that is amorphous and suggests the formation of polymer dots. These polymer dots have molecular fluorophore moieties embedded, causing the enhancement of the QY and making it more difficult to obtain TEM images [34]. Both fractions determine the optical characteristics of the final nanomaterial to be employed as an optical probe. In this sense, the use of the microreactor is of special importance because it allows better control of the synthetic conditions (temperature, pressure and precursors mixing) than batch methods. This assures to obtain not only more homogeneous CDs but also a high reproducibility between the different syntheses [36].

Selectivity is an important issue to assess the application of synthesized CDs as fluorescent probes. To evaluate selectivity, emission spectra of the CDs in the presence of different metal ion solutions (Ca$^{2+}$, Cd$^{2+}$, Co$^{2+}$, Cu$^{2+}$, Cr$^{3+}$, Fe$^{3+}$, Hg$^{2+}$, Mg$^{2+}$, Na$^{+}$, Ni$^{2+}$, Pb$^{2+}$, Zn$^{2+}$) were recorded. As can be seen in Fig. 4, the fluorescence intensity of CDs was only quenched by Co$^{2+}$ among all the other metal ions studied, suggesting that the synthesized CDs are selective to Co$^{2+}$. The interactions between Co$^{2+}$ ions and the functional groups of the surface of the CDs (-COOH, -OH, -CONH-) formed non-luminescent complexes, which can explain the observed decrease in fluorescence intensity [29, 33].

## Analytical performance

Different concentrations of cobalt were used to evaluate the analytical performance of the system. Figure 5a shows the transient fluorescence intensity signal of the microsystem by injecting the 100-time diluted CD dispersions into 0.1 M citric/citrate buffer (blank) and solutions of different concentrations of Co$^{2+}$. The obtained calibration plot (Fig. 5b) shows a good linear correlation ($R^2 = 0.996$) in the range of 0.02 to 1 mg·L$^{-1}$ of Co$^{2+}$. The Stern–Volmer quenching constant, which is equivalent to the sensitivity, obtained is 0.31 ± 0.01 L·mg$^{-1}$.

The repeatability of the system was calculated as the % RSD, obtaining a value of 1.3%, thus indicating good repeatability. Additionally, the LOD and LOQ were calculated, obtaining the values of 7 μg·L$^{-1}$ and 21 μg·L$^{-1}$ of Co$^{2+}$, respectively. The maximum admissible limit of cobalt in drinking water is not mentioned by the World Health Organization (WHO) nor the European Union (EU). As a reference value, the United States Environmental Protection Agency (US EPA) has fixed the maximum admissible limit at 0.1 mg·L$^{-1}$ [5].

The analytical features of other reported CD-based optical methods are summarized in Table 1. As it can be seen, these methods reach slightly lower LODs and wider linear ranges. However, the method presented in this work allows obtaining CDs with the highest QY, which ensures a strong signal even in case of possible reagent decomposition and as optical probes in the developed analyzer; they procure an LOD that is well below the reference value for Co$^{2+}$ set by the US EPA for drinking water. The automated synthesis of the CDs in the LTCC microreactor and its direct use for the determination of Co$^{2+}$ without any purification saves time and manual intervention. Compared to the reported manual methods based on batch fluorescence measurements, the

**Fig. 4** Representative study showing the selectivity by the representation of the ratio between the fluorescence after the addition of various metal ions to the CDs and the fluorescence of the CDs

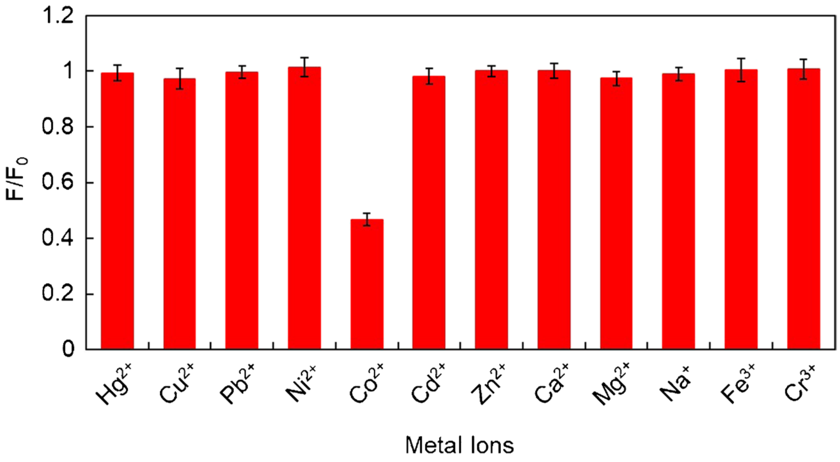

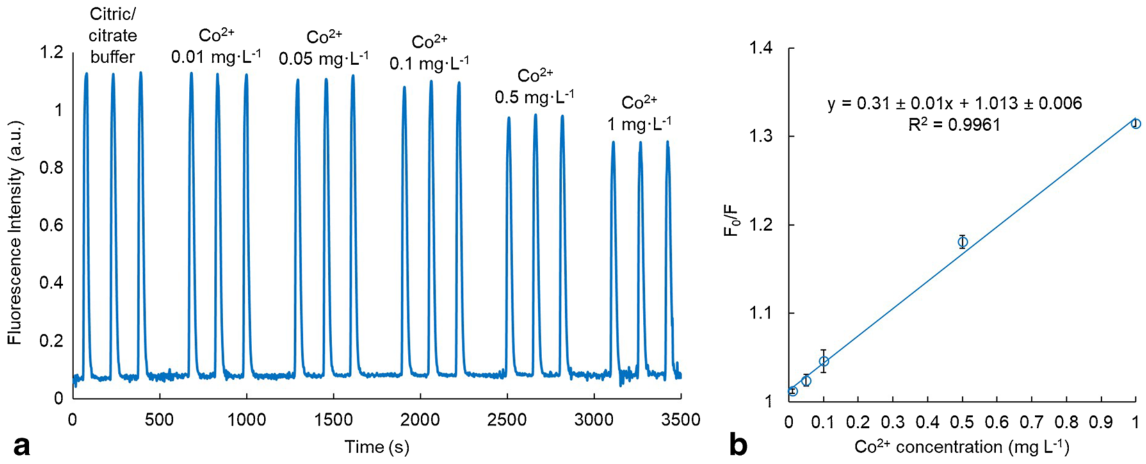

**Fig. 5** (**a**) Fluorescence intensity signal of the microsystem (obtained with an excitation source emitting at 365 nm, a CDs injection volume of 500 µL, and a flow rate of 1.5 mL·min$^{-1}$), where different peaks appear when the CDs were injected into the buffer (intensity value in the absence of the quencher ($F_0$)) and different standard solutions of the quencher (F). (**b**) Stern–Volmer plot of the quenching effect of $Co^{2+}$ on the fluorescence of the CDs

**Table 1** An overview of recently reported CD-based optical methods for the determination of $Co^{2+}$ ions

| Precursors | QY (%) | LOD (µg·L$^{-1}$) | Linear range (mg·L$^{-1}$) | Reference |
|---|---|---|---|---|
| Pyridoxal 5-phosphate and ethanediamine | 15 | 3 | 0–3.5 | [15] |
| L-cysteine | 27 | 2 | 0.06–2.9 | [37] |
| p-phenylenediamine and asparagine | 16 | 1 | 0.02–3.8 | [7] |
| Carbopol 934 and diethylenetriamine | 39 | 27 | 0–2.4 | [29] |
| Citric acid and L-cysteine | - | 5 | 0.005–5.9 | [38] |
| Acrylic acid and ethylenediamine | 23 | 15 | 0.06–3.5 | [27] |
| Acrylic acid and ethylenediamine | 44 | 7 | 0.02–1.0 | This work |

proposed analytical method fulfills other analytical features such as automation and portability.

Regarding the Stern–Volmer quenching constant ($K_{SV}$), it has been doubled (0.31 ± 0.01 L·mg$^{-1}$) compared with the synthetic method in batch (0.14 L·mg$^{-1}$) [27] indicating an improvement in the sensitivity.

Taking into consideration that the response time of the CDs-$Co^{2+}$ interaction to generate the analytical signal is approximately 2 min, the overall sample throughput was calculated at 30 h$^{-1}$. If, for monitoring purposes, an analyte was determined in the process solution to be monitored 4 times a day and the analyzer was calibrated with 5 standard solutions and the blank, all of them per triplicate, once a day, 30 measurements a day would be necessary to perform. This involves the synthesis of 150 µL of CDs a day (they are diluted 100 times in the system before the injection). In this situation, the microreactor would continuously perform the synthesis during 15 min. If other monitoring schedules were performed, the synthetic procedure would last differently.

The present modular prototype also has some limitations. To demonstrate its applicability for on-site monitoring, it would be necessary to compact the whole instrumentation to make it more portable, robust, automatic, and autonomous. Long-term studies of the performance in continuous operation of the system should be carried out to detect possible instrumental instability problems related to the fluidic microsystem or other interference effects derived from analyzing complex polluted sample matrices. Accuracy should also be assessed by comparison with a reference method for $Co^{2+}$ determination in water samples.

## Real sample analysis

The high selectivity and sensitivity of the synthesized CDs toward $Co^{2+}$ suggest that the current fluorescent sensor based on CDs can be applied for measuring $Co^{2+}$ in real water samples. To confirm that, spiked tap water and river water samples were analyzed. The results obtained are summarized in Table 2. The calculated recoveries are in the range between 98 and 104%, and RSD for three measurements is lower than 4% in all cases. This validates the application of the proposal for online $Co^{2+}$ determination in real water samples.

**Table 2** Determination of $Co^{2+}$ in spiked tap and river water samples ($n = 3$)

| Sample | $[Co^{2+}]$ added ($mg \cdot L^{-1}$) | $[Co^{2+}]$ found ($mg \cdot L^{-1}$) | Recovery (%) | RSD (%) |
|---|---|---|---|---|
| Tap water | 0.10 | 0.104 ± 0.007 | 104 | 2.8 |
| | 0.25 | 0.25 ± 0.02 | 101 | 2.5 |
| | 0.50 | 0.50 ± 0.02 | 100 | 1.6 |
| | 0.75 | 0.77 ± 0.05 | 102 | 2.5 |
| River water | 0.10 | 0.10 ± 0.01 | 102 | 3.8 |
| | 0.25 | 0.24 ± 0.02 | 98 | 2.9 |
| | 0.50 | 0.49 ± 0.02 | 99 | 2.0 |
| | 0.75 | 0.75 ± 0.04 | 100 | 2.0 |

## Conclusions

In this work, we describe a new analytical strategy for the direct use of freshly synthesized nanoparticles by microreactor technology as optical probes in automatic microanalyzers. The complete system is modular and consists of three main parts: a CD synthesis module with an LTCC microreactor, a dilution interface for the CDs obtained, and a fluorescence detection module containing a COC microsystem. All of this is computer-controlled for the automatic determination of heavy metals by fluorescence quenching. As a model system for the validation of the proposal, we synthesized highly efficient (high QYs) N-doped CDs from acrylic acid and ED to selectively determine $Co^{2+}$ ions in water samples.

To demonstrate the adequate performance of the system, $Co^{2+}$ was selectively detected among other heavy metal and metal ions usually present in water with high sensitivity and an LOD and LOQ of 7 $\mu g \cdot L^{-1}$ and 21 $\mu g \cdot L^{-1}$, respectively, that are well below the reference value set by the US EPA for drinking water. The target analyte was successfully determined in spiked tap water and river water samples with good accuracy and precision, thus demonstrating the viability to integrate the synthesis of the CDs prior to the analysis and their application as optical probes for $Co^{2+}$ determination in water. This represents an advantage not only in terms of automation of the synthesis but also in terms of the use of a fresh optical material that has not undergone any degradation prior to analysis. The reduced dimensions of the microreactor and the microfluidic platform allow for minimizing the amounts of reagents, which would favor less maintenance in a real application for heavy metals monitoring.

The proposed system offers the possibility of expanding the number of analytes to determine by synthesizing other types of selective CDs by alternating other precursors (containing N, S, P, etc.) and the reaction conditions (molar ratios and temperatures).

Further miniaturization and integration of the different modular parts are currently being performed for fluidic management by using computer-controlled micropumps and microvalves to improve portability and robustness. To demonstrate the applicability of the equipment in real on-site monitoring and for validation purposes, it will be necessary to evaluate the effect of organic matter present in water samples in the fluorescence quenching of the CDs, to perform long-term studies, compare results with a reference method, and analyze certified reference materials.

**Author contribution** Alex Pascual-Esco: conceptualization, methodology, investigation, formal analysis, validation, and writing – original draft; Pere Lleonart: investigation and formal analysis; Antonio Calvo-López: conceptualization and methodology; Julián Alonso-Chamarro: resources, project administration, funding acquisition, and writing – review and editing; Mar Puyol: conceptualization, resources, supervision, project administration, funding acquisition, writing – original draft, and writing – review and editing.

**Funding** Open Access Funding provided by Universitat Autonoma de Barcelona. This work is part of the grant PRE2018-084834 funded by MCIN/AEI/https://doi.org/10.13039/501100011033and by the "ESF Investing in your future." This work has been financially supported by the Spanish Ministry of Science and Innovation (MCIN) through project CTQ2017-85011-R and project PID2020-117216RB-I00, co-funded by FEDER (Fondo Europeo de Desarrollo Regional), and the Catalonia Government through project 2021SGR00124.

**Data Availability** Data will be made available on request.

## Declarations

**Conflict of interest** The authors declare no competing interests.

**Open Access** This article is licensed under a Creative Commons Attribution 4.0 International License, which permits use, sharing, adaptation, distribution and reproduction in any medium or format, as long as you give appropriate credit to the original author(s) and the source, provide a link to the Creative Commons licence, and indicate if changes were made. The images or other third party material in this article are included in the article's Creative Commons licence, unless indicated otherwise in a credit line to the material. If material is not included in the article's Creative Commons licence and your intended use is not permitted by statutory regulation or exceeds the permitted use, you will need to obtain permission directly from the copyright holder. To view a copy of this licence, visit http://creativecommons.org/licenses/by/4.0/.

## References

1. Mansuriya BD, Altintas Z (2021) Carbon dots: classification, properties, synthesis, characterization, and applications in health care - an updated review (2018–2021). Nanomaterials 11:2525. https://doi.org/10.3390/nano11102525
2. Qiu J, Zeng D, Lin Y, Ye W, Chen C, Xu Z, Hu G, Liu Y (2023) Carbon-polymer dot-based UV absorption and fluorescence performances for heavy metal ion detection. Spectrochim Acta A 285:121913. https://doi.org/10.1016/j.saa.2022.121913
3. Salahinejad M, Sadjadi S, Abdouss M (2021) Investigating fluorescence quenching of cysteine-functionalized carbon quantum dots by heavy metal ions: experimental and QSPR

studies. J Mol Liq 334:116067. https://doi.org/10.1016/j.molliq.2021.116067

4. Hebbar A, Selvaraj R, Vinayagam R, Varadavenkatesan T, Kumar PS, Duc PA, Rangasamy G (2023) A critical review on the environmental applications of carbon dots. Chemosphere 313:137308. https://doi.org/10.1016/j.chemosphere.2022.137308
5. Lace A, Cleary J (2021) A review of microfluidic detection strategies for heavy metals in water. Chemosensors 9:60. https://doi.org/10.3390/chemosensors9040060
6. Crawford SE, Kim KJ, Baltrus JP (2022) A portable fiber optic sensor for the luminescent sensing of cobalt ions using carbon dots. J Mater Chem C 10:16506–16516. https://doi.org/10.1039/d2tc02560d
7. Tian M, Liu Y, Wang Y, Zhang Y (2019) Facile synthesis of yellow fluorescent carbon dots for highly sensitive sensing of cobalt ions and biological imaging. Anal Methods 11:4077–4083. https://doi.org/10.1039/c9ay01244c
8. Ymbern O, Berenguel-Alonso M, Calvo-López A, Gómez-de Pedro S, Izquierdo D, Alonso-Chamarro J (2015) Versatile lock and key assembly for optical measurements with microfluidic platforms and cartridges. Anal Chem 87:1503–1508. https://doi.org/10.1021/ac504255t
9. Asif M, Tait RN, Berini P (2021) Hot embossing of microfluidics in cyclic-olefin co-polymer using a wafer aligner-bonder. Microsyst Technol 27:3899–3906. https://doi.org/10.1007/s00542-020-05188-8
10. Sodzel D, Khranovskyy V, Beni V, Turner APF, Viter R, Eriksson MO, Holtz PO, Janot JM, Bechelany M, Balme S, Smyntyna V, Kolesneva E, Dubovskaya L, Volotovski I, Ubelis A, Yakimova R (2015) Continuous sensing of hydrogen peroxide and glucose via quenching of the UV and visible luminescence of ZnO nanoparticles. Microchim Acta 182:1819–1826. https://doi.org/10.1007/s00604-015-1493-9
11. Berenguel-Alonso M, Ortiz-Gómez I, Fernández B, Couceiro P, Alonso-Chamarro J, Capitán-Vallvey LF, Salinas-Castillo A, Puyol M (2019) An LTCC monolithic microreactor for the synthesis of carbon dots with photoluminescence imaging of the reaction progress. Sens Actuators B Chem 296:126613. https://doi.org/10.1016/j.snb.2019.05.090
12. Chen T, Yin S, Wu J (2021) Nanomaterials meet microfluidics: improved analytical methods and high-throughput synthetic approaches. Trends Anal Chem 142:116309. https://doi.org/10.1016/j.trac.2021.116309
13. Zu F, Yan F, Bai Z, Xu J, Wang Y, Huang Y, Zhou X (2017) The quenching of the fluorescence of carbon dots: a review on mechanisms and applications. Microchim Acta 184:1899–1914. https://doi.org/10.1007/s00604-017-2318-9
14. Aswathy AO, Anju SM, Jayakrishna J, Vijila NS, Anjali Devi JS, Anjitha B, George S (2020) Investigation of heavy atom effect on fluorescence of carbon dots: NCDs and S, N-CDs. J Fluoresc 30:1337–1344. https://doi.org/10.1007/s10895-020-02607-x
15. Liao S, Zhu F, Zhao X, Yang H, Chen X (2018) A reusable P, N-doped carbon quantum dot fluorescent sensor for cobalt ion. Sens Actuators B Chem 260:156–164. https://doi.org/10.1016/j.snb.2017.12.206
16. Huang SW, Lin YF, Li YX, Hu CC, Chiu TC (2019) Synthesis of fluorescent carbon dots as selective and sensitive probes for cupric ions and cell imaging. Molecules 24:1785. https://doi.org/10.3390/molecules24091785
17. Zuo P, Lu X, Sun Z, Guo Y, He H (2016) A review on syntheses, properties, characterization and bioanalytical applications of fluorescent carbon dots. Microchim Acta 183:519–542. https://doi.org/10.1007/s00604-015-1705-3
18. Naik V, Zantye P, Gunjal D, Gore A, Anbhule P, Kowshik M, Sv B, Kolekar G (2019) Nitrogen-doped carbon dots via hydrothermal synthesis: naked eye fluorescent sensor for dopamine and used for multicolor cell imaging. ACS Appl Bio Mater 2:2069–2077. https://doi.org/10.1021/acsabm.9b00101
19. Liu T, Zhang S, Fan X, Yang D, Wang M, Shao X, Wang S, Yue Q (2022) Inner-filter effect induced fluorescence quenching of carbon dots for Cr(VI) detection with high sensitivity. J Fluoresc 32:2343–2350. https://doi.org/10.1007/s10895-022-03028-8
20. Hu G, Ge L, Li Y, Mukhtar M, Shen B, Yang D, Li J (2020) Carbon dots derived from flax straw for highly sensitive and selective detections of cobalt, chromium, and ascorbic acid. J Colloid Interf Sci 579:96–108. https://doi.org/10.1016/j.jcis.2020.06.034
21. Yu C, Zhuo C, Yundong W, Jianhong X (2022) Continuous synthesis of N, S co-coped carbon dots for selective detection of CD(II) ions. J Photochem Photobiol A 429:113910. https://doi.org/10.1016/j.jphotochem.2022.113910
22. Chen L, Wang CF, Liu C, Chen S (2022) Facile access to fabricate carbon dots and perspective of large-scale applications. Small 2206671:1–24. https://doi.org/10.1002/smll.202206671
23. Rao L, Tang Y, Li Z, Ding X, Liang G, Lu H, Yan C, Tang K, Yu B (2017) Efficient synthesis of highly fluorescent carbon dots by microreactor method and their application in Fe3+ ion detection. Mater Sci Eng C 81:213–223. https://doi.org/10.1016/j.msec.2017.07.046
24. Tang Y, Rao L, Li Z, Lu H, Yan C, Yu S, Ding X, Yu B (2018) Rapid synthesis of highly photoluminescent nitrogen-doped carbon quantum dots via a microreactor with foamy copper for the detection of Hg2+ ions. Sens Actuators B Chem 258:637–647. https://doi.org/10.1016/j.snb.2017.11.140
25. Golonka LJ, Zawada T, Radojewski J, Roguszczak H, Stefanow M (2006) LTCC microfluidic system. Int J Appl Ceram Technol 3:150–156. https://doi.org/10.1111/j.1744-7402.2006.02072.x
26. Lahti M, Kautio K, Karppinen M, Keränen K, Ollila J, Karioja P (2020) Review of LTCC technology for millimeter waves and photonics. Int J Electron Telecommu 66:361–367. https://doi.org/10.24425/ijet.2020.131886
27. Jing N, Tian M, Wang Y, Zhang Y (2019) Nitrogen-doped carbon dots synthesized from acrylic acid and ethylenediamine for simple and selective determination of cobalt ions in aqueous media. J Lumin 206:169–175. https://doi.org/10.1016/j.jlumin.2018.10.059
28. Bano D, Kumar V, Chandra S, Singh VK, Mohan S, Singh DK, Talat M, Hasan SH (2019) Synthesis of highly fluorescent nitrogen-rich carbon quantum dots and their application for the turn-off detection of cobalt(II). Opt Mater 92:311–318. https://doi.org/10.1016/j.optmat.2019.04.045
29. Kong D, Yan F, Han Z, Xu J, Guo X, Chen L (2016) Cobalt(II) ions detection using carbon dots as an sensitive and selective fluorescent probe. RSC Adv 6:67481–67487. https://doi.org/10.1039/c6ra12986b
30. Pascual-Esco A, Alonso-Chamarro J, Puyol M (2022) Rapid warning microanalyzer for heavy metals monitoring in natural waters. Sens Actuators B Chem 368:132180. https://doi.org/10.1016/j.snb.2022.132180
31. Crosby GA, Demas JN (1971) The measurement of photoluminescence quantum yields. A review. J Phys Chem 75:991–1024. https://doi.org/10.1021/j100678a001
32. Martínez-Cisneros CS, Gómez-de Pedro S, Puyol M, García-García J, Alonso-Chamarro J (2012) Design, fabrication and characterization of microreactors for high temperature syntheses. Chem Eng J 211–212:432–441. https://doi.org/10.1016/j.cej.2012.09.101
33. Song Y, Zhu S, Xiang S, Zhao X, Zhang J, Zhang H, Fu Y, Yang B (2014) Investigation into the fluorescence quenching behaviours and applications of carbon dots. Nanoscale 6:4676–4682. https://doi.org/10.1039/c4nr00029c
34. Wang J, Zhang P, Huang C, Liu G, Leung KCF, Wang YXJ (2015) High performance photoluminescent carbon dots for in vitro and in vivo bioimaging: effect of nitrogen doping ratios. Langmuir 31:8063–8073. https://doi.org/10.1021/acs.langmuir.5b01875
35. Smith BC (1999) Infrared spectral interpretation: a systematic approach. CRC Press LLC, Boca Raton. ISBN: 0-8493-2463-7
36. Gómez-de Pedro S, Puyol M, Izquierdo D, Salinas I, de la Fuente JM, Alonso-Chamarro J (2012) A ceramic microreactor for the synthesis of water soluble CdS and CdS/ZnS nanocrystals with on-line optical characterization. Nanoscale 4:1328–1335. https://doi.org/10.1039/c2nr11525e
37. Sun L, Liu Y, Wang Y, Xu J, Xiong Z, Zhao X, Xia Y (2021) Nitrogen and sulfur Co-doped carbon dots as selective and visual

sensors for monitoring cobalt ions. Opt Mater 112:110787. https://doi.org/10.1016/j.optmat.2020.110787

38. Chen Y, Shang P, Dong Y, Chi Y (2017) Regulating the overlap between the absorption spectrum of metal ion-chromogenic agent and the emission spectrum of carbon-based dots to improve the sensing performance for metal ions. Sens Actuators B Chem 242:1210–1215. https://doi.org/10.1016/j.snb.2016.09.102

**Publisher's Note** Springer Nature remains neutral with regard to jurisdictional claims in published maps and institutional affiliations.